

Simulation of Imaging Fourier Transform Spectrometers Using DIRSIG

by

François Alain

B.Eng., Computer Engineering
Royal Military College of Canada
1994

A thesis submitted in partial fulfillment of the
requirements for the degree of Master of Science
in the Chester F. Carlson Center for Imaging Science
of the College of Science
Rochester Institute of Technology

1999

Signature of the Author _____

Accepted by _____
Coordinator, M.S. Degree Program Date

CHESTER F. CARLSON
CENTER FOR IMAGING SCIENCE
COLLEGE OF SCIENCE
ROCHESTER INSTITUTE OF TECHNOLOGY
ROCHESTER, NEW YORK

CERTIFICATE OF APPROVAL

M.S. DEGREE THESIS

The M.S. Degree Thesis of François Alain
has been examined and approved by the thesis committee
as satisfactory for the thesis requirement for the
Master of Science degree

Dr. John R. Schott, Thesis Advisor

Dr. Roger Easton

Mr. Scott Brown

Maj. Wayne Farrell

Date

THESIS RELEASE PERMISSION
ROCHESTER INSTITUTE OF TECHNOLOGY
COLLEGE OF SCIENCE
CHESTER F. CARLSON
CENTER FOR IMAGING SCIENCE

Title of Thesis:

**Simulation of Imaging Fourier Transform
Spectrometers Using DIRSIG**

I, François Alain, hereby grant permission to Wallace Memorial Library of R.I.T. to reproduce my thesis in whole or in part. Any reproduction will not be for commercial use or profit.

Signature _____

Date

Simulation of Imaging Fourier Transform
Spectrometers Using DIRSIG

by
François Alain

Submitted to the
Chester F. Carlson
Center for Imaging Science
College of Science
in partial fulfillment of the requirements
for the Master of Science Degree
at the Rochester Institute of Technology

Abstract

Imaging Fourier Transform Spectrometers are becoming popular sensors for hyperspectral remote sensing. To evaluate sensor design artifacts and properties, it is useful to simulate their designs using a radiometrically correct ray-tracing tool. The Digital Imaging and Remote Sensing Image Generation model allows for such design and simulation of sensor properties.

Two different design types are evaluated and simulated. The first one is a Michelson-type interferometer. The sensor collects the image by operating in “stare mode”. The interferogram is collected over time by scanning one of the mirrors to generate the required optical path difference between the signals. The second design is a triangle-path (Sagnac) interferometer. With this design, the interferogram is collected spatially on the detector array, with one spatial dimension collected in the orthogonal coordinate (Hammer, et al., 1995). The sensor is operated in pushbroom mode to collect the other spatial dimension.

Simulated images and the effects of design artifacts are presented, along with the theory allowing their understanding. The effects of design artifacts are presented both individually and in combination with other artifacts. Results of the simulation of a full scene are shown and help indicate where those sensors can be useful. Finally, recommendations and future improvements to this research are listed.

Acknowledgements

I would like to thank Mr. Scott Brown for many hours spent modifying DIRSIG and explaining its inner-workings. Dr. John Schott, for the suggestion that lead to this project and for the advice that allowed the completion of this project. Dr. Roger Easton, who made it possible for me to understand the Fourier Transform process. Mr. Jim Chetwynd, for his help in getting me started with Fascode. Mr. Erich Hernandez-Baquero was also very helpful in reviewing my proposal. Dr. Bruce Rafert, from Michigan Technical University (MTU), is also to be thanked for reviewing a preliminary draft of this thesis and also providing me with simulation parameters for a Sagnac sensor. Thanks also go to Mr. Chia Chang and Mr. Chuck Farnung for their help in getting me started with DIRSIG.

To the Canadian Forces (CF), for allowing me to pursue my education as an integral part of my career, also many thanks. In a technological world such as the one we live in, it is important for an organization like as the CF to allow their members to understand the state of the art in technology. That's why I think the Post Graduate Training program is so important to the CF.

Finally, to my friends at the Chester F. Carlson Center for Imaging Science, the School of Photographic Arts and Sciences, and the Rochester area, thank you for your friendship over the past two years. As our contacts grow fainter over the coming years, you may rest assured I will still remember you.

Dedication

Dédié à ma famille:

Lucie et Yvon

Christine

Mireille, Erick, Maxime, Audrey et Arianne

Jean-Pierre

Table of Contents

List of Figures	x
List of Tables	xiii
1 Introduction	1
2 Background—Literature Review	4
2.1 Historical Perspective	4
2.2 Definition of Terms	5
2.3 Image Simulation and Modeling	6
2.3.1 MODTRAN/FASCODE	7
2.4 The Image Chain	9
2.5 Interferometry	10
2.6 Fourier Transform Spectrometers	13
2.6.1 Temporal FTS	15
2.6.2 Spatial FTS	18
2.6.3 Combination Spatial/Temporal instruments	23
2.6.4 Current Instruments (Existing Designs or Prototypes)	26
2.7 Advantages/Disadvantages	29
2.7.1 FTS vs Dispersive and Filtered Spectrometers	29
2.7.2 Michelson vs. Sagnac	31
2.8 Artifacts and Properties of FTS	32
2.8.1 Aliasing	33
2.8.2 Apodization	34
2.8.3 Source Temporal Spectral Variation	35
2.8.4 Dynamic Range	37
2.8.5 Off-Axis (Obliquity) Effects	41
2.8.6 Spectral Response (Detector, Amplifier, Optics)	45
2.8.7 Lenses and Optics	46
2.8.8 Error in Path Difference	48
2.8.9 Jitter Noise	49
2.8.10 Detector	50
2.8.11 Self-Emission and Thermal Noise	57
2.8.12 Vignetting	57
2.8.13 Dynamic Mirror Alignment	59
2.8.14 Miscellaneous	60

3	Approach	62
3.1	Program Design	62
3.1.1	User Interface Module	63
3.1.2	Input Radiance Modules	63
3.1.3	Optical Effects Module	65
3.1.4	Interferometer Module	66
3.1.5	Detector Module	66
3.1.6	FFT Module	66
3.1.7	Image Cube Module	66
3.1.8	Noise Module	67
3.1.9	Documentation	67
3.2	Testing	67
3.2.1	Scene One	68
3.2.2	Scene Two	68
3.2.3	Scene Three	68
3.2.4	Scene Four	69
3.2.5	Scene Five	70
3.2.6	Final Demo Scene	70
3.2.7	Tests for Architecture Compatibility	70
4	Results	71
4.1	Artifacts	71
4.1.1	Aliasing	72
4.1.2	Apodization	75
4.1.3	Source Temporal Spectral Variation	75
4.1.4	Dynamic Range	79
4.1.5	Off-Axis Effects	87
4.1.6	Spectral Response	90
4.1.7	Error in Optical Path Difference	91
4.1.8	Jitter Noise	93
4.1.9	Detector	95
4.1.10	Beamsplitter	108
4.1.11	Spatial oversampling (subpixel sampling)	109
4.1.12	Dynamic Mirror Alignment	115
4.2	Final Demo	115
4.2.1	Foxbat scene	115
4.2.2	NTS scene	116
4.3	Computation Time	125
5	Conclusions and Recommendations	126
5.1	Conclusions	126
5.2	Recommendations	126
5.3	Future Work	127
5.4	Timetable	128
A	Beamsplitter Transmission and Reflection Effects	130
A.1	Michelson	130
A.2	Sagnac	132

B Interference of Misregistered Pixels	135
B.1 Monochromatic Radiation	136
B.2 Polychromatic Case	138
B.3 Conclusion	138
C Validation of the Integration of FASCODE in the Atmospheric Database Generator	140
C.1 Introduction	140
C.2 MODTRAN <i>tape5</i> values	141
C.3 Graphic input file name definitions	144
C.4 TAU2 Comparison	145
C.5 PATH Thermal Comparison	149
C.6 Conclusion	154
D Source Code	155
D.1 Modifications to <i>make_adb</i>	155
D.1.1 Changes to <i>make_adb.nw</i>	155
D.1.2 New <i>fascode.nw</i> File	156
D.2 FTS sensor module	156
D.3 Changes to the main DIRSIG file	156
D.4 IDL IFTS parameter generation widget	156
D.4.1 IDL widget	157
D.4.2 Help files	157
D.5 Miscellaneous	168
Bibliography	169
Glossary	175

List of Figures

2.1	Solar energy paths used in DIRSIG	8
2.2	Thermal energy paths used in DIRSIG	9
2.3	Possible image chain for an imaging Fourier transform spectrometer	9
2.4	Non-imaging Michelson interferometer	11
2.5	Interferogram (left) and spectrum (right) for monochromatic source and infinite path difference	12
2.6	Interferogram (left) and spectrum (right) for monochromatic source and finite path difference	12
2.7	Interferogram (left) and spectrum (right) for monochromatic source and apodized interferogram. The interferogram is apodized by $\text{TRI}(\sigma/\delta_{\text{MAX}})$	12
2.8	Interferogram (left) and spectrum (right) for real polychromatic source	13
2.9	Elementary FT pair example: (a) SINC-like spectrum, (b) resulting interferogram.	15
2.10	Imaging Michelson Interferometer (Bennett, et al., 1993)	16
2.11	Rotary Turbo FTS (Wadsworth and Dybwad, 1997)	18
2.12	Effect of Fourier Optics (Sellar and Rafert, 1994). The source and the image (interferogram) are located at their respective focal distance from the lens.	19
2.13	Optical diagram of Sagnac interferometers using (a) lenses (Hammer, et al., 1992), (b) parabolic mirrors to avoid chromatic aberrations (Sweedler and Denton, 1989).	21
2.14	Source doubling interferometer optical diagram (Caulfield, 1979)	21
2.15	Optical diagram of a birefringent DASI (Author unknown, 19XXc)	22
2.16	Optical diagram of a tilted grating DASI (Hammer, et al., 1992)	23
2.17	Optical diagram for IRISHS	24
2.18	Interferogram collection process for IRISHS	25
2.19	Simple HEIFTS optical diagram	26
2.20	Spectral variation simulation input spectra: (a) start spectrum, (b) end spectrum, (c) sum of (a) and (b)	36
2.21	Spectral variation simulation interferograms: (a) interferogram of linear combination of spectra, (b) with apodization, (c) apodized interferogram with sudden change of spectra	36
2.22	Spectral variation simulation output spectra: (a) linear combination spectra, (b) apodized linear combination, (c) apodized sudden change	37
2.23	Example of signal input to detector and quantizer	38
2.24	Examples of different step sizes for 4-bit quantization	38
2.25	Original spectrum used for the quantization experiment	39
2.26	Interferogram (a) and spectrum (b) obtained with 12 bits quantization	40
2.27	Interferogram (a) and spectrum (b) obtained with 8 bits quantization	40
2.28	Change in GIFOV with pointing angle	42

2.29	Off-axis wave front propagation in Michelson interferometer	44
2.30	Frequency shift map for an 8×8 focal plane array (Oermann and Smithson, 1995) .	45
2.31	Reflected and transmitted paths through a beamsplitter	46
2.32	Similar noise distribution for a signal and FT pair	51
2.33	Skewed noise distribution for a signal and FT pair	53
2.34	Examples of step and scan delta sampling	55
2.35	Examples of mirror scanning blur simulations: (a) oversampled delta functions, (b) averaged delta functions	55
2.36	Examples of mirror scanning blur simulations: (a) for a below Nyquist frequency signal, (b) frequency signal above Nyquist	56
2.37	Effects of vignetting: (a) signal added to interferogram to simulate vignetting, (b) magnitude of Fourier transform of (a)	58
2.38	Vignetting simulation: (a) interferogram with vignetting, (b) recovered spectrum . .	58
2.39	Comparison of the effects of mirror misalignment on non-imaging and imaging FTS at the focal plane	60
3.1	Need for a radiance field at each view angle for imaging Michelson FTS	64
3.2	Test pattern for scene three	69
3.3	Test pattern for scene four	70
4.1	Example of aliasing	74
4.2	Step in interferogram amplitude due to periodicity: (a) original interferogram, (b) periodic interferogram over shifted window	75
4.3	Interferograms of tall wall for different collection methods from moving platform . .	77
4.4	Spectra of target and background	78
4.5	Spectra of tall wall for different collection methods from moving platform	79
4.6	Quantization example for pixel [1,1]	81
4.7	Quantization example for pixel [2,2]	82
4.8	Clipping example	84
4.9	Dramatic clipping example for pixel [0,0]	85
4.10	Example of side-lobes clipping	86
4.11	FPA arrangement for off-axis simulations	87
4.12	Example of off-axis effects on 8×8 FPA	89
4.13	Example of off-axis effects on 9×9 FPA	90
4.14	Example of spectral response simulation	91
4.15	Interferogram center for 3 OPD jitter simulations	92
4.16	Spectra with error in OPD	93
4.17	Scene hit point of jitter simulation	94
4.18	Target and background for the jitter scene	94
4.19	Effects of jitter on interferogram and spectrum	95
4.20	Noise distribution for Michelson simulation	96
4.21	Noise free pixel [2,2] (mean = 0.0, std dev = 0.0): (a) interferogram, (b) spectrum .	98
4.22	Bias shift for pixel [2,3] (mean = $1.0 \cdot 10^{-6}$, std dev = 0.0): (a) interferogram, (b) spectrum	98
4.23	Bias and noise for pixel [2,4] (mean = $1.0 \cdot 10^{-8}$, std dev = $1.0 \cdot 10^{-8}$): (a) interferogram, (b) spectrum	99
4.24	Noise for pixel [2,5] (mean = 0.0, std dev = $3.0 \cdot 10^{-8}$): (a) interferogram, (b) spectrum	99
4.25	Noise distribution for Sagnac simulation	100
4.26	Examples of noisy Sagnac data	101
4.27	Examples of defective pixels with noisy Sagnac data	102

4.28	Graphical description of interferogram oversampling	104
4.29	Results of 3x and 7x interferogram oversampling	105
4.30	Examples of “hot” and “cold” pixels	106
4.31	Spectra calculated from interferograms of Figure 4.30	108
4.32	Target hit points for delta sampling, 2x and 3x oversampling for an 8x8 image	110
4.33	Comparison of delta and subpixel sampling cases on pointing accuracy simulation — interferogram	111
4.34	Comparison of delta and subpixel sampling cases on pointing accuracy simulation — spectrum	111
4.35	Interferogram of tall wall for different collection methods from moving platform with subpixel sampling	113
4.36	Spectra for interferograms in figure 4.35	114
4.37	Foxbat scene as seen by a Sagnac IFTS	116
4.38	Gas absorbance spectra for plume gases over 680-1220 cm^{-1} range	118
4.39	Spectra of gas plume, background, and difference spectra	118
4.40	Gas absorbance spectra for plume gases over 2400-3072 cm^{-1} range	119
4.41	Spectra of gas plume, background, and difference spectra	119
4.42	NTS scene simulation: (a) $\sigma = 856.8 \text{ cm}^{-1}$ band, (b) $\sigma = 747.6 \text{ cm}^{-1}$ band	120
4.43	Interferogram corruption due to changing background when sensor rock point is above ground	122
4.44	Comparison of spatial blurring for two collection methods: (a) with rock point at ground level, (b) with rock point at plume level	123
4.45	Spectra of plume and background: (a) with rock point at ground level, (b) with rock point at plume level	124
4.46	Difference spectra for two collection methods	125
A.1	Michelson interferometer constructive interference intensity limits	132
A.2	Detected intensity for Sagnac destructive interference	134
A.3	Range of possible interference (constructive - destructive) for Sagnac interferometers	134
B.1	One cause of image misregistration is mirror misalignment	136
B.2	Effect of phase shift on addition of waveforms	138
B.3	Interferogram and spectrum obtained from misregistered pixels.	139
C.1	LOWTRAN vs. MODTRAN band model	143
C.2	Comparison with FASCODE	144
C.3	TAU2 LOWTRAN comparison, downsampled 2800 to 2900 cm^{-1} range	145
C.4	TAU2 LOWTRAN comparison, 3100 to 3200 cm^{-1} range	146
C.5	TAU2 LOWTRAN comparison, 3450 to 3550 cm^{-1} range	146
C.6	TAU2 LOWTRAN comparison, entire range	147
C.7	TAU2 MODTRAN comparison, 2500 to 2600 cm^{-1} range	148
C.8	TAU2 MODTRAN comparison, 2800 to 2900 cm^{-1} range	148
C.9	TAU2 MODTRAN comparison, 3200 to 3300 cm^{-1} range	149
C.10	Path LOWTRAN comparison, downsampled 2800 to 2900 cm^{-1} range	150
C.11	Path LOWTRAN comparison, 3100 to 3200 cm^{-1} range	150
C.12	Path LOWTRAN comparison, 3450 to 3550 cm^{-1} range	151
C.13	Path LOWTRAN comparison, entire range	152
C.14	Path MODTRAN comparison, 2500 to 2600 cm^{-1} range	153
C.15	Path MODTRAN comparison, 2800 to 2900 cm^{-1} range	153
C.16	Path MODTRAN comparison, 3200 to 3300 cm^{-1} range	154

List of Tables

2.1	Imaging Fourier Transform Spectrometers	27
2.2	Artifacts and Properties of FTS	33
3.1	Modules for FTS implementation with DIRSIG	63
4.1	Prediction of off-axis spectral shift	88
4.2	Comparisons of spectral shifts for an 8x8 FPA	89
4.3	Comparisons of spectral shifts for a 9x9 FPA	90
4.4	Noise mean and standard deviation	97
4.5	Detector noise description for a Sagnac interferometer	100
4.6	Spectra modulation factor for 3 simulations of finite sampling distance effects	105
4.7	Contents of a gain and bias description file	106
C.1	Graph input data file origins	144

Chapter 1

Introduction

Ever since mankind developed the technology necessary to acquire images of the environment, we have strived to extract the most information from them using all available cues. Some of the cues used in photo-interpretation to identify objects are (Schott, 1997): shape, size, tone, texture, pattern, shadow, and site. The term “tone” represents the brightness level in a monochrome image, or the color when multispectral images are considered. The color or spectrum of an object can tell a lot about its composition (*i.e.*, what the material is made off). Shape, size, pattern, and site refer to spatial characteristics of the image, while texture and shadow are cues that require both spatial and spectral information. Each of these cues contributes to the identification of the components of the image.

Humans use shape cues primarily to recognize and classify objects, while some objects or materials can only be recognized based on their color. For example, it is possible to tell which class of material is dissolved in water by evaluating its color. Most people would not be able to distinguish gold and silver from shape cues only, but the color of the metal can be used to readily tell them apart. One can see that the identification of components is more accurate and precise if all cues are available to the user, hence the need for images to include both spatial and spectral information. This is the domain of imaging spectrometers.

“Tell me what color you are and I will tell you what you are made of.”

This saying, based on the popular “Tell me what you eat and I will tell you who you are” version, simply qualifies the need for multispectral and hyperspectral images. Whereas the eye can only detect three colors, each being a large portion of a narrow region of the electromagnetic (EM)

spectrum, spectrometers can use a much larger portion of the EM spectrum and divide it in a multitude of narrow bands.

To identify individual exposed minerals, studies have shown that spectral resolutions of 20 nm or less were required (Goetz, 1995). Even better spectral resolution is required to identify gases. Generally, better spectral resolution leads to improved discrimination of objects.

Imaging spectrometers come in a multitude of flavors (Rapp and Register, 1995; Pritt, et al., 1997; Eismann, et al., 1996) including dispersive, filtered, and Fourier transform designs. These families are classified based on the general technical approach used to produce the required spatial/spectral image cube. Dispersive and filtered designs are generally intuitive and well understood. Because Fourier transform spectrometers (FTS) rely on the Fourier transform of the interference pattern to produce the spectral information, they are more complex to define and operate. The advent of fast computers and the development of the Fast Fourier Transform algorithm (FFT) enabled the use of FTS.

Because of the inherent complexities of FTS, the design of such instruments can be lengthy and complex. Simulation and modeling can bring a lot of insights to the final product. A recent publication summarizes this point (Blonski, et al., 1997):

Numerical simulations of the virtual device provide predictions of the performance characteristics which can be expected from the real device. Quantitative insights and understanding gained from the computational prototyping guide and accelerate the design work.

Advanced knowledge of the operational capabilities of a sensor is priceless, especially when the sensor in question will be carried by a satellite that will not be accessible for modifications and adjustments once launched. Accelerating the design work often leads to lower design costs. Simulations can provide managers with a better picture of the multiple design options, each having their advantages and limitations, and allow for an enlightened decision on the final product. Simulations of designs also allow for software developers to create and validate the algorithms that will be used with the new sensor. Other reasons for using synthetic image generation can be found in Schott (1997).

For IFTS to be selected for hyperspectral imaging, they must have some clear advantage to compensate for their complexity. The multiplex (Felgett) and throughput (Jacquinot) advantages are among the reasons to use FTS over other spectrometer designs (Mertz, 1965; Bell, 1972; Steel, 1983; Griffiths and de Haseth, 1986; Wolfe, 1997; Descour, 1996; Bennett, et al., 1993; Hayden

Smith and Schempp, 1991). These advantages usually result in a better signal-to-noise ratio (SNR) for the FTS over dispersive or filtered spectrometers.

In this research, the Digital Imaging and Remote Sensing laboratory (DIRS) Image Generation model (DIRSIG) was used to simulate different FTS operating parameters. To simulate the effects of the atmosphere on the final image, DIRSIG requires a radiative transfer model to simulate the transmission, scattering and emission of the atmosphere. The radiative transfer model used in DIRSIG at the start of this project is the moderate resolution atmospheric radiance and transmittance code (MODTRAN) , which is limited to a nominal resolution of 2.0 cm^{-1} (Wang, et al., 1996). Because temporal FTS have the possibility of achieving greater resolutions, the Fast Atmospheric Signature CODE (FASCODE) was incorporated in the DIRSIG atmospheric database builder to supplement MODTRAN. High-resolution spectra are required to demonstrate the improved spectral resolution that can be obtained by FTS.

Chapter 2 describes the inner workings of FTS and its associated artifacts. Chapter 3 contains preliminary design and testing strategies for the planned simulations. Chapter 4 presents the results of the simulations compared to the theoretical values. Chapter 5 presents a summary of this research, lists recommendations and future work on simulating FTS and using/modifying DIRSIG. The appendices contain a derivation of the effect of beamsplitter reflectance and transmittance on FTS, a derivation of the effects of misregistered pixels due to misaligned mirrors, and a validation of FASCODE's integration within *make_adb*. Some of the code developed for this project is also included in the appendix.

Chapter 2

Background—Literature Review

2.1 Historical Perspective

“Holographic spectroscopy” and “interferometric spectrometry” are names that were once commonly used to represent Fourier transform spectrometry (Caulfield, 1979). The name “holographic spectrometry” comes from the fact that an interference pattern is recorded on photographic media (film), and the spectrum of the source is reconstructed by illuminating with a coherent source. This process is similar to the process used for holography. With this process, the time interval between the collection of the interferogram and generating the spectrum can be fairly long. Use of computers and electronic detectors helped reduce these delays.

Until fairly recently, all FTS were point devices that did not create images, but rather spectra of single objects. These spectrometers were used mainly in laboratories or for remote chemical content analysis. Many spaceborne and interplanetary mission probes carry “single-point” FTS (Persky, 1995). Since more information can be extracted from data when both spatial and spectral information are present, the need for imaging FTS (IFTS) became obvious. Also, only recently has computer processing power been readily accessible to attempt Imaging-type FTS. Currently, only a few of a multitude of airborne and spaceborne spectrometers are FTS (Nieke, et al., 1997).

In addition to computer costs and power, the limited field of view (FOV) also constrained the usage of FTS as imaging spectrometers (Horton, 1996).

2.2 Definition of Terms

Most people describe the electromagnetic spectrum in terms of wavelength, λ (in μm or nm). For people working with FTS, it is more convenient refer to wavenumbers, σ (in cm^{-1}). The conversion is simply $\lambda = 10000/\sigma$, with λ in nm and σ in cm^{-1} . The wavenumber is a convenient method of representing FTS-borne spectra since it is proportional to the spatial frequency of the interferogram fringe pattern, which can be related to the optical path difference (OPD). Note that the wavenumber is not a unit, but a description that indicates that the frequency is represented in units of reciprocal distance. ν and k are also commonly used in the literature to designate a wavenumber (Schumann, et al., 1997; Bohlender, 1994).

The intensity of the signal observed at the detector plane as a function of the OPD is known as the interferogram (Johnston, 1991). The peak intensity of an interferogram from a polychromatic source is located where all optical paths are equal, i.e., at the zero path difference (ZPD) location. This is also known as the “center burst” of the interferogram.

Spectrometers are usually qualified in terms of resolution, which describes the width of the passband. The resolving power (RP) is a method of qualifying the resolution of a spectrometer and is defined as (Wolfe, 1997):

$$RP = Q = \frac{\lambda}{\delta\lambda} = \frac{\sigma}{\delta\sigma} \quad (2.1)$$

where λ and σ are the center wavelength and wavenumber, respectively, and $\delta\lambda$ and $\delta\sigma$ are the spread of the band in wavelength and wavenumber. These are usually defined as the full width at half maximum (FWHM) of the line spread function. In reality, $\sigma/\delta\sigma = -\lambda/\delta\lambda$, but this fact is overlooked because it doesn't change the significance of the equation. Better resolution is indicated by a larger RP. In electronics, Q is known as the quality factor of a circuit. Also of importance is the fact that the resolving power is equivalent whether one uses wavelength or reciprocal centimeter units.

Some confusion always arises when interferograms are represented in terms of frequency. Temporal frequency units only make physical sense when the interferogram is collected temporally. For a scanning mirror Michelson interferometer, the frequency relates to the wavenumber in the following way:

$$f[\text{sec}^{-1}] = 2v\sigma \text{ [cm/sec} \cdot \text{cm}^{-1}] \quad (2.2)$$

where v is the speed of the scanning mirror. The fringe frequency f is a function of the radiation at wavenumber σ . The wavenumber spatial frequency can also be confused with the image spatial frequency [lines/mm]. For this reason, I will use the term “spatial frequency” when describing the image spatial resolution. I will represent interferogram fringes frequency in terms of wavenumbers [cm^{-1}] or Hertz [sec^{-1}], or simply in terms of data samples.

To test and explain some of the properties of the FTS, many one-dimensional special functions will be used such as SINC, RECT, and Dirac delta. The definitions for these functions can be found in Gaskill (1978).

2.3 Image Simulation and Modeling

Images of simulated environments may be generated with physical 3-D models and/or with computerized models. Physical models are outside the scope of this research. DIRSIG is a model used for image simulation and modeling.

The DIRSIG model is an integrated collection of independent first principles based submodels which work in conjunction to produce radiance field images with high radiometric fidelity in the 0.3 - 20 micron region. This modular design creates a high degree of flexibility and interchangeability within the model, as well as the capability to diagnose and improve the model by isolating and analyzing each submodel (Brown, 19XX).

The submodels are: scene geometry, ray tracing, thermal, radiometry, and sensor. Each submodel contributes to the final image by simulating a different part of the imaging chain. The output of one submodel is cascaded to the next submodel. The scene geometry submodel is the process by which 3-D objects and their associated properties are inserted in the scene. The ray tracer submodel acts on the scene to determine which objects will contribute to the radiance of a pixel. The thermal submodel calculates the temperature of objects and background in the scene. This information is required by the radiometry submodel to calculate the self-emission component of the radiance computation. *MODTRAN* is used to compute all atmospheric components. Finally, the sensor submodel simulates the effects of the sensor on the radiance image.

Prior to this project, the sensor submodel in DIRSIG could not simulate any FTS-type sensor. The goal of this research was to create the tools necessary for such modelling. FTS modelling programs do exist (Holbert, et al., 1995; Rafert, et al., 1995; Hammer, et al., 1993; Blonski, et al., 1997), but no IFTS sensor had ever been adapted to DIRSIG.

2.3.1 MODTRAN/FASCODE

MODTRAN's spectral resolution is limited to 2 cm^{-1} (20 cm^{-1} in the UV) (Calfas, 19XX). A study has shown that *MODTRAN*-calculated spectra degraded to a spectral resolution of 4 cm^{-1} were in better agreement with instrument measurements (Wang, et al., 1996). Note that the instrument measurements were also degraded to 4 cm^{-1} . Because FTS, especially Michelson devices, can achieve better spectral resolution than 2 cm^{-1} , DIRSIG's radiometry submodel needed to be upgraded to use a first-principles line-by-line atmospheric radiative transfer code known as *FASCODE*. It uses information in the High-resolution TRANsmission (HITRAN) molecular absorption database to calculate the required radiance and transmittance. *FASCODE* was adapted to DIRSIG's atmospheric database generator in support of this project. *FASCODE* has a few limitations that are not shared by *MODTRAN* (Wang, et al., 1996). First, *FASCODE* is slower to compute by a factor of 100. Secondly, *FASCODE* is limited to a 525 cm^{-1} spectral range per calculation. A wider spectral range requires many runs. Improvements to *FASCODE* that will increase this range are under development (Author unknown, 19XXb). A third limitation is that solar and lunar contributions are not included in *FASCODE*, which may cause disagreements between collected and simulated spectra when exoatmospheric sources are present, especially at shorter wavelengths. However, the requirement for solar and lunar contributions in conjunction with the use of *FASCODE* will not occur frequently. In long-wave infrared radiation, the contributions of exoatmospheric sources are negligible. Therefore, *FASCODE* can be used without fear of introducing large errors in the simulation. In the visible near-infrared region, *MODTRAN*'s 2 cm^{-1} resolution is more than adequate for identifying mineral spectra and gases. At a wavelength of 450 nm , a resolution of 2 cm^{-1} is equivalent to 0.0405 nm in resolution. At $1.1\text{ }\mu\text{m}$, it is 0.242 nm . In the mid-wave infrared, while the exoatmospheric sources are important enough to warrant their use in the simulations, *MODTRAN*'s resolution limit does not allow for clear identification of gases spectra. This is why *FASCODE* is used only for collecting the sensor path transmission and path thermal emission parts of the atmospheric database. *MODTRAN* is still used for the remaining parts of the atmospheric database, with *MODTRAN*'s output being interpolated to the required resolution. See Appendix C for a validation of *FASCODE*'s integration in *make_adb*. Figures 2.1 and 2.2 illustrate the solar and thermal energy paths. In the solar regime, *MODTRAN* is used for all radiance and transmission calculations. In the thermal regime, *FASCODE* is used for the path thermal and path transmission only if the required resolution is below 2.0 cm^{-1} .

“Therm” is the program that models the energy emission from scene objects and *MODTRAN* is used for the remainder of the calculations.

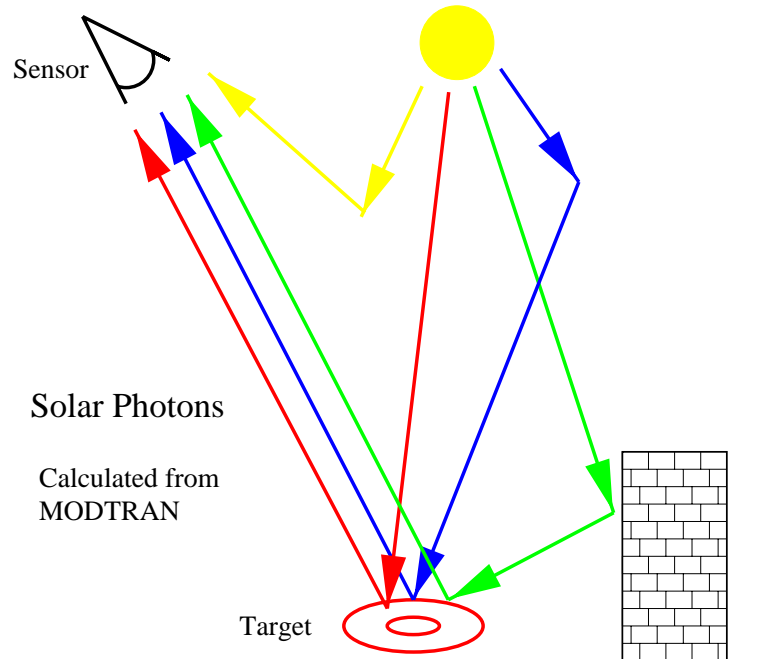


Figure 2.1: Solar energy paths used in DIRSIG

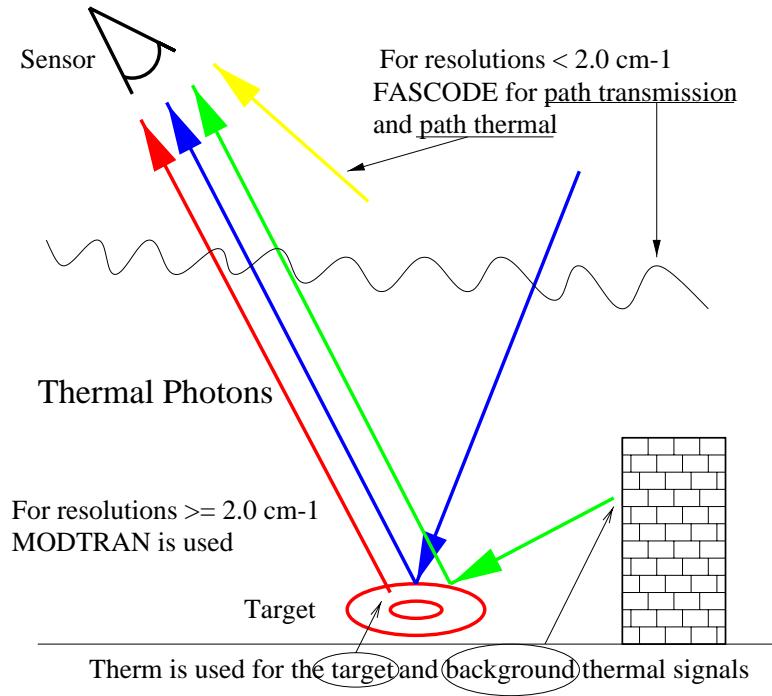


Figure 2.2: Thermal energy paths used in DIRSIG

2.4 The Image Chain

The final image (print, computer image, etc) viewed by an observer is the result of all interactions that occurred to a photon, or a chemical or electrical signal, from the time it was generated to the time the image is viewed. Figure 2.3 shows an appropriate image chain for a FTS. The “links” displayed in this image represent a stage in the image chain that will be independently simulated in this project. One of the objectives of this research is to design the FTS simulator in a way such that all steps in the image chain can be viewed if necessary.

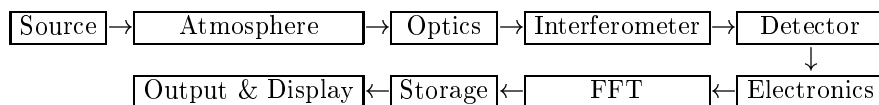


Figure 2.3: Possible image chain for an imaging Fourier transform spectrometer

Much of DIRSIG’s current functionality can be reused to simulate a FTS image chain. The

scene geometry, ray tracing, thermal, and radiometry submodels represent the source and atmosphere stages of the image chain. The only modification required to these submodels was the implementation of *FASCODE*. The sensor submodel regroups the optics, interferometer, detector, electronics, and FFT stages. Since much of the required functionality does not exist or is not appropriate for FTS usage, a different sensor submodel was required. However the new sensor submodel can hide this fact to the user and maintain the “feel” of the current sensor submodel. The storage and output & display stages, although depicted last in the image chain, can be duplicated and inserted almost anywhere. This flexibility is required to allow a user to see every step of the image chain. It also has the added advantage of providing the possibility of generating “before” and “after” images.

2.5 Interferometry

The wave nature of EM radiation is the basis for interferometry. An interferometer is an instrument that causes light to traverse more than one path from its source to the point of detection (Steel, 1983). When the radiation is recombined at the point of detection, constructive or destructive interference occurs depending on the phase shifts between interfering beams. Constructive interference occurs where the phase shift between two coherent monochromatic beams is an even multiple of π so that the two waves add. If the phase shift is an odd multiple of π , the beams will cancel. Intermediate phase shifts produce a combination of the two modes. For polychromatic light, the sum of the interference amplitude for each wavelength produce the interferogram.

The mode of operation of a simple Michelson interferometer (Wolfe, 1997) is illustrated in Figure 2.4. Two beams of light coming from a source are generated by the “beamsplitter”, which is a partial reflector created by applying a coating to an optical flat. For a typical beamsplitter, about half of the radiation is reflected and the other half transmitted. The reflected portion is directed towards a fixed mirror and returned to the beamsplitter while a moveable (“scanning”) mirror reflects the transmitted portion of the beam. When these two beams rejoin at the beamsplitter, they interfere to different degrees depending on the difference in optical path. Moving one mirror will produce a different interference pattern at the detector plane. Note that while not explicitly shown on the image, about half of the radiation reflected from the mirrors and recombined at the beamsplitter will be returned to the source, thereby reducing the amount of light available at the detector plane. The spectrum is recovered by taking the Fourier transform (FT) of the interferogram.

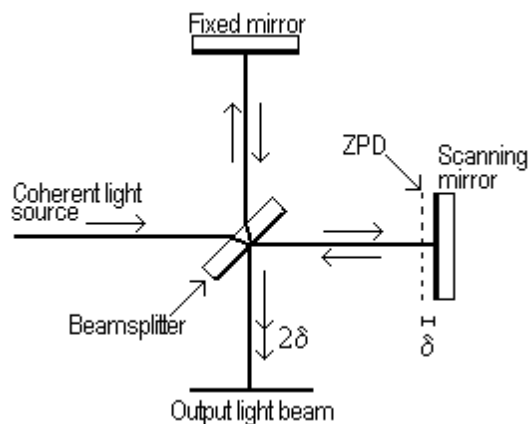


Figure 2.4: Non-imaging Michelson interferometer

Although not shown in Figure 2.4, Michelson FTS devices often include an optical “compensator”, which is made of the same material and has the same thickness as the beamsplitter. Its purpose is to ensure that both beams will traverse the same optical path when the mirrors are located at the same physical distance. The requirement for the compensator is due to the fact that the semi-reflective coating is generally on one of the side of the beamsplitter. This causes one of the beams to travel through the beamsplitter three times while the other goes through once. The compensating plate is a way of adding the two missing passes through the beamsplitter material for one of the beams.

Figures 2.5 to 2.8 depict different forms of interferograms and the resulting spectra (Persky, 1995). Figures 2.6 and 2.7 show examples of spectra. The resolution would be considered to be the full width at half maximum (FWHM) of the main lobe of the spectrum. Note that windowing with a triangle function (Figure 2.7) has the property of reducing “ringing” in the spectrum at the expense of slightly worse resolution. For interferograms of polychromatic sources, windowing is not necessary as long as the extrema of the interferogram are located close to the mean interferogram amplitude, as shown in Figure 2.8.

MONOCHROMATIC SOURCE ($-\infty < \delta < \infty$)

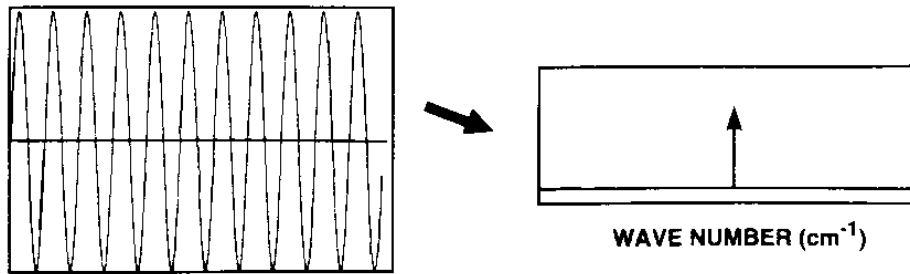


Figure 2.5: Interferogram (left) and spectrum (right) for monochromatic source and infinite path difference

MONOCHROMATIC SOURCE ($-\delta_{\text{MAX}} < \delta < +\delta_{\text{MAX}}$)

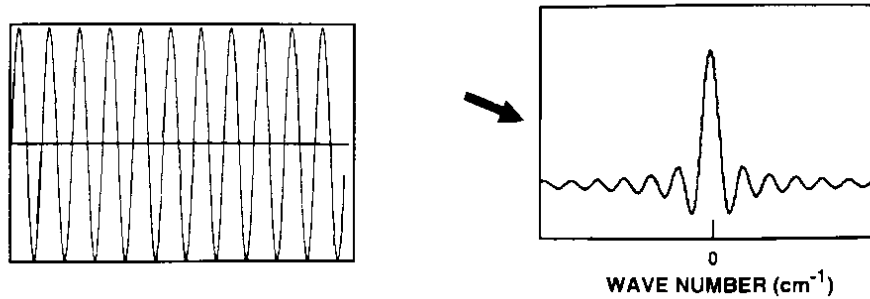


Figure 2.6: Interferogram (left) and spectrum (right) for monochromatic source and finite path difference

MONOCHROMATIC SOURCE (With Apodization)

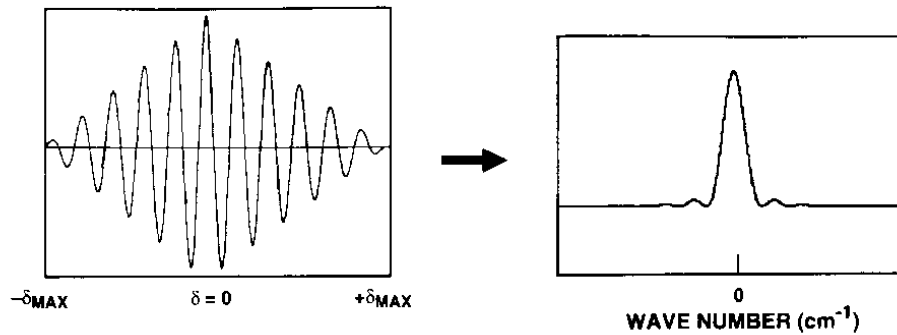


Figure 2.7: Interferogram (left) and spectrum (right) for monochromatic source and apodized interferogram. The interferogram is apodized by $\text{TRI}(\sigma/\delta_{\text{MAX}})$.

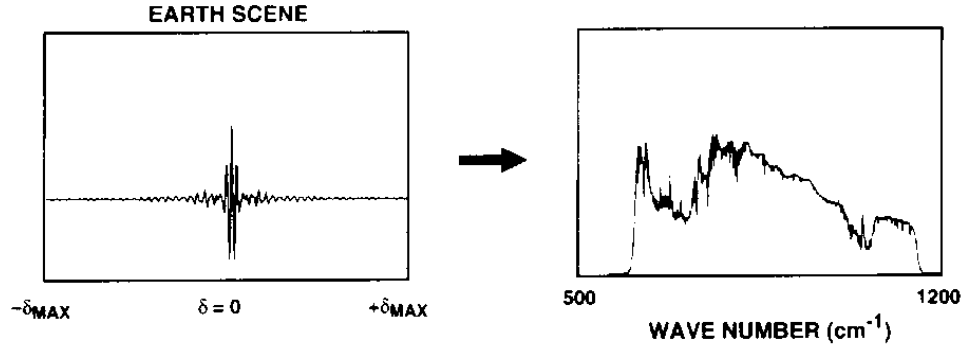


Figure 2.8: Interferogram (left) and spectrum (right) for real polychromatic source

2.6 Fourier Transform Spectrometers

The intensity of the signal observed by the detector is a function of the OPD δ . This function is often referred to as the “interferogram” and may be expressed as:

$$I(\delta) = \frac{1}{2} \int_{-\infty}^{+\infty} S(\sigma) \{1 + \cos(2\pi\sigma\delta)\} d\sigma \quad (2.3)$$

where $S(\sigma)$ represents the intensity of the source as a function of wavenumber σ modulated by the characteristics of the instrument, and δ is the OPD. This equation is derived in Beer (1992). A general equation is derived in Appendix B. Since negative wavenumbers have no physical meaning, Equation 2.3 may be expressed as a single-sided integral:

$$I(\delta) = \int_0^{+\infty} S(\sigma) \{1 + \cos(2\pi\sigma\delta)\} d\sigma \quad (2.4)$$

The only effect on the integral is a factor of two. The significance of the additive unit in the equation is that the intensity of the interferogram at the detector cannot be negative. The Fourier transform of 1 is a Dirac delta function located at the origin, so this DC term does not affect the recovered spectrum. However, the resulting Dirac delta function has large amplitude and if it is displayed on the same graph as the spectrum, it can lead to scaling problems. Because of this, each interferogram will be processed to remove its average value before the FFT is performed on it. The DC term is used only to accurately simulate the image chain process. The interferogram after removing the DC term is, in fact, what most people call the interferogram (Griffiths and de Haset, 1986; Bell, 1972),

but the former is an acceptable alternative and will be used throughout this document. With the DC term removed, Equation 2.4 becomes the cosine transform of the spectrum.

This realization has important implications when one tries to understand the effects of generating an interferogram for any member of a known Fourier transform pair. First, only real functions are valid as spectra. The real part of the Fourier transform of a spectrum is the interferogram. The following example illustrates this point. Consider the Fourier transform of a translated function.

$$\mathcal{F}\{f(x \pm x_0)\} \rightarrow e^{\pm j2\pi x_0 \xi} F(\xi) \quad (2.5)$$

But, as mentioned earlier, the interferogram of a FT is the real part only. Therefore, Equation 2.5 becomes:

$$\Re\{\mathcal{F}\{f(x \pm x_0)\}\} \rightarrow \cos(\pm 2\pi x_0 \xi) F(\xi) \quad (2.6)$$

where I is used to represent the interferogram operation. The spectrum shown in Figure 2.9 (a) is $\text{SINC}((\sigma - \sigma_o)/\Delta\sigma) + 0.212$. The DC offset 0.212 is added because a spectrum cannot have negative values. From FT theory, we know that the FT of the DC offset yields a Dirac delta function at the origin. The FT of the SINC yields a RECT and the translation produces the cosine described in Equation 2.6, as seen in Figure 2.9 (b). Basically, the resulting interferogram is the conventional RECT modulated by a cosine, with the addition of the Dirac delta function that accounts for the spectrum's DC term, and the interferogram's DC term as explained earlier in this section. Every known FT pair needs to be modified in this fashion to be used as test spectrum/interferogram pairs. It can also be said that the envelope of the interferogram is the magnitude of the FT of the spectrum. Because this is an ideal simulation, the recovered spectrum would be identical to the input spectrum.

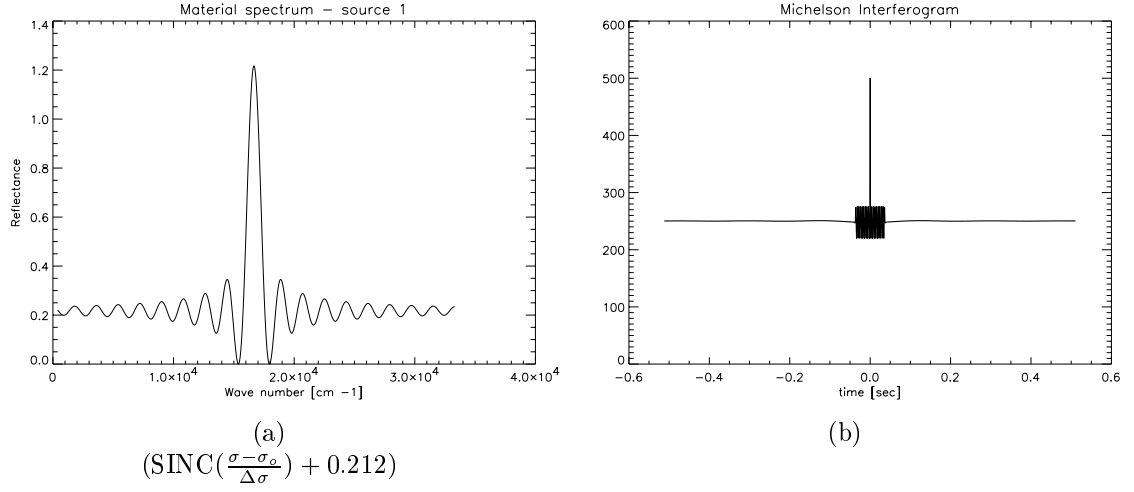


Figure 2.9: Elementary FT pair example: (a) SINC-like spectrum, (b) resulting interferogram.

2.6.1 Temporal FTS

Temporal FTS systems collect the interferogram by translating one of the interferometer mirrors in Figure 2.4 over time. The spatial information is collected on a detector array. Two types are common: the imaging Michelson interferometer and the rotary, or rapid scan (Turbo FT), interferometer.

With a continuously scanning mirror FTS, the OPD is twice the distance traveled by the scan mirror. The factor of two is due to the doubling of the reflected path. The OPD is expressed as:

$$\delta = 2vt \tag{2.7}$$

where v is the speed of the scanning mirror and t it the integration time. Inserting Equation 2.7 in Equation 2.4 yields the interferogram that would be observed at the detector plane:

$$I(t) = \int_0^{+\infty} S(\sigma)\{1 + \cos(2\pi\sigma 2vt)\}d\sigma \tag{2.8}$$

Note that the interferogram is now a function of time instead of OPD, hence the name temporal FTS.

Imaging Michelson Interferometer

The interferometers presented thus far were only good to measure the interferogram from a single-point source. To transform a Michelson interferometer into an imaging Michelson interferometer, the light from a single point must be collimated into parallel rays at the input of the interferometer and refocused to a point at the output of the interferometer. This is achieved by adding collimating lenses at the input and output of the interferometer. Figure 2.10 illustrates this configuration. The image and object planes are located at the focal points of their respective lens. The diagram demonstrates that the light radiating from one point on the object plane is re-imaged to a point on the image plane. The interferogram is collected by reading the intensity at the image plane while scanning the moveable mirror. The Figure also demonstrates that:

$$\theta = \frac{y}{f} = \frac{y'}{f'} \quad (2.9)$$

where θ is the angle between the collimated rays and the optical axis, y and y' are the off-axis distance on the object and image plane, and f and f' are the respective focal length of the collimating lenses. The effects of this angle on the interferogram will be discussed in section 2.8.

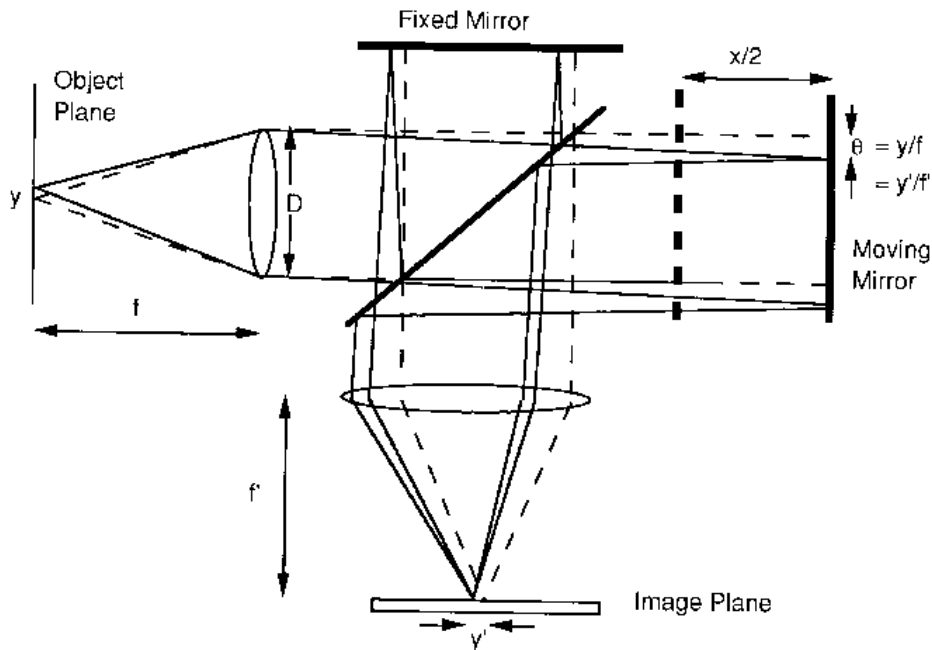


Figure 2.10: Imaging Michelson Interferometer (Bennett, et al., 1993)

The resolution of these FTS is a function of the the maximum OPD and the number of interferogram samples. For equivalent maximum OPD, the greater the number of samples, the better the resolution.

Rotary Interferometer

Another method of producing a temporally varying OPD between two coherent beams is to use a rotating refractive element, as shown in Figure 2.11. The radiation emitted from a point at one focal distance of the input collimating lens is separated at the beamsplitter, reflected by mirrors M to the rotating refractor R, folded back on its path by the end mirrors ME to finally recombine at the beamsplitter. The recombined beams are then refocused onto the image plane. Because the refractor's thickness is less than its length, and that the beams that pass through it are mutually perpendicular, the optical path traversed by each beam is different depending on the angular position of the refractor. For each detector on the focal plane array, this configuration produces 4 interferograms per revolution of the refractor. Because the OPD is a non linear function rotation angle, the interferogram is usually collected within a range of $\pm 15^\circ$ from horizontal or vertical to reduce the effects of the non linearity. These limits represent 120° per revolution (360°), or a duty cycle of 33%. The refractor is rotating at a constant speed and so is not as susceptible to errors in path difference as Michelson interferometers. This research did not simulate a rotary FTS, but, the required modification should not be extensive. The index of refraction of the refractor is ultimately responsible for the resolution of the recovered spectrum. The reader is directed to Wadsworth (1997) for more information on this type of design.

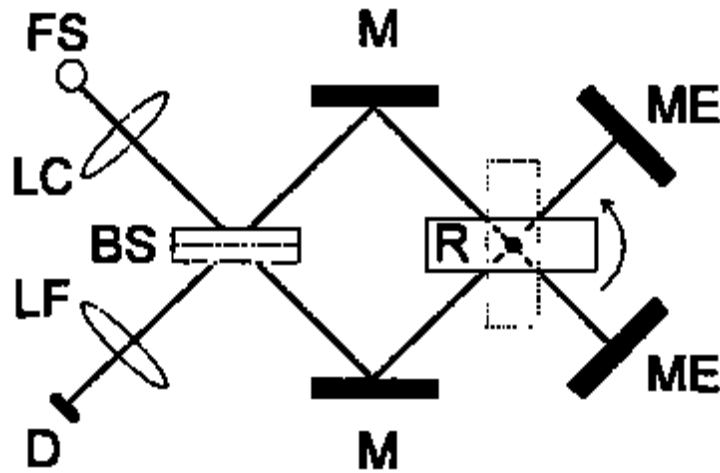


Figure 2.11: Rotary Turbo FTS (Wadsworth and Dybwad, 1997)

2.6.2 Spatial FTS

As just described, temporal FTS systems delay one planar wavefront travelling parallel to each other to produce interference. Spatial FTS systems act by translating one wavefront “sideways”. It can be seen in Figure 2.12 that the shear produced by a lens on the two wavefronts emitted from two coherent point sources—actually a single point source whose beam was split then shifted—produces different degrees of interference depending on the spatial location of the observer along the detector plane. For this design to work, the radiation from the source must be split so that the two resulting coherent virtual sources are located at the focal length of the Fourier lens. The interference pattern will be located at the image plane, also at one focal length from the Fourier optic.

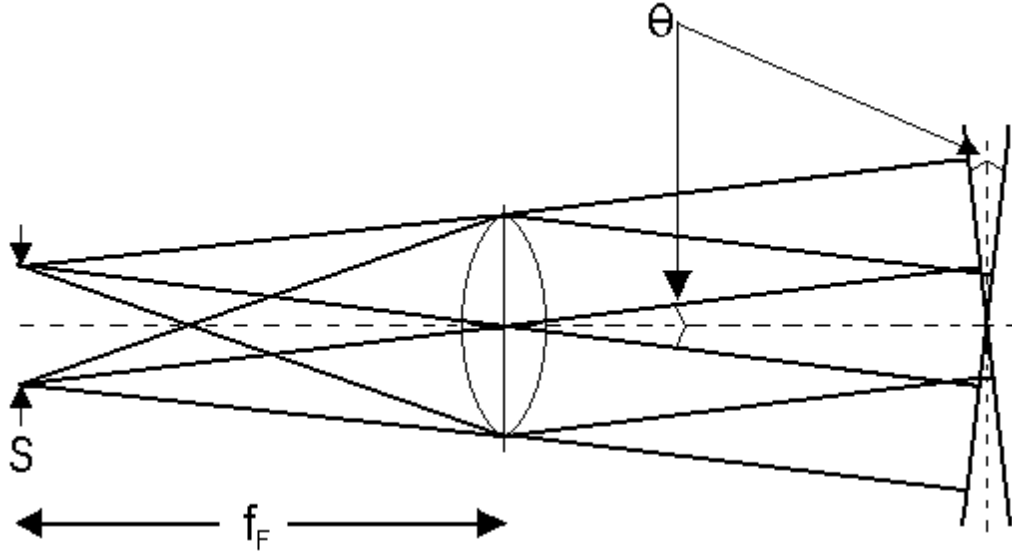


Figure 2.12: Effect of Fourier Optics (Sellar and Rafert, 1994). The source and the image (interferogram) are located at their respective focal distance from the lens.

In a spatial FTS, the interferogram for a single source is collected spatially and simultaneously along one dimension of the detector array. The information for one image spatial dimension is collected in the orthogonal dimension on the detector array. A cylindrical lens is required to achieve the spatial resolution in this dimension. See Hayden Smith (1991) for more details on the mode of operation of the cylindrical lens. The second image spatial dimension is collected temporally by operating the sensor in pushbroom mode, i.e., lines are collected one by one as the sensor sweeps the scene.

The form of the equation representing the interferogram is similar to that of Equation 2.8, except that it is a function of spatial coordinates. The other differences are due to the method of generating the OPD. For a Sagnac (triangle-path) interferometer, the interferogram equation at spatial position x is:

$$I(x) = \int_0^{+\infty} S(\sigma) \{1 + \cos(2\pi\sigma x \ell / f)\} d\sigma \quad (2.10)$$

where x is the off-axis distance of the detector pixel, ℓ is distance between the virtual sources ($\ell = \sqrt{2}d$ (Hayden Smith and Schempp, 1991), where d is the mirror shift from zero split distance (see Figure 2.13)), and f is the focal length of the Fourier optics. In a Sagnac design, once the Fourier lens

and detector are selected the only change that can be done to obtain a different spectral resolution is to move the mirror to a different position (change ℓ). Of course, not every spatial FTS uses a lens to shear the radiation. The Mach-Zehnder interferometer, the double-mirror interferometer, Lloyd's mirror and Fresnel's biprism are but a few examples of interferometers that operate without a shear producing lens (Horton, 1996; Steel, 1983; Junttila, 1992; Caulfield, 1979). Even Young's classic double-slit experiment can be considered a spatial interferometer. Please note that due to the impossibility of inserting a cylindrical lens in the designs, some of these interferometers are limited to the measurement of single-point interferograms. For the purpose of this research, two beam splitting/shearing designs will be presented in more detail. Although the Sagnac based FTS can be considered part of the Digital Array Scanned Interferometer (DASI), it will be discussed as a separate entity because it is one of the designs that will be simulated with DIRSIG.

Sagnac Interferometer

The optical diagrams for two slightly different triangle-path (Sagnac) interferometers are shown in Figure 2.13. The design on the left uses one spherical and one cylindrical lens to produce instantaneous spatially defined interferograms. The second design uses a parabolic mirror instead of a spherical lens to produce the interferogram. This reduces the chromatic aberrations due to the dispersion of the lens. Some designs use parabolic cylindrical mirrors instead of cylindrical lenses for the same reasons. The folding of the beams by the mirrors give the added advantage of a more compact instrument. In both cases, a slit aperture limits the field of view of the interferometer to a line. As such, the sensor must be scanned across the object plane in "pushbroom" mode.

In this design, no moving parts are necessary. Moving the mirror has the effect of increasing or decreasing the distance between the coherent virtual sources. The result on the interferogram is to provide a different resolution and wavenumber range. Figure 2.14 represents source doubling and also illustrates the path of the radiation with the mirror located at the symmetrical "zero-split" position. Because the radiation follows identical optical path, these interferometers form a class of "common-path" interferometers.

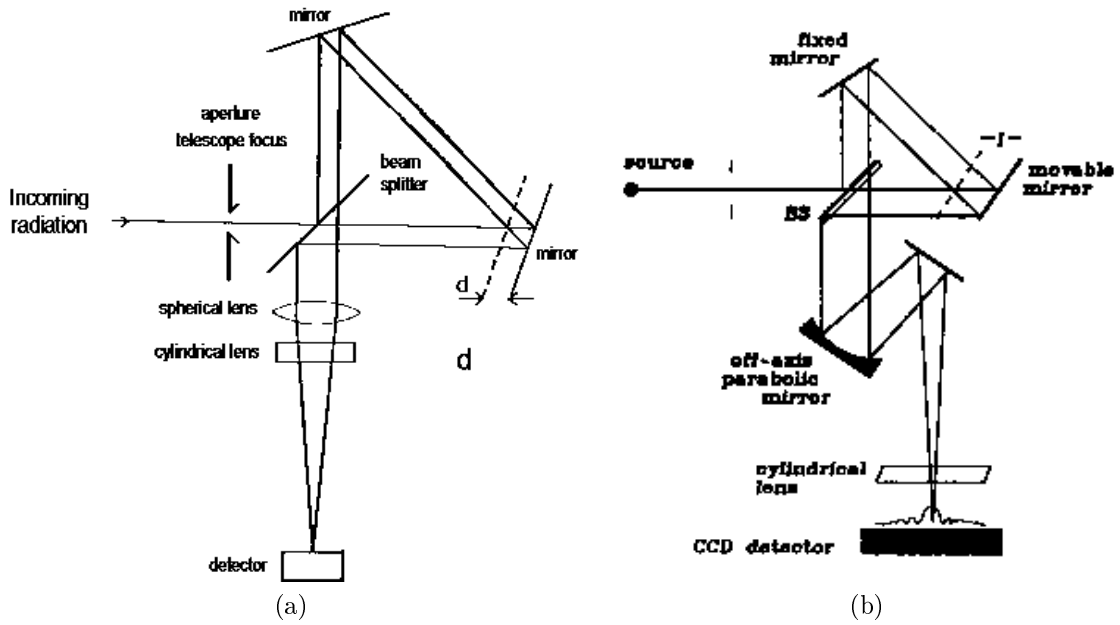


Figure 2.13: Optical diagram of Sagnac interferometers using (a) lenses (Hammer, et al., 1992), (b) parabolic mirrors to avoid chromatic aberrations (Sweedler and Denton, 1989).

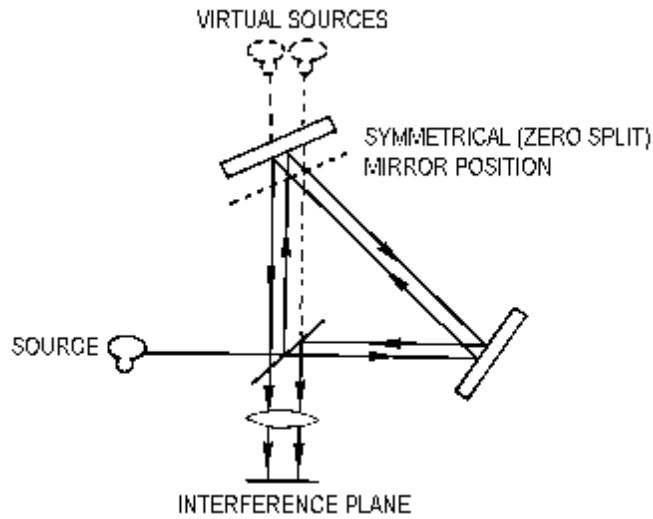


Figure 2.14: Source doubling interferometer optical diagram (Caulfield, 1979)

Considering the radiation coming from a point source, one realizes that the Fourier optics collimate the radiation to create planar wavefronts. Because the wavefronts are coherent and occupy

two dimensions, it is impossible to determine the source location by looking at the interference pattern generated at the interference plane. This is the reason where the cylindrical lens. When located at one focal length of the image plane, the lens collapses the planar wavefront into a line that can be resolved spatially. On a detector array, the length of the line is orthogonal to the spatial dimension of the array, and aligned with the spectral dimension of the array. The reader can refer to Smith and Schempp (1991) and Sellar and Rafert (1994) for an analysis of the effects of the cylindrical lens and spatially resolved interferogram images.

Digital Array Scanned Interferometer

The DASI is covered here for completeness but will not be part of the sensors simulated for this research. The DASI family encompasses a wide variety of FTS designs. A few designs will be discussed briefly. In addition to triangle-path (Sagnac) interferometers, DASIs have been demonstrated with birefringent interferometers and with a tilted grating (Hammer, et al., 1992; Okamoto, et al., 1986; Aryamanya-Mugisha and Williams, 1985; Smith and Hammer, 1996). The birefringent interferometer uses a filter that exhibits different indices of refraction for different polarizations. The filter-polarizer combination is used to split a beam of light, which is then passed through an imaging and a cylindrical lens onto the output plane. As seen in Figure 2.15, the reimaging elements of a birefringent DASI are similar to that of a Sagnac based FTS (spherical and cylindrical lenses).

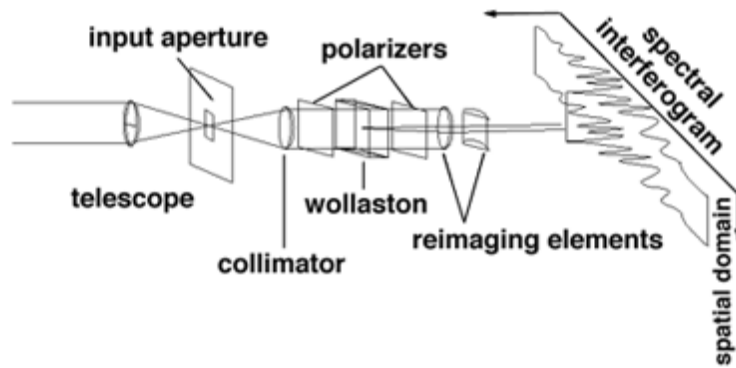


Figure 2.15: Optical diagram of a birefringent DASI (Author unknown, 19XXc)

A second DASI system uses a tilted grating (Hammer, et al., 1992) or mirror (Aryamanya-Mugisha and Williams, 1985)) to shear the wavefront to produce the interferogram. This design allows for very high resolution and can easily be used for ultraviolet and visible light. The design

is similar to the Michelson except that the scanning mirror is replaced by a fixed grating or tilted mirror, as in Figure 2.16. The other difference from the Michelson design is that the image plane is not located at the focal distance of the lens, but rather at a distance that allows the interferogram to be registered onto the detector array.

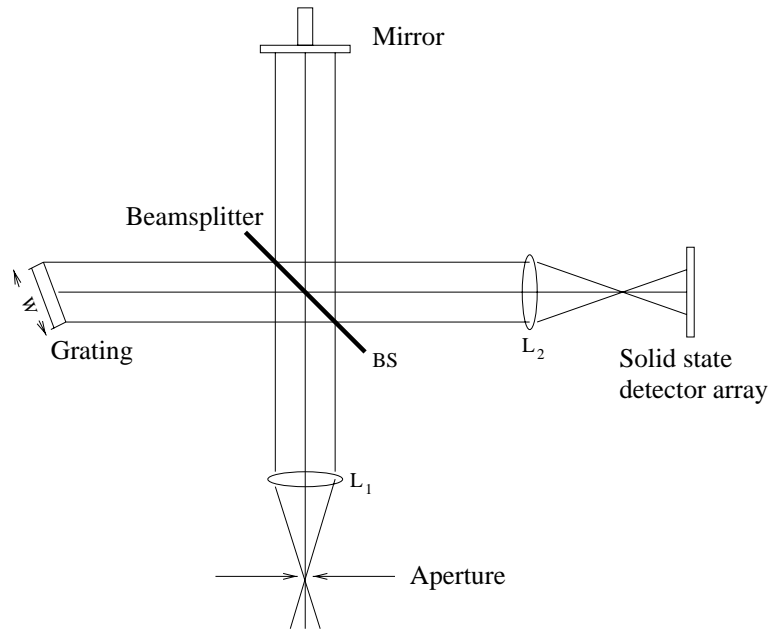


Figure 2.16: Optical diagram of a tilted grating DASI (Hammer, et al., 1992)

2.6.3 Combination Spatial/Temporal instruments

This section is an introduction for two spatially modulated IFTS systems that do not collect the entire interferogram simultaneously. Instead, the scene must be scanned across the image plane. It is this requirement for scanning that gives those IFTS systems a combination of the spatial and temporal IFTS attributes. These sensor types were not simulated as part of this project.

Infrared Imaging Spatial Heterodyne Spectrometer (IRISHS)

Figure fig:irishs shows the optical layout for the infrared imaging spatial heterodyne spectrometer (IRISHS) (Cooke, et al., 1999). The design is similar to a Michelson interferometer with each mirror replaced by combination grating/collimating lens. Of special interest is that the spectral range of the spectra starts at the Littrow wavenumber of the grating instead of 0. “The Littrow

wavenumber is defined as that which retro-reflects from the gratings and produces no spatial fringe pattern at the focal plane (sensor array) because the recombined wavefronts [are] in phase everywhere” (Laubscher, et al., 1999). This reduced spectral range loosely translates to a better resolution for the same number of pixels on the focal plane array (FPA), a clear advantage when the spectral resolution is a function of the number of pixels in the FPA. This “spatial heterodyne” is an effect of the dispersive nature of the gratings. The interferogram equation is complicated by the fact that the optical path difference is a function of the Littrow wavenumber, the optical wavenumber, and the position on the FPA.

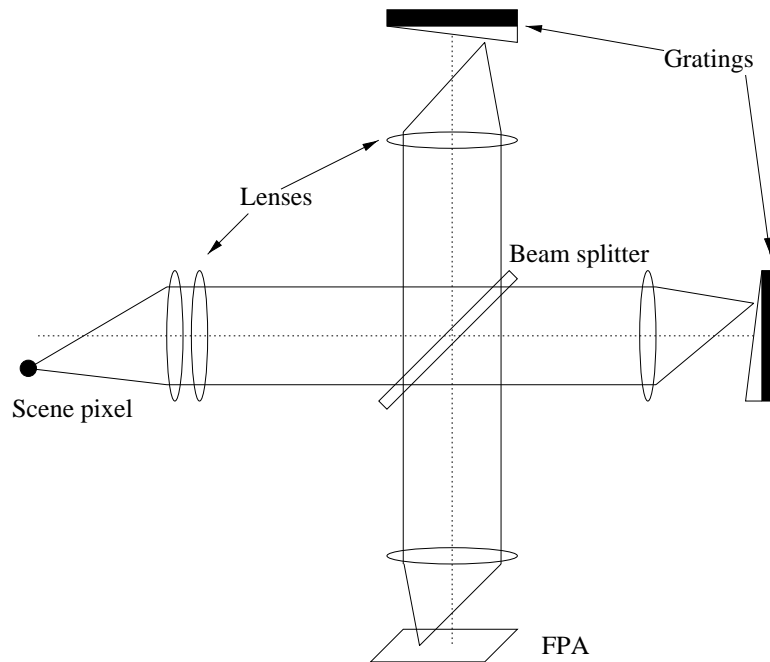


Figure 2.17: Optical diagram for IRISHS

With this design, the interferogram is a function of its location on the FPA, i.e., the optical path difference varies along one of the FPA dimensions. This is why this design belongs to the class of spatially modulated IFTS. The FPA collects spatial (image) information in both dimensions. For any given image collected by IRISHS, only one of many interferogram samples necessary for inversion to spectra is generated for a pixel on the ground. Interferogram samples with a different OPD will be collected by a subsequent image as the platform passes over the scene. Figure 2.18 illustrates this process. Similar to a Michelson design, the interferogram is vulnerable to pointing

jitter and temporally varying spectra. Just like a Sagnac design, the interferogram is collected by a row of detectors. Variations in detector gain, bias and noise characteristics all affect the resulting interferogram.

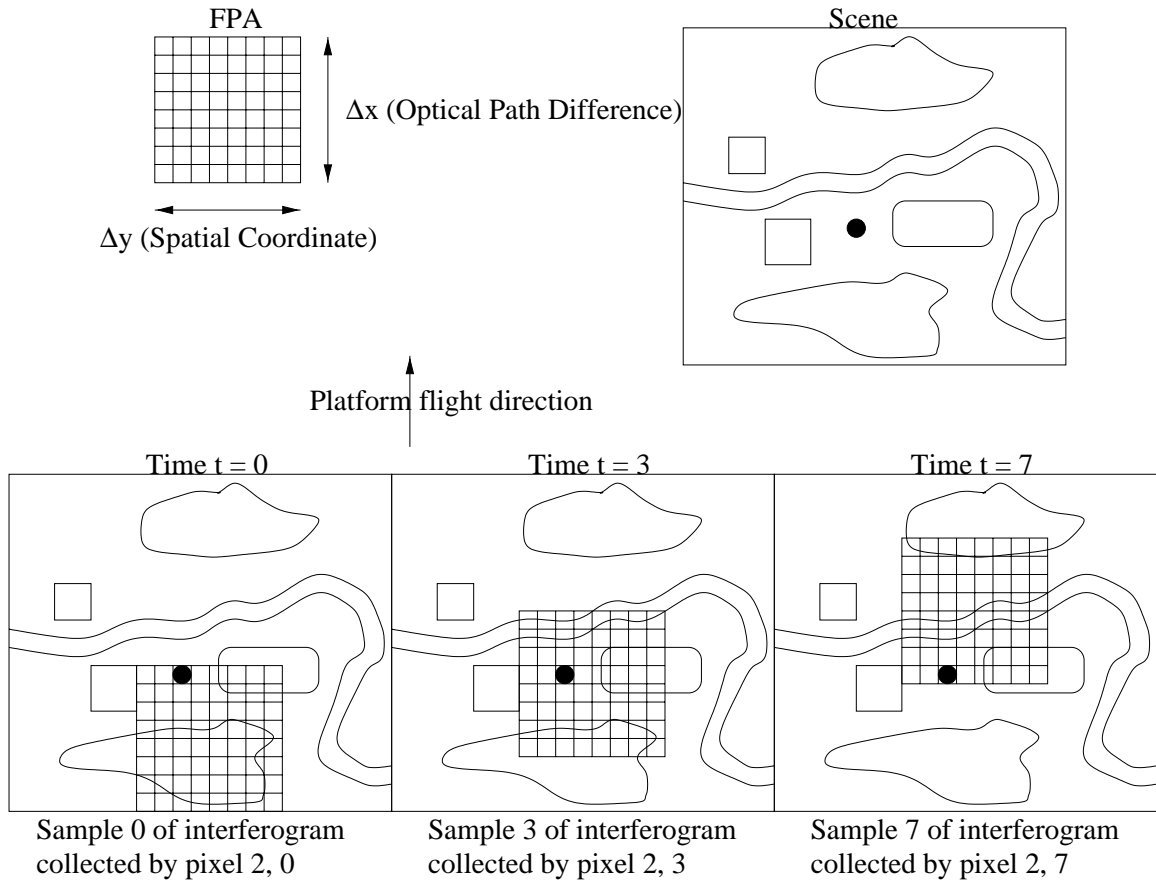


Figure 2.18: Interferogram collection process for IRISHS

High Étendue Imaging Fourier Transform Spectrometer (HEIFTS)

The high étendue imaging Fourier transform spectrometer (HIEFTS) (Horton, et al., 1997) needs to be operated in the same way as IRISHS. This sensor does not enjoy the “spatial heterodyne” advantage. The ray trace in Figure 2.19 illustrates the operation of the system. An image is formed at the object plane by the fore-optics of the system. The arrangement of beamsplitters and mirrors in the interferometer produces a pair of wavefronts which are tilted with respect to one another. The tilt introduces an optical path difference that varies linearly across the focal plane. The entire

interferogram for a pixel on the ground is collected as the platform passes over the scene.

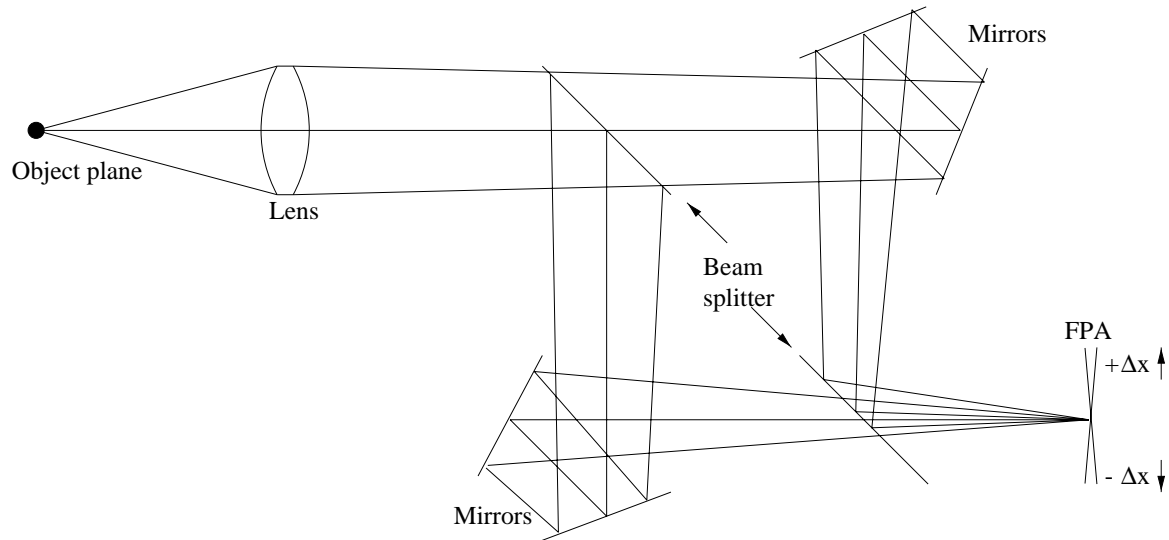


Figure 2.19: Simple HEIFTS optical diagram

2.6.4 Current Instruments (Existing Designs or Prototypes)

To illustrate the fact that very few IFTS platform designs exist, either under the form of an instrument, a prototype, or a design, the following list tries to give a complete coverage of the available IFTS sensors. Sensors that were designed as a laboratory experiment with no field usage in sight are omitted from this list. FTS used for astronomy are equally omitted from this list. Some sensors are in the list more than once because they have multiple settings that give different results. IRISHS and HEIFTS are also excluded from this list.

Temporal Imaging Fourier Transform Spectrometers				
Name	Type	Range [μm]	Resolution [cm^{-1}]	Other
LIFTIRS 1	Michelson	3.3–4.9	0.25 to 64 (variable)	IFOV: 0.35 mrad
LIFTIRS 2	Michelson	8–12.5	0.25 to 64 (variable)	IFOV: 0.55 mrad
IRIFTS	Michelson	1.25–?†	6	Spatial resolution of 2.5 mrad †[Range 0 to 7899 cm^{-1}]
IISRB	Michelson	3.5 to 5	1–5	FOV: 4 or 16 mrad
IISR II	Michelson	2–5.3	1,2,4,8,16,32,64	FOV: 1 or 4 mrad
IISR	Michelson	1.8–5.5	1–16	FOV: 43 mrad
CIS (Turbo FT)	Rotary FTS	2–14	2	
Spatial Imaging Fourier Transform Spectrometers				
Name	Type	Range [μm]	Resolution [cm^{-1}]	Other
SMIFTS	Sagnac	1–5	50	
SMIFTS	Sagnac	1–5.2	95	
SMIFTS	Sagnac	3–5	35	FOV: 8°
DASI	Unknown	1.1–2.2	266	FOV: 7.7°, IFOV: 0.53 mrad
DASI	Tilted grating	Vis/NIR	0.2 at 500 nm	Lab experiment
DASI	Wollaston	0.5 to 1	485	
DASI	Wollaston	0.4 to 1.0	300	FOV: 5°
DASI	Wollaston	1.1 to 2.2	300	FOV: 5°
FTHSI	Sagnac	Vis/NIR	2–6 nm	15 km ground swath
FTVHSI	Sagnac	0.44–1.15	250	FOV: 15° full angle
FTVHSI	Sagnac	0.45–1.0	87	FOV: 0.26 rad

Table 2.1: Imaging Fourier Transform Spectrometers

LIFTIRS

The Livermore Imaging Fourier Transform Infrared Spectrometer (LIFTIRS), from the Lawrence Livermore National Laboratory, is a Michelson FTS design with scanning mirror (Carter, et al., 1995; Norton, et al., 1995). Two interchangeable infrared focal plane arrays allow for two spectral regions of operation. The maximum OPD produces a spectral resolution of 0.25 cm^{-1} . The OPD can be adjusted to give the required spectral resolution. Image sizes are 128×128 or 256×256 pixels, depending on the focal plane array being used.

IRIFTS

The IRIFTS, or Infrared Imaging Fourier Transform Spectrometer, was a prototype instrument from the Lawrence Livermore National Laboratory, probably the precursor to LIFTIRS (Bennett,

et al., 1993). Little is reported on this sensor because of a patent application still pending at the time of publication of the article.

IISRB, IISR, IISR II

The IISR, Infrared Imaging Spectro-Radiometers, is a family of imaging spectrometers based on the Bomem MR or MB series interferometer (Villemaire, et al., 1995; Oermann and Smithson, 1995; Norton, et al., 1995). The early IISR generation had a 4×8 pixel detector at the focal plane while the later model has an improved image, to 8×8 . The different FOV can be obtained by changing the input telescope. The spectral range is from 1.8 to $5.5 \mu m$, and is once again dependent on the focal plane array and the speed of the instrument.

CIS

The Chemical Imaging Spectrometer (CIS) is based on a rotary FTS design (Wadsworth and Dybwad, 1997). It is also known as Turbo FT and is made by Design & Prototypes, LTD. The spectral resolution is 2 cm^{-1} from 2 to $14 \mu m$. Only a single pixel detector had reportedly been tried on the prototype at the time of this writing. A 3×3 detector was acquired for further testing and development.

SMIFTS

The Spatially Modulated Imaging Fourier Transform Spectrometer (SMIFTS) is a Sagnac-based IFTS design (Rafert, et al., 1992; Lucey, et al., 1993; Lucey, et al., 1995; Norton, et al., 1995). It has two modes of operation. One allows a spectral resolution of 95 cm^{-1} over 1 to $5.2 \mu m$ while the second has a resolution of 35 cm^{-1} from 3 to $5 \mu m$. Because it uses a 256×256 array, one spatial dimension of the image is set at 256 pixels. The second spatial dimension is collected by operation this sensor in the pushbroom mode. It has a FOV of 8° or 0.14 rad.

DASI

Digital Array Scanned Interferometers covers a broad range of spatial FTS designs (Hammer, et al., 1995; Hammer, et al., 1992; Author unknown, 19XXa; Hammer, et al., 1993). However, the only designs employed as imaging spectrometers were based on either the Sagnac or the birefringent

interferometer (Lucey, et al., 1995). Because the designs vary greatly, the spectral range and resolutions also vary greatly. Refer to Table 2.1 for more details.

FTHSI, FTVHSI

The Fourier Transform HyperSpectral Imager (FTHSI) or Fourier Transform Visible HyperSpectral Imager (FTVHSI) are acronyms for a suite of sensors by Kestrel Corporation (Otten III, et al., 1995; Meigs, et al., 1996; Otten III, et al., 1996; Nieke, et al., 1997). Depending on the design, the spectral coverage of the instrument can range from 350 nm and 1150 nm. The spectral resolution varies from 87 cm^{-1} to about 250 cm^{-1} . The FOV of this sensor is 13° to 15° . 450 spatial channels are reported in one spatial dimension. The sensor needs to be operated in the pushbroom mode for the second spatial dimension. This sensor uses a small aircraft as its platform. A similar sensor was scheduled to be launched in March 98 on Mighty Sat II.

2.7 Advantages/Disadvantages

What advantages and disadvantages does the FTS design confer over other spectrometer designs? Since FTS are more complex to design and operate—the legacy of the Fourier transform—than dispersive and filtered designs, no one would construct these systems without a distinct advantage. The advantages/disadvantages are first discussed by comparing a general FTS design to dispersive and filtered spectrometers. In a second round of comparisons, temporal (Michelson) FTS are put in relation to spatial (Sagnac) FTS.

2.7.1 FTS vs Dispersive and Filtered Spectrometers

The two advantages commonly referred to in the literature are the Jacquinot and Fellgett advantages. These result in improvements in the SNR of the system. The Jacquinot advantage, from P. Jacquinot who brought it to our attention, is also known as the throughput or étendue advantage. Because dispersive spectrometers use slits the view angle of the spectrometer is limited, and the flux of radiation to the detector is reduced. A FTS is not limited by a slit, thus collects more photons in the same time, hence a better SNR. Figures of 200 times more power for a FTS compared to a grating spectrometer have been reported (Bell, 1972). When a FTS is used for imaging, the

throughput advantage is reduced as the number of imaging elements in the focal plane increases (Descour, 1996).

The Fellgett (from P. Fellgett), or multiplex advantage, also assumes a single (non-imaging) detector. This advantage can be applied over both filtered and dispersive designs. Basically, each detector in a FTS system will detect the full wavelength range during the collection of the interferogram. On the other hand, filtered or dispersive spectrometers can only detect a narrow part of the spectrum. For equivalent collection times, the FTS will have collected more photons and hence has a better SNR. The multiplex advantage of a detector noise-limited FTS over a scanning device is listed as being anywhere from $(N)^{1/2}$ to $(N/8)^{1/2}$ in the literature (Treffers, 1977), where N is the number of samples per interferogram. However, The multiplex advantage is limited to Michelson devices (Horton, 1996). In a photon-noise limited case, the multiplex advantage can become a multiplex disadvantage (Hammer, et al., 1995; Smith and Hammer, 1996). This is because the Fourier transform operation tends to accentuate the noise level in the spectrum. In a FTS, the entire spectral range contributes to the noise level in the interferogram. This makes the noise in a given band of the output spectrum a function of the noise that is present in the entire input spectrum.

It can be concluded that, given the same number of detection elements, the same collection times, and various parameters, FTS enjoy étendue (throughput) and multiplex advantages over dispersive systems, and a multiplex advantage (Michelson only) over filtered systems.

A third, less commonly talked about advantage is the Connes advantage. It states that “the wavenumber scale and instrumental line shape are precisely determined, and are independent of wavenumber” (Bennett, et al., 1993). The same paper reports that the sensitivity of FTS is likely to be inferior to that of dispersive or filtered devices for low resolution measurements. For high resolution measurements, FTS have a better sensitivity. FTS are also reported to reduce stray or unwanted flux problems (Bell, 1972).

Their main disadvantage lies in the complexity inherent to the recovery of the spectra. It is one of the main obstacles to their adoption. The sensitivity of FTS to noise is also one known disadvantage.

2.7.2 Michelson vs. Sagnac

As seen in the previous section, Michelson and Sagnac devices share many properties. Besides the obvious temporal and spatial collection differences between the two designs, many other differences are reported. Following is a look at temporal design advantages over spatial devices. The most important advantage offered by a Michelson device is the ability to vary the resolution of the spectrometer very painlessly assuming the mirror has sufficient range of motion. The maximum resolution is limited by the maximum OPD and the number of samples collected. Any lower resolution can be achieved simply by reducing the scanning mirror travel range (in effect reducing the number of samples per interferogram). The resolution of Sagnac devices is limited by the number of pixels in the spectral direction of the focal plane array (FPA). Technology, FPA field of view, and costs currently limit the size of the FPA. Temporal FTS also enjoyed the multiplex advantage over their spatial counterparts.

The advantages of spatial FTS over temporal devices are numerous. The fact that a spatially modulated FTS requires no moving parts is a big advantage. Vibrations, alignment problems, and maintenance costs are all reduced. Resistance to mechanical failure is improved. In many temporal FTS instruments, a reference wavelength is used to ensure that the interferogram is sampled at constant displacement. A spatial FTS always samples the interferogram at constant locations (Persky, 1995). The size of the instrument also is reduced because there is no requirement for a rail to support the scanning mirror. Another advantage is that "... spatially modulated systems are particularly attractive for applications where the target and/or the instrument is moving, or where the spectral characteristics of the target are changing rapidly" (Sellar and Rafert, 1994). This is because all samples of the interferogram are collected simultaneously. In the case mentioned in the quote, it would be difficult to resolve the spectrum using a Michelson FTS. A Sagnac interferometer can enjoy a wider field of view than a Michelson interferometer. Sagnac FTS systems also are better adapted to remote sensing from airborne or spaceborne platforms. While a temporal FTS must stare at a point, which puts stringent requirements on the pointing accuracy, spatial FTS operate in the pushbroom mode. The pointing accuracy requirement can be relaxed, and the image can be post-processed to correct roll, pitch and yaw effects. The last advantage I will point out here, which can probably be considered negligible most of the time, is the common path traversed by the beams in a Sagnac FTS. As such, they will acquire the same effects due to the path. Beams travel in two

separate arms in a Michelson interferometer, and the results are affected by minute differences in their path.

2.8 Artifacts and Properties of FTS

The aim of this research is to provide the user with a model of the image chain of two FTS designs. Many effects that were simulated occur naturally at different locations in the image chain and all efforts were taken to respect this occurrence order. Artifacts that were not simulated as part of this project are considered negligible or too complex to simulate. The basis of each simulation was an ideal image chain, without artifacts or degradations. Starting with a clean image chain has the advantage of isolating the effects of a single design property or operating condition. Degradation associated with the fact that the simulation is done using digital approximations to the real world are considered negligible. In the real world, artifacts and degradation are an inherent part of the actual image chain, but they must be added to a simulation since a simulation is ideal to start with. It is of philosophical interest that people simulating sensors do their best to include realistic artifacts in their images, and that people operating real sensors spend their lives trying to get rid of such effects.

Table 2.2 lists some of the artifacts and properties associated with different FTS designs. The theory behind each of these will be explained and effects will be indicated. The checkmarks indicate which designs are affected by the artifacts. Some artifacts are given the same name from one design to the other but actually exist for different reasons. In simulating these artifacts, reuse of existing programs from previous simulations and DIRSIG code was done wherever possible.

Artifacts and Properties	FTS type	
	Temporal	Spectral
Aliasing	✓	✓
Apodization (windowing)	✓	✓
Source spectral variation over scan time	✓	
Detector dynamic range	✓	✓
Quantization error	✓	✓
Clipping	✓	✓
Off-axis effects (obliquity)	✓	
Spectral response (Detector, amplifier)	✓	✓
Chromatic aberration	✓	✓
Error in path difference	✓	✓
Jitter noise	✓	✓
Detector related effects	✓	✓
Self-emission and thermal noise	✓	✓
Beamsplitter	✓	✓
Vignetting	✓	✓
Dynamic Mirror Alignment	✓	
Miscellaneous	✓	✓

Table 2.2: Artifacts and Properties of FTS

2.8.1 Aliasing

Aliasing occurs when an interferogram is sampled less than twice per period of any fringe component. Aliasing is not necessarily a bad thing; it can be used to augment the resolution of an a FTS, as long as the spectral range is reduced to avoid spectral confusion (Hayden Smith and Schempp, 1991). In short, larger spectral frequencies will be made to look like low frequencies. In most cases the false frequencies in the recovered spectrum render the data unusable.

Aliasing can be avoided by filtering the input spectrum, or by selecting a detector with a limited passband. Once aliasing is present in the interferogram it is impossible to tell aliased frequencies apart from original frequencies without prior knowledge of the spectrum. Therefore aliasing must be avoided.

Aliasing has first-order effects on the generation of spectra via FTS and was treated as a first priority in this research. Gaskill (1978) is a good source for understanding aliasing effects.

2.8.2 Apodization

Figure 2.6 shows the “ringing” associated with the truncated interferogram of a monochromatic source. The ringing is due to the side lobes of the SINC function associated with the Fourier transform of the truncating rectangular window. The interferogram in Figure 2.6 is a sinusoidal function multiplied by the window modulation. A property of the Fourier transform (Gaskill, 1978) is that the transform of a product is equivalent to the convolution of the transforms of each function. Note that Equation 2.11 is valid as written if only the positive spatial frequencies are considered for the transform of the COS function. (The negative frequency component of the impulse pair is ignored.) Symbol “*” represents the convolution operation (Gaskill, 1978).

$$\begin{aligned}\mathcal{F}\{\text{COS}(2\pi\xi_o x) \cdot \text{RECT}(x)\} &= \mathcal{F}\{\text{COS}(2\pi\xi_o x)\} * \mathcal{F}\{\text{RECT}(x)\} \\ &= \delta(\xi - \xi_o) * \text{SINC}(\xi) \\ &= \text{SINC}(\xi - \xi_o)\end{aligned}\tag{2.11}$$

Since the transform of a sinusoidal function at positive spatial frequencies is a Dirac delta function located at the frequency of the sinusoidal signal and the transform of a RECT gives a SINC, the transform of the product indeed gives a shifted SINC, from the sifting property of the delta function. It is this SINC that defines the resolution of the spectrometer. In general, the resolution is defined as the FWHM of the SINC.

The effects of this ringing are more severe when the spectrum has isolated, narrow peaks. The convolution of the SINC with those peaks generates side lobes that will affect the general shape of the spectrum. Figure 2.6 illustrates the ringing present in the spectrum when the input spectrum is a Dirac delta. If, on the other hand, the spectrum is generally constant, the SINC will only blur the spectrum a little and will not affect its shape.

Ringling may be reduced by using other windowing functions. Apodization (from the Greek, “to cut off the feet”) is the action taken to reduce the “ringing” of the side lobes. Many other windowing functions are available, each having different effects on the ringing and the resolution of the spectrum. A triangular function can be used as an apodizing function (see Figure 2.7). It is a simple, yet effective, means to reduce ringing at the cost of a slightly worst resolution. A rule of thumb is that if the extrema of the interferogram are located at the mean interferogram amplitude on the abscissa with little variation, apodization will not reduce ringing enough to be worthwhile.

Because most spectra used in this simulation are not monochromatic over the spectral range and

do not have sharp peaks, apodization by itself will have minimal effects on the simulation. However the spectra of some gases do exhibit sharp peaks which may require some degree of apodization. Apodization can reduce many artifacts of FTS designs. Although apodization does not produce first-order effects with an ideal interferogram, it can be used to recover spectra that appears corrupted (ringing). As such, it was implemented as part of this research.

2.8.3 Source Temporal Spectral Variation

With its very fast interferogram collection times, the Sagnac interferometer is virtually immune to this effect. Because the Michelson FTS must stare at a fixed point for an extended period of time and through extended view angles, spectra can be perceived as varying during the collection time. This temporal spectral variation could be due to a true temporal variation in the spectrum of the target or to a different target blocking the line-of-sight to the previous target. The latter situation occurs when objects move during the collection process or when the height of an object causes its projection on the object plane to move relative to the background as the view angle changes. For example, consider a sensor that stares at the base of a wall at the start of the collection process. The imaginary point that the sensor tracks during the collection is known as the “rock point”. As the sensor moves forward, the view angle is reduced until nadir viewing conditions are reached. At this point, the viewing angle starts to increase again. This time, the wall blocks the view of the base. The sensor instead images the roof or whatever is on the other side of the wall. A drift in the pointing accuracy of the sensor could also cause similar problems. Even though the results are similar, they must be simulated differently.

Random variations in a spectrum result in non symmetrical interferograms, which in turn can be seen as noise in the derived spectrum (Bennett, et al., 1995). This lack of symmetry of the interferogram can cause many unrecoverable errors if one derives the spectrum via the cosine transform (real part of the Fourier transform). On the other hand, recovery of the spectrum from magnitude of the Fourier transform can generate reasonable results. To illustrate this point, simulations of a temporally varying spectral source are shown in Figures 2.20 to 2.22. The spectrum of the source varies from a SINC-like form to a RECT-like form. Two methods that generate varying spectra were used with similar results. The first assumes a temporally linear variation while the second method simulates sudden variation of the spectrum when ZPD is reached. In the latter case,

half of the interferogram is from the first source and half from the second source. Because the Fourier transform operation is linear, the FT of the sum of two interferograms is equivalent to the sum of the spectra. This holds true as long as the extrema of the interferogram are at the same abscissa. If they are not at the same amplitude, apodization can be used to salvage some of the spectrum. Otherwise, noise masks the spectrum.

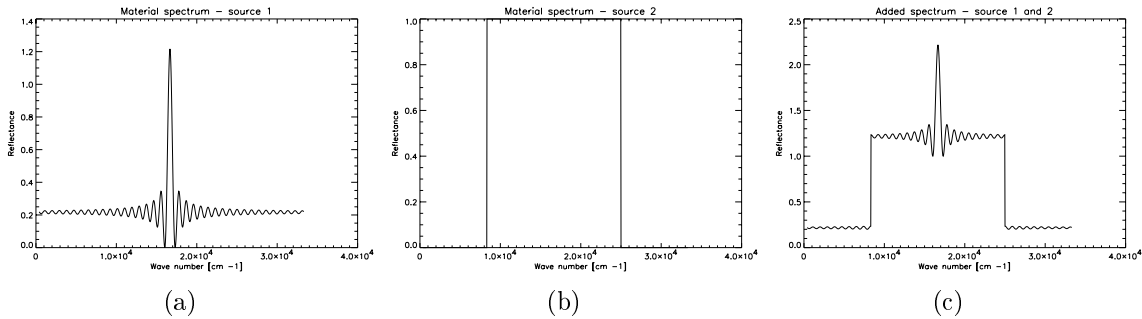


Figure 2.20: Spectral variation simulation input spectra: (a) start spectrum, (b) end spectrum, (c) sum of (a) and (b)

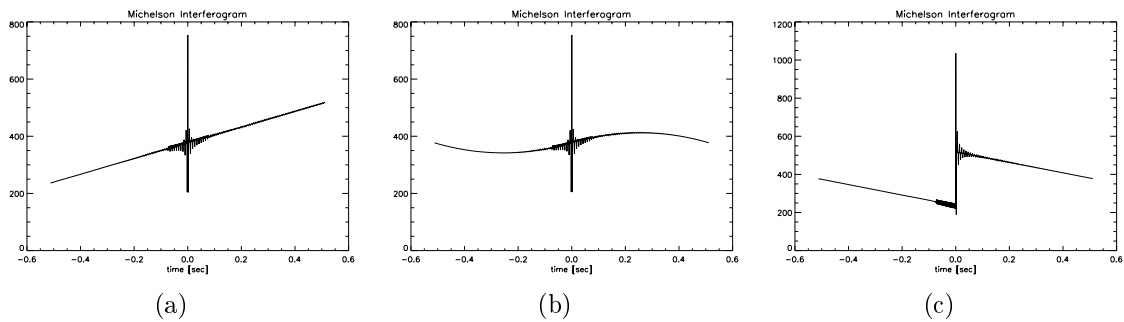


Figure 2.21: Spectral variation simulation interferograms: (a) interferogram of linear combination of spectra, (b) with apodization, (c) apodized interferogram with sudden change of spectra

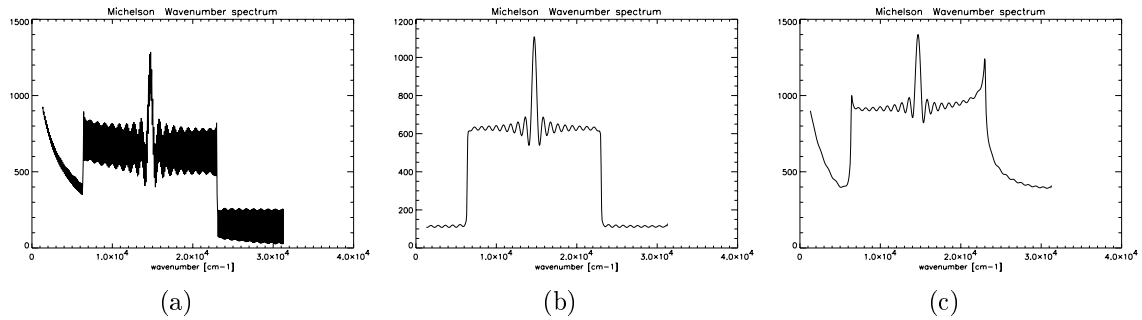


Figure 2.22: Spectral variation simulation output spectra: (a) linear combination spectra, (b) apodized linear combination, (c) apodized sudden change

2.8.4 Dynamic Range

“Dynamic range” describes the ability of a detector to detect the amplitude of a signal. Clipping occurs when the dynamic range of a detector is exceeded (the detector saturates). Dynamic range may be characterized as “Signal-to-Noise Ratio” by some authors (Griffiths and de Haseth, 1986). In digital systems, dynamic range is closely associated to the size of the quantization levels. The action of a quantizer is described by the number of levels and the step size. Figure 2.23 represents a noisy signal (ideal + noise) that will be quantized. It is assumed that the signal will not cause the detector to saturate. Given 4-bit quantization (16 levels) and closely spaced steps to quantize the signal, clipping will occur while many bits of information will be used to sample noise variations in the signal (Figure 2.24, top). Although the signal is not clipped, widely spaced steps will not result in a properly quantized signal since some information will be lost from the signal due to the unused quantization levels (Figure 2.24, middle). The trick is to balance the maximum signal intensity with the number of levels and step size so that the noise in the signal covers only a few steps. This way, all the signal information will be gathered, and little space will be wasted on sampling noise (Figure 2.24, bottom).

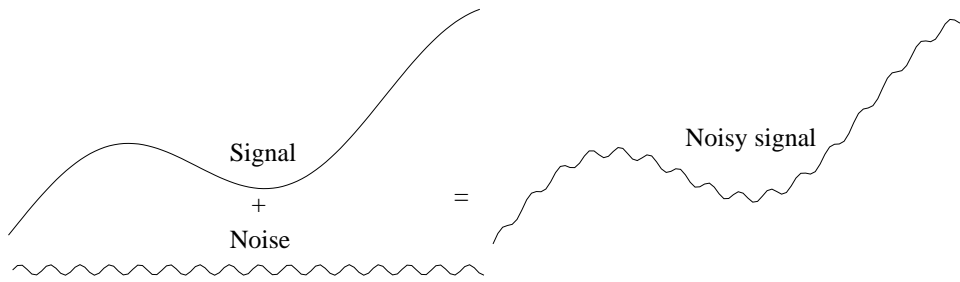


Figure 2.23: Example of signal input to detector and quantizer

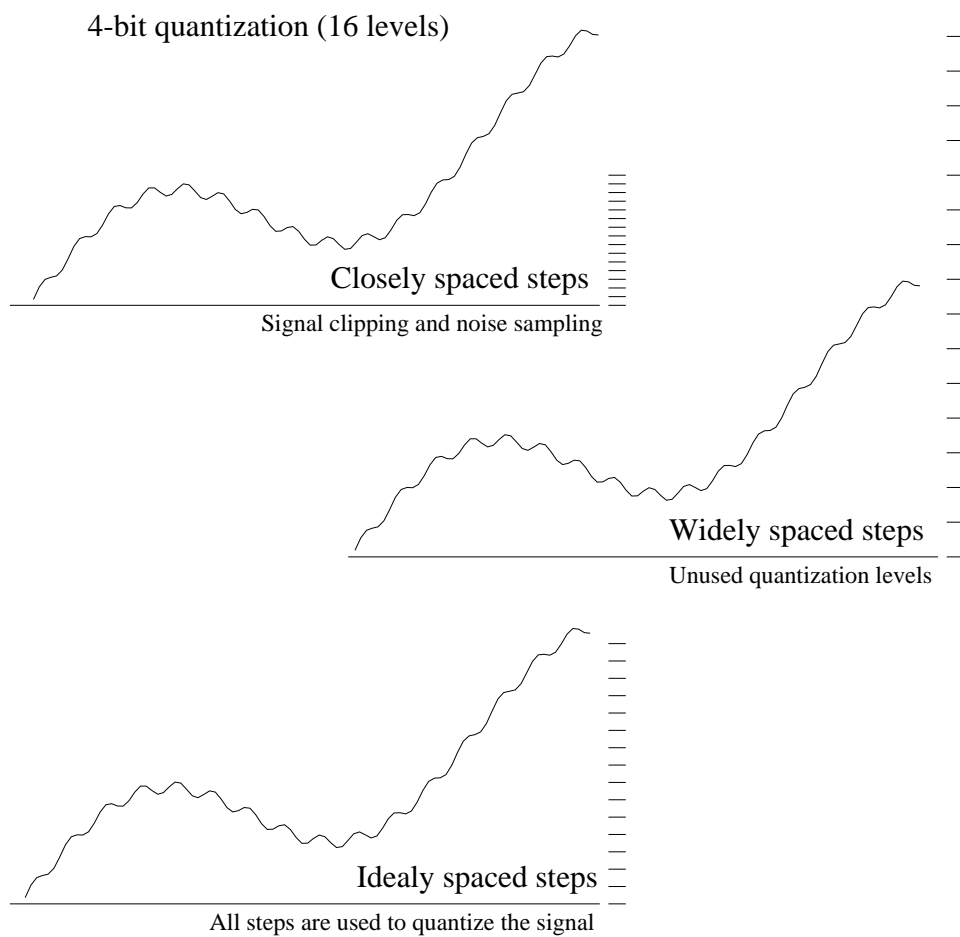


Figure 2.24: Examples of different step sizes for 4-bit quantization

New detectors tend to make this problem obsolete. CCDs for example, have a very large dynamic range and quantizers have many quantization levels. However, if dynamic range is still too

large, methods are available to compress it. Mertz (1965) proposed the method called “chirping”, which modifies the interferogram collection process. It operates by “spreading” the frequencies in different samples of the interferogram which results in a “center burst” of reduced amplitude. When chirping is used, a different inversion method is required to recover the spectrum. Because dynamic range is so tightly linked to quantization and clipping, the effects of each will be treated as subsets of this section.

Quantization

If an interferogram is processed in a digital computers, it must be quantized. When quantizing a signal, the amplitude of each sample is assigned to one of a limited number of levels by a truncation or rounding process. This results in errors which in turn introduce incorrect frequencies. Figures 2.25 to 2.26 show the effects of quantization. The effect of 12-bit quantization is barely noticeable to the eye (Figure 2.26), while 8-bit quantization (Figure 2.27) disrupts the frequencies in the wings of the spectrum.

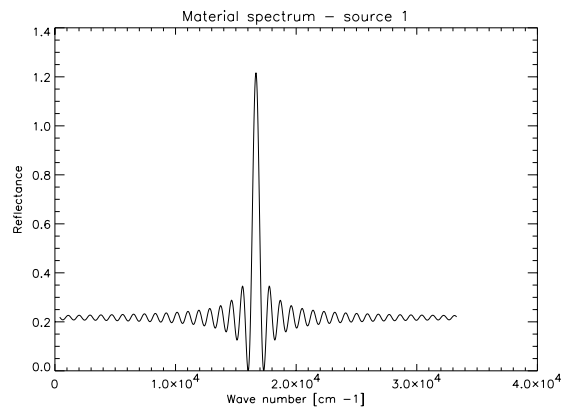


Figure 2.25: Original spectrum used for the quantization experiment

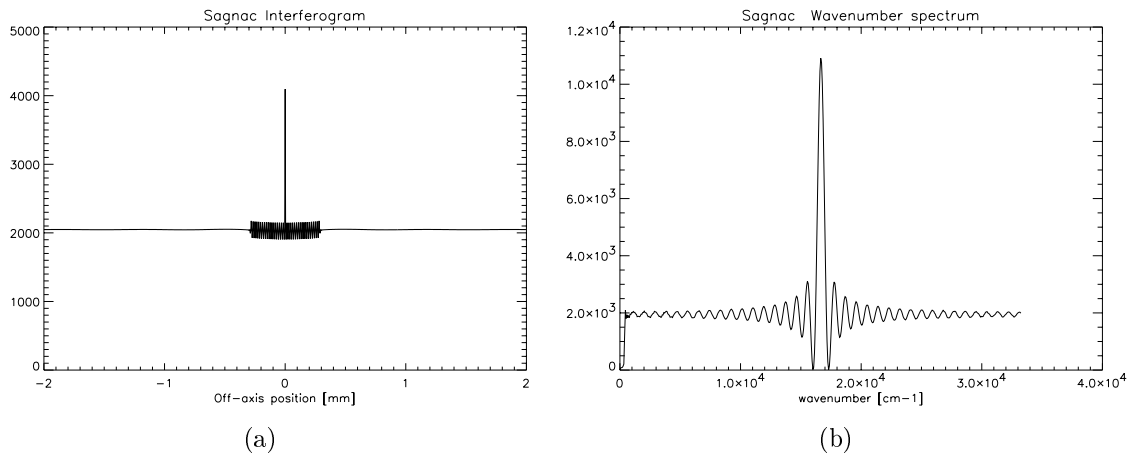


Figure 2.26: Interferogram (a) and spectrum (b) obtained with 12 bits quantization

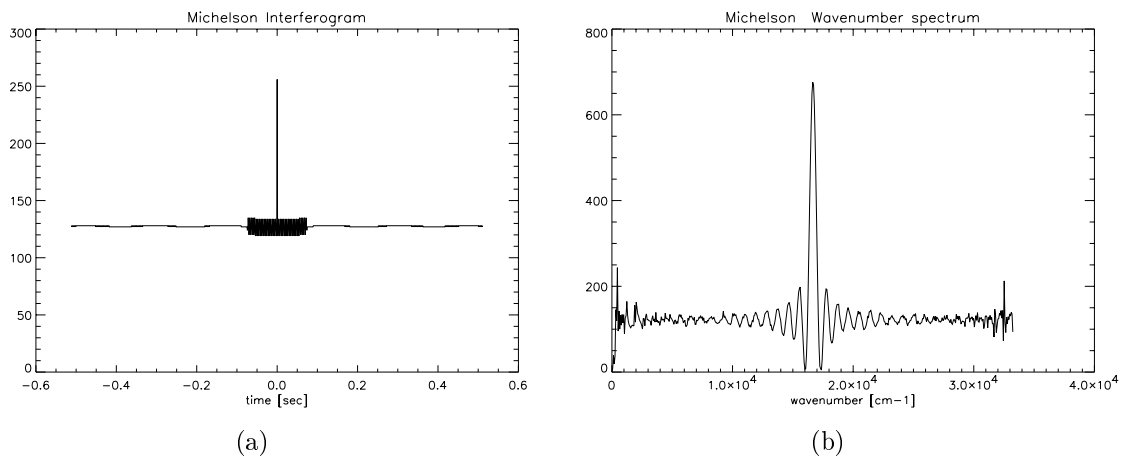


Figure 2.27: Interferogram (a) and spectrum (b) obtained with 8 bits quantization

Clipping

Clipping (also called saturation) occurs when the input signal amplitude exceeds the capacity of the detector. In this research, clipping is modeled as part of the detector module. The effects of clipping are automatically generated when taking the Fourier transform of a clipped interferogram. Clipping depends on the quantum efficiency of a detector, the well depth, the photon arrival rate, and the integration time. For the simulations, a maximum detector intensity value was used as the clipping limit.

The ZPD location (center burst) is the part of the interferogram most likely to suffer from clipping because it has the largest amplitude. Any amplitude larger than the detector capacity is reduced to the maximum value. To understand the effects of clipping, consider that the Fourier transform of a pair of delta functions shifted on either side of the origin is a cosine function whose frequency depends on the shift from the origin. In the case of an interferogram, the origin is the ZPD position.

When clipping occurs at the ZPD, the resulting interferogram is equivalent to the ideal (non clipped) interferogram minus a Dirac delta function. The transform of a Dirac delta is a constant value across all frequency ranges. Since the FT operation is linear, the interferogram minus a Dirac delta function transforms to the spectrum minus a constant. The resulting spectrum will be shifted down in amplitude, and values that had zero amplitude will now be negative.

The amplitude of an ideal interferogram is symmetrical about the ZPD position. If a sample is clipped on one side of the interferogram, its mirror equivalent also will be clipped. Clipping a side-lobe is akin to removing a shifted Dirac delta function from the interferogram. The FT of an even pair of Dirac delta is a cosine. Following the same reasoning as the previous example, side-lobe clipping has the effects of modulating the spectrum with a cosine. For non symmetrical or single-sided interferograms, clipping also results in the modulation of the spectrum by a sinusoidal waveform whose frequency and phase depends on the shift from ZPD.

Clipping can be considered to be one type of non linearity of detected signal with intensity. Other non linearity problems occur with detectors but they are not treated in this research.

2.8.5 Off-Axis (Obliquity) Effects

Off-axis effects occur when the radiation travels through the optics of the sensor at an angle to the optical axis, and are relevant only for Michelson FTS. One effect is related to the tangent distortion (Schott, 1997) and the angular field of view associated with the sensor. When operating from an airborne platform, a Michelson IFTS must stare at a location on the ground while the platform travels forward in the sky above. To understand this effect, consider the Ground Instantaneous Field Of View (GIFOV), which is the projection of one pixel on the ground at any given moment. The GIFOV will to change with staring angle in both size and location. Figure 2.28 illustrates how the size of pixel projection can change with pointing angle. When the scene contains spectrally

diverse objects, the changing pixel size causes the sensor to see spectral variations due to different concentrations of spectrally different objects within each pixel. In short, the pixels are mixed in different proportions. In some cases, the ground projection of a given off-axis pixel at the beginning of the scan may not overlap with the projection of the same pixel at the end of the scan. The effect on the spectrum is the same as for spectral variations (see section 2.8.3). This effect may be reduced by registering the off-axis pixels, which ensures that the entire interferogram is a result of the same object. However, registering the off-axis pixels was not implemented as part of this research because such a procedure does not exist on current FTS systems.

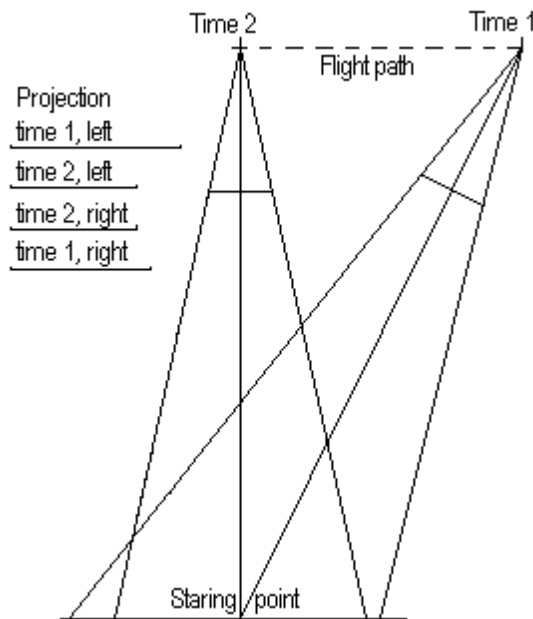


Figure 2.28: Change in GIFOV with pointing angle

The second off-axis effect considered here is the spectral shift. To understand this effect, one needs to consider the path taken by a beam of light from the object plane to the image plane. The radiation coming from a point located on-axis at the object plane will be collimated into a beam travelling parallel to the optical axis until it is focused to the image plane by the second lens. By comparison, radiation emanating from an off-axis will be collimated so that the wavefronts travel at a small oblique angle to the optical axis. Because the angle is constant for the whole path in the interferometer, it is easy to calculate that the OPD of the off-axis beam $\delta / \cos \theta$ (or $\delta \sec \theta$). At

least, this is what is implied in Wolfe (1997), and it is also the intuitive feel I had for this effect. It took many publications to convince me otherwise (Bell, 1972; Villemaire, et al., 1995; Bennett, et al., 1993; Yap, et al., 1982). In the end it is the effect of the collimating lenses that convinced me. One must think, not in terms of rays, but in terms of wave fronts.

In a Michelson interferometer, the collimating lens is responsible for the off-axis angle of a wave front, θ , (Equation 2.9). Radiation from a point in the object plane located at a distance y from the optical axis will create a collimated wave front at an angle θ to the optical axis. Similarly, any wavefront whose normal is at an angle θ to the optical axis will be focused by the second collimating lens to a point on the image plane at a distance y' from the optical axis. Figure 2.29 shows the propagation of off-axis wave fronts in a Michelson interferometer for mirrors separated by a distance d . The OPD between the wave fronts reflected by the fixed and scanning mirror can be calculated from this figure. The OPD is $2d \sec \theta$ minus the correction required for the shift in the wavefront (see Fig. 2.29) . This correction due to the shift is:

$$\begin{aligned}
 \text{OPD}_{\text{shift}} &= \frac{2d}{\cos \theta} \sin \theta \sin \theta \\
 &= \frac{2d \sin^2 \theta}{\cos \theta} \\
 &= \frac{2d[1 - \cos^2 \theta]}{\cos \theta} \\
 &= 2d \left[\frac{1}{\cos \theta} - \cos \theta \right]
 \end{aligned} \tag{2.12}$$

The OPD is:

$$\begin{aligned}
 \text{OPD} &= \frac{2d}{\cos \theta} - \text{OPD}_{\text{shift}} \\
 &= \frac{2d}{\cos \theta} - 2d \left[\frac{1}{\cos \theta} - \cos \theta \right] \\
 &= 2d \cos \theta
 \end{aligned} \tag{2.13}$$

which is consistent with the result found in the literature.

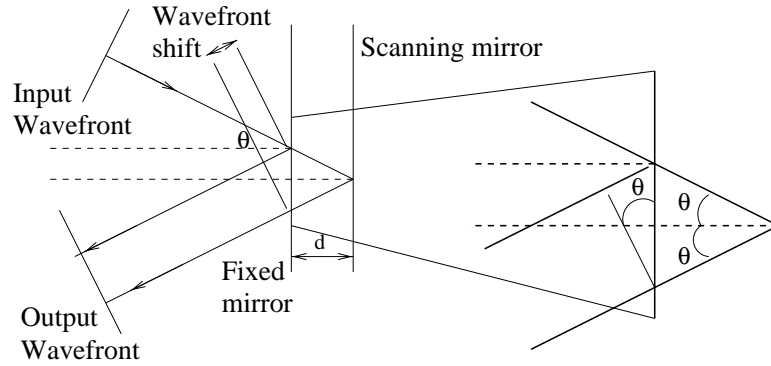


Figure 2.29: Off-axis wave front propagation in Michelson interferometer

The discrete Fourier transform makes the resolution of each domain related by the expression (Gonzalez and Woods, 1993):

$$\Delta u = \frac{1}{N \Delta x} \quad (2.14)$$

where Δu and Δx are the frequency and spatial domain resolutions, respectively, and N is the number of samples in the sampled sequence. Using Equation 2.14, the spectral frequency resolution of the spectrum can be expressed as:

$$\Delta \sigma = \frac{1}{N \cdot OPD} \quad (2.15)$$

where N is the number of samples in the interferogram. It is easy to see that a decrease in OPD by a factor of $\cos \theta$ will lead to an increase in the frequency increment. For off-axis pixels, the result will be a shorter spectral range (in wavenumbers), $\sigma' = \sigma \cos \theta$. Figure 2.30 illustrates this effect. The shift from the center pixel to the edge pixel is shown to be 3 cm^{-1} .

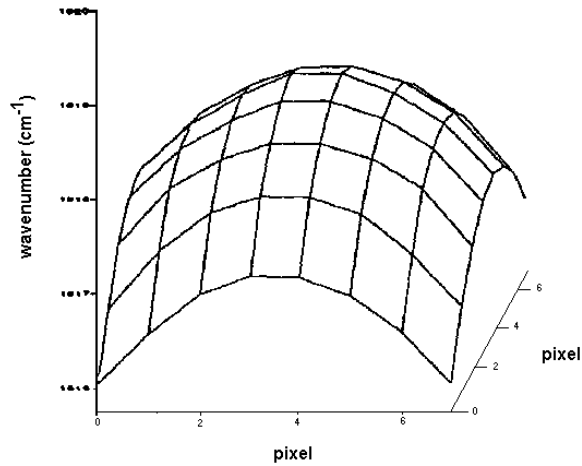


Figure 2.30: Frequency shift map for an 8×8 focal plane array (Oermann and Smithson, 1995)

The off-axis spectral shift effect was implemented as part of the DIRSIG FTS simulation. Other off-axis spectral effects include reduced resolution due to the broadening of the instrument lineshape (ILS), and reduced ringing in the side lobes of the ILS (Villemaire, et al., 1995). These are due to the finite size of each object pixel and thus to the finite solid angle subtended by each pixel. These secondary effects were not simulated as part of this research.

2.8.6 Spectral Response (Detector, Amplifier, Optics)

The radiance reaching the sensor must traverse elements which attenuate the radiance before it can reach the detector. The intensity of a spectrum therefore depends on the spectral response of the detector and other elements of the image chain. The spectral response is what limits the spectral range that can be collected by a FTS. For simulation purposes, the spectral response of any system may be calculated, bundled together with the spectral response of other systems, and simply used as a modifier to the input spectrum. This research simulated the spectral response effects for an arbitrary part of the image chain. The spectral effects for the entire image chain may be bundled in one modifier. The spectral effects for the beamsplitter will be discussed separately.

2.8.7 Lenses and Optics

Many artifacts present in IFTS are caused by lenses or optical elements. This section first discusses the effects of chromatic aberration followed by a discussion on the effects of beamsplitters.

Chromatic Aberration (Index of Refraction)

The index of refraction of materials used in the fabrication of refractive optics vary as a function of the wavelength; as such, different wavelengths exhibit different dispersion, which is the cause of chromatic aberration. These effects must be considered for the Michelson interferometer when a thick, non-symmetrical beamsplitter is used. A beamsplitter is a semi-reflective coating supported upon a rigid, but transparent, material. The varying index of refraction this support material causes chromatic aberrations. In a Sagnac interferometer, dispersion will cause the virtual object separation to be a function of wavelength (Hayden Smith and Schempp, 1991).

Figure 2.31 shows the path of the reflected and transmitted beams through a beamsplitter in a Michelson design. The thick line represents the semi-reflective layer. It can be seen that the reflected beam will propagate through the glass three times, compared to one time for the transmitted beam. To reconcile the two beams, a “compensating plate” made from the same material and the same thickness as the beamsplitter is inserted into the other arm of the interferometer. The compensating plate equalizes the dispersion of the two beams. More information on this topic can be found in Steel (1983).

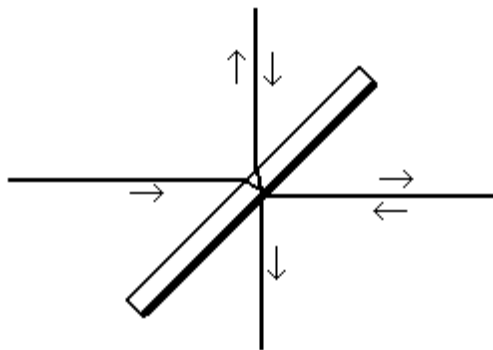


Figure 2.31: Reflected and transmitted paths through a beamsplitter

It is possible to avoid the need for a compensating plate by using symmetric beamsplitters, which

consist of semi-reflective coatings sandwiched between two identical layer of supporting material. All transmitted or reflected beams will follow equivalent optical paths. Beamsplitters will be covered in more details in a subsequent section.

Lenses (for collimation, Fourier transformation, etc...) are also culprits of chromatic aberration. To avoid chromatic aberration due to lenses, some spatial FTS designs use parabolic and cylindrical mirrors instead of spherical and cylindrical lenses (Lucey, et al., 1993; Sweedler and Denton, 1989).

This topic of chromatic aberrations is not covered well in the FTS literature, which means either that its effect is negligible or are directly derived from other sensor types. In any case, more research is required on the subject before it can be implemented as a source of error in this simulation. Therefore, chromatic aberrations were not considered as part of this project.

Beamsplitter

An ideal beamsplitter would transmit exactly 50% of the radiation and reflect 50% over the entire spectral range. In reality, beamsplitters actually have spectrally varying transmission and reflection. While this has little effect on a Michelson interferometer — each beam is reflected once and transmitted once — it can cause problems in the case of a Sagnac interferometer since each beam will either be reflected twice or transmitted twice. This will have an effect on the interferogram and the recovered spectrum. However, the fix is a simple one: the interferogram's DC level must be subtracted before taking the Fourier transform of the interferogram. See Appendix A for a confirmation of this statement. Careful calibration of the instrument is necessary to maintain the radiometric accuracy.

Derivation of the beamsplitter transmittance and reflectance effects for both the Michelson and Sagnac interferometers is found in Appendix A. Since the effect of beamsplitter transmittance and reflectance on the interferogram is minimal unless the beamsplitter deviates from the ideal case by more than $\pm 5\%$, this effect was not simulated.

Absorption can be modeled by modulating the input radiance field by a value proportional to the spectral absorption multiplied by the number of passages through the beamsplitter (or compensating plate).

Beamsplitters are responsible for yet another artifact. Everyone that has seen the reflection of an object in a window knows that transparent objects are not 100% transparent. Some reflection occurs at the surface of the window. The same effect occurs in beamsplitters. This unwanted reflection

is coherent with the source and thus will interfere and introduce noise in the interferogram. For Michelson FTS, this “noise” is highly correlated to the “noiseless” interferogram, since the noise is an attenuated and translated version of the ideal interferogram. Since the interferogram is shifted, the magnitude of its Fourier transform will be proportional to the expected spectrum. Therefore, the shape of the spectrum will not be changed due to this parasitic reflection. This is an unwanted effect especially when one uses inverse cosine transform instead of the magnitude of Fourier transform since the cosine transform is not shift invariant.

For Sagnac FTS, the unwanted reflection will produce a third virtual object that will not be affected by the beamsplitter to the same degree as the other two virtual objects, and will have a different shift than the others. It will interact with the other two objects with unknown consequences. Beamsplitter parasitic reflections were not simulated as part of this project.

When an antireflective coating is applied to the beamsplitter, the effect can be greatly reduced. Symmetric beamsplitters have two surfaces from which this effect can arise. Prism beamsplitters do not suffer from this problem since the surfaces of the beamsplitter are normal to the wavefront and therefore do not generate unwanted reflections.

2.8.8 Error in Path Difference

The discrete Fourier transform (DFT) or fast Fourier transform (FFT) assume that the interferogram is collected at equal sampling intervals. This assumption is an important factor in determining the intensity of the spectrum. If the interferogram generated from monochromatic light is sampled at the Nyquist frequency—at the location of peaks and troughs—then any random shift in the sample location will cause a different amplitude value to be recorded. The FT of this interferogram will then exhibit false frequencies. Sampling at rates exceeding the Nyquist rate may minimize this effect. Lower frequencies are less affected by error in sampling intervals because their interferogram fringe frequencies have larger periods, and a small variation in sampling location will not produce a large change in recorded fringe amplitude.

For the Michelson interferometer, the total distance traveled by the scanning mirror during integration determines the interval between the samples. For the Sagnac interferometer, the interval depends on the inter pixel distance of the focal plane array.

If the error in sampling interval is periodic, it can lead to aliasing, as frequencies at the limit

of being aliased are sometimes sampled above and sometimes below the Nyquist sampling limit. The error in sampling interval generally has a small effect and it can be considered as noise in the spectrum. Error in path difference can be simulated by adding a random normally distributed error sequence with zero mean and offset to the scanning location (pixel or mirror position). A value of 0.1 of the inter-sample distance could be used as the standard deviation for the error sequence. This would allow an evaluation of the effect of the error in sampling distance on the interferogram and spectrum.

A recent article by Cohen (1999) states that sampling noise can be removed by averaging several interferograms of the same scene taken under identical conditions. It is also a way to detect whether sampling noise is present in the signal. This approach would not work with my simulations simply because the pseudo-random sequences used as the sampling error are always identical. The code would need to be modified to enable a random, or user-defined seed. Cohen also predicts the effects of sampling errors based on the type of OPD jitter distribution. Also noted is the fact that OPD jitter is a form of multiplicative noise that resembles data.

2.8.9 Jitter Noise

Line-of-sight (LOS) jitter is the rapid vibration that affect the pointing accuracy of the sensor. The LOS jitter can be divided in two classes: high-frequency and low-frequency jitter, measured relative to the integration time. The effect of low-frequency LOS jitter can be simulated by introducing a random normally distributed variation in the pointing location about the staring point. Since the image has to be collected, there is very little computational overhead in simulating low-frequency LOS jitter along with collecting the image. For the Michelson, jitter affects the spectrum causing apparent temporal variation of the source spectrum. For the Sagnac interferometer, the effects are the same as for any pushbroom dispersive sensor due to roll, pitch, and yaw.

For dispersive systems, the common approach to simulating pointing jitter is to multiply the spatial FT of the image by the Modulation Transfer Function (MTF) associated with jitter (Tantalo, 1996). The result in a blurred image. Jitter affects the image indirectly in FTS systems. Blurring the spatial slice of the interferogram image cube with the jitter MTF could effectively simulate the effect of high-frequency jitter on FTS. Memory constraints prevent storage of the entire interferogram image cube during the simulation. This makes simulation of high-frequency LOS jitter with MTF

impossible. However, similar effects could be achieved with the use of spatial oversampling and a slightly modified version of the sensor point spread function (PSF). For this project, high-frequency LOS jitter will not be simulated. Techniques to reduce the sensitivity of FTS to LOS jitter have previously been described (Bennett, 1997).

2.8.10 Detector

Any effect present on a band of an image cube collected from a dispersive or filtered imaging spectrometer that is a result of detector design will also affect a slice of the interferogram image cube in a similar way for an FTS sensor. For example, while detector noise affects the image produced by a dispersive sensor, it also affects the interferogram of an FTS sensor. Detector noise, the effects of the sampling elements finite size, and the effects of FPA pixel sensitivity variations are discussed hereafter.

Noise

Two primary sources of noise are associated with photodetectors: Johnson (thermal) noise and shot noise (Dorf, 1993). For simulation, both types of noise can be bundled into one term. Because the noise affects the detector, it must be added to the interferogram instead of the image. In simulating noise, one must ensure that a different noise image is added to the detector output for every integration time: the same noise image cannot be reused. The spectrum of additive white noise is additive Gaussian noise. The expected noise distribution can be shown through simple simulations. First, noise is added to a simple signal. The histogram of the noise distribution is calculated. Both the ideal and noisy signals are then Fourier transformed and the magnitude is computed. The histogram of the noise distribution is also calculated for this signal. Under given conditions, the noise distributions of both the spatial-domain and frequency-domain signals will be similar. The conditions for this approach to work are that the noise distribution is Gaussian and the FT of the ideal signal is large enough so that no negative values are generated in the complex FT of the noisy signal. The relevance of the second condition is that the magnitude operator used in this simulation following the FT makes the negative values positive, hence skewing the noise distribution of the transformed signal. A simulation that respects both conditions is shown in Figure 2.32. It can be seen that the noise follows a Gaussian distribution in both cases.

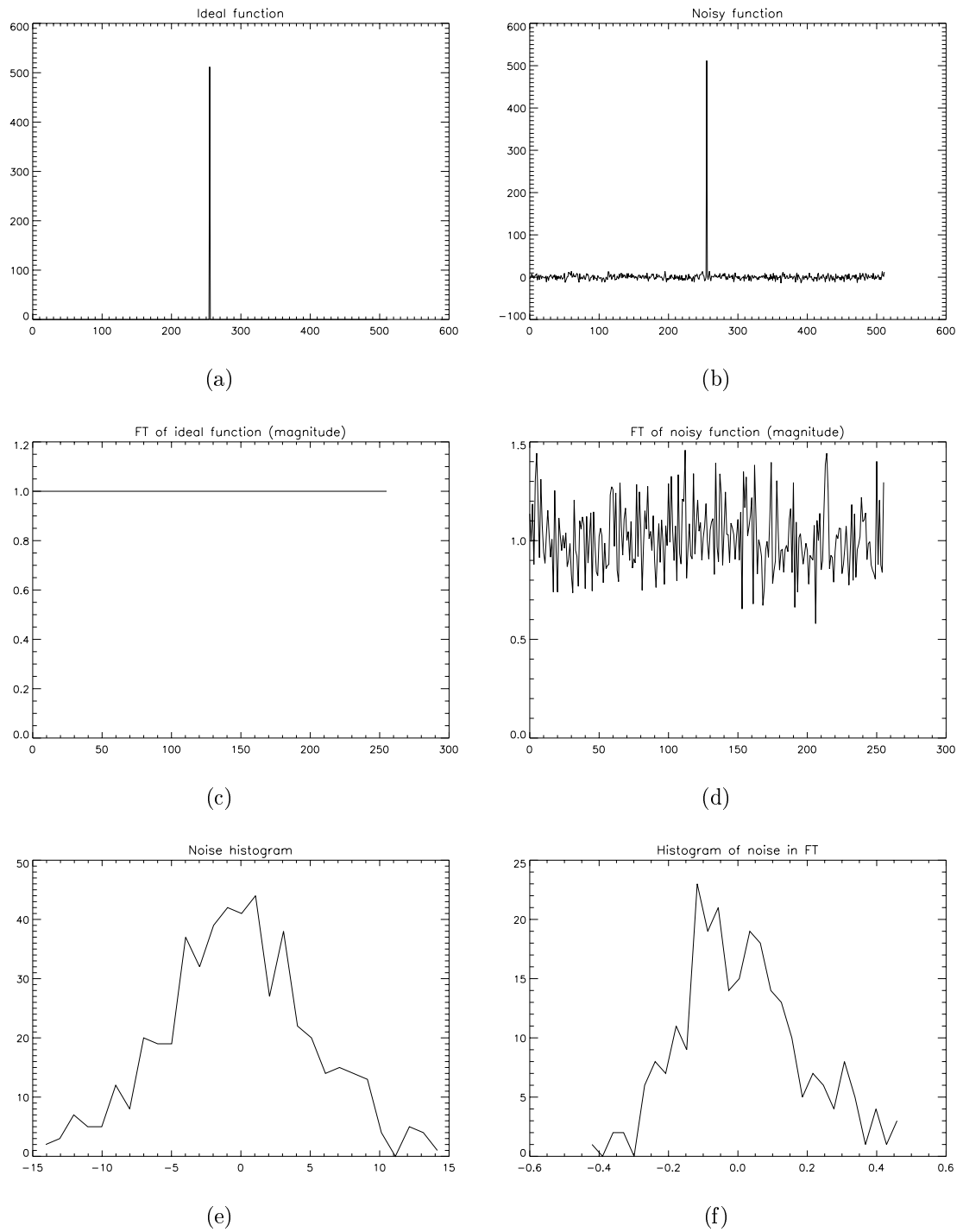


Figure 2.32: (a) ideal signal, (b) noisy signal, (c) magnitude of FT of (a), (d) magnitude of FT of (b), (e) histogram of noise distribution of (b) - (a), (f) histogram of noise distribution of (d) - (c)

Figure 2.33 repeats the same simulation but fails to respect the second condition. The result is that the noise distribution of the FT signal is shifted towards positive values rather than being centered around zero. This is because the spectrum of the ideal signal approaches zero. The FT of the noisy signal will then have negative values. The magnitude operator makes those values positive, hence shifting the noise distribution. The noise distribution is a combination of two other distributions: a Gaussian distribution resulting from the noise in the section of the spectrum which is too large to be made negative through the addition of noise (in this case, the part of the spectrum from 0 to 75 in graph (c)) and a Rayleigh distribution from the part of the spectrum which may become negative through the addition of noise (from 75 to 255 in graph (c)). The addition of those two distributions yields the distribution seen in Figure 2.33 (f). The magnitude operator is important because it is used in the simulations when inverting the interferogram to recover the spectrum.

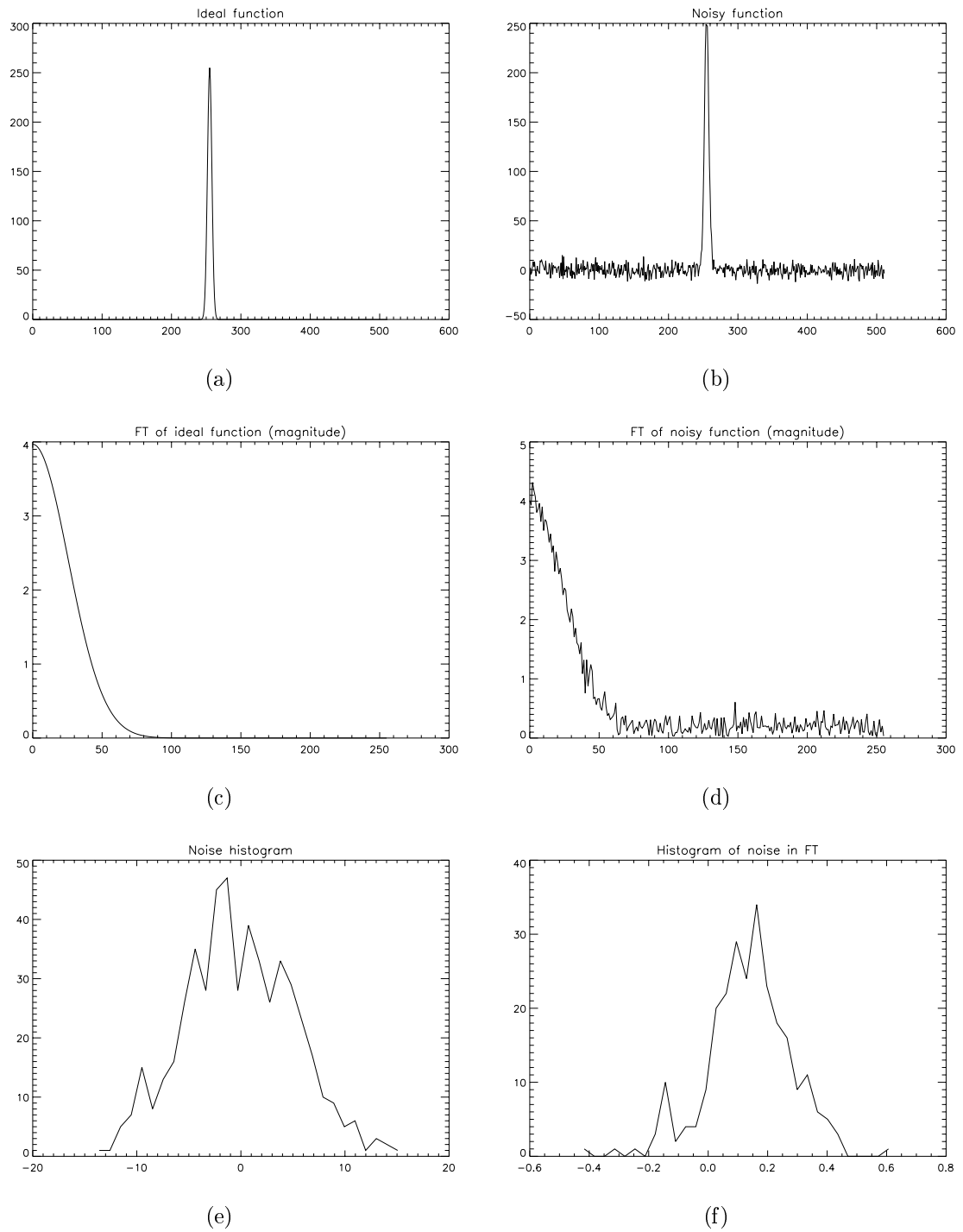


Figure 2.33: (a) ideal signal, (b) noisy signal, (c) magnitude of FT of (a), (d) magnitude of FT of (b), (e) histogram of noise distribution of (b) - (a), (f) histogram of noise distribution of (d) - (c)

Detector Sampling

Ideal reconstruction of a sampled signal is appropriate for a signal that is sampled over an infinite domain by true Dirac delta functions. Since the elements of a true detector are of finite size and because the signal is sampled over a finite domain, perfect reconstruction is impossible. The effect of finite sampling elements will be discussed here.

For a Michelson FTS, the finite size of sensor elements has effects only on the spatial coordinates of the image cube. The spectral coordinate is affected by the motion of the scanning mirror during the integration time. In a Sagnac FTS, the finite sampling size affects the spectral and one spatial dimension. The second spatial dimension is blurred by the forward motion of the sensor platform during the collection time. In both cases, the result is a blurring of the interferogram cube in all dimensions.

Both designs can simulate blurring of the interferogram cube by applying the appropriate MTF as described by Tantaló (1996), Feng, *et al.*, (1994) and Scott (1997). The same argument holds true for blurring due to the platform motion on a Sagnac FTS. The mirror scanning blur of a Michelson FTS is derived in Schumann, *et al.* (1997). The finite size of the sampling elements and mirror motion during scan will reduce the amplitude of the spectrum at high spectral frequencies. To limit this degradation in intensity, it is usually recommended to scan with an OPD of $\frac{1}{10 * \sigma_{\max}}$. Figures 2.34 to 2.36 illustrate some differences between ideal sampling and oversampling followed by averaging. Figure 2.35 demonstrates the degradation of high-frequency intensity caused by the mirror scan blur. In figure 2.36, the frequency of the signal in (b) would alias to the same frequency as (a), but with a lower intensity even though both input signals have the same amplitude.

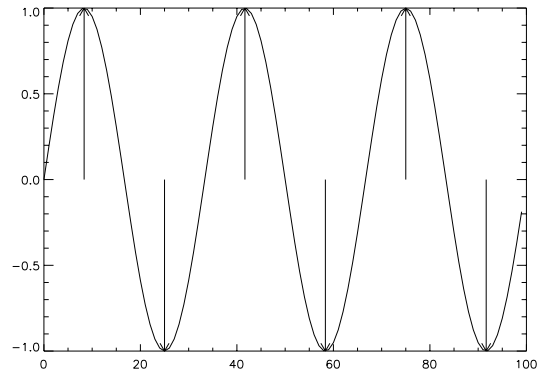


Figure 2.34: Examples of step and scan delta sampling

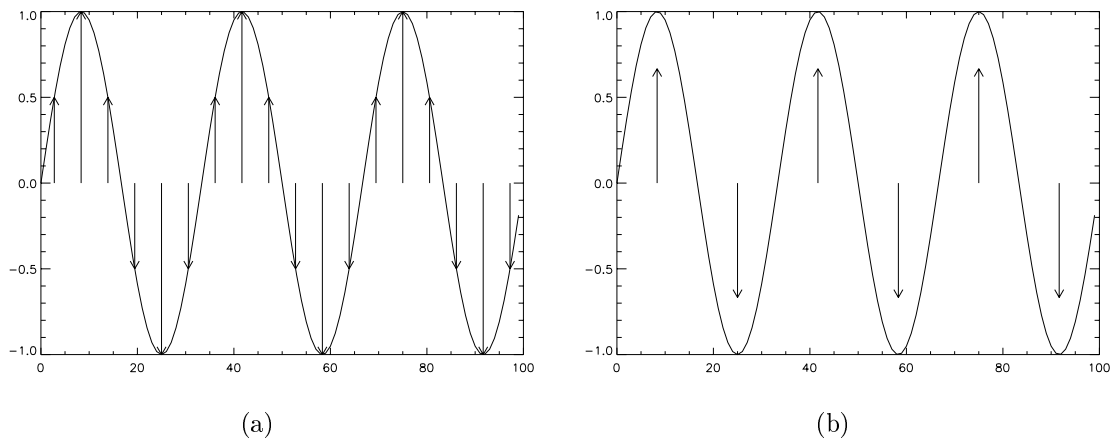


Figure 2.35: Examples of mirror scanning blur simulations: (a) oversampled delta functions, (b) averaged delta functions

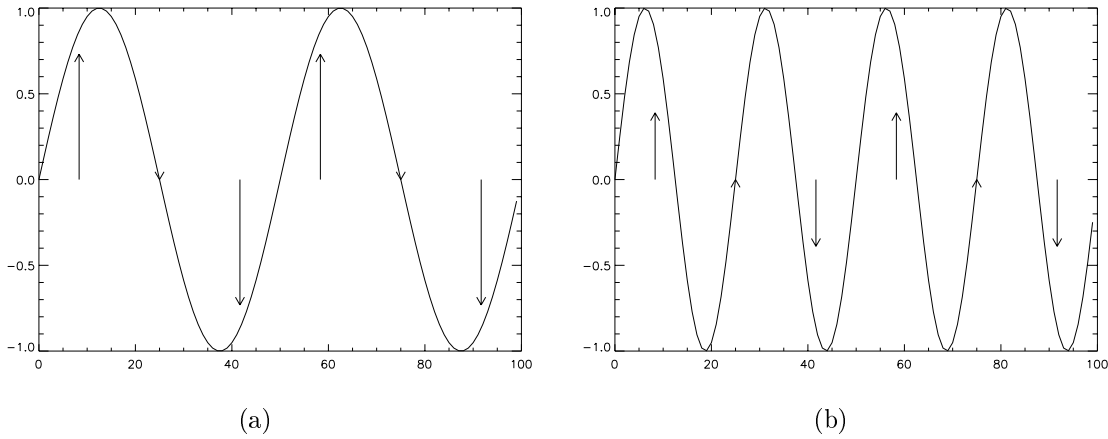


Figure 2.36: Examples of mirror scanning blur simulations: (a) for a below Nyquist frequency signal, (b) frequency signal above Nyquist

Oversampling is required to simulate blurring of the image cubes. Because of the increase in computation time most simulations are implemented first with delta function sampling. Once the required resources required are more clearly defined, spatial and spectral oversampling may be used for a more realistic simulation. Note that, though mirror-scanning blur can be simulated with a SINC-like MTF, I prefer using the oversampling followed by averaging technique. This is because using the SINC technique does not account for the possibility of error in path difference. This does not make much difference in the final results and takes slightly more computation time.

FPA Pixel Sensitivity Variations

Because the Sagnac device uses many detectors to record a single interferogram, it will be subject to artifacts due to variations in detector gain or sensitivity. This error in the interferogram translates to noise in the recovered spectrum (generation of false frequencies). Calibration and gain adjustment can correct this problem. A Michelson device collects the entire interferogram with a single detector, and so is immune to this problem since it will only affect the amplitude of the spectrum, i.e., no false frequencies are generated. Spectral amplitudes may be corrected through proper calibration. This effect was simulated for this project. The user must provide a default gain and bias value for the entire detector, and specific gain and bias corrections for other pixels.

A similar problem is that of bias shifts during the interferogram collection time. Despite the similarities, this effect was not considered in this research. The bias is assumed to be constant

throughout the simulation.

2.8.11 Self-Emission and Thermal Noise

FTS that cover the thermal IR range are susceptible to thermal noise from any of their components. Cooling the sensor greatly reduces this source of noise.

One study has indicated that beamsplitter emissions affect absolute radiance calibration (Revercomb, et al., 1988). Since the study was limited to one FTS model, “it is not known whether the problem is common or rare in other FTIR applications”. Mertz (1965) also noted this effect.

A different study concluded that “radiation entering the interferometer from the detector port contributes to the interferogram measured by the detector and causes a systematic error in the spectrum” (Tanner and McCall, 1984). This means that the detector acts as a thermal source. It is also noted that interferometers built with cat’s-eye mirrors do not suffer from this ailment since the radiation does not return to the source, which happens also to be the detector, i.e., the detector does not detect its own radiation. Other than the detector noise treated in section 2.8.10, noise was ignored in this project’s simulations.

2.8.12 Vignetting

Vignetting is the effect of obscuration or reduction in intensity of the image due to the limited aperture of the optical elements. In a sensor, vignetting affects the signal received by pixels located at the edge of the focal plane array. Because a single pixel collects the entire interferogram in a Michelson design, vignetting will reduce the amplitude of the interferogram, which will transform to the correct spectrum, but also with reduced amplitudes. Because an entire row of pixels collects an interferogram in a Sagnac design, the analysis is more complicated. The central region of the interferogram will be unchanged, but the extrema of the interferogram will have a reduced amplitude. False frequencies appear in the recovered spectrum.

Vignetting may be simulated by subtracting amplitude from the extrema of the recorded interferogram. Since the FT operation is linear, the resulting spectrum can be expressed as the ideal spectrum minus the Fourier transform of the signal that was subtracted from the extrema of the interferogram. Figure 2.37 (a) illustrates a signal that could be added to an interferogram to simulate vignetting. Figure 2.37 (b) is the magnitude of the FT of (a). That signal would be added

to the ideal spectrum in a simulation of vignetting. The effect is large at low wavenumbers but rapidly dies off, as shown in Figure 2.38. Apodization, by restoring the extrema of the interferogram to near their ideal level, can help reduce the effects of vignetting.

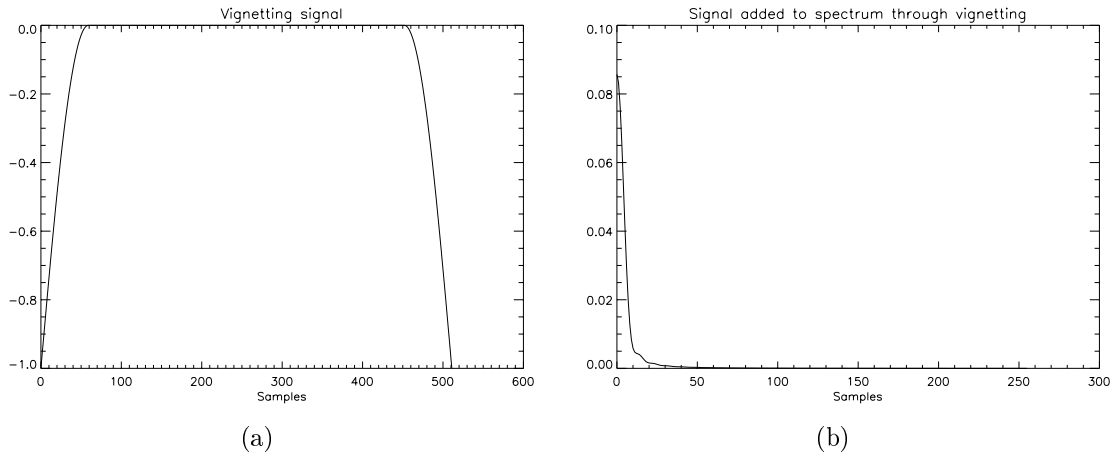


Figure 2.37: Effects of vignetting: (a) signal added to interferogram to simulate vignetting, (b) magnitude of Fourier transform of (a)

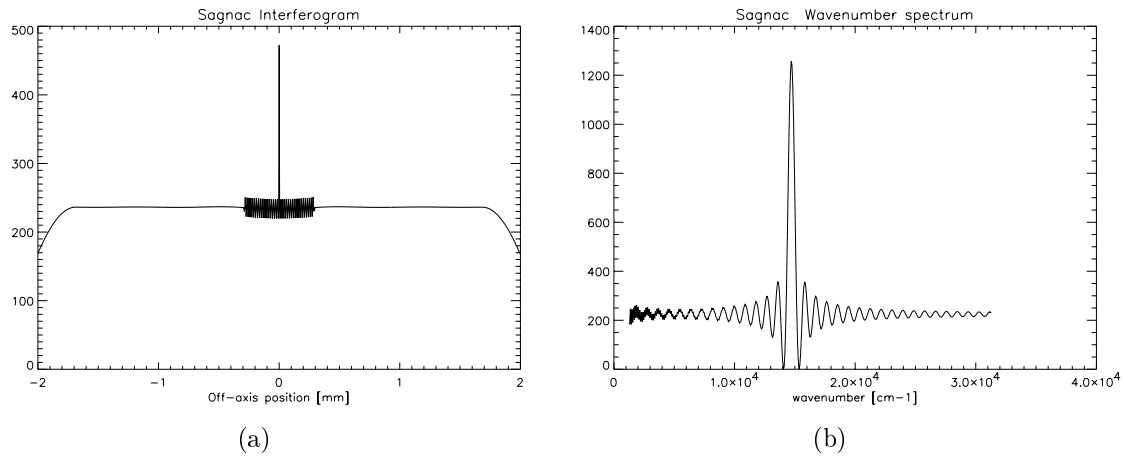


Figure 2.38: Vignetting simulation: (a) interferogram with vignetting, (b) recovered spectrum

The sensor is also inclined to be affected by the lens falloff— $\cos^n \theta$ —that governs the off-axis viewing exposure (Schott, 1997). The response of a FTS to such imaging concept would be similar to that of vignetting. However, since most FTS have a limited FOV, this effect can be considered negligible for the purpose of this research.

2.8.13 Dynamic Mirror Alignment

When a Michelson interferometer collects data, the moving mirror is subject to variations its alignment due to self-inflicted vibrations, such as friction between mirror and rail, and/or vibrations originating from platform interaction sources such as the engine and turbulence. When projecting the view from a detector pixel to the ground through the misaligned mirror of a Michelson interferometer, the location of the ground hit points for the misaligned mirror will differ from that of the fixed mirror. The interfering beams can no longer be considered coherent. Under those conditions, the usual interferogram equation cannot be used. A more general equation is derived in Appendix B, and effects are briefly discussed. The literature contains some discussion of the effects of mirror misalignment only in single-detector (non-imaging) interferometers (Cohen, 1997). Although much of the same analysis may be reused for imaging FTS, some important differences exist. One can be explained with the help of Figure 2.39. The top of the image is the ideal case with no misalignment. The bottom of the image shows the effect of misalignment of one of the mirrors. In the non-imaging case, there is a single detector on the focal plane. Any misalignment causes the amplitude of the spectrum to be smaller than for the ideal case. It can be shown that the reduction is a function of misalignment angle and has the shape of a “sombbrero” function (Gaskill, 1978). In the imaging FTS case, there is no certainty about whether the intensity detected by any pixel will increase or decrease with view angle. For that reason, the conclusions reached for the non-imaging system cannot be applied to the imaging FTS.

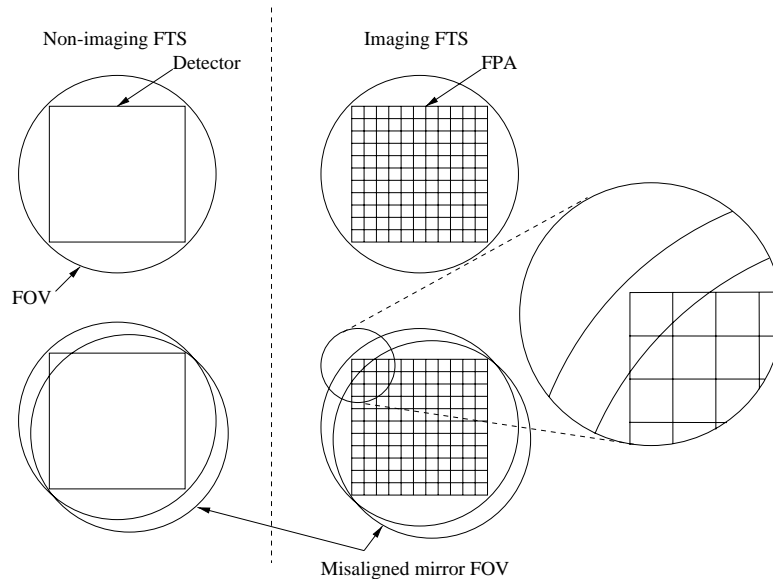


Figure 2.39: Comparison of the effects of mirror misalignment on non-imaging and imaging FTS at the focal plane

2.8.14 Miscellaneous

The image of the object must be located at the focal plane of the collimating lens to obtain sharp images (Bennett, et al., 1993). The same is true for the image plane. When the sensor is flown at very low altitudes, height variation in the scene may cause some objects to lie outside the depth of field. This effect was ignored in this simulation.

Effects such as detector cross talk and streaking also were not considered. These can be simulated as correlated noise by convolving the interferogram cube with a kernel that makes the current pixel a function of previous or neighboring pixels. They can also be included as part of the MTF of the sensor signal processing electronics (Tantalo, 1996; Schott, 1997).

The subject of atmospheric MTF has been touched upon by many authors. For a Sagnac FTS, the blurring effects of a turbid atmosphere will be constant over the image (as long as the view angle is constant). For a Michelson FTS, the MTF will be a function of view angle. For sensors operating at high altitude, the variation of MTF with view angle can be neglected, but should be considered for low-altitude collections. For the systems described herein, the atmospheric MTF must be used to blur the input radiance image (not the interferogram image).

For the Michelson interferometer, the fact that the two beams travel different paths also may

mean that they encounter different blurring conditions. Differences in atmospheric conditions (dust, humidity), mirror irregularities and alignment between the two arms may introduce irregularities in the interferograms and spectra. These were not simulated in this project.

Errors due to permanent misalignment of any optical component (end-mirror, beamsplitter, lenses) were not simulated in this project. See Griffiths and de Haseth (1986) or Persky (1995). Similarly, nonlinearity in detector response (other than clipping) was not considered (Herring, et al., 1993).

Interferograms may be one-sided or two-sided (symmetrical). The advantage of having a two-sided interferogram is averaging of that errors. Alignment problems can also lead to position errors in the interferograms.

Chapter 3

Approach

Prior to this work, DIRSIG included all ray-tracing computation to derive radiance fields at the sensor, but it lacked the ability to simulate FTS. The code necessary to generate synthetic FTS images needed to be designed, coded, tested and debugged. A rough design of the code is presented in this chapter. Each step in the process is to be considered. An added benefit of this design is that it can be used as a teaching tool to show all steps in the image chain. It also simplifies access to debugging information.

3.1 Program Design

As pointed out earlier, the simulation code is modular. This design allows for reusability, maintainability, and interchangeability of modules that use different algorithms. Each module represents a step in the image chain. The inputs, outputs, parameters, and usage of each module are described below. For this project, the FTS sensor package was written in C++ as an object. Each “module” was implemented as one or more “methods” acting on the object, where a “method” is simply a routine that has inputs and/or outputs and that affects the data content. Table 3.1 contains a list of very general methods that were used for the simulation. Methods that apply to both temporal and spatial FTS designs are in both columns. Some methods already existed in DIRSIG and were reused for the FTS applications.

Temporal FTS	Spatial FTS
User Interface Module	
Staring radiance	Pushbroom radiance
Michelson interferometer	Sagnac interferometer
Detector module	
FFT	
Image cube production	
Noise module (goes anywhere)	

Table 3.1: Modules for FTS implementation with DIRSIG

New methods can be inserted as necessary to generate artifacts and modify design properties of the FTS. The description of each module follows.

3.1.1 User Interface Module

Currently, DIRSIG uses configuration files as inputs to its simulations, with little or no run-time user interaction. The user interface module allows the user to define parameters of the sensor. The interface requires a formatted input file that contains the relevant information for the proper operations of the sensor. A method acting on the sensor object loads that file. As a starting point, an IDL widget is used as the user interface for setting up the parameter file and DIRSIG configuration file. The sensor object is initialized from the FTS parameter file. The method that loads the parameter file for the sensor object actually reuses many configuration routines developed for DIRSIG. There are talks under way to create a standard GUI for DIRSIG. The FTS configuration module is standard with DIRSIG so that the interface can eventually be upgraded to a graphic user interface (GUI) that is also standard with the rest of DIRSIG.

3.1.2 Input Radiance Modules

For a temporal FTS, the radiance field is collected in a staring mode (framing array), and in pushbroom mode for spatial FTS. The module requires the sensor altitude, speed, integration time (per sample), and collection time (for the entire image) to calculate the view angles and radiance field reaching the sensor. Effects such as roll, yaw, and pitch errors may be introduced at this point.

This is already supported for the pushbroom sensors present in DIRSIG. The implementation of this module therefore required only reusing existing code.

Under the temporal FTS mode, the output is the spectral radiance fields that correspond to each integration location—one spectral image cube per viewing location—for all integration positions. Figure 3.1 helps illustrate this point. This no longer represents a 3-D image cube as we know it, since it requires a fourth dimension (two spatial, one spectral, and one temporal). This enormous amount of data required many alternative schemes before restricting the output of this module to a single pixel at a time. Not only does this greatly reduce the memory requirements but it also speeds up the computation since the thermal model does not need to run multiple times for the same facet.

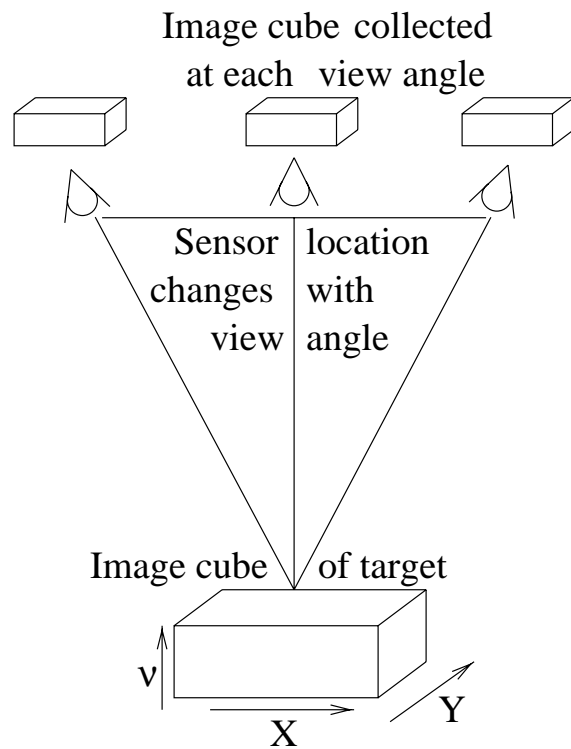


Figure 3.1: Need for a radiance field at each view angle for imaging Michelson FTS

The aforementioned radiance collection method has the disadvantage of requiring as many DIRSIG runs as there are viewing angles. A second method for obtaining the radiance fields is to generate radiance fields for a limited number of viewing angles. A simple linear interpolation of the two radiance fields closest to the required view angle is used to compute the intermediate radiance

field. For example, to collect radiance fields at $\pm 10^\circ$ off nadir, one could collect 800 radiance fields separated by $1/40^\circ$ or collect 5 radiance fields separated by 5° and use linear interpolation to derive those in between. In its limit, the radiance field can be generated for only one view angle, thus simulating a stationary sensor. It also is possible to collect radiance fields at more view angles than necessary—oversampling—to simulate a continuous scan, rather than scan at discrete locations. It is to be noticed that artifacts do not occur naturally in FTS sensors could be introduced in the simulated images if radiance field interpolation is used. One would then have to differentiate between the design artifacts and the simulator artifacts when viewing an image. This depends on the scene being imaged. This method can speed up the radiance field generation and reduce simulation run time while retaining the necessary accuracy. The number of entries in the sensor flight profile determines the number of view angles used for each simulation.

For spatial FTS, the input radiance is collected in the pushbroom mode. Much of the code already used in DIRSIG for simulating pushbroom sensors was reused. To follow the approach taken by the temporal interferometer, the input radiance is collected one pixel at a time.

3.1.3 Optical Effects Module

DIRSIG's sensor submodel already contains the functionality required for simulating the geometric effects of the optics in the FTS. These are the calculation of the FOV and ground hit points from the focal length, pixel size, number of pixels, spacing between lines, etc... Since a temporal FTS behaves like a framing array, the code for the framing array was originally reused for the Michelson implementation. However, since the framing-array implementation of the sensor in DIRSIG does not include roll and yaw effects, the implementation of the Michelson FTS was changed to a pushbroom sensor with multiple lines in the FPA. This change does not affect the “feel” of the sensor, as it still behaves as a framing array, but rather is simply a trick used to avoid extensive rewriting of a DIRSIG module. Since this change is transparent to the user, the Michelson type FTS will be described as a framing-array sensor. The only place where this is important is in the preparation of the configuration file. Since the IDL widget automatically accounts for this problem, the user needs not know that the Michelson is actually simulated with a pushbroom sensor. For the Sagnac FTS, the functionality of the pushbroom sensor also was reused. Effects such as blurring and apodization due to optics are not simulated at this point.

3.1.4 Interferometer Module

This module operates in different ways depending on the type of interferometer selected. For a temporal FTS, the module simulates a Michelson imaging interferometer. Parameters include mirror scan speed and precision, detector integration time, total scanning time, temporal (interferogram) oversampling, off-axis effects flag, etc.

For a spatial FTS design, the module simulates a Sagnac imaging interferometer. Parameters include mirror displacement, focal length Fourier optics, detector integration time, etc. The detector size also is required whenever the effect of the finite size of the detector on the sampling of the interferogram must be simulated.

3.1.5 Detector Module

This module controls detector parameters such as quantization, spectral response, clipping, apodization, gain, and bias. This module should be integrated in the Interferometer Module since the interferogram depends on the characteristics of the detector. Some inputs to this module are found in the BAND section of the DIRSIG configuration file. These are the number and size of pixels on the focal plane array and spatial oversampling.

3.1.6 FFT Module

This module processes the interferogram data cube to generate the spectra. Algorithms from Press, *et al.*, (1992) were used to implement this module.

3.1.7 Image Cube Module

This module takes the output data from any other module as an input and saves it to a file that can be read by the visualization tools available in the DIRS laboratory (e.g., ENVI). This module can be used to save the interferogram image cube, the spectral image cube, or the outputs from any intermediate step (after appropriate modification of code). Reuse of code already found in DIRSIG greatly simplified the writing of this module. Because the input radiance field for the Michelson can be collected over many view angles, the spectral image cubes for the input radiance fields are not saved. That is because the image cube would have four dimensions instead of three, and that no software tools exist to view that data. The fourth (temporal) dimension corresponds to a given view

angle. Even if tools were available to view the truth data, this would be very impractical due to the file size. As an example, if one wants to simulate an FTS with a 256×256 detector array and 400 bands, the radiance field would require 800 image cubes (temporal dimension—one for each view angle) of 256×256 pixels (spatial dimension), each containing 400 bands (spectral dimension). The total number of data elements would be $800 \times 256 \times 256 \times 400 \cong 21 \cdot 10^9$. At 4 bytes per element, this represents 84 Gbytes of uncompressed data. In contrast, the output image cube would require 105 Mbytes of data ($256 \times 256 \times 400 \times 4$). The interferogram image cube would include 210 Mbytes.

3.1.8 Noise Module

This module is used to simulate the presence of noise in the system at the detector level (interferogram). A database of the noise characteristics of the entire FPA and of specific pixels generates additive noise. The algorithms of Press, *et al.*(1992) were used to implement this module.

3.1.9 Documentation

Any software requires documentation to be useful. This is one part of the documentation, covering the theory and results that may be obtained with this tool. Code documentation is present as file headers and in-line comments. User manuals also were prepared in the form of help and “readme” files. More information on these texts is available in Appendix D.

3.2 Testing

Some artifacts associated with FTS appear only under specific conditions. As such, test scenes will be required to stress the envelope of the design. Early testing of the FTS sensor module was done with spectra shaped like one part of a known Fourier transform pair. The resulting interferograms and spectra can be predicted by Fourier theory. Known transform pairs were used to test the basic operations of the FTS. Because DIRSIG automatically includes the effects of the atmosphere in the simulations, it is impossible to perform these tests within DIRSIG. Instead, the tests with FT pairs required a stand-alone program that called the sensor object like DIRSIG, but used known FT pairs as input spectra. The inputs and outputs are easily modified and compared for testing purposes. To evaluate the imaging characteristics of the FTS, test scenes are required.

For comparison purposes, I also imaged some of the scenes with a model of a dispersive or filtered spectrometer with resolution similar to the FTS — already available in DIRSIG — or with an ideal version of the same FTS (no artifacts enabled). This helps provide a better understanding of the characteristics of the FTS.

3.2.1 Scene One

A simple test scene containing a single, spectrally simple object (little band-to-band variation, low spectral frequency), was used to validate the basic operation of the simulated FTS by verifying that the collected spectra match the object spectra. Solid objects generally have relatively simple spectra. The first tests consisted of collecting the interferogram with a fixed platform.

3.2.2 Scene Two

To test the spectral resolution of the sensors, a spectrally simple material is replaced with a spectrally complex material, such a gas. A synthetically generated sinusoidal spectrum with known frequency may be used to compare spectral resolution. The correct spectrum is returned when the spectral resolution is high enough. If the resolution is too low, an averaged or aliased spectrum is returned.

3.2.3 Scene Three

This scene contains strips of spectrally diverse objects [metals, rocks, and liquids]. Seven different materials were randomly assigned to the objects. The widths of the objects varied. With oversampling enabled, this scene allows characterization of the interactions of two objects, i.e., to view mixed pixels. The user can select where to point the sensor to view closely spaced lines or distant strips.

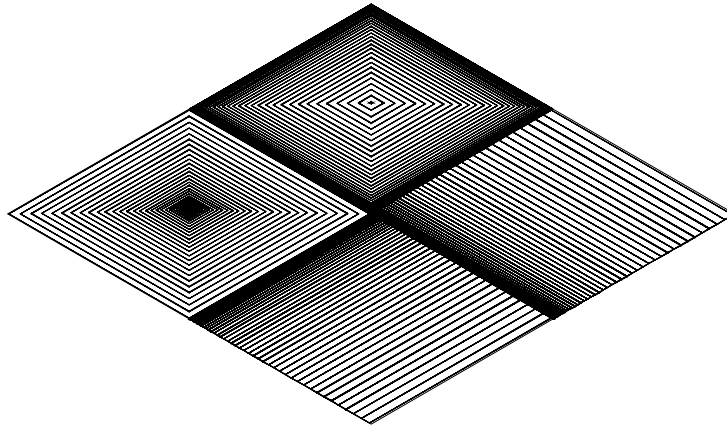


Figure 3.2: Test pattern for scene three

3.2.4 Scene Four

Because object height affects the scene viewed by the Michelson FTS, scene three was modified to include 3-dimensional objects. Tall walls were used, with top and sides made of different materials. This enables simulating the effects of varying spectra during the collection of the interferogram cube. The assumption is that the resulting spectrum will bear little resemblance to the spectra of the target, as long as the intensity and spectral shape of the spectra vary from spectrum to spectrum. Figure 3.3 shows the positions of the walls. Each wall has a different thickness, varying from 2.5, 5, 10, and 20 meters.

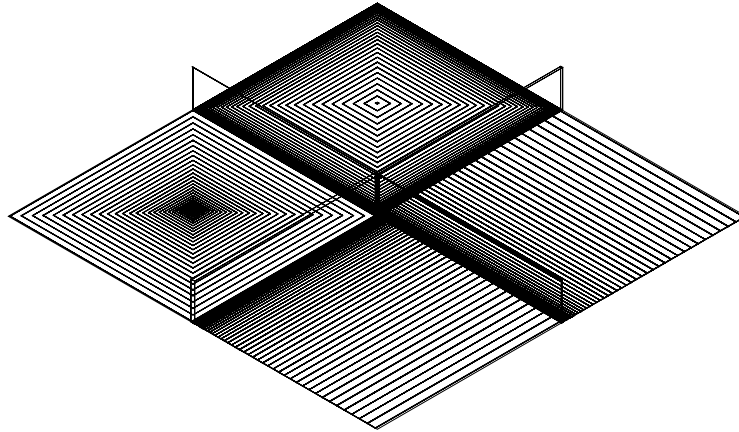


Figure 3.3: Test pattern for scene four

3.2.5 Scene Five

A demo scene is more successful when the audience can recognize and identify objects. During the lifetime of DIRSIG, many scenes were developed that resemble actual objects. Examples are the “Airport” and “Foxbat” scenes, which are ideal for such demonstrations. The “Foxbat” scene was used in these tests.

3.2.6 Final Demo Scene

A more complex scene was selected for the last test: the “NTS” scene including a gas plume. This will allow simulation of the effects of seeing a background through a gas cloud. Differences in the sensor rock point altitude can be simulated for a Michelson design. The rock point is the imaginary rotation point for the line of sight of the sensor. Tracking the top of the smokestack rather than the bottom should produce slightly different results.

3.2.7 Tests for Architecture Compatibility

DIRSIG can run on many UNIX architectures. The g++ compiler was used to compile my code. This code is therefore expected to run on any machine that is supported by the g++ compiler, barring a few operating system specific calls that might have to be converted.

Chapter 4

Results

While the routines were developed and tested for this project, DIRSIG was also being changed from Version 2 to Version 3. The new implementation has a friendlier user interface and faster execution. Because of the concurrent development of DIRSIG and the IFTS sensor model, many sanity checks were performed to ensure that the new DIRSIG version was performing as intended. Among the checks were verification of the correct ground hit point and FOV of the sensor, the correct material and temperature. These checks are not part of the results presented herein since the premise in doing this research is that DIRSIG performs all non-IFTS related simulations correctly.

This chapter compares the results of the simulations to the theoretical values. Most graphs in this chapter are either interferograms or spectra. Interferograms are displayed as the detected radiance ($\text{watts/cm}^2 \text{ sr cm}^{-1}$) as a function of the interferogram sample. Spectra are displayed in radiance units ($\text{watts/cm}^2 \text{ sr cm}^{-1}$) as a function of wavenumber (cm^{-1}).

4.1 Artifacts

Many artifacts were simulated using known Fourier transform pairs for the spectrum and interferogram using the stand-alone program. Remember that DIRSIG automatically generates the exoatmospheric sources, path thermal, downwelled, and transmissive effects. It is therefore impossible to simulate the DIRSIG results with known FT pairs. Even doctoring the atmospheric database to remove the effects of the atmosphere does not result in a perfect FT pair since the material emissivity is multiplied by a blackbody to obtain the spectrum of the material. The results

presented herein were generated with DIRSIG and are therefore do not use FT pairs.

To see the effects of a given artifact on an interferogram and its corresponding spectrum, the simulations must include only one type of artifact at a time. Unless specified otherwise, all results presented in this section demonstrate the effects of a single artifact.

4.1.1 Aliasing

Aliasing can be both a help and a hindrance to FTS. When frequencies above the Nyquist frequency of the system can be detected by the sensor, aliasing may occur. Aliased frequencies appear in the spectrum as lower-frequency components. Aliased and non-aliased frequencies cannot be distinguished. However, if the designer selects a system with a null spectral response above the Nyquist frequency, aliasing is prevented, but no information will be gathered at these frequencies. An alternate solution is to filter out all frequencies below the Nyquist frequency and pass higher frequencies. The active frequency range should be bounded by consecutive integer multiples of the Nyquist frequency to avoid corrupting the spectrum through aliasing, i.e., if the Nyquist frequency is 10000 cm^{-1} , then one could filter all frequencies below 10000 cm^{-1} and let frequencies from 10000 to 20000 cm^{-1} through. With that scheme, recovering the right frequencies would be as simple as inverting the recovered spectrum and shifting all values by 10000 cm^{-1} . Great care must be taken because the higher frequencies are much more sensitive to error in the scanning position and finite scanning distance. This is a trick that can be used with step-and-scan interferometers where delta sampling of the interferogram is assumed. This limitation makes it very unlikely that this effect may be used in a sensor which samples the interferogram over a finite distance. Aliasing is a good test case to verify the correct implementation of the code.

Simulations were conducted to demonstrate the effects of aliasing. The sensor spectral response was kept constant for all three simulations. The spectral response was unity for wavenumbers between 4492 to 9984 cm^{-1} and zero outside that range. The aliasing was generated by changing the speed of the scanning mirror. Note that these simulations assume that step and scan integration is being used rather than continuous scanning. Information on the effect of the scanning mirror is in section 4.1.9. The integration time was set to 0.004 sec and 512 samples were collected per interferogram. The first simulation is the ideal case without aliasing. The interferogram and spectrum are presented in Figure 4.1 (a) and (b), respectively. For this simulation, the mirror speed

was set at 0.00626 cm/s. The results shown in (c) and (d) were collected with a mirror speed of 0.0125 cm/s. At that speed, the maximum spectral frequency that the interferometer can collect without aliasing is 5000 cm^{-1} . Given that the region of the non zero spectral response is about 5000 cm^{-1} wide, all of the spectrum is mirrored in the 0-5000 cm^{-1} range. Since the spectral response is null below 5000 cm^{-1} , there is no interaction between the aliased and un-aliased parts of the spectrum. Only flipping and shifting the computed spectrum are required to recover the actual spectrum. Graphs (e) and (f) were collected with the mirror speed set at 0.009375 cm/s. This gives a maximum frequency of 6666.67 cm^{-1} . The region of the spectrum from 6666.67 to 10000 cm^{-1} is aliased so that the frequencies appear in the 3333.33 to 6666.67 cm^{-1} range. This causes an overlap of data in the 5000 to 6666.67 cm^{-1} range. Without prior knowledge of the spectrum, it is impossible to recover from this effect.

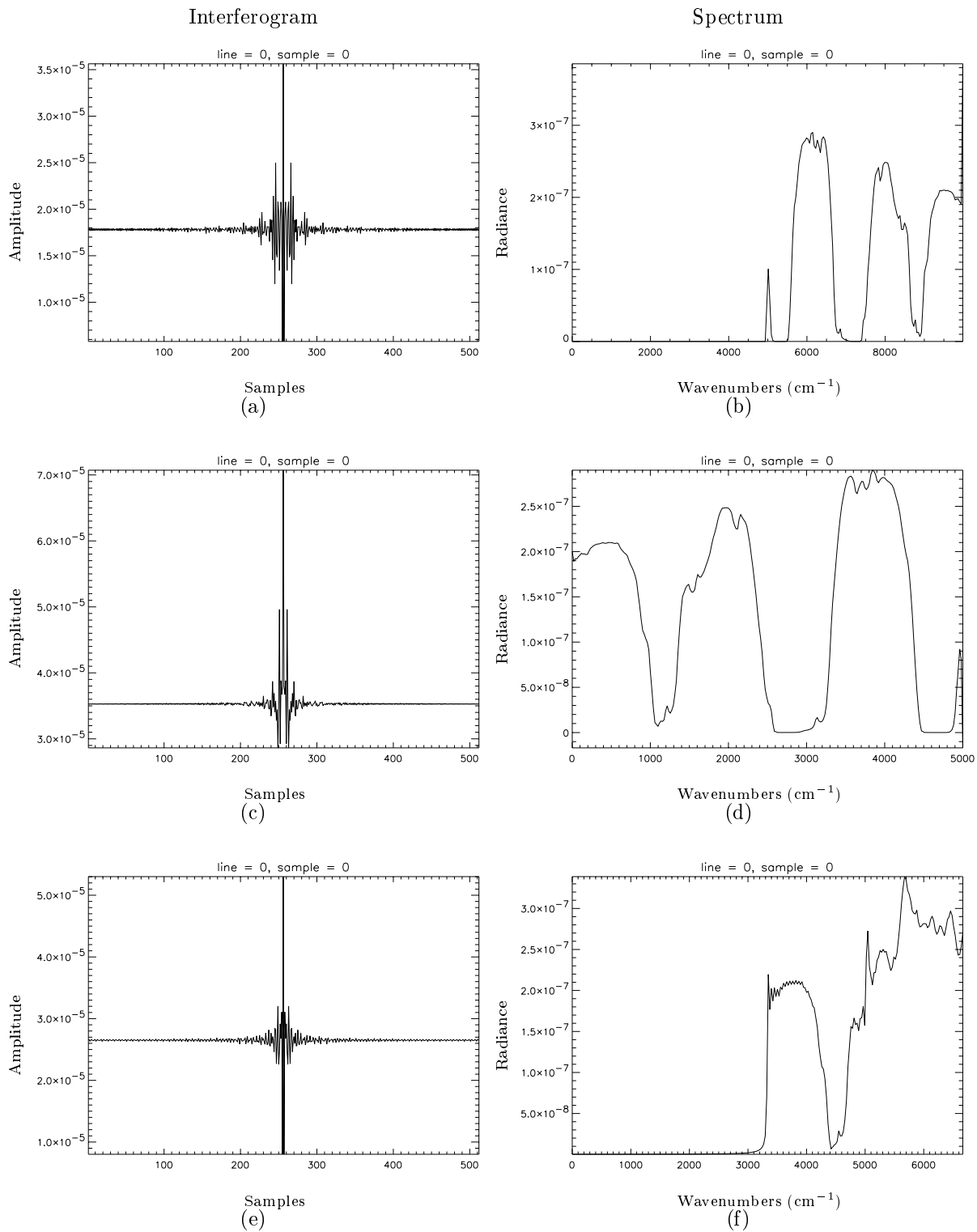


Figure 4.1: Examples of aliasing: (a) reference interferogram for no aliasing, (b) spectrum of (a), (c) full aliasing, (d) spectrum of (c), (e) partial aliasing, (f) spectrum of (e)

4.1.2 Apodization

When the interferogram is discrete, ringing is usually present in the recovered spectrum. The DFT operation assumes that the interferogram is periodic. If the amplitude of the extrema of the interferogram are different, a step is created in every period, as seen in Figure 4.2 (b). This problem can be resolved in part by apodization. If a discrete step is near the center of the interferogram, apodization will not have a significant effect on the recovered spectrum. The price to pay for the reduction in ringing is a small loss in resolution. In this simulation, only triangular apodization was used. Because the code was developed in a modular fashion, implementing different apodizations is a very simple matter. Apodization in itself is not an artifact of the design of a FTS, but rather a technique to reduce the “ringing” associated with a non-ideal interferogram. Because it was necessary to introduce other artifacts to see the effects of apodization, the results are shown in section 4.1.3.

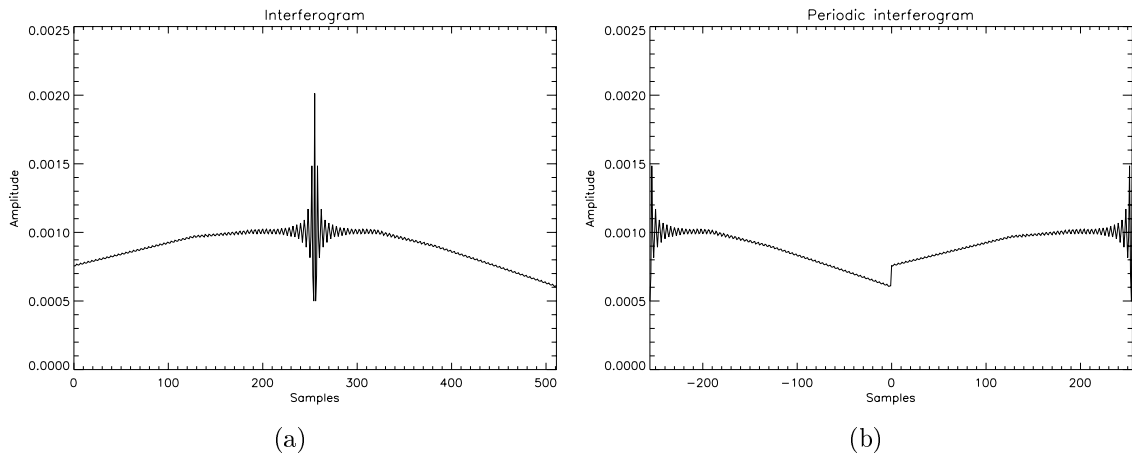


Figure 4.2: Step in interferogram amplitude due to periodicity: (a) original interferogram, (b) periodic interferogram over shifted window

4.1.3 Source Temporal Spectral Variation

As described in section 2.8.3, when data are collected from a moving platform, a Michelson FTS may record different spectra for a given pixel. The test scene in Figure 3.3 was developed to study this effect. The sensor stared at the base of a wall 200 meters tall, and 10 meters wide. The sides and top of the wall were made from different materials. The sensor measured 512 temporal samples in each interferogram. The platform travelled at a speed of 100 meters/sec, and the integration time was 0.005 sec, resulting in a total collection time of 2.56 sec. At an altitude of 4000

meters, the angular range is $\pm 1.83^\circ$. The simulation was performed in four ways. The most obvious simulation used DIRSIG to compute the spectrum at every view angle along the flight path and collect one interferogram sample for each point. This required 512 DIRSIG runs and generated as many interferogram samples. In a second simulation, the input spectrum was collected at 9 view angles; intervening spectra were computed by linear interpolation from the two closest spectra. This simulation scheme speeds up computation. A 16x16 image required about 12 minutes with interpolated values compared to more than one hour for the simulation using the 512 view angles. The artifacts introduced by the interpolation method and its effects are presented in Figure 4.3. The same interpolation scheme was repeated for 3 view angles. The final simulation assumed a stationary platform and required a single input spectrum. The results of the last simulation are deemed ideal because it is assumed that the target is the spectrum of the top of the wall. This assumption is based on the fact that the sensor pointed straight down at the target at the mid-point collection location. The changes in sensor pitch with view angle are simply artifacts of a moving platform and the need to track a fixed point on the target. The results are compared to the ideal spectrum. In the interferogram with 512 view angles, it is easy to see where the gaze of the sensor switched from the side of the wall to the top of the wall. Other than these two discontinuities, the edges of the interferogram have different amplitudes. The sharp variation in the interferogram at the side-to-top transition region is partly due to the fact that DIRSIG currently performs ideal delta sampling of the detector pixels. This results in the detector only seeing pixels containing a single material. A detector with finite area would result in a smoother transition. The detector might see pixels containing multiple materials (mixed pixels). This is why spatial oversampling is required for these simulations.

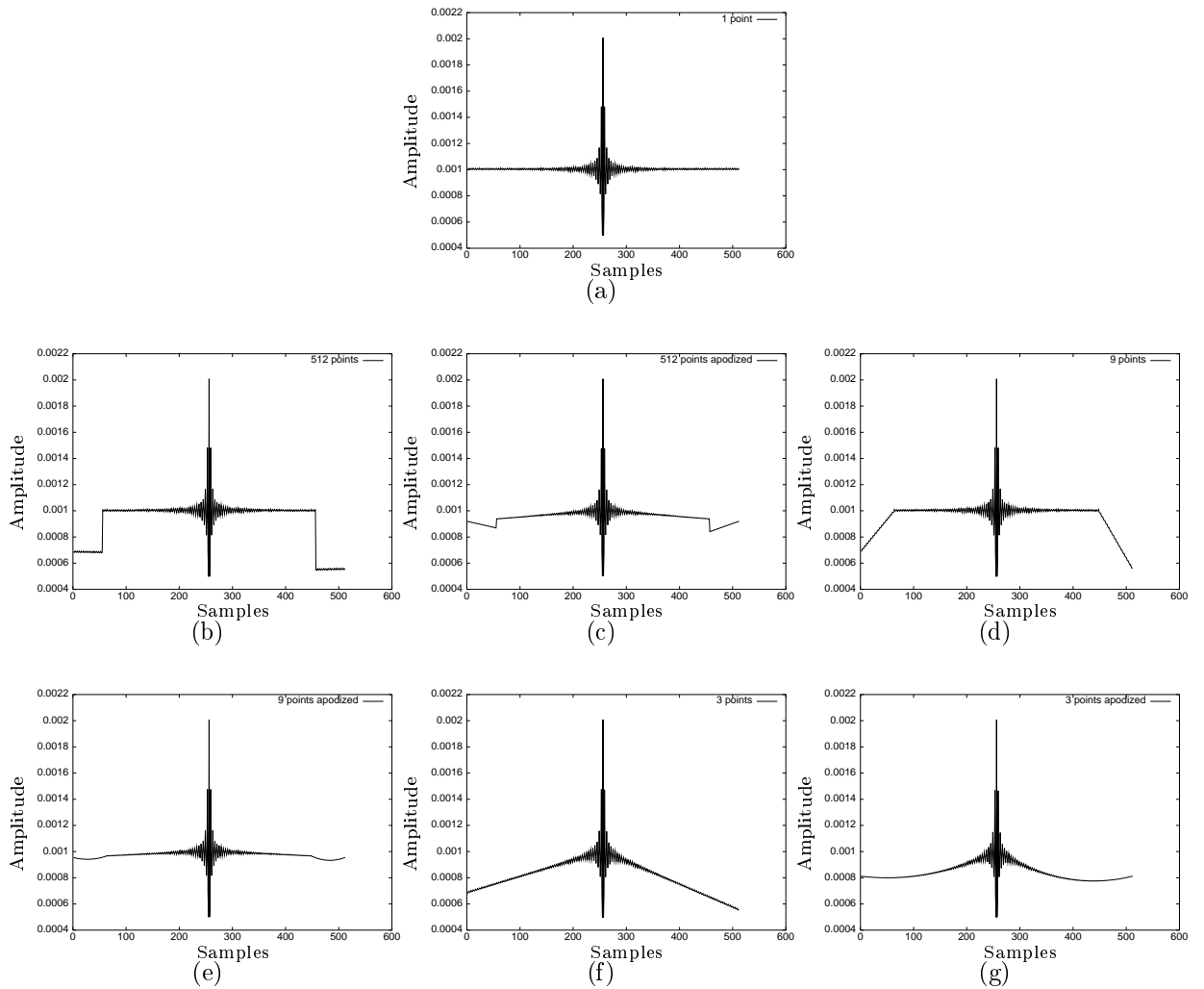


Figure 4.3: Interferograms of tall wall for different collection methods from moving platform: (a) ideal interferogram, (b) 512 view angles, (c) apodized version of (b), (d) 9 view angles interpolated to 512, (e) apodized version of (d), (f) 3 view angles interpolated to 512, (g) apodized version of (f)

Because spectra are mixed together in the interferogram, it is important to compare their shapes to that of the target. Spectra that are very different from the target spectrum would introduce artifacts in the calculated spectrum. When the shape is similar, less noise is introduced. The target and background are compared in Figure 4.4.

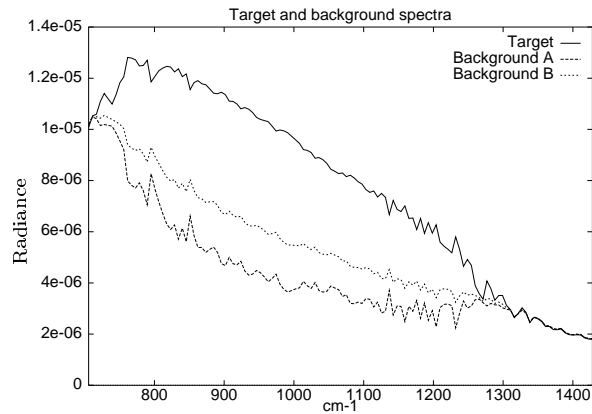


Figure 4.4: Spectra of target and background. Background A is the lower curve, and affects the interferogram in Figure 4.3 (b) in the 450-511 sampling range. Background B, the middle curve, affects the same interferogram in the 0-50 range. The target is the top curve and is responsible for the central portion of the interferogram.

The spectra generated from the interferograms are compared to the ideal spectrum. Notice how apodization greatly reduces ringing whenever sharp discontinuities are present in the interferogram. In all cases, the continuum closely follows the ideal spectrum.

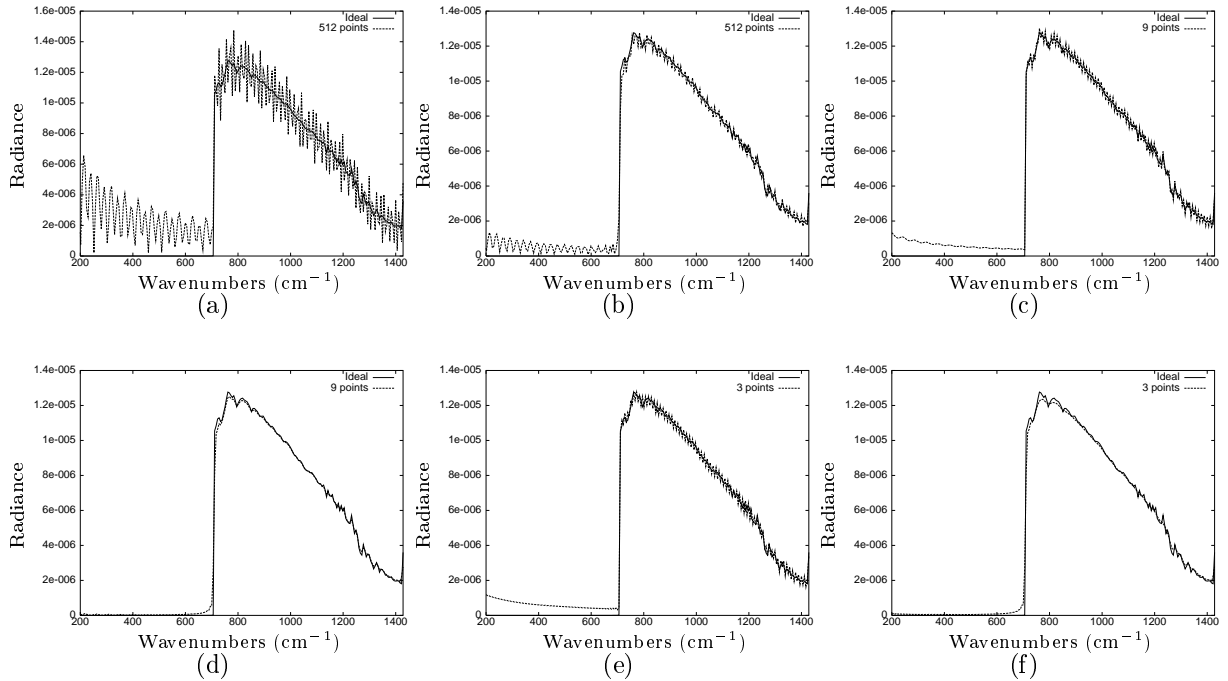


Figure 4.5: Spectra of tall wall for different collection methods from moving platform compared to ideal spectrum: (a) 512 view angles, (b) apodized version of (a), (c) 9 view angles interpolated to 512, (d) apodized version of (c), (e) 3 view angles interpolated to 512, (f) apodized version of (e)

4.1.4 Dynamic Range

The results of simulations that measure the effect of the dynamic range of the sensor are divided into tests of quantization effects and clipping effects. Because this section of the code operates identically for both Sagnac and Michelson sensors, only the results from a Michelson design are presented.

Quantization

To reduce the quantity of information to a manageable amount prior to the inversion to spectrum, the data must be quantized. While quantization produces banding in the images of dispersive spectrometers, the banding effect is found in the interferogram image cube for IFTS. This results in noise in the inverted spectrum. Quantization to more levels leads to less noise in the spectrum. If the dynamic range of the quantizer matches that of the signal, the amount of quantization noise will be minimized. Interferograms that do not fill this range will suffer from increased quantization

noise.

Results of quantization simulations are presented here to illustrate the previous comments. All simulations assumed a Michelson sensor with an 8x8 FPA. The signals were quantized to 8 bits (256 levels) because it readily illustrates the effects of quantization on the recovered spectrum, even though the industry standard is usually 12 or more bits. The dynamic range determines the quantization step size. For a dynamic range of $4 \cdot 10^{-5}$ units and 8 bits of quantization, the width of each step would be $\frac{4 \cdot 10^{-5}}{256} \sim 1.6 \cdot 10^{-7}$. This configuration was used for one simulation. Inspection of the interferogram from pixel 2, line 2, about sample 214 shows the following result:

Sample	Amplitude
213	$2.34375 \cdot 10^{-6}$
214	$2.50000 \cdot 10^{-6}$
215	$2.34375 \cdot 10^{-6}$

which proves that the quantization step size is correct. The simulation's results are compared to their ideal counterpart. Using double-precision floating-point numbers for the calculations is akin to quantization to about 50 bits, which leads to negligible quantization noise. Here, I assume that some bits are lost by the representation of the sign of the number and mantissa, and that the dynamic range used does not cover the entire range available to numerical representation.

The examples presented in Figure 4.6 use a dynamic range of $4.0 \cdot 10^{-5}$. Quantization noise can readily be seen in the spectrum, even though visual inspection of the two interferograms does not reveal many differences. Note that the peak of the quantized interferogram was clipped due to the dynamic range of the detector. This does not add to the quantization noise, but rather shifts the spectrum down in amplitude a bit. For more information about clipping, see the next section.

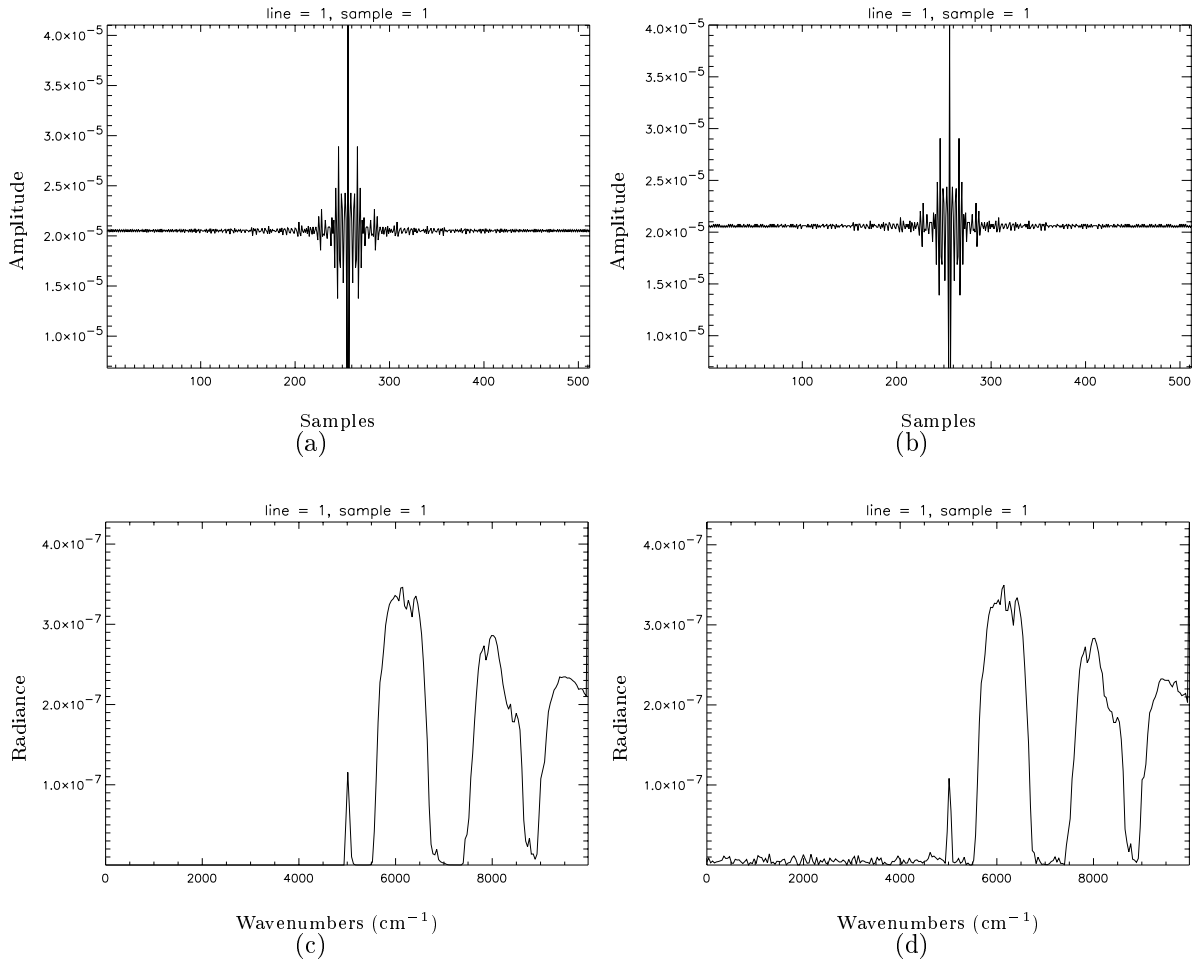


Figure 4.6:]

Quantization example at 8 bits for pixel [1,1], dynamic range of $4.0 \cdot 10^{-5}$: (a) ideal interferogram, (b) quantized interferogram, (c) ideal spectrum, (d) spectrum with quantization noise

Figure 4.7 is the result of the simulation for pixel [2,2]. The intensity of the spectrum reaching that pixel is about an order of magnitude weaker than for pixel [1,1]. Therefore, many of the quantization levels will be unused, which results in more quantization noise in the spectrum. The loss of resolution and introduction of false frequencies in the spectrum are readily apparent. The discrete quantization steps are also visible in the interferogram.

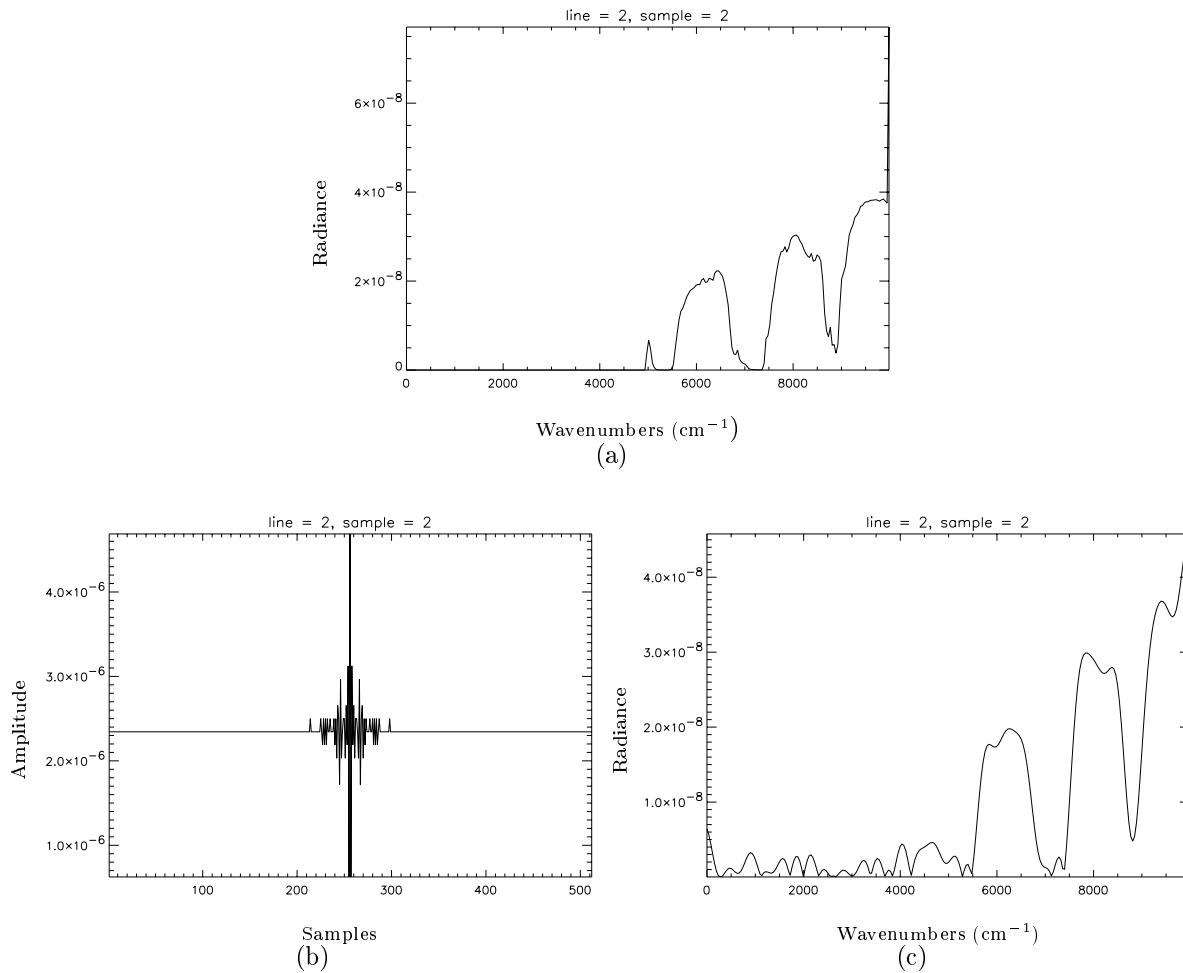


Figure 4.7:]

Quantization example at 8 bits for pixel [2,2], dynamic range of $4.0 \cdot 10^{-5}$: (a) reference spectrum, (b) interferogram, (c) spectrum with quantization noise

Clipping

Clipping or saturation of the center burst (ZPD intensity level) in the interferogram reduces the mean amplitude of the spectrum. If the interferogram cube is saved for transmission and later processing, the effects of clipping can be reduced. One way to correct this problem is to assume that the average interferogram intensity— $I(\infty)$ —is $\frac{1}{2}$ of the ZPD intensity (given no vignetting or other

artifacts), or:

$$I(\text{ZPD}) = 2 \cdot I(\infty) \quad (4.1)$$

Correcting the ZPD interferogram amplitude to the expected value and inverting the interferogram would yield the right spectrum. This can be done only if clipping affects only the ZPD interferogram value.

The effect of clipping is to shift down the amplitude of the spectrum. Because the magnitude of the inverted interferogram is used to represent the spectrum, any downward shift in the amplitude that would lead to a negative value is automatically mirrored as a positive value. Keeping track of the phase of the calculated signal would point to the regions where the spectra was inverted. This information could later be used for spectrum correction, in the case where a designer decided not to keep the interferogram.

Figure 4.8 illustrates the effect of clipping on the spectrum calculated by a stationary Michelson. Some quantization noise can be seen in the straight part of the spectrum between 0 and 5000 cm^{-1} (where the sensor spectral response is zero). The spectrum should also be zero over that range. Every amplitude below the straight part level is questionable, i.e., they could either be due to the real spectrum or the mirrored part of the negative spectrum. Observing the continuum can help the user figure out whether a part of the spectrum was “flipped” or not. A very rapid change in the continuum probably indicates that the spectrum was inverted at that point.

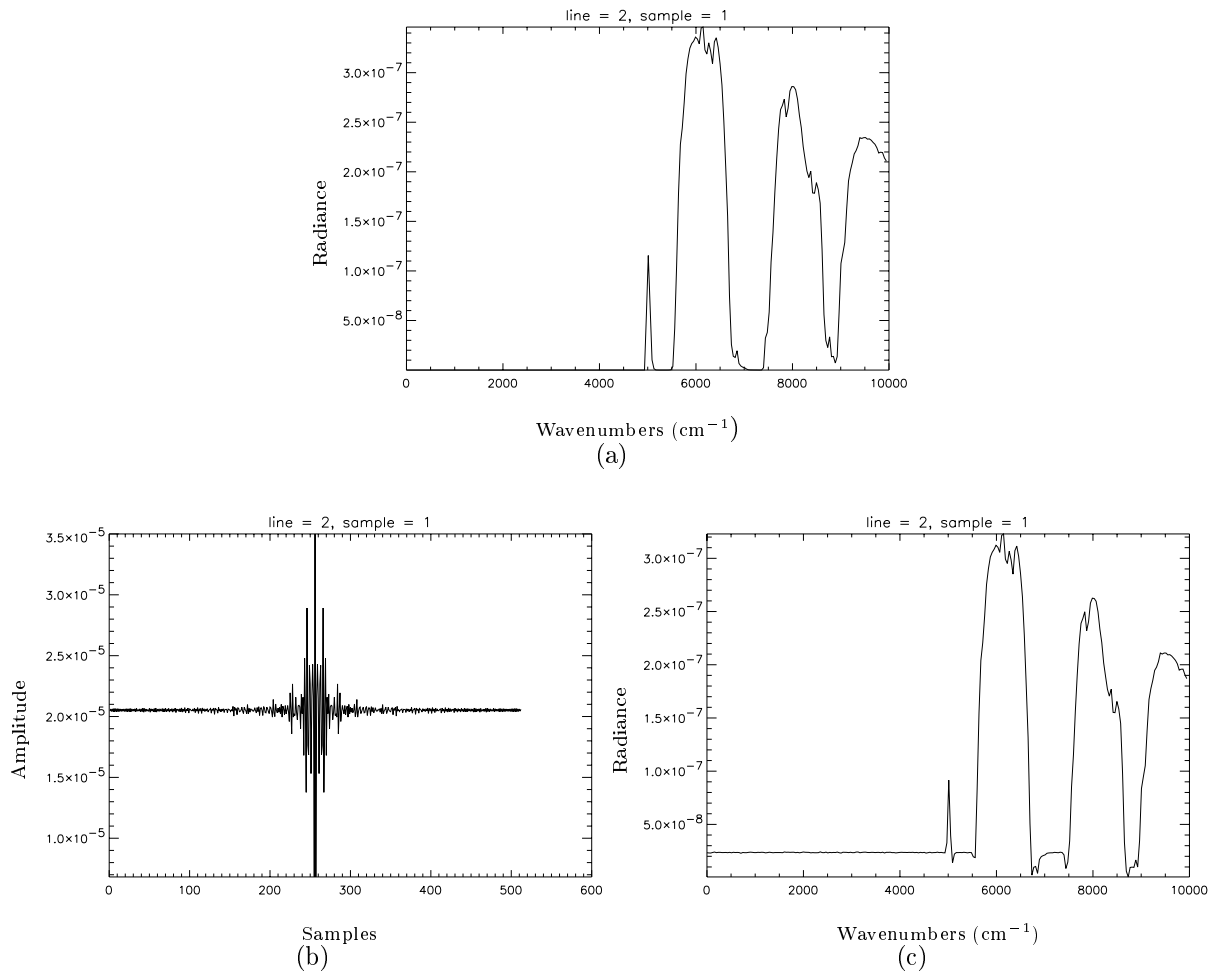


Figure 4.8: Image (a) is the spectrum seen by the interferometer and (b) is the corresponding interferogram. The ZPD intensity was limited to $3.5 \cdot 10^{-5}$ units. Without clipping, the ZPD value would have been about $4.1 \cdot 10^{-5}$. The interferogram was also quantized to 12 bits level. Image (c) shows the recovered spectrum.

The previous example showed what happens if only the center burst is affected by the dynamic range of the detector. Clipping examples with dynamic range limits of $1.0 \cdot 10^{-5}$ and $2.5 \cdot 10^{-5}$ are presented and show the outcome of clipping more than the center burst. No quantization was performed on these simulations. With a dynamic range of $1.0 \cdot 10^{-5}$, almost all of the interferogram information is lost and the recovered spectrum bears no resemblance to the real spectrum (Figure 4.9).

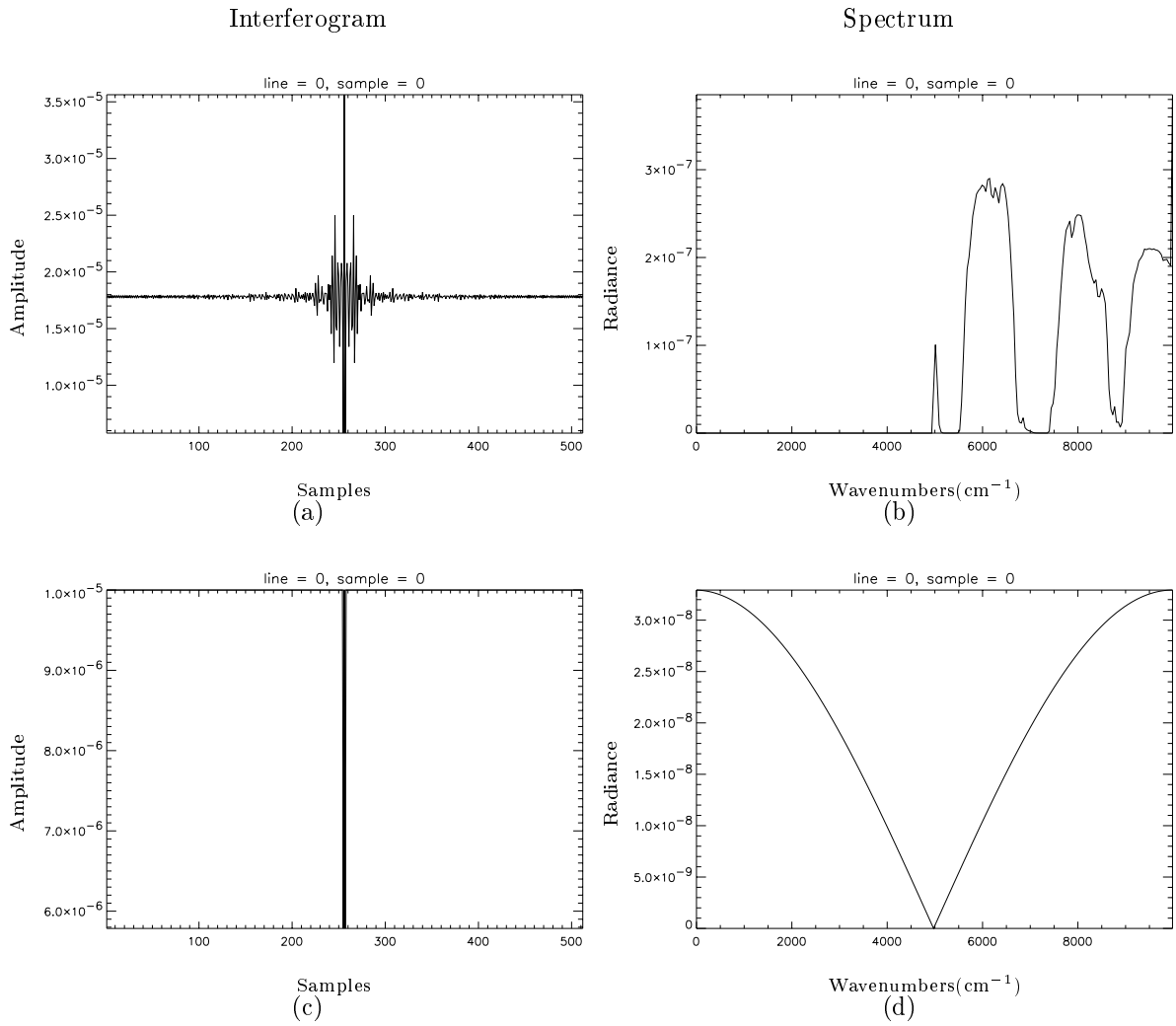


Figure 4.9:]

Dramatic clipping example for pixel [0,0], dynamic range of $1.0 \cdot 10^{-5}$: (a) ideal interferogram, (b) ideal spectrum, (c) clipped interferogram, (d) recovered signal

As pointed out in the Chapter 2, an ideal interferogram will be symmetrical about the ZPD position. If values on either side of the interferogram center are clipped, they will have the effect of modulating the spectrum with a sinusoidal function. A simulation with a dynamic range of $2.5 \cdot 10^{-5}$ was used to illustrate this effect. The spectra seen by pixel [0,0] and pixel [1,1] are very similar except that the latter is about 15% more intense. The clipping level was chosen such that only the center burst of pixel [0,0] is clipped. However, because the spectrum of pixel [1,1] is more intense,

the secondary lobes are clipped in that interferogram. The results of clipping and the recovered spectra are shown in Figure 4.10.

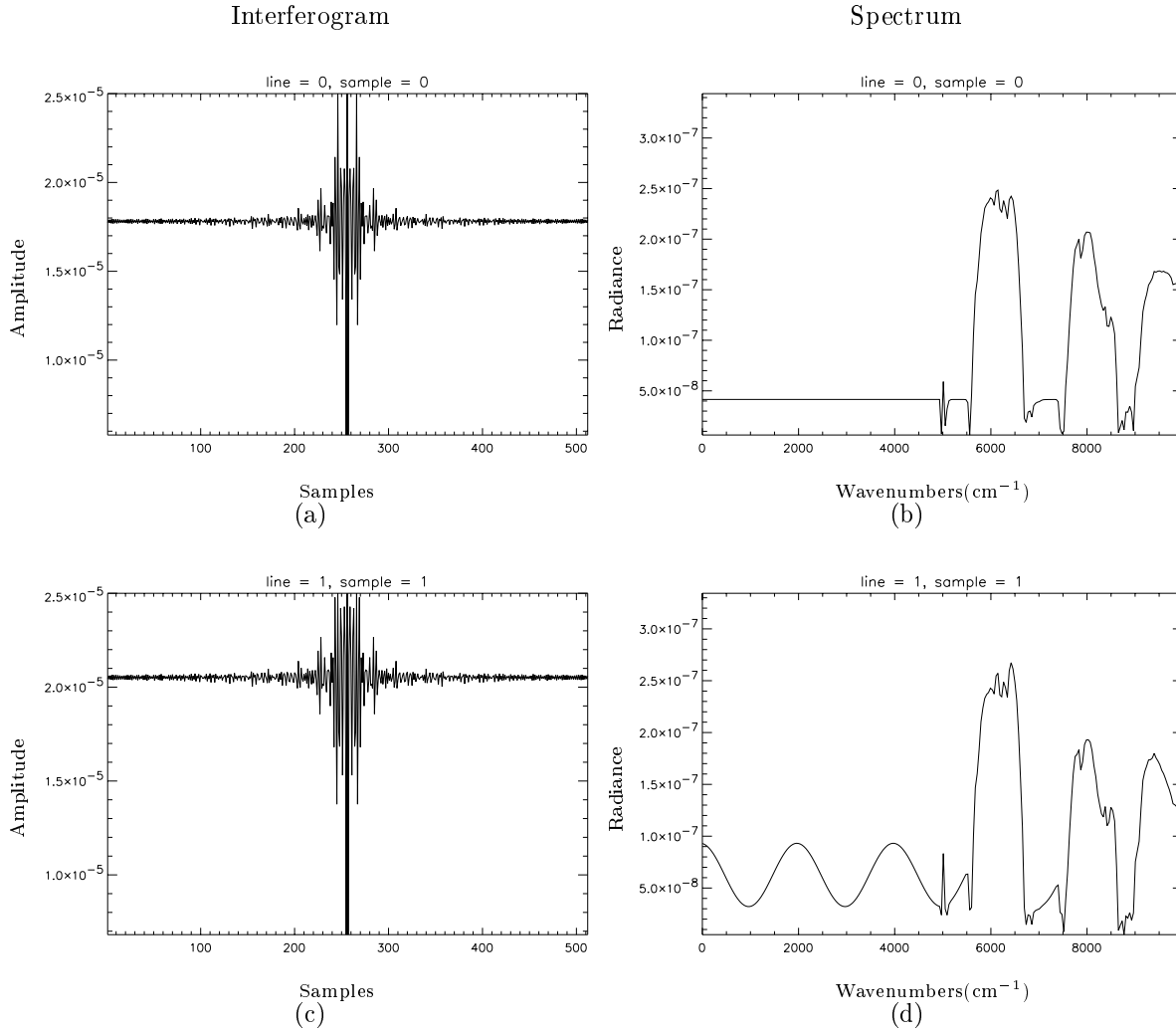


Figure 4.10: Example of side-lobe clipping, dynamic range of $2.5 \cdot 10^{-5}$: (a) center burst clipping only, (b) spectrum of (a), (c) center burst and side lobes clipping, (d) spectrum of (c)

As previously stated, the spectrum in (c) could be corrected by analyzing the DC part of the spectrum where the sensor spectral response is null. By analyzing the sinusoidal and DC parts of the spectrum in (d) over the 0-5000 cm⁻¹ range, the spectrum could also be corrected by tedious computation. The ideal spectrum for pixel [1,1] can be found in Figure 4.6 (c).

4.1.5 Off-Axis Effects

The tests of this Michelson design artifact were done by pointing a fixed sensor at a uniform target and comparing the on-axis and off-axis spectra. Without off-axis effects, the spectra should be identical. With the off-axis effects included, the off-axis spectrum is compressed by a factor of $\cos(\theta)$. Simulations for an 8x8 array a 9x9 array were performed. Both simulations were run with FPA sizes of 2.0 mm by 2.0 mm. The off-axis effect also depends on the focal length of the collimating lens, which was set to 15.0 mm. This combination was chosen because it produces relatively large off-axis effects. The expected results for off-axis spectral shifts are listed in Table 4.1. The simulation assumes that the FPA is centered: at pixel [4,4] for a 9x9 FPA and in the 8x8 array case, four pixels are equally distant from the center ([3,3], [3,4], [4,3], and [4,4] if the pixels are numbered from 0 to 7) (Figure 4.11).

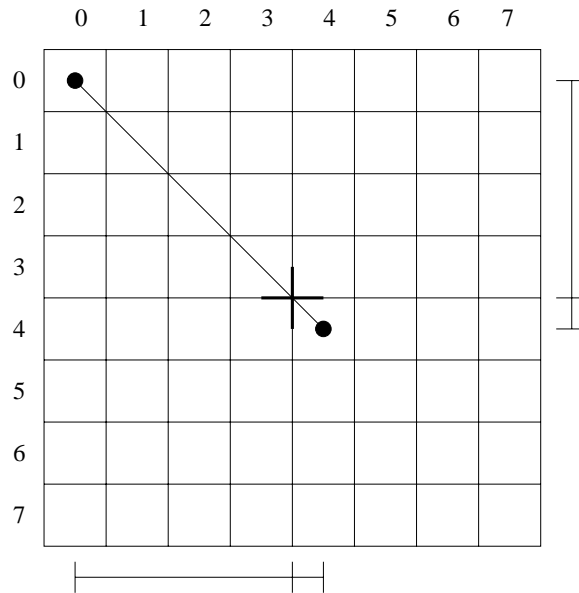


Figure 4.11: FPA arrangement for off-axis simulations

	8x8 FPA		9x9 FPA	
	pixel [0,0]	pixel [4,4]	pixel [0,0]	pixel [4,4]
X distance (mm)	0.875	0.125	0.8889	0
Y distance (mm)	0.875	0.125	0.8889	0
off-axis distance (mm)	1.237437	0.176777	1.257079	0
θ (degrees)	4.715982	0.675206	4.790493	0
Spectral shift	0.338551 %	0.006944 %	0.349327 %	0

Table 4.1: Prediction of off-axis spectral shift

Using spectral frequency shift of $\sigma' = \sigma \cos \theta$, it is possible to correct the off-axis spectral shift of calculated spectra. Figure 4.12 shows the results of off-axis spectral shift for an 8x8 FPA. The three curves are for pixel [0,0], pixel [4,4] with off-axis effects, and the results of a simulation without the off-axis effects included (ideal on-axis pixel). The spectral shift for pixel [0,0] is clearly noticeable. The shift of pixel [4,4] is much more subtle. The features used for comparison are indicated by arrows. Looking for the same features on the spectra and comparing the shifts to the predicted values produce the results found in Table 4.2. The resolution for this simulation was 2.6 cm^{-1} , which means that values reported for the graphical shift can happen only at integer multiples of this resolution. The difference between predicted and simulated values is due mostly to the sampled nature of the results. Finer resolution would be required to achieve better discrimination. The differences presented herein are all less than half of the resolution distance, as required. The difference between predicted and simulated values can be shown to be a function of the spectral frequency. For instance, the difference would be nearly zero at a frequency of 4591.6 cm^{-1} .

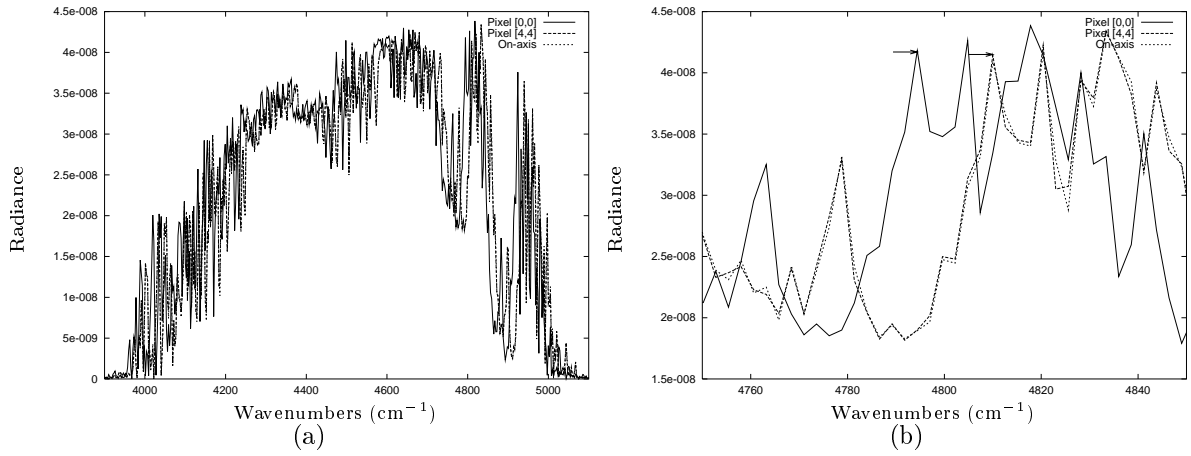


Figure 4.12: Example of off-axis effects on 8x8 FPA: (a) 3900 to 5100 cm^{-1} spectral range, (b) 4750 to 4850 cm^{-1} spectral range

	reference spectrum	pixel [0,0]	pixel [4,4]
Position of feature (cm^{-1})	4810.0	4794.4	4810.0
Graphical shift (cm^{-1})	—	15.6	0.0
Calculated shift (cm^{-1})	—	16.28	0.334
Difference (cm^{-1})	—	0.68	0.334

Table 4.2: Comparisons of spectral shifts for an 8x8 FPA

Figure 4.13 present similar results for the 9x9 array. Because pixel [4,4] is exactly on-axis in the simulation, its calculated spectrum is identical to the ideal spectrum. For this reason, no “on-axis” spectrum is found in this figure, instead, that of pixel [4,4] is used as the reference spectrum. The same conclusions as the 8x8 FPA case apply here.

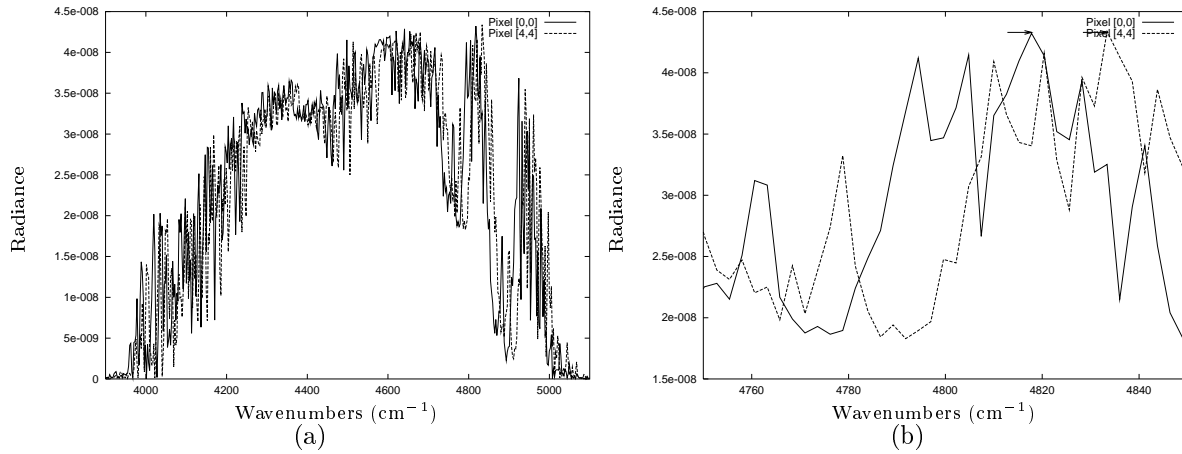


Figure 4.13: Example of off-axis effects on 9x9 FPA: (a) 3900 to 5100 cm⁻¹ spectral range, (b) 4750 to 4850 cm⁻¹ spectral range

	pixel [4,4]	pixel [0,0]
Position of feature (cm ⁻¹)	4833.4	4817.8
Graphical shift (cm ⁻¹)	—	15.6
Calculated shift (cm ⁻¹)	—	16.88
Difference (cm ⁻¹)	—	1.284

Table 4.3: Comparisons of spectral shifts for a 9x9 FPA

4.1.6 Spectral Response

The spectral response of the detector directly affects the spectrum. One could say that the spectrum observed by the detector is in effect the spectrum multiplied by the spectral response. Therefore, the recovered spectrum is an artifact of the spectral response.

To simulate the filter response of an IFTS, it was necessary to modify the mode of operation of the original DIRSIG spectral response function, which is applied to the output spectrum. The IFTS requires that the spectral response be applied to the input spectrum. In the default mode where no spectral response is specified, the response is unity over the spectral range and null outside the range. If specified, a spectral response must be of type INTEGRATED and must have the same resolution as the input spectrum, over the same range. Figure 4.14 shows the spectral response and the results of the simulation. The spectral response (a) has a Gaussian shape that is clearly visible in the output spectrum (b). The second spectrum in graph (b) is that of the input spectrum prior

to the application of the spectral response.

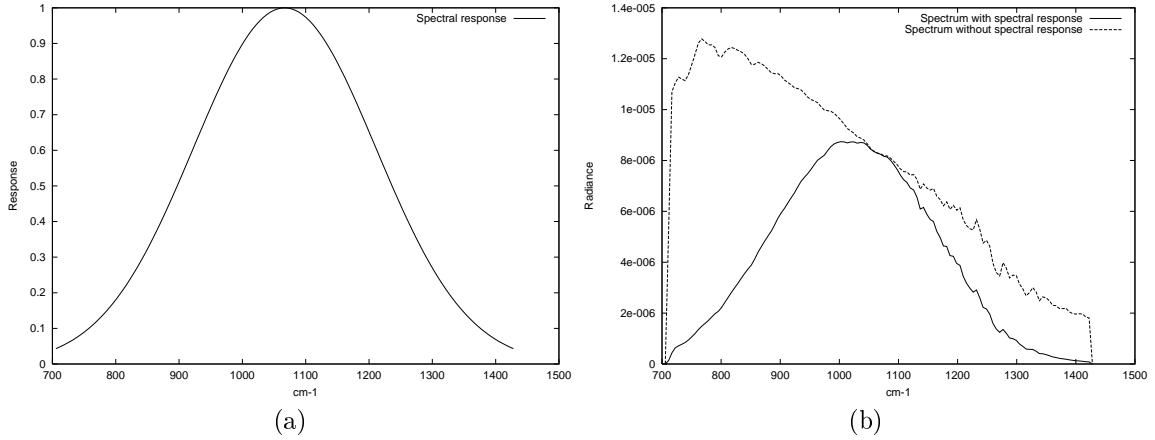


Figure 4.14: Example of spectral response simulation: (a) spectral response, (b) input and output spectra

4.1.7 Error in Optical Path Difference

The error in path difference in the Michelson interferometer design is due to the uncertainty in the mirror position during the scan. Slight variations in mirror speed and scan intervals translate into errors in the scan position. These errors result in noise in the recovered spectrum. At any given time, the entire image suffers from the same error in path difference. High spectral frequencies are more affected. Errors in the Sagnac interferometer are due to slight differences in detector width and location. In general, those are very small differences, and therefore translate to very little noise in the recovered spectrum. Because the FPA location is constant, the effect of errors in path difference for a Sagnac interferometer will differ for pixels in the across-track direction but will be the same for pixels in the along-track direction. For this simulation, both the Sagnac and Michelson platforms behave exactly the same, i.e., the effect in the across-track direction for Sagnac platforms will be identical. A simple fix for this limitation would require regenerating the OPD jitter vector after every scan of the pushbroom scanner, which is within the capability of the current code.

The error in OPD was simulated by adding a fraction of the delta sampling interval to the total sampling interval prior to OPD calculations. The size of the increment is decided by adding a random number from a Gaussian distribution with zero mean and a user-defined standard deviation specified as a fraction of the delta sampling interval. The random sequence is then lowpass filtered.

This smoothes out extreme OPD jitter variations that would not occur in real life, i.e., the smoothed value correlates with the previous value. Because the seed used in the random number generator is fixed, two simulations of OPD jitter will yield identical OPD error sequences.

Results of two simulations are presented, using standard deviations of $\frac{1}{30}$ and $\frac{1}{10}$, respectively. A third simulation with no error in path difference is used for reference. Figure 4.15 is an enlargement of the center portion of the interferogram. The values depart from the ideal interferogram as the standard deviation is increased. The variations occur at the same locations for both simulations because the pseudo random sequences were identical, an artifact of the hard-coded seed.

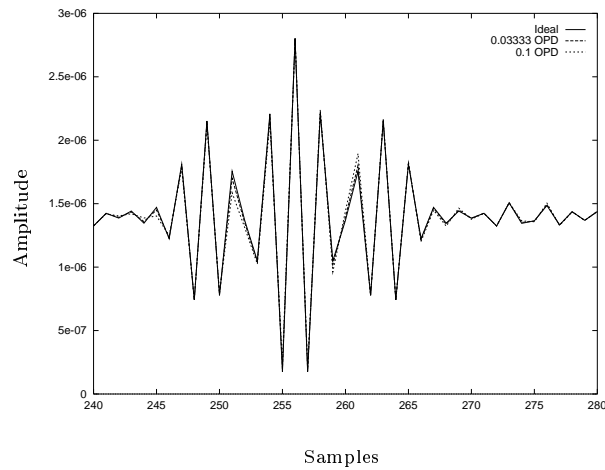


Figure 4.15: Interferogram center for 3 OPD jitter simulations

Figure 4.16 illustrates the fact that variations in the interferogram result in false frequencies being generated in the spectrum. Some false amplitudes are generated in the 0 to 3000 cm^{-1} range. In general, the shape of the spectrum is not corrupted to the point of being rendered useless.

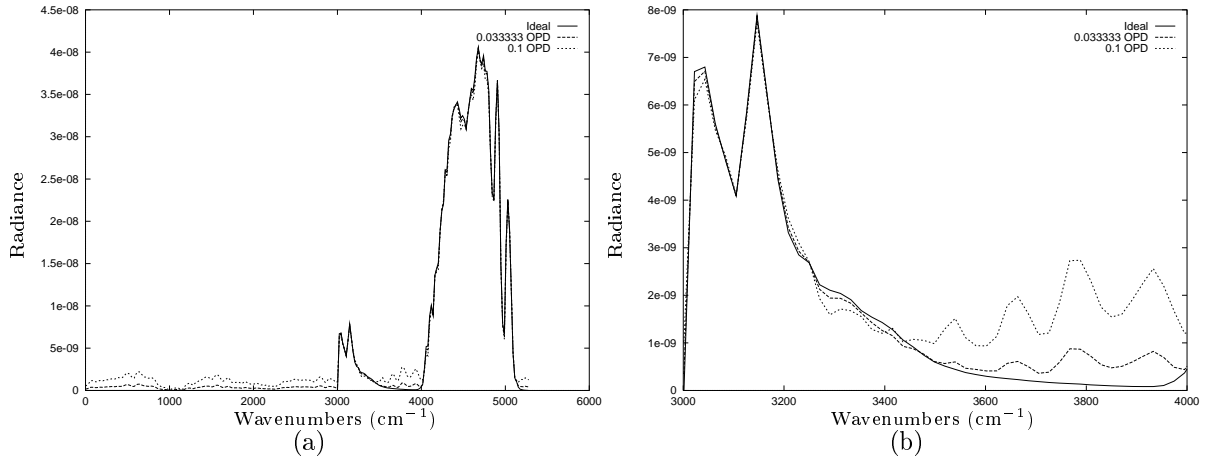


Figure 4.16: Examples of spectra with error in OPD: (a) full range, (b) magnified view for 3000 to 4000 cm⁻¹ range

4.1.8 Jitter Noise

Slight shifts in gaze location result in different spectra being detected by the sensor. Without spatial oversampling of the pixel, changes between material types show up as a discrete step in the interferogram, which leads to ringing in the recovered spectrum. With oversampling enabled, changes of material type are smoother, reducing the noise in the spectrum. Line-of-sight jitter was simulated for a Michelson sensor at an altitude of 4 km. The target was the center of quadrant II of scene 3, which is a pyramid of square objects made of different materials. The top square is 2 meters on a side. Below it are squares of 6, 12, and 20 meters on a side. The rest of the scene is not incorporated in this simulation. Random materials were assigned to the objects from 6 possible values, and the top two squares were assigned the same material. This reduces the scene to an equivalent scene containing three objects of 6, 12 and 20 meters on a side. To evaluate the jitter, the ground hit point of each of the 512 samples was plotted as determined from the flight profile and assuming a scene altitude of 0 meter. The results are in Figure 4.17 (a). The actual values recorded at simulation time are found in Figure 4.17 (b), along with an overlay of the borders of the 6 and 12 m objects. The differences in hit point can be attributed to the fact that the actual scene altitude is about 30 meters versus 0 meter. Also, note that the hit points of the simulation were recorded only when a different facet is hit. Therefore not all ground hit points are present in this graph.

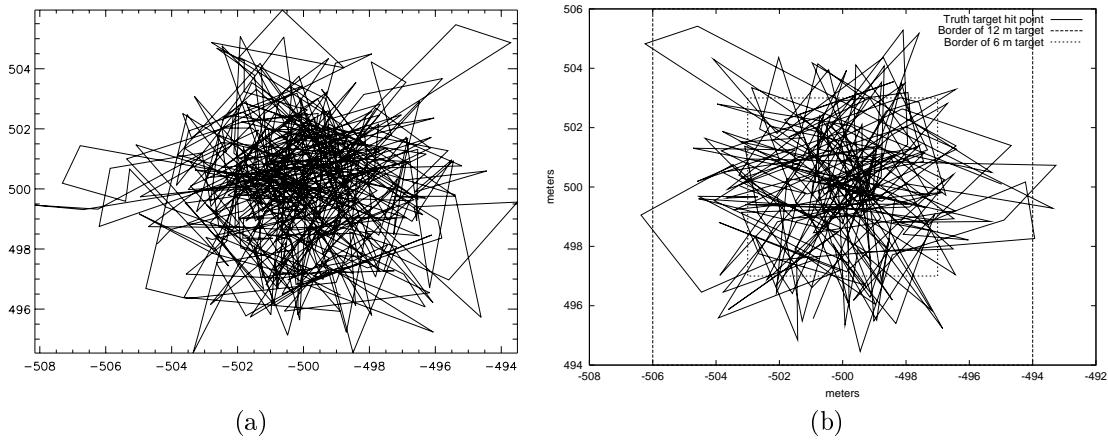


Figure 4.17: Scene hit point of jitter simulation: (a) predicted values, (b) actual values

Figure 4.18 shows the spectra of the target and background. Material 3 is the lowest curve, and represents the spectra for the 12-m object in Fig. 4.17 (b). The scene object for material 2 is the outermost object in Fig. 4.17 (b) and has a spectrum represented by the middle curve in Fig. 4.18. The small difference in the spectra is sufficient to generate a fair amount of noise in the recovered spectrum.

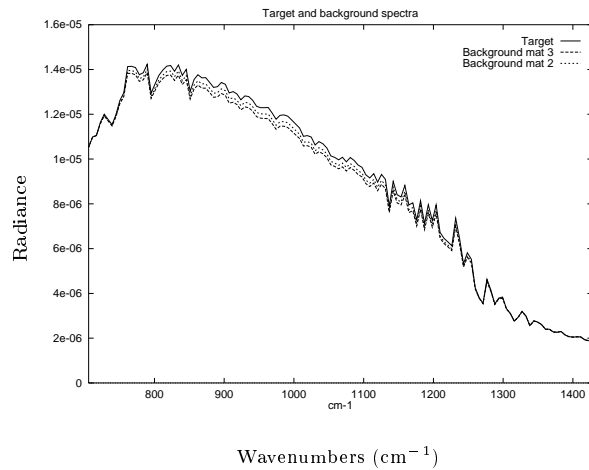


Figure 4.18: Target and background for the jitter scene

The effect of jitter on both the interferogram and the spectrum are shown in Figure 4.19. These results are compared to an ideal simulation where no jitter is present. When jitter causes the sensor

to drift to a different material, the spectrum and intensity detected at the sensor also vary. This produces the equivalent to noise in the interferogram, and results in a noisy spectrum. Had spatial oversampling been used instead of spatial delta sampling, the transitions of materials would be smoother and would result to less noise in the spectrum. Results of jitter used in conjunction with spatial oversampling are found in section 4.1.11.

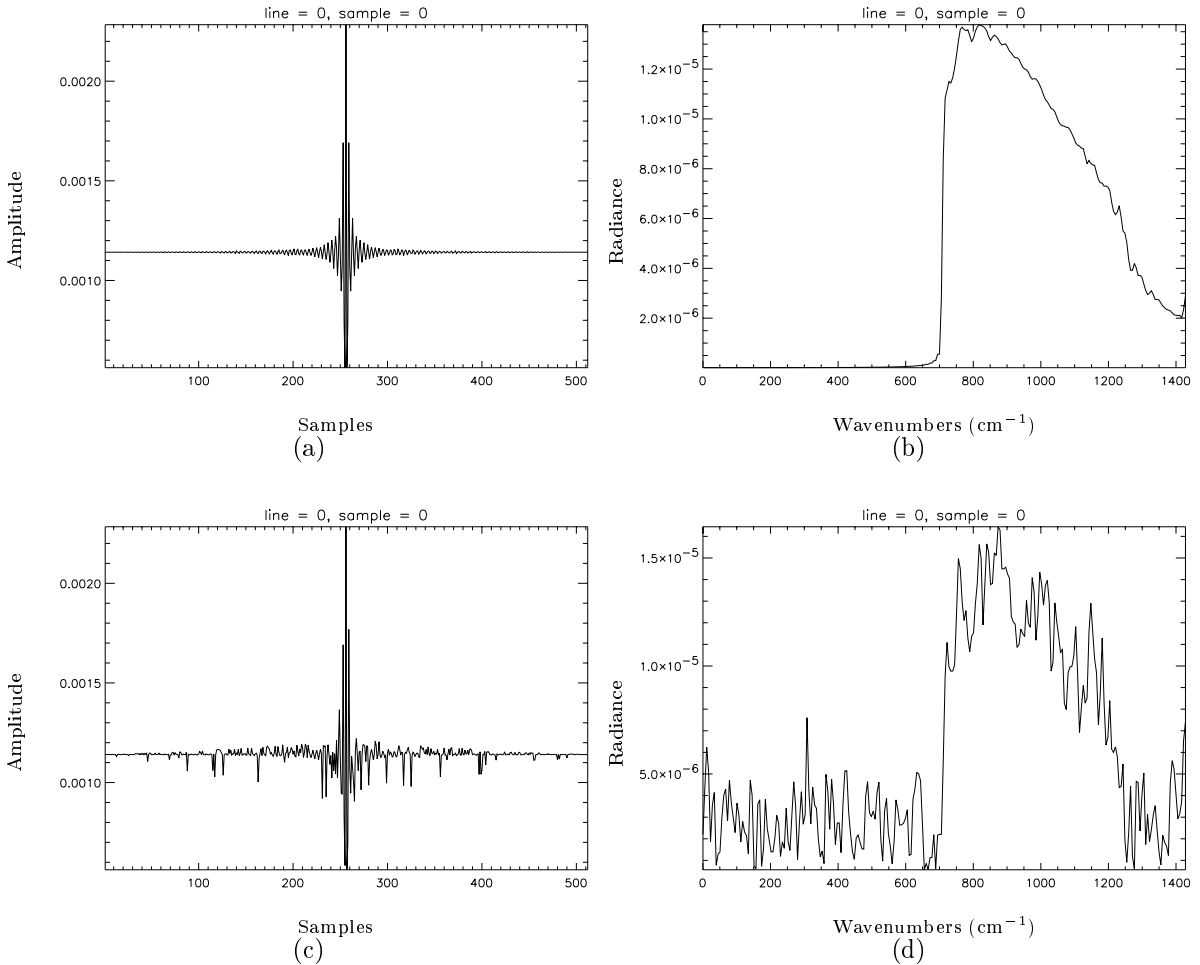


Figure 4.19: Effects of jitter on interferogram and spectrum: (a) ideal interferogram, (b) spectrum derived from (a), (c) interferogram with jitter errors, (d) spectrum derived from (c)

4.1.9 Detector

This section is subdivided into the effect of detector noise on the recovered spectrum and the effect of finite detector sampling distances.

Noise

Noise from a Gaussian distribution was added to the interferograms so that the corresponding spectra also contain noise. Gaussian noise added to the interferogram results in the real and imaginary part of the spectrum being also Gaussianly distributed (see section 2.8.10), as long as detector noise is the only artifact affecting the interferogram. To verify this claim, a histogram of the noise distribution was derived. The noise was calculated by subtracting the amplitude of the ideal spectra from the corresponding noisy data. This was done for both interferogram and spectrum. The results for two simulations are presented here. Figure 4.20 shows noise histograms for pixel [0,0] of a Michelson 8x8 IFTS. Graph (a) shows the interferogram, the spectrum noise distribution over the 0-10000 cm^{-1} range is in (b), and the range was cut from 5000 to 10000 cm^{-1} in (c). The standard deviation used for this simulation was $3.0 \cdot 10^{-8}$. From the interferogram noise distribution, we can see that all of the noise is comprised within 3 standard deviations of the mean. Because the magnitude of the Fourier transform of the interferogram is used to generate the spectrum, the noise distribution of the spectrum differs from a Gaussian distribution. In taking the magnitude, some spectral values that would otherwise have been negative become positive. This has the effect of shifting the mean of the noise distribution towards positive numbers, as shown in Fig. 4.20 (b). The bias of noise values from negative to positive values occurs near zero amplitude of the signal. This is especially true where the sensor spectral response is zero. For this reason, Fig. 4.20 (c) is the distribution of noise for the section of the spectrum where the spectral response is non zero. This has the effect of slightly shifting the peak of the distribution towards zero.

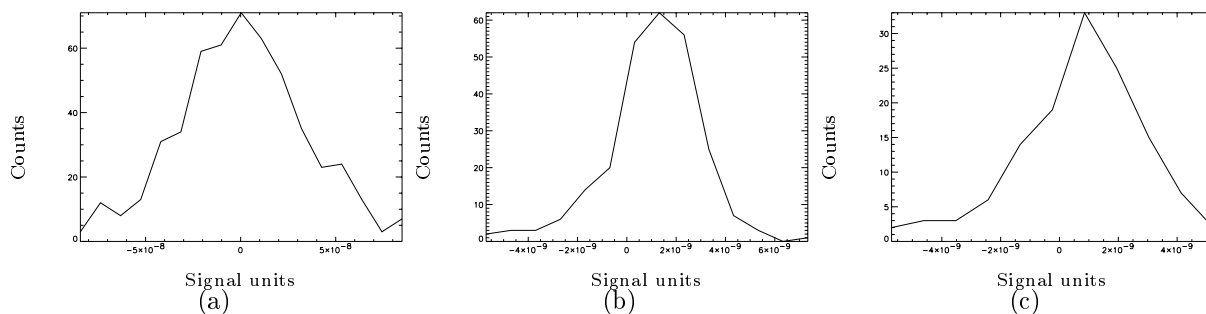


Figure 4.20: Noise distribution of detector noise for Michelson simulation: (a) interferogram, (b) spectrum for 0-10000 cm^{-1} range, (c) spectrum for 5000-10000 cm^{-1} range. The horizontal axis represents the deviation from the ideal value.

In a Michelson design, a single detector collects the entire interferogram. Detector noise will

therefore affect the entire interferogram equally, assuming no drift in the detector noise properties during the collection. For this project, a system that specifies global noise properties for the FPA was created. If it is desired to specify the properties of a single detector pixel, a value can be given that will override the global values. The file that contains the noise information is read at the time of sensor initialization. Note that if only a few pixels are specified, this process will execute rapidly. However, if the list of defective or different pixels is large, performances will suffer. Table 4.4 is an example of the content of the noise mean and standard deviation description file used for Michelson simulation.

	Row	Column	Mean	Standard deviation
Default	8	8	0.0	$3.0 \cdot 10^{-8}$
	2	2	0.0	0.0
	2	3	$1.0 \cdot 10^{-6}$	0.0
	2	4	$1.0 \cdot 10^{-8}$	$1.0 \cdot 10^{-8}$

Table 4.4: Noise mean and standard deviation

The first line is the default noise value for the entire FPA. Pixel [2,2] is noise free, pixel [2,3] has a $1.0 \cdot 10^{-6}$ bias added to its signals, and pixel [2,4] has a standard deviation and a mean of $1.0 \cdot 10^{-8}$. Note that the addition of a bias term to the interferogram has no effect on the spectrum since it only contributes a DC term, which is removed when the average value of the interferogram is subtracted prior to taking the FT. Figures 4.21 to 4.24 show results of noise simulations for pixels [2,2], [2,3], [2,4], and [2,5], in the order listed. The input spectrum for these pixels are identical. Pixel [2,2] shows an ideal interferogram and spectrum. Pixel [2,3] shows the same interferogram with a $1.0 \cdot 10^{-6}$ bias. The spectrum is identical to that of pixel [2,2]. Pixel [2,4] has a noisy spectrum, due to the noise in the interferogram. Once again, the bias in the interferogram is nullified by the average subtraction operation prior to the FT operation. Pixel [2,5] shows an even noisier spectrum with no bias on the interferogram.

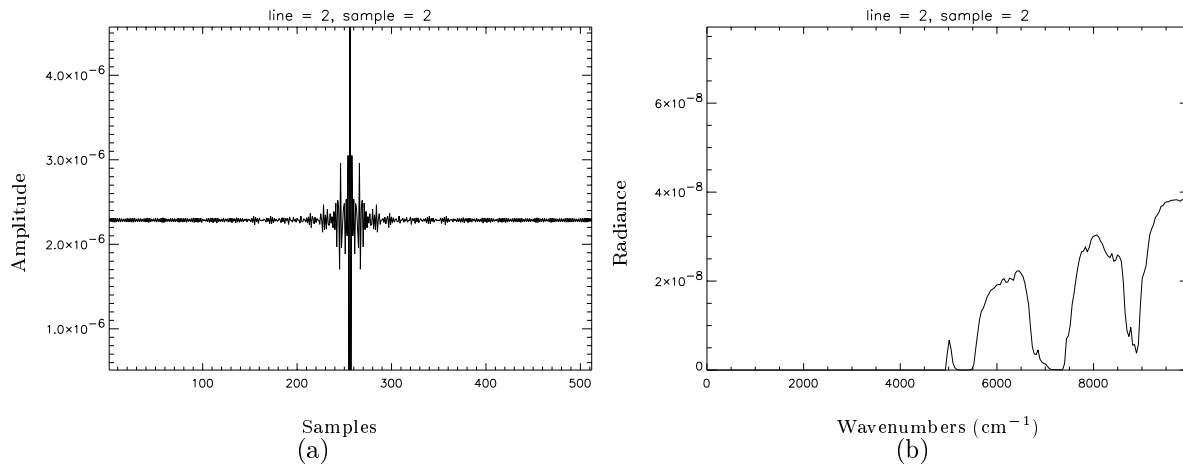


Figure 4.21: Noise free pixel [2,2] (mean = 0.0, std dev = 0.0): (a) interferogram, (b) spectrum

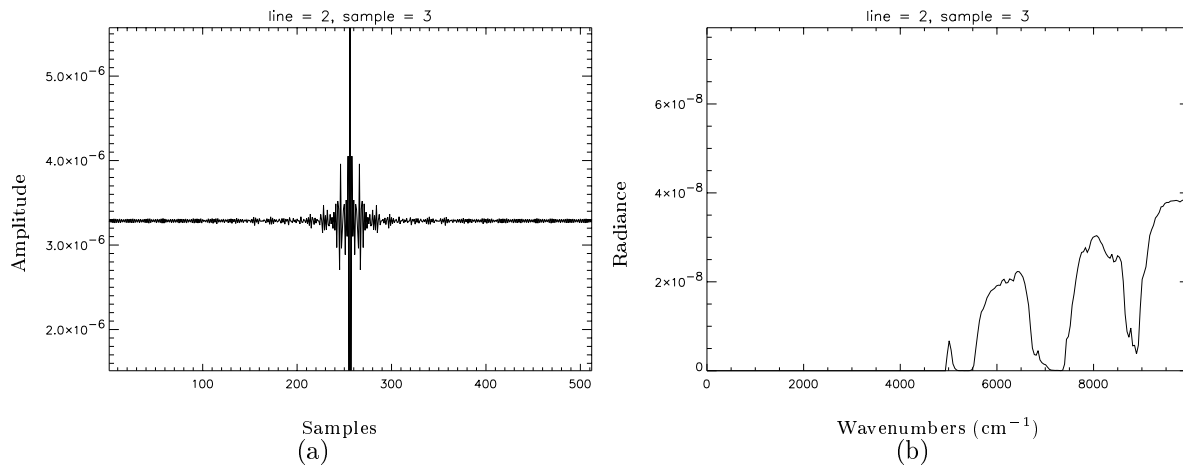


Figure 4.22: Bias shift for pixel [2,3] (mean = $1.0 \cdot 10^{-6}$, std dev = 0.0): (a) interferogram, (b) spectrum

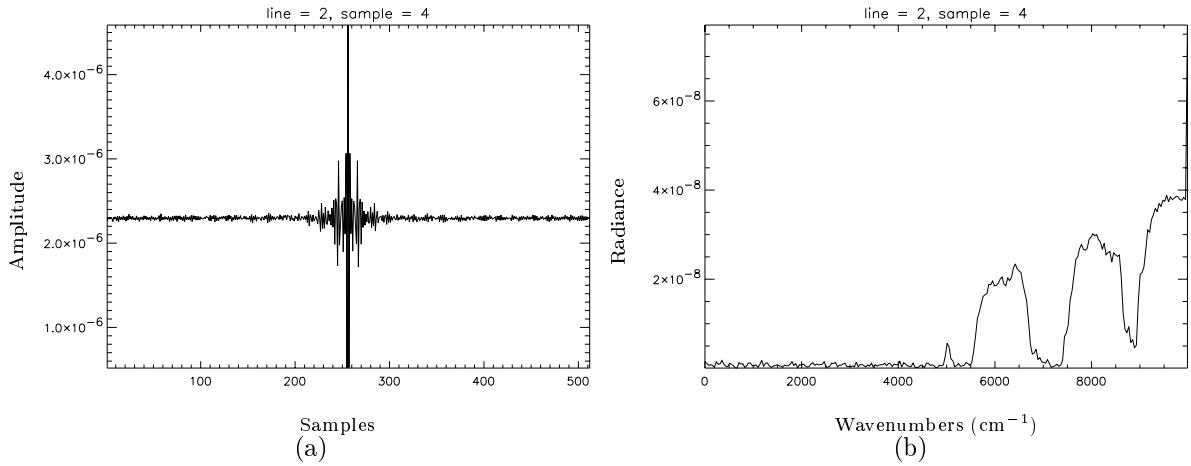


Figure 4.23: Bias and noise for pixel [2,4] (mean = $1.0 \cdot 10^{-8}$, std dev = $1.0 \cdot 10^{-8}$): (a) interferogram, (b) spectrum

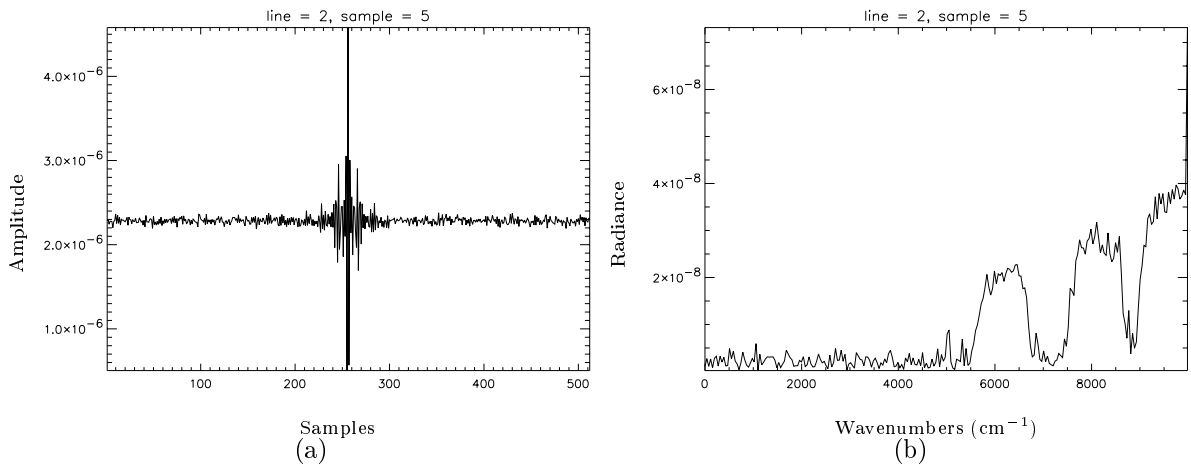


Figure 4.24: Noise for pixel [2,5] (mean = 0.0, std dev = $3.0 \cdot 10^{-8}$): (a) interferogram, (b) spectrum

A row of detectors collect the Sagnac interferogram. If the detectors have different noise properties, the interferogram will be corrupted. The noise distribution analysis performed for the Michelson design is repeated for the Sagnac in Figure 4.25. The standard deviation is $1.0 \cdot 10^{-8}$ for the noise distribution added to the interferogram. Fig. 4.25 (a) shows that all the noise is within 3 standard deviations of the mean of zero. Fig. 4.25 (b) shows the noise distribution for spectrum over the 0-10000 cm^{-1} range. Note that the mean is also shifted towards positive values for the same reasons as the Michelson. Reducing the range to allow only the non zero sensor spectral response improves the location of the mean, as shown in Fig. 4.25 (c).

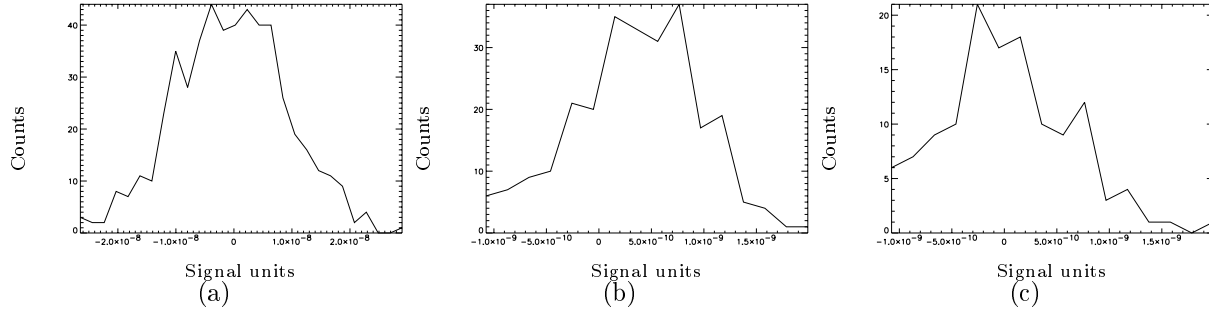


Figure 4.25: Noise distribution of detector noise for Sagnac simulation: (a) interferogram, (b) spectrum for 0-10000 cm^{-1} range, (c) spectrum for 5000-10000 cm^{-1} range. The horizontal axis represents the deviation from the ideal value.

Table 4.5 shows the contents of the detector noise specification file for the Sagnac noise simulation. The FPA is a 512x8 detector, and has a standard deviation of $1.0 \cdot 10^{-8}$ for the noise distribution. Pixels [64,2], [128,3], and [300,4] have values that differ from the rest of the FPA. Because the Sagnac is a pushbroom scanner, the noise of a single detector will affect interferograms of a given column at the same location for all collected lines of an image. Two interferograms and two spectra collected over column 2 are shown in Figure 4.26. The fact that there is more noise in line 1 than line 0 is reflected in the spectrum, where the amplitude variation of the noise is larger for line 1.

	Row	Column	Mean	Standard deviation
Default	512	8	0.0	$1.0 \cdot 10^{-8}$
	64	2	0.0	$1.0 \cdot 10^{-6}$
	128	3	$1.0 \cdot 10^{-6}$	0.0
	300	4	$1.0 \cdot 10^{-6}$	$1.0 \cdot 10^{-6}$

Table 4.5: Detector noise description for a Sagnac interferometer

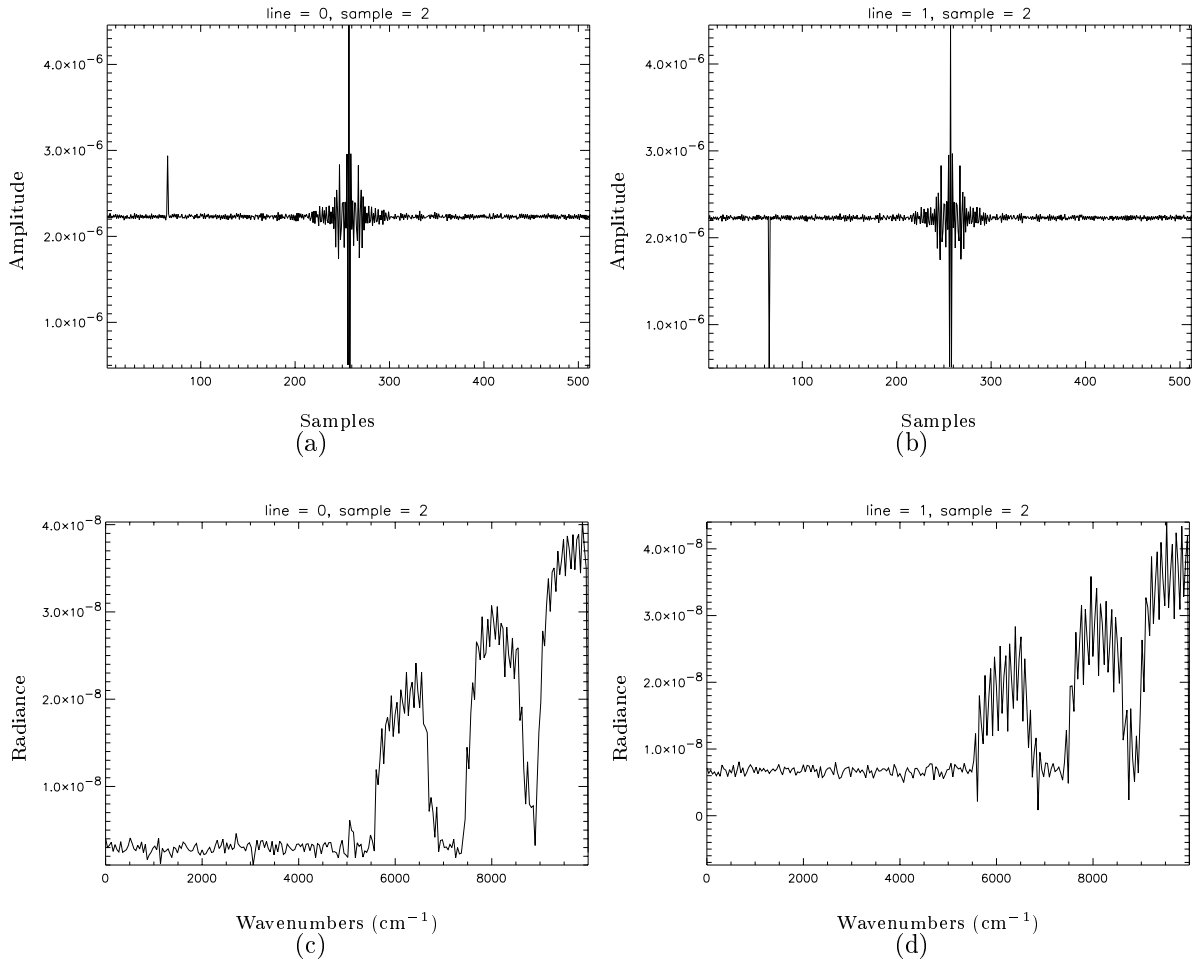


Figure 4.26: Example of noisy Sagnac data with pixel 64 of column 2 being defective: (a) line 0 interferogram, (b) line 1 interferogram, (c) spectrum of (a), (d) spectrum of (b).

If the defective pixel is close or far from to the ZPD location, the spectrum will be modulated with a low-frequency or high-frequency sinusoidal signal, respectively. The amplitude of the sinusoidal signal depends on the distance of the defective signal from its expected value, as confirmed by Figure 4.27. Note that this quantity of noise likely does not occur in real sensors. However, a dead pixel could be crudely simulated by assigning it a negative mean. If one had access to the interferogram data, this pixel could be manually corrected by assigning it a value close to its expected value. If a two-sided interferogram is used, the mirrored value could be used to substitute for the defective pixel.

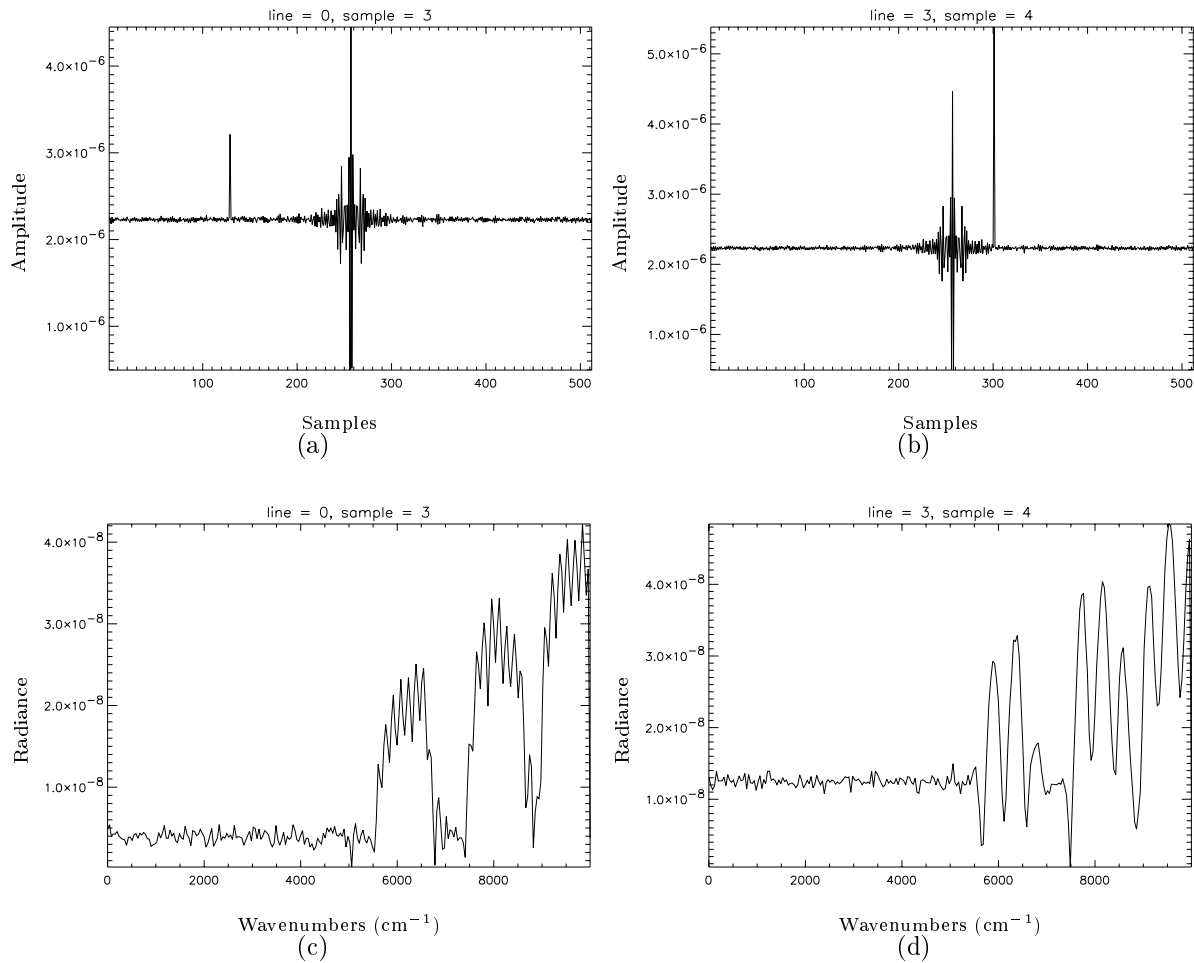


Figure 4.27: Example of noisy Sagnac with defective pixels in column 3, pixel 128, and column 4, pixel 300: (a) column 3 interferogram, (b) column 4 interferogram, (c) spectrum of (a), (d) spectrum of (b)

Detector Sampling

Up to this point, all interferograms were collected using ideal delta sampling. This assumes an infinitesimally large detector (Sagnac) or a step-and-scan mirror approach (Michelson). In real life, detectors have a finite surface area and scanning mirrors travel at a constant speed. Two approaches to this problem were evaluated. The first stems from Fourier transform analysis. While scanning, the mirror covers a finite range of OPD values. This range can be expressed as the width of a RECT function. Since the range depends on the scanning rate v (cm/sec) and the integration time Δt

(sec), the sampling function is:

$$\text{RECT}\left(\frac{x}{2\Delta tv}\right) \quad (4.2)$$

with x in cm. The FT of this RECT is:

$$\text{SINC}(2v\sigma\Delta t) \quad (4.3)$$

with σ the spectral frequency in cm^{-1} . The SINC describes how a given frequency will be modulated in the recovered spectrum. For instance, given $\Delta t = 0.004$ sec and $v = 0.00626$ cm/sec, the maximum frequency that can be detected without aliasing is 9984 cm^{-1} . The modulation factor at that frequency is $\text{SINC}(0.5)$ or 0.637 . As stated in section 2.8.10, high frequencies are affected more than low frequencies. This result also indicates that the effect of finite detector sampling can be removed from the spectrum simply by multiplying the spectrum by the inverse of the SINC. This works as long as aliasing does not affect the spectrum, which complicates things a little more.

The second approach to simulating the finite sampling distance is to use ideal sampling at a finer scale and to average a number of these samples. For instance, if one decides to sample at intervals of one-third the required size for ideal sampling, three samples would be averaged together. Figure 4.28 is a graphical illustration of this process. If the previous example is repeated with this approach and 3x oversampling, the results are very similar. From the data above, the OPD change is $2v\Delta t = 5.008 \cdot 10^{-5}$. The important part of the interferogram in this case is $\cos(2\pi\sigma(OPD)) = 0.5, 1, \text{ and } 0.5$ for the first, second, and third samples respectively. The average is $2/3$, which is a reasonable approximation to the result of the first approach (0.637). Oversampling by a factor of seven yields a modulation factor of 0.642 for the maximum frequency. With this method, more oversampling yields better approximations at the cost of increased computation. A general equation to calculate the modulation factor of the spectrum as a function of the spectral frequency when oversampling is used is:

$$\sum_{n=-\frac{N}{2}}^{\frac{N}{2}} \frac{\cos(2\pi\sigma \frac{\delta}{2N}(2n+1))}{N} \quad (4.4)$$

where N is the oversampling factor and δ is the OPD interval, defined as $2v\Delta t$ for a Michelson and $\ell\Delta x/f$ for a Sagnac.

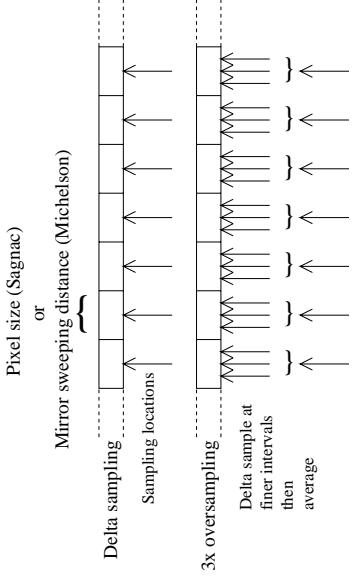


Figure 4.28: Graphical description of interferogram oversampling

The first approach has the advantage of being very fast. All that is required is to multiply the spectrum by the modulating SINC function. This can be done either to the input or output spectrum. Notwithstanding the increased computation, the second approach was used to simulate this artifact because the SINC technique does not account for possible error in path difference. Although this has not been tested, I believe that the error in path difference combined with the finite sampling distance affect the spectrum differently than simply modulating by the SINC function to obtain the results of the OPD error simulation. If the processing burden of the second approach is too great, it would be easy to revert to the first approach.

Simulations of finite sampling distances were done for 3x and 7x oversampling and are compared to the ideal case. Figure 4.29 (a) shows an enlargement of the three overlapping interferograms. The interferogram with the maximum variation is the reference. At this scale, it is harder to distinguish between the results of 3x and 7x oversampling. The corresponding spectra are presented in (b). It is clear that high frequencies are more affected than lower frequencies. Table 4.6 shows that the modulation is equivalent to the predicted results.

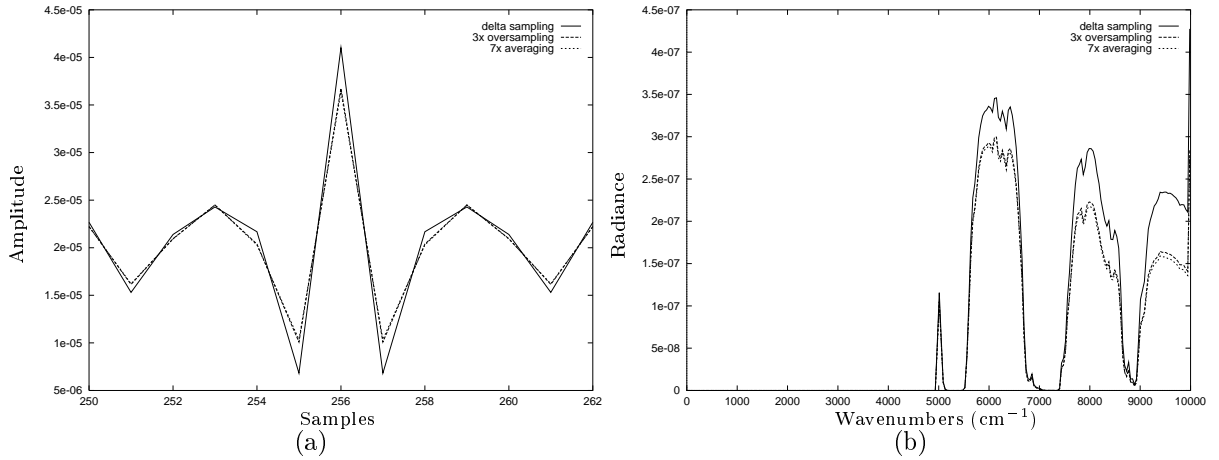


Figure 4.29: Results of ideal, 3x and 7x oversampling for finite sampling distance simulations: (a) central section of the interferogram, (b) resulting spectra

Oversampling	Frequency (cm ⁻¹)	Result	Ratio (result/ideal)	Predicted ratio
Ideal (delta)	9984.0	$4.27531 \cdot 10^{-7}$	—	—
3x	9984.0	$2.85021 \cdot 10^{-7}$	0.667	2/3
7x	9984.0	$2.74472 \cdot 10^{-7}$	0.642	0.642

Table 4.6: Spectra modulation factor for 3 simulations of finite sampling distance effects

FPA Pixel Sensitivity Variations

In a Michelson IFTS design, the gain and bias of the sensor has no effect on the shape of the spectrum. Because a single detector detects the entire interferogram, the bias adds a constant amplitude, which is removed when the interferogram is averaged prior to the FT. If the bias is constant throughout the collection and if no saturation occurs at the detector, the bias has no effect on the spectrum of a Michelson type IFTS. If the same conditions apply for the gain, the effect will be only a scaling of the interferogram and spectrum. Because no distortions are introduced in the spectrum for this design, no examples are shown.

Variations in sensitivity affect the Sagnac interferometer differently. A “hot” or “cold” pixel in the FPA introduces noise in the recovered spectrum, much like differences in noise characteristics presented in section 4.1.9. As in the noise case, a defective pixel close to the center burst results in a spectrum modulated by a low-frequency sinusoidal signal. If the defective signal is far from the center burst, the spectrum will be modulated by a high-frequency signal. In this simulation,

the gain and bias values found in Table 4.7 were used. Note that only pixel [300,4] is biased. The default gain is 1.0 and the bias is 0. The resulting interferograms are shown in Figure 4.30.

	Row	Column	Gain	Bias
Default	512	8	1.0	0.0
	64	2	1.5	0.0
	128	3	0.5	0.0
	300	4	1.0	$1.0 \cdot 10^{-6}$

Table 4.7: Contents of a gain and bias description file

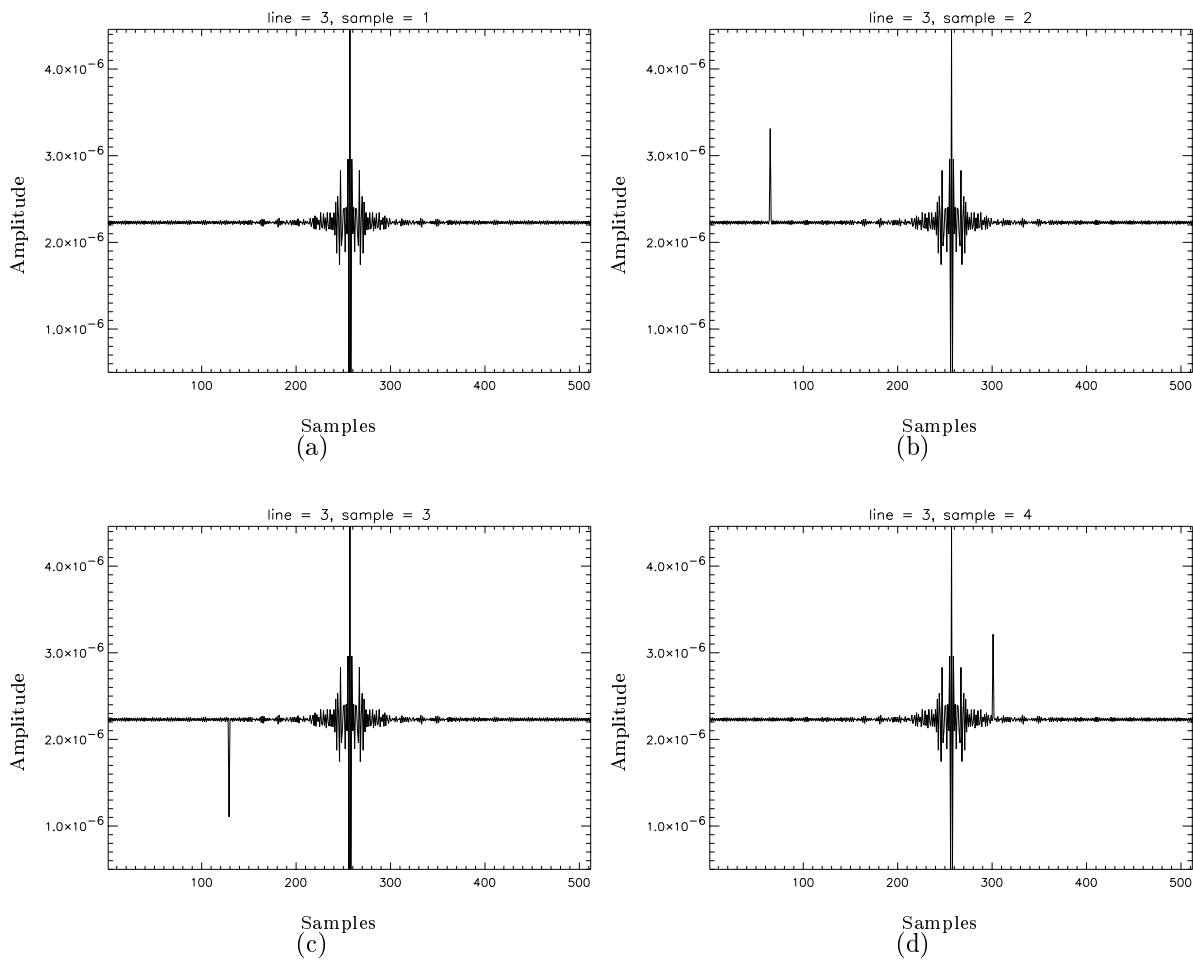


Figure 4.30: Examples of “hot” and “cold” pixels on Sagnac interferograms: (a) ideal interferogram (gain = 1.0, bias = 0.0), (b) pixel 64 with gain of 1.5, (c) pixel 128 with gain of 0.5, (d) pixel 300 with bias of $1.0 \cdot 10^{-6}$

The effect of a single pixel with a different sensitivity is explained by linear system theory. The

detected interferogram may be expressed as the ideal interferogram with an Dirac delta function that has been translated. The ideal interferogram yields a real-valued spectrum, and the shifted delta to a complex-valued sinusoidal function. The magnitude of the FT yields a constant for the complex-valued sinusoid wherever the spectrum is zero, and a cosine function where the spectrum has non-zero values. The specific FT algorithm being used in this project scales the results of the FT by $\frac{2}{N}$, where N is the number of sample points in the interferogram. In Figure 4.30 (b) the added peak has a height of about $1.1 \cdot 10^{-6}$ units. When scaled by $\frac{2}{512}$, this becomes $4.3 \cdot 10^{-9}$ units. This is the same result that can be observed for the constant level in Figure 4.31 (b). The other figures also obey this effect. In (c), the value of the Dirac delta function is subtracted instead of added. This has no effect on the location of the constant value part of the spectrum due to the magnitude operator. The value occurs at the same levels as in (b). In (d), the bias of $1.0 \cdot 10^{-6}$ translates to a constant level of $3.9 \cdot 10^{-9}$.

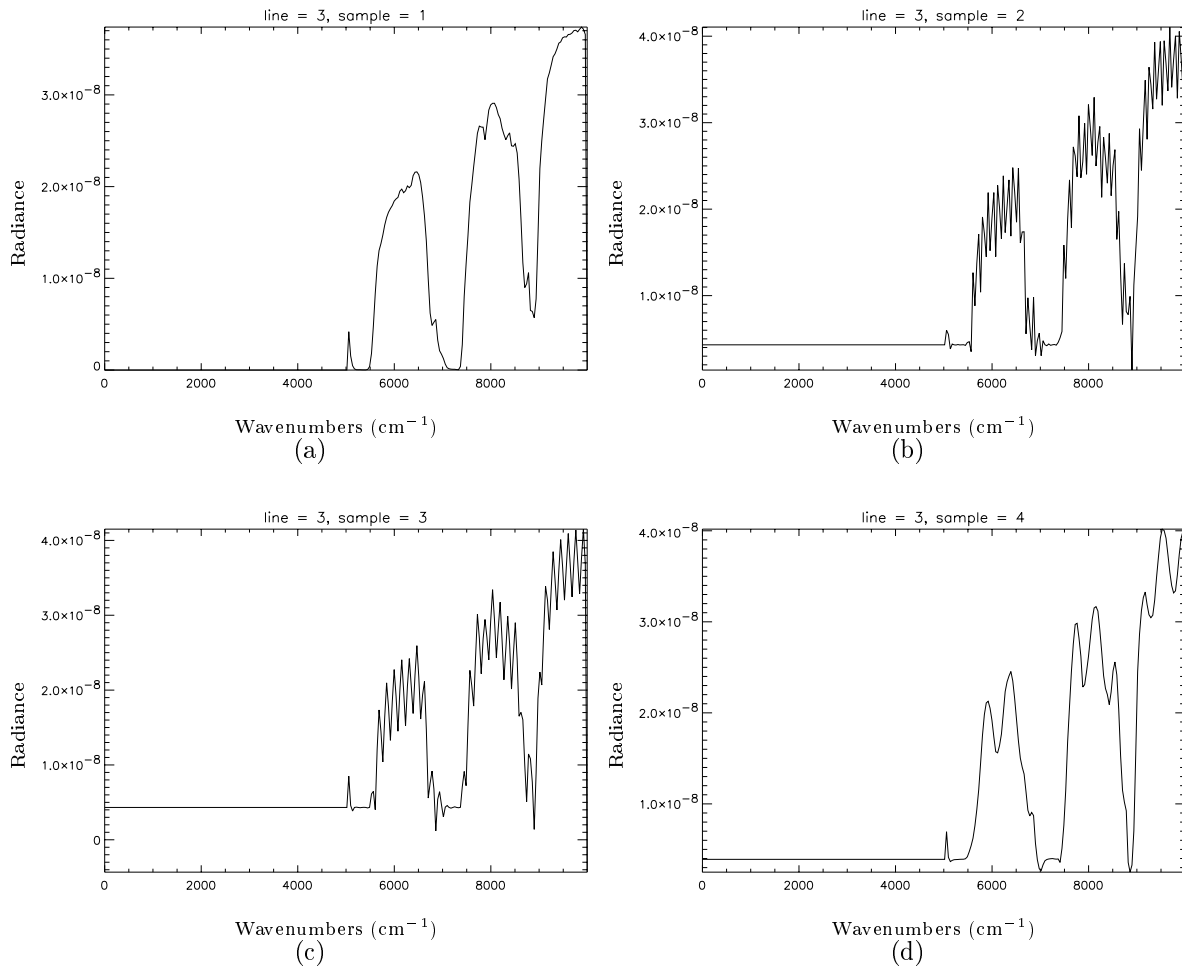


Figure 4.31: Spectra calculated from interferograms of Figure 4.30

4.1.10 Beamsplitter

As indicated in section 2.8.7, this artifact was not simulated as part of this research. The effects of the reflection/transmission (RT) product of a beamsplitter may be incorporated as part of the spectral response of the signal for Michelson IFTS. For the Sagnac IFTS, the results derived in Appendix A may be used to simulate this effect.

4.1.11 Spatial oversampling (subpixel sampling)

Computer simulations are the programmer’s representation of reality. Sometimes, the results are better than reality because naturally occurring artifacts are not specifically simulated. Examples are signals without detector noise, or ideal rather than realistic sampling of interferograms over a finite mirror-scan distance. However, there are also cases where it is not possible to simulate continuous events. The ideal sampling of a spatial pixel is an example. Whenever the jitter in pointing accuracy of the sensor is enabled or when changes in view angles cause the sensor to view different regions of a scene, ideal sampling produces worse results than expected because the FT operation is very sensitive to sudden amplitude variations. A continuous interferogram creates less noise than a sudden variation, which will generate ringing in the spectrum. One way to minimize sudden amplitude variations in the interferogram is to oversample the detector pixels. The transitions that occur when a pixel shifts between materials will be smoother. With this in mind, sampling was enabled at the subpixel level for the simulation of IFTS. This is the first time that a DIRSIG simulation includes subpixel sampling. The OVERSAMPLE keyword was added in the BAND section of the configuration file. The default value selects ideal sampling. A value of 3 means that each pixel in the FPA is divided into a 3-by-3 array of subpixels. The radiance collected by each subpixel is summed and scaled to produce the pixel’s detected radiance. With the OVERSAMPLE option, DIRSIG may now generate mixed spectra.

Since this new feature was implemented specially for the IFTS project, it is necessary to validate the results. To ensure that the subpixels are sampled at expected locations, a few simulations of an 8x8 image were run for different amounts of oversampling. This was performed for a spatially and spectrally uniform scene. The target hit points were recorded and compared to expected values. Figure 4.32 is a plot of the target hit points for three oversampling cases. Symbol “□” represents the target hit points for ideal sampling. Symbols “+” and “◇” indicate cases where the oversampling parameter is set to 2 and 3, respectively. The coordinate units are in meters. The target hit point for the sensor was set at [500, -498] for a sensor flying directly overhead. For this simulation, the projection of the pixel on the ground is 5 meters in size, as shown in the figure. The target hit points for each sub-sampled pixel indeed match the expected values. Because the scene contains a single target, the spectra collected by ideal sampling and subpixel sampling are identical. This indicates that subpixel sampling does not introduce additional artifacts in the simulation.

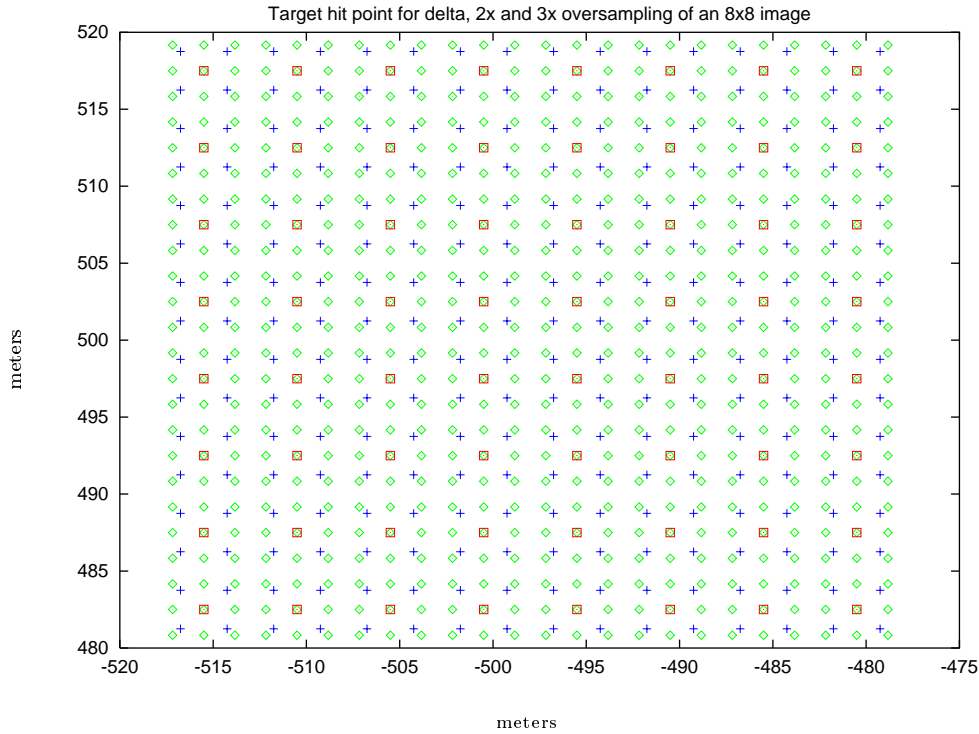


Figure 4.32: Target hit points for delta sampling, 2x and 3x oversampling for an 8x8 image

Subpixel sampling significantly increases the computation time of a simulation. Significant improvements in the simulation are required to justify this expense. Two cases where the results show marked improvements with the use of subpixel sampling over ideal sampling are presented in the next section.

Effect of pointing accuracy and subpixel sampling

This repeats the simulation of section 4.1.8. The ground instantaneous field of view of a detector pixel was set to 5 meters, which is slightly smaller than the target (6 meters). With oversampling enabled, the transitions from object to object spread over many interferogram samples. This contributes to reduced noise in the recovered spectrum. A comparison of the interferograms for the pointing jitter simulation with and without oversampling are found in Figure 4.33. Notice how the interferogram has a more consistent shape when oversampling is enabled. For this simulation, a subpixel sampling frequency of 9x was selected, which produces a 9x9 array of subpixels.

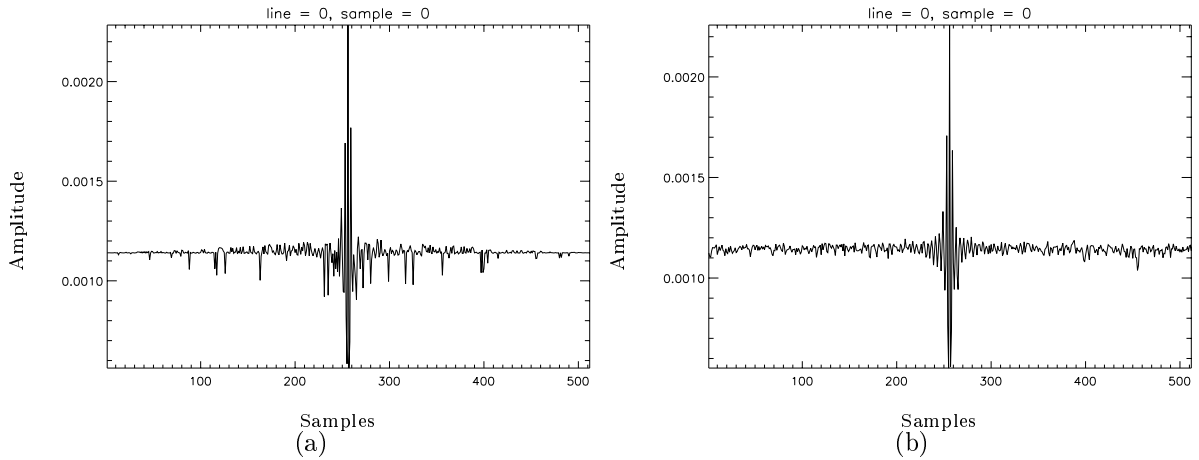


Figure 4.33: Comparison of delta and subpixel sampling cases on pointing accuracy simulation — interferogram: (a) with delta sampling, (b) with 9x subpixel sampling

The effect of oversampling is also apparent in the recovered spectra shown in Figure 4.34. The ideal spectrum is overlaid in this graph.

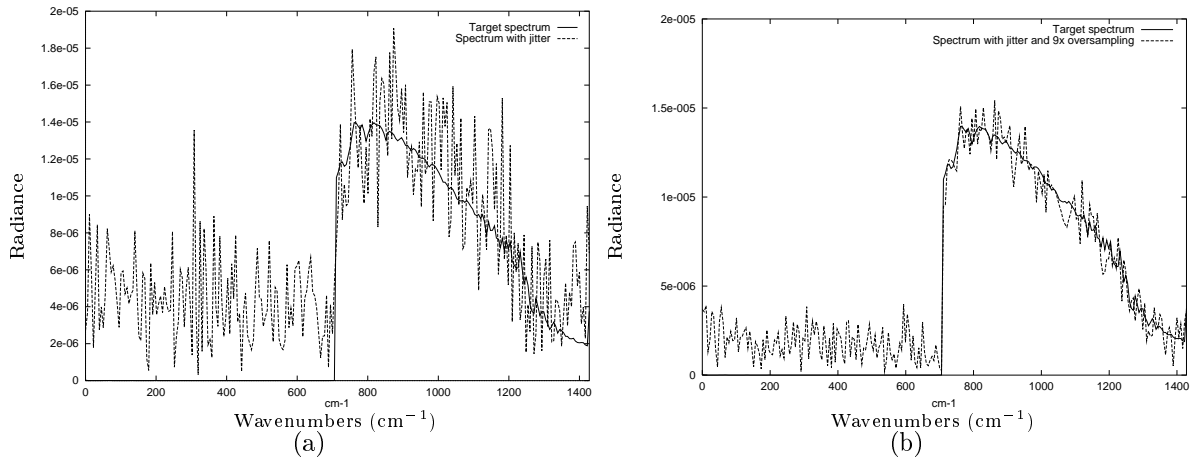


Figure 4.34: Comparison of ideal and subpixel sampling cases on pointing accuracy simulation — spectrum: (a) with delta sampling, (b) with 9x subpixel sampling

Effect of view angle and subpixel sampling

This simulation repeats some of the simulations of section 4.1.3. Figure 4.35 shows the interferograms and Figure 4.36 shows the respective spectra. It is possible to see that the best results are obtained when subpixel sampling is used in conjunction with interpolation in view angles and apodization as shown in Fig. 4.36 (f). That is because both the subpixel sampling and the view-angle

interpolation filter out the discrete effects of the simulation. The results can be interpreted as continuous rather than discrete, and may resemble real-world results more closely than the simulation with 512 view angles and ideal sampling.

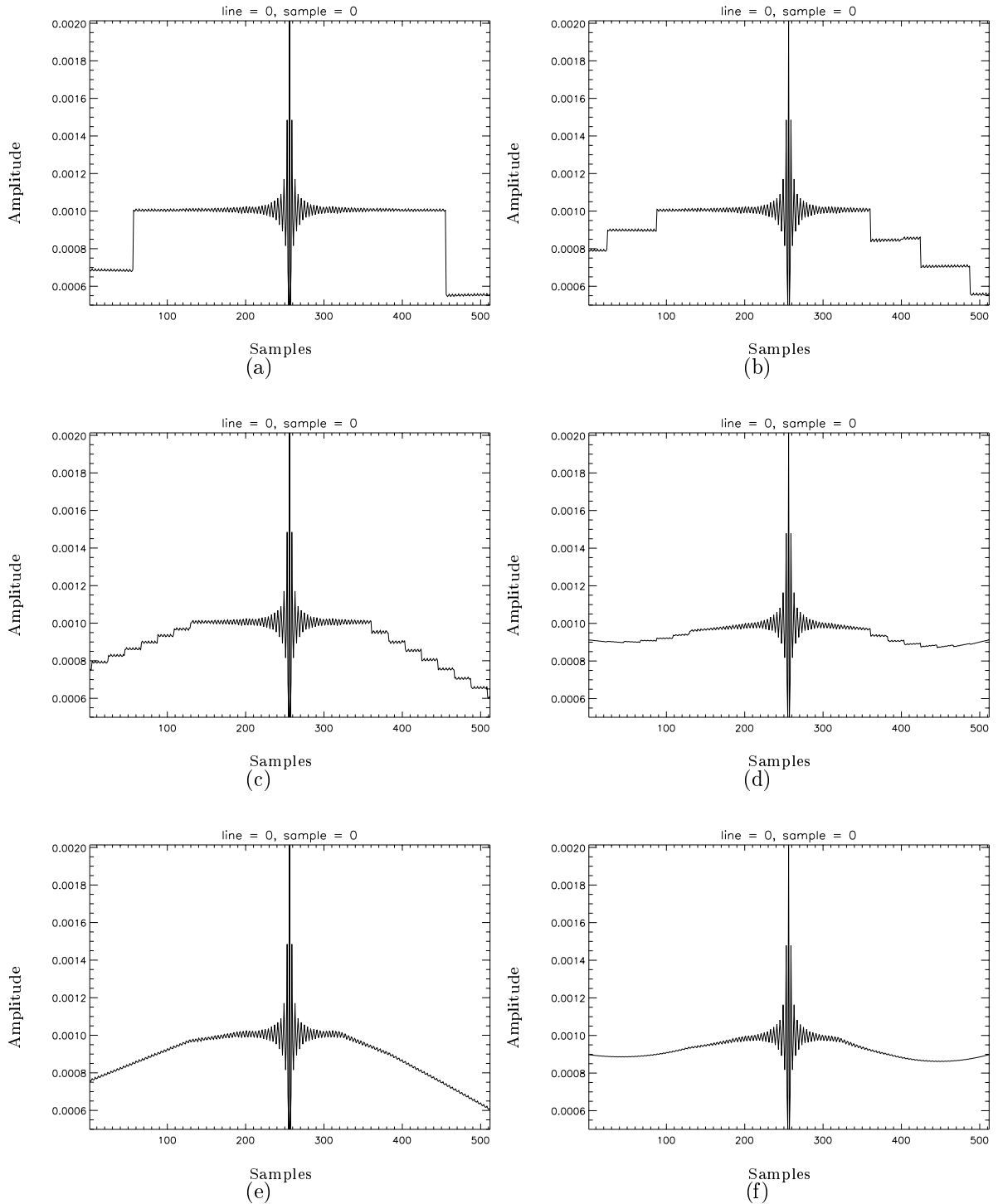


Figure 4.35: Interferogram of tall wall for different collection methods from moving platform with subpixel sampling: (a) delta sampling 512 view angles, (b) 3x subpixel sampling for 512 view angles, (c) 9x oversampling for 512 view angles, (d) apodized version of (c), (e) 9 view angles interpolated to 512 with 9x oversampling, (f) apodized version of (e)

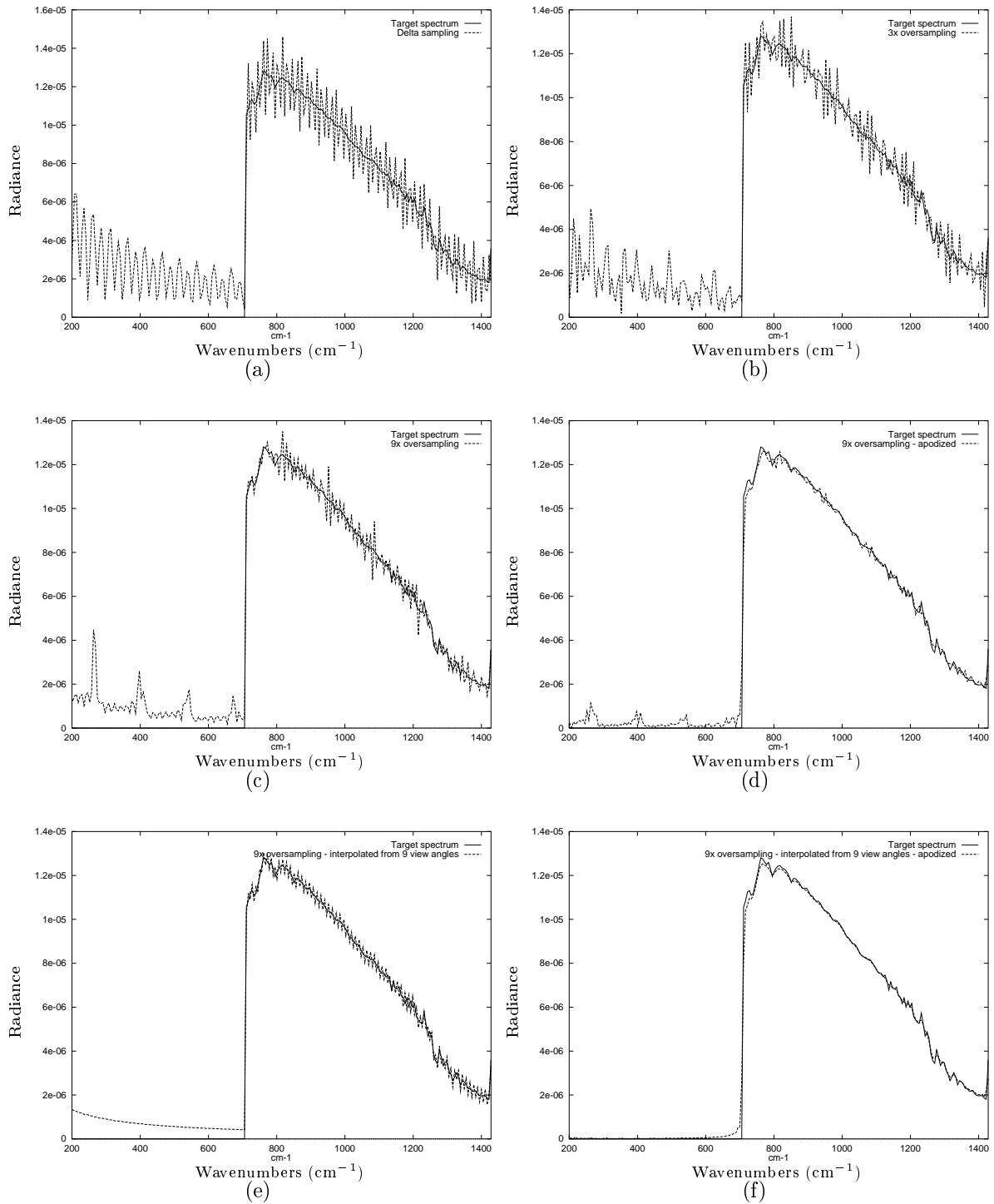


Figure 4.36: Spectra for interferograms in figure 4.35

4.1.12 Dynamic Mirror Alignment

Although some simulations were run to check for correct computation, implementation of this routine within DIRSIG is yet to be completed. Also, there is not enough information about how phase differences affect the interference of wavefronts emitted by slightly misregistered ground pixels for the accurate simulation of this condition. Appendix B presents more details on this topic.

4.2 Final Demo

Up to this point, all results presented covered the spectrometer functions of the IFTS. This section shows that the simulation program can indeed provide both images and spectra, i.e., image cubes. Two scenes were selected for the simulations. The Foxbat scene, which contains hangars, airplanes, tarmac, and grassy areas, was selected for simulations in the VIS/NIR region of the spectrum. For midwave IR and longwave IR simulations, the NTS scene was selected because it contains a gas plume, which will produce narrow spectral absorption lines that require a high-resolution sensor.

4.2.1 Foxbat scene

The parameters used for the simulation of this scene were provided by Dr. Bruce Rafert of Michigan Technical University (MTU). One of the parameters was modified to match the spectral range of the sensor. The original design called for a spectral range from 1.7-5 μm . This simulation covers the range from 0.45-1.1 μm . The image in Figure 4.37 is the image cube of the simulation. The default parameter values were used for this simulation, which means that no artifacts were enabled. The spectral resolution of 178.7 cm^{-1} used in this simulation translates to $\Delta f = 3.6 \text{ nm}$ at $f = 0.45 \mu m$ and $\Delta f = 23.2 \text{ nm}$ at $f = 1.14 \mu m$.

The image clearly shows texture in the central grassy area, but none in the grass fields in the corners of the image. The simple explanation is that the scene is constructed with three different types of grass of material ID 4, 10, and 60, respectively. The central field is ID 60 and the other grass visible in this image is of type 10. Grass fields of material ID 4 are not visible in this image. Using multiple material IDs to simulate grass allows for the simulation of healthy and sick vegetation. When texture is required, the texture maps must be included in the configuration file on a per

material basis. Although the texture file was loaded for materials 4 and 60, no texture map was loaded for material 10.

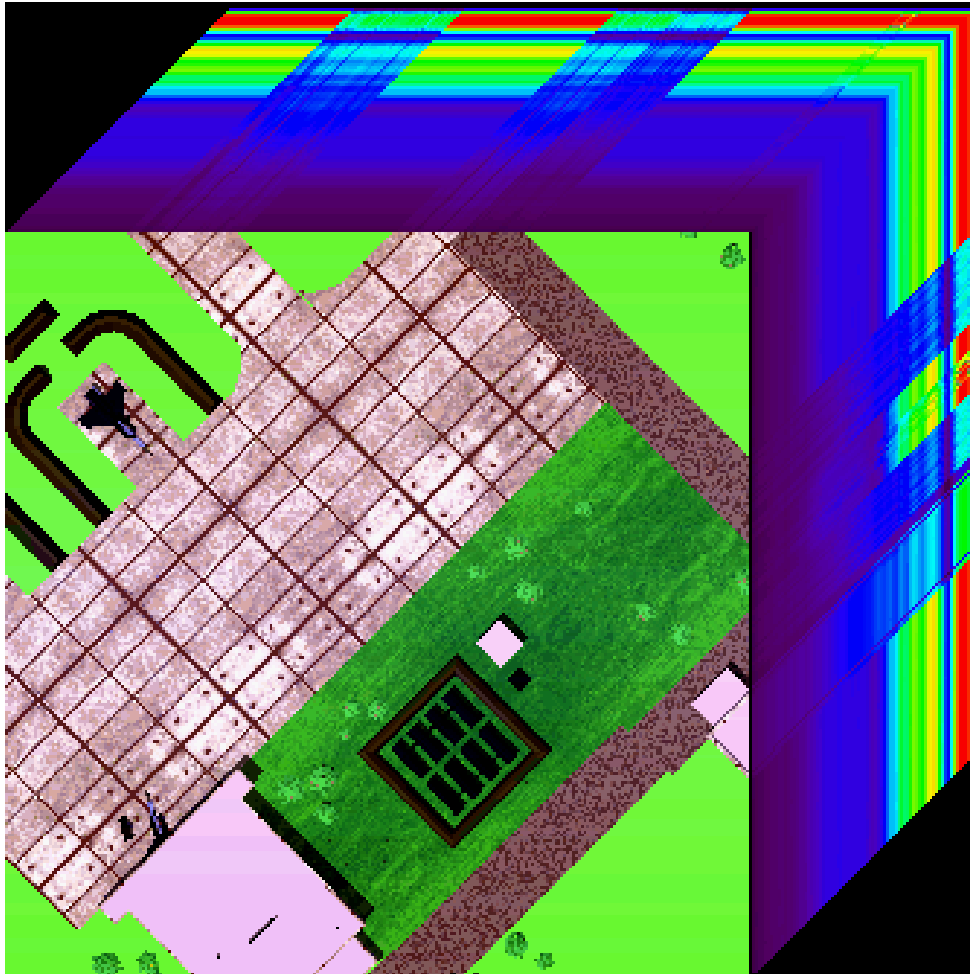


Figure 4.37: Foxbat scene as seen by a Sagnac IFTS

4.2.2 NTS scene

The IFTS simulation of a complex scene containing a gas plume was repeated for different IFTS designs and parameters. The gases released from the smoke stack in concentrations sufficient to be detected are: C_6H_6 , SO_2 , CH_3Cl , and HCl . The absorbance spectra for these gases over the spectral ranges of interest are in Figures 4.38 and 4.40. To detect the absorption lines of the gases, high resolution is required. The spectral range and frequencies used for the thermal region simulations

were respectively

```
MINIMUM_FREQUENCY = 679.2  
MAXIMUM_FREQUENCY = 1228.8  
DELTA_FREQUENCY = 1.2
```

and

```
MINIMUM_FREQUENCY = 2400.0  
MAXIMUM_FREQUENCY = 3072.0  
DELTA_FREQUENCY = 3.0
```

These represents $8.13 \mu m \leq \lambda \leq 14.72 \mu m$ and $3.26 \mu m \leq \lambda \leq 4.17 \mu m$, respectively. The simulation of the first spectral range used a resolution smaller than 2.0 cm^{-1} and required the use of *FASCODE* to create the atmospheric database. Because *FASCODE* runs slower than *MODTRAN*, this process took about twice as long as was required to build the second atmospheric database. The spectral ranges were selected after comparing the transmission of the atmosphere to the absorbance spectra of the gases. Wherever the atmosphere is opaque, there is no point in looking for the plume. For both simulations, the spectra of the target and background are shown, along with the difference spectra, in Figures 4.39 and 4.41. The arrows indicate which gas is mostly responsible for the spectral features.

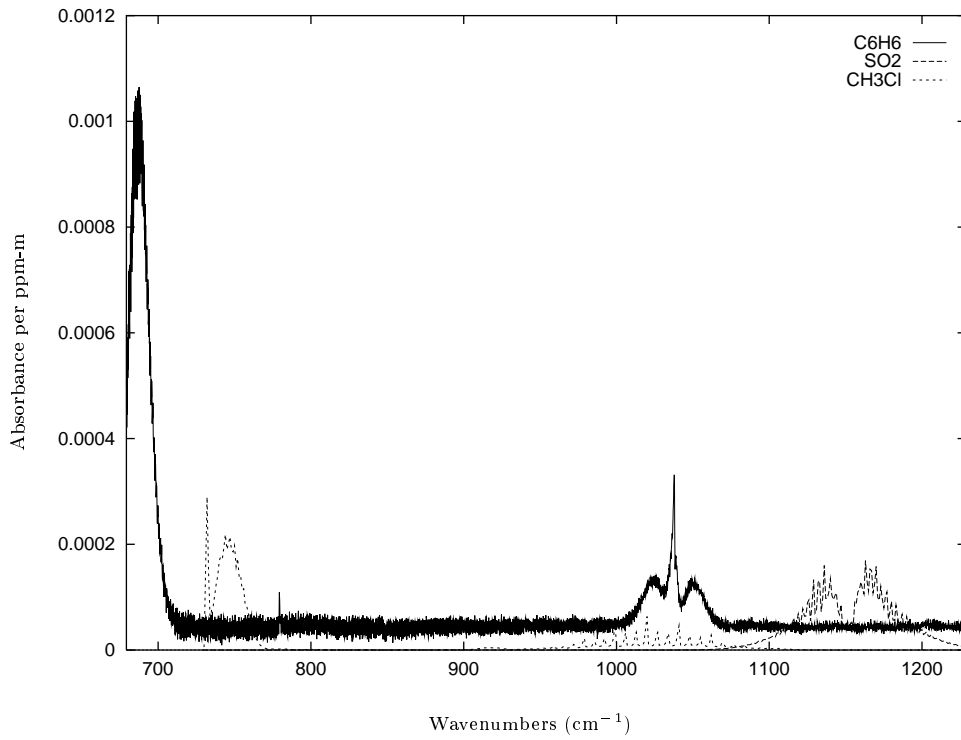


Figure 4.38: Gas absorbance spectra for plume gases over 680-1220 cm^{-1} range

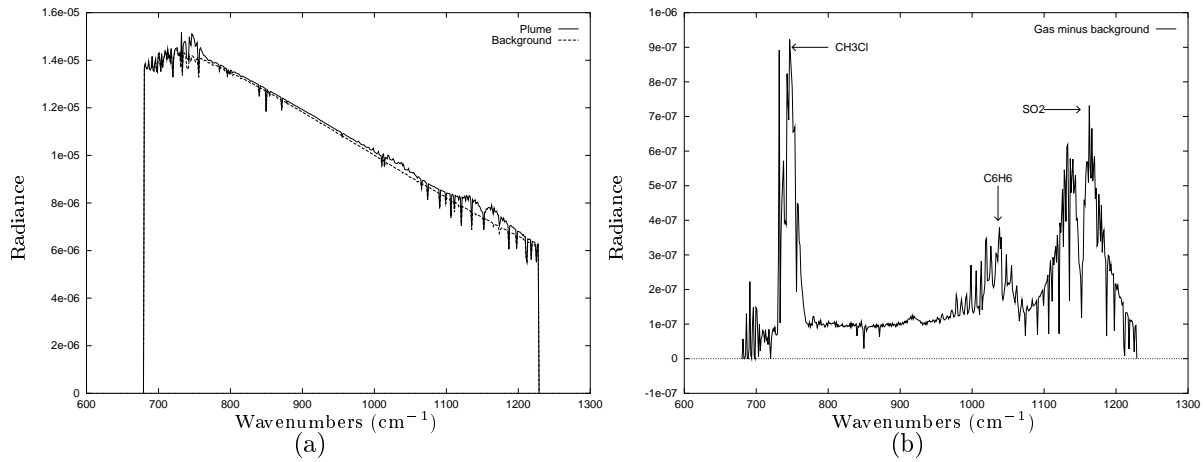


Figure 4.39: Spectra for spectral range 680-1220 cm^{-1} : (a) spectra of gas plume and background, (b) difference spectra for gas plume and background

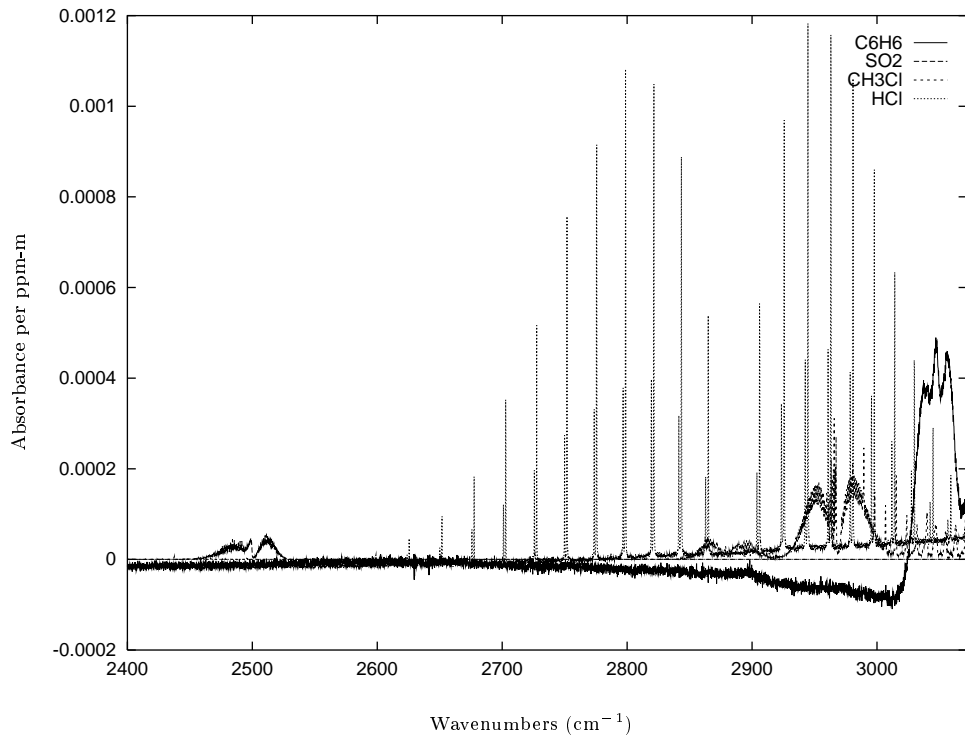


Figure 4.40: Gas absorbance spectra for plume gases over 2400-3072 cm^{-1} range

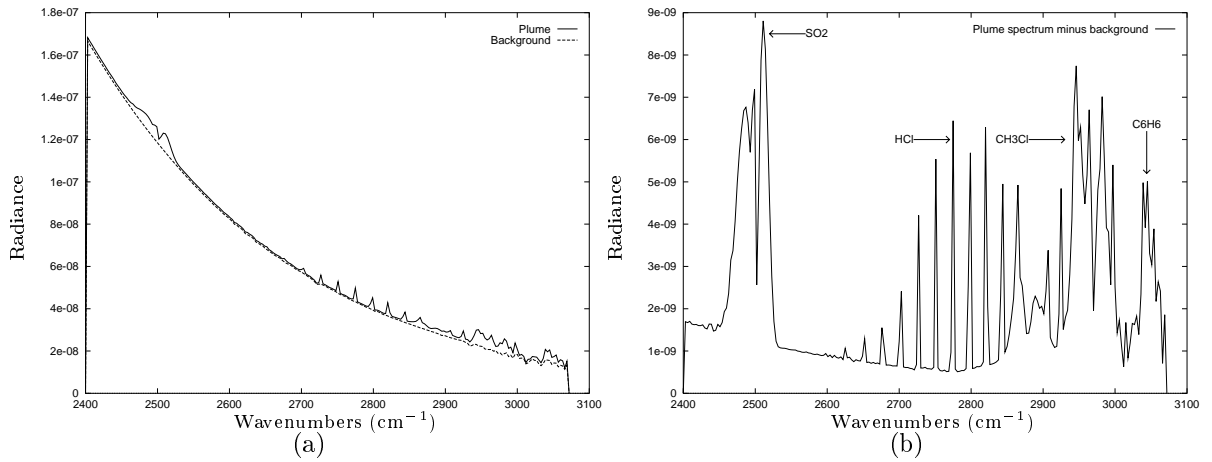


Figure 4.41: Spectra for spectral range 2400-3072 cm^{-1} : (a) spectra of gas plume and background, (b) difference spectra for gas plume and background

Slices of the image cube show that the plume can be detected only at some wavelengths as shown in Figures 4.42 (a) and (b). The simulation is identical to that shown in Fig. 4.39. The

two slices are at $\sigma = 856.8 \text{ cm}^{-1}$ and $\sigma = 747.6 \text{ cm}^{-1}$, respectively. While the outline of the plume cannot be seen in image (a), it is apparent in image (b). This demonstrates that high resolution is required to detect gas spectra. In a lower-resolution system, the plume would most likely show up faintly in every band, rather than being clear in some bands and not at all others. This would hinder any attempts to identify gas species.

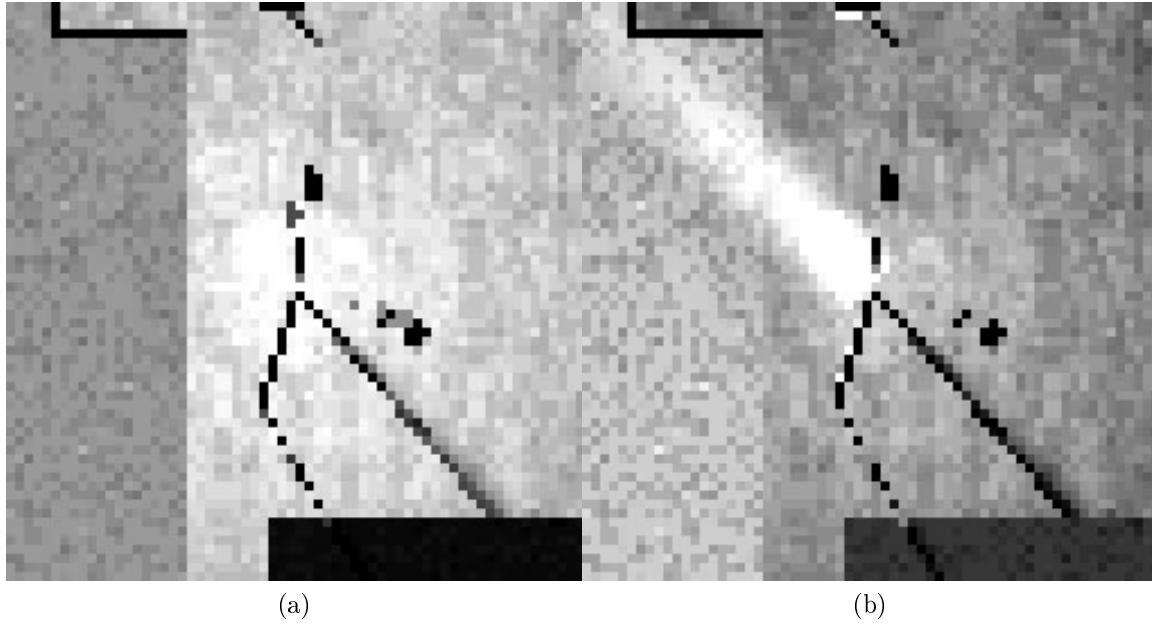


Figure 4.42: NTS scene simulation: (a) $\sigma = 856.8 \text{ cm}^{-1}$ band, (b) $\sigma = 747.6 \text{ cm}^{-1}$ band

The previous gas-plume simulation (Fig. 4.42) was performed with a stationary Michelson IFTS. To make the simulation more realistic, it was repeated with 16-bit quantization, detector noise, spatial oversampling (5×5) and target tracking over multiple view angles (17 interpolated to 1024). The detector noise characteristics used in this simulation were set so that the interferogram signal-to-noise ratio would be about 4000. Note that other factors such as quantization and atmospheric effects contribute to the noise in the detected signal. As mentioned before, noise in the interferogram produces noise in the spectrum. The tracking of the target over ± 2.5 degrees of flight path also contributes to noise in the spectrum. These factors make for a more realistic simulation but decreased the SNR of the spectrum. This reduces the ability to detect the effects of the gas plume on the spectrum.

There are two obvious ways of looking at the scene. If one is interested in the spectra of the ground-level objects, the sensor should be pointed at a rock point at ground level, which is the base of the smoke stack. However, if one is interested in the spectrum of the plume, it might be more logical to track the plume at the top of the smoke stack. In this simulation, the rock point is 21.64 meters above ground. Both of these collection schemes were simulated. In both cases, the platform followed the same flight path at an altitude of 175 meters. Only the pitch was changed to account for the new rock-point altitude. At this flight altitude the ground sampling distance is 0.35 meter. As the sensor scans each view angle, the ground hit point is constant as long as the rock point is at ground level. For the simulation with the rock point at 21.64 meters above ground, the scan line ground travel distance has a range of ± 1.0 meter around the target ground pixel. This is equivalent to 6 pixels. In other words, 6 ground pixels will contribute to the formation of one image pixel. The background of the plume must be uniform to avoid corrupting the interferogram. This effect is visible when looking at objects that are about one pixel in size, as in the NTS scene. One object in the scene is angled about 45° relative to the scene coordinates. This object is slightly larger than one pixel, and therefore affects more than 6 pixels. Also, this condition is compounded because it is angled at 45° . Figure 4.43 shows how neighboring interferograms are affected by the object. Interferograms of sample 10, lines 7 to 15 are displayed. The line is a darker object (lower intensity spectrum), which translates to a dip in the amplitude level of the interferogram. Portions of the interferogram affected by the object are at a lower level than the rest of the interferogram. In every interferogram where the wings are at different levels, the corresponding spectrum will contain ringing, which could be removed by apodization.

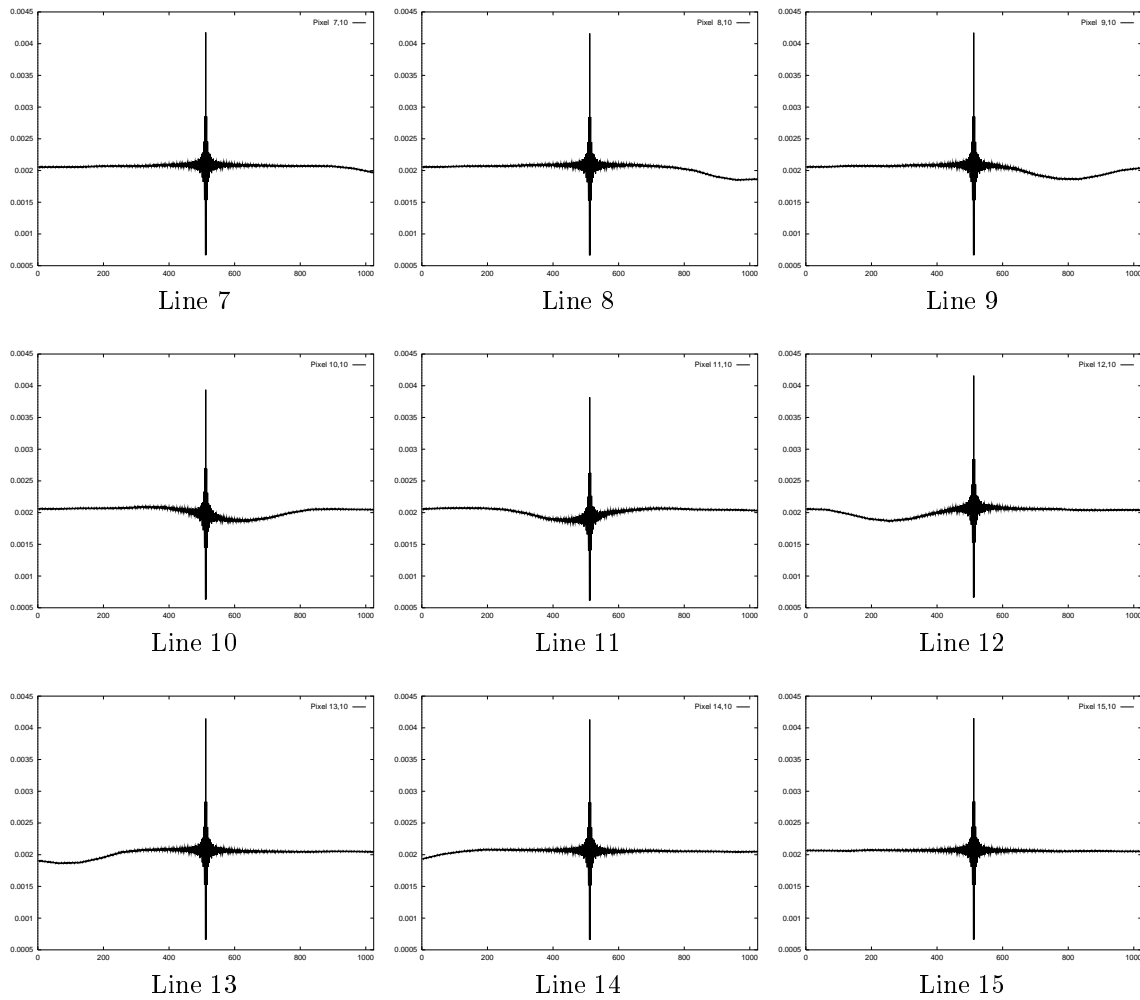


Figure 4.43: Interferogram corruption due to changing background when sensor rock point is above ground

A ground pixel that is located at a point other than the rock-point altitude blurs the spatial and spectral dimensions of the image cube. Comparison between a slice of the image cube of the same band for both simulations shows that the line running at 45° is slightly blurred in the simulation with the rock point at stack level (Figure 4.44). The blur shown in the image is equivalent to the blur that would be present in an image if the target distance is 14% greater than the rock point distance, and the sensor travels over a 5° range in view angle.

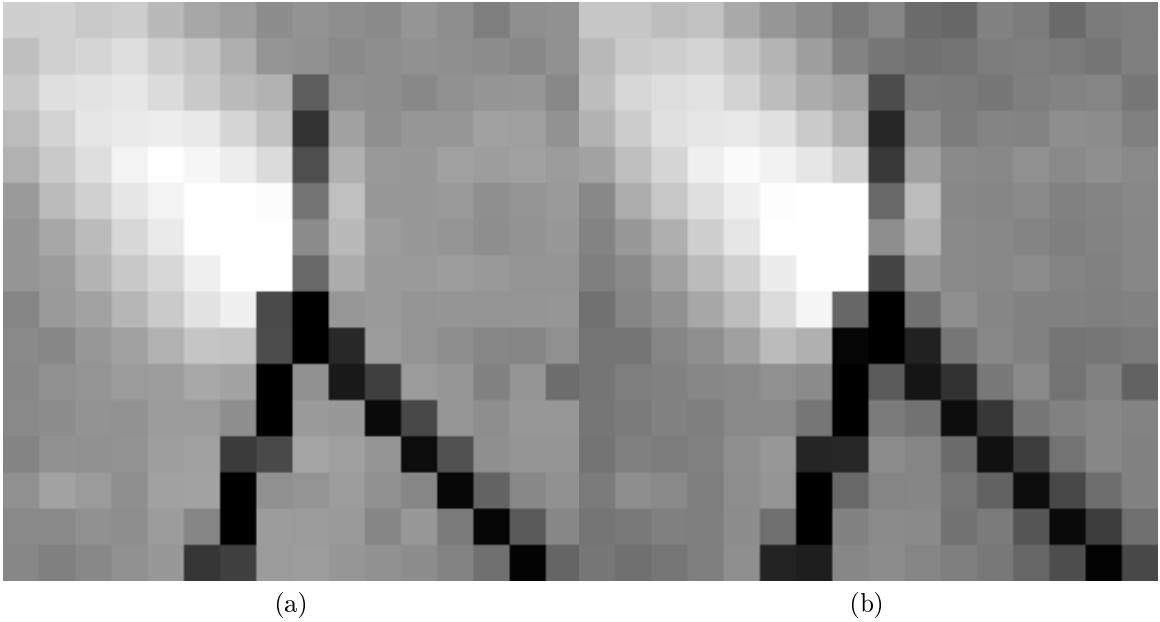


Figure 4.44: Comparison of spatial blurring for two collection methods: (a) with rock point at ground level, (b) with rock point at plume level

When the rock point is at ground level, the scan line travel distance at an altitude of 21.64 meters has a spread of ± 0.88 meter about the location of the ideal pixel. This spread is equivalent to 5 “plume-level” pixels. Since the exit diameter of the smoke stack is 1 meter, some parts of the scan will miss the plume altogether or see only a diluted version. Just as in the previous case, this condition corrupts the interferogram. However, since the contribution of the plume to the interferogram is very small compared to the contribution of the background, this effect cannot be visually detected by looking at the image cube.

These two simulations both permit the plume to be identified. The plume and background spectra shown in Figure 4.45 show very little noticeable difference between the two methods. Both graphs show the effects of the plume added on to the background. The background values were collected by disabling the plume modeling and re-running the simulation.

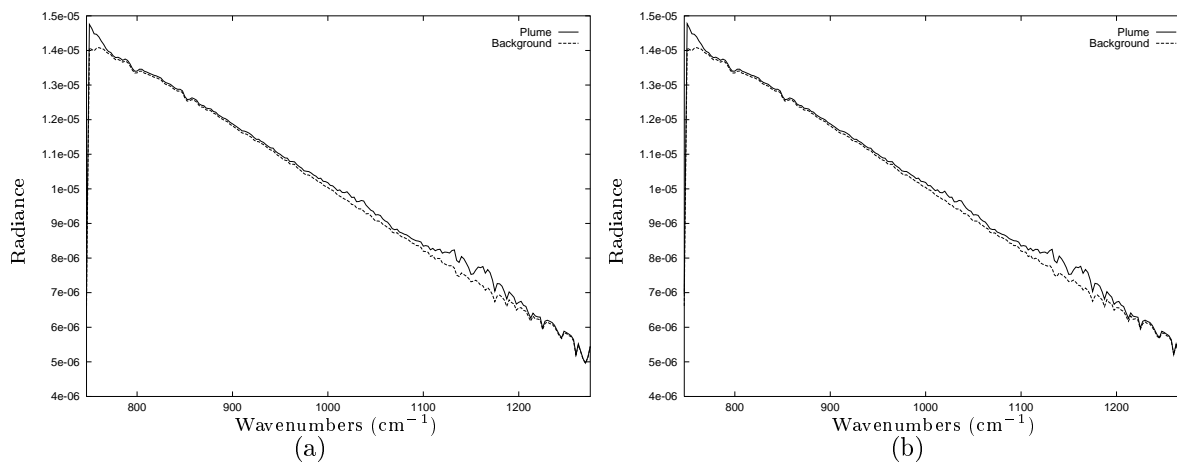


Figure 4.45: Spectra of plume and background: (a) with rock point at ground level, (b) with rock point at plume level

To select the best collection method, the difference spectra (plume minus background) are plotted for both methods (Figure 4.46). These results show that the difference spectrum is slightly more intense when the sensor rock point is located at the level of the plume release point. This is valid only because the background of the plume is fairly uniform. A non uniform background would lead to ringing in the spectrum, which would “drown” the gas spectra. The simulated noise present in the difference spectra partially hides narrow absorption lines but the broader regions are still clearly apparent. It is difficult to distinguish the narrow spectral features of CH_3Cl between 960 and 1080 cm^{-1} from the noise. The fact that they are also mixed with the spectrum of C_6H_6 does not help either. Had the detector noise level been increased by an order of magnitude, it would have been difficult to separate the effects of the plume from the effects of the noise. The gas absorption spectra are shown in Figure 4.38.

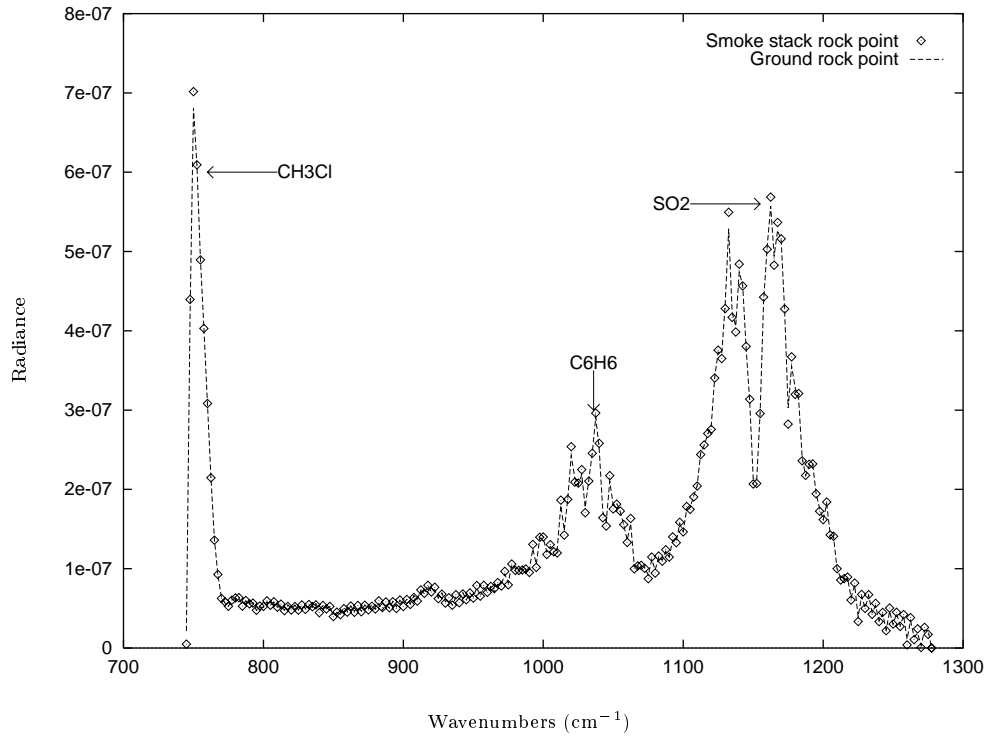


Figure 4.46: Difference spectra for two collection methods

4.3 Computation Time

After DIRSIG is completely initialized, the spectra for each pixel are collected and saved to generate the image cube. Most of the running time is spent collecting the input spectra, generating the interferogram and computing the FT of the interferogram. The relative amount of time spent in each location depends on which options are used, how many interferogram points are required, and how many view angles are used. An 8x8 image can run in about 10 seconds on a 266 Mhz Pentium II when no options are enabled, with one view angle. The same simulation with BRDF and thermal options enabled, and with 512 view angles requires about one hour. Oversampling will also lengthen the simulation time almost linearly. The spectral range in use is also a very important factor. There is no simple answer to this question, but a rule of thumb is that as more artifacts are enabled, the longer the simulation time.

Chapter 5

Conclusions and Recommendations

5.1 Conclusions

The goal of this research was to simulate realistic design artifacts in images collected from imaging Fourier transform spectrometers. The computation tool that was created provides the user with the ability to change parameters and visualize their effects at every step of the imaging chain. Two IFTS designs were evaluated: a Michelson staring sensor for temporal interferogram collection and a Sagnac pushbroom design for spatial collection of the interferogram.

The examples and their analysis shown in Chapter 4 indicate that the simulated artifacts produced the expected results. No validation with real sensor data was performed.

The implementation of *FASCODE* within the atmospheric database generator (*make_adb*) was also successful. Although requiring longer computation, an atmospheric database generated with *FASCODE* is much more accurate than *MODTRAN*'s interpolated equivalent at resolutions below 2.0 cm^{-1} . Some spectral lines that do not register with *MODTRAN* are present in the simulation when the *FASCODE* atmospheric database is used.

5.2 Recommendations

A computer simulation implies discrete rather than continuous inputs and outputs. Therefore, some of the artifacts found in the simulation would not be found in a real system. This is especially true for the Michelson IFTS. Examples are the ideal sampling of a spatial pixel and the sudden

transition in ground hit points from one object to another as the zenith angle is varied. To overcome these problems and obtain a more realistic simulation, spatial pixel oversampling and inter-view angle interpolation should be applied when the Michelson IFTS is used in multiple-view acquisition mode. Inter-view angle interpolation, requires collecting the spectra at 20 or so view angles and interpolating to generate the required 512 or 1024 input spectra. This combination of simulation parameter reduces simulation-borne artifacts.

The user interface to DIRSIG 3.1 is a dramatic improvement over the previous release of DIRSIG. The reduction in the number of required configuration files and inclusion of tags for parameter identification simplifies the DIRSIG learning curve. It is recommended that the FTS configuration file be included as a new section of the main configuration file prior to IFTS sensors being included into a future release of DIRSIG. This would not only eliminate the need for setting an environment variable and using the “-fts” mode, but it would also eliminate the need for some configuration parameters that are currently required in both the main configuration file and the IFTS configuration file. The plume configuration file also should be standardized. The current version of the plume configuration file tends to be confusing to novice users.

Most of the efforts in this project were geared towards Michelson FTS versus Sagnac FTS. This is why some artifacts listed in the background Chapter were not simulated. At the beginning of the project, it was felt that Michelson designs were more attractive mainly because of their aptitudes for higher spectral resolution. After having searched FTS literature, it has become obvious that most of the IFTS sensors currently being flown use spatially modulated IFTS. The first spaceborne IFTS aboard MightySatII.1 will also be a spatially modulated design. This is why more effort effort is required to understand and simulate spatially modulated designs.

The final recommendation is already being considered. The generation of test scenes with the current *AUTOCAD* routines is difficult and does not always generate the expected results, especially when the orientation of normals are taken into account. This is why I believe that the version of the DIRSIG GUI being developed is a step in the right direction.

5.3 Future Work

Because routines are modular, it should be easy for a user with working knowledge of C/C++ to implement other types of Fourier transform spectrometers, such as the birefringent-filter FTS,

rotary FTS, or spatial heterodyne FTS. Artifacts that were not simulated as part of this project also could be implemented, including self-emission and thermal noise, beamsplitter effects, vignetting, and chromatic aberration. The comparison of these products with a real IFTS would be difficult, but is critical to validate this work. Any reduction to computation time would also be a welcome.

The effects that were briefly discussed in section 2.8.14 also could be implemented. The realism of some artifacts that are currently simulated could be improved, such as the streaking and blooming that usually accompany detector saturation (clipping).

One important feature of Sagnac IFTS that was not considered in this project is the aperture function of the sensor. The interferogram in a Sagnac design is modulated by the aperture function. For a Michelson design, the interferogram will have a constant DC signal since a single detector collects the entire interferogram. This DC signal is removed from the interferogram prior to the conversion to spectrum by subtracting the average interferogram amplitude from the interferogram. In a Sagnac IFTS, the bias of the interferogram varies with spatial location on the FPA. The interferogram could be modulated by the aperture function for Sagnac IFTS. This change would require to modify the method that is used to subtract the bias from interferograms by subtracting the aperture function for the Sagnac rather than subtracting the average amplitude of the interferogram.

Although it was assumed to be only a minor source of error, the effect of dynamic mirror misalignment should be simulated. The code necessary to generate the interferogram from two spectra generated by misaligned mirrors has been developed. It is still necessary to provide DIRSIG with the means to compute the spectrum of the target that is viewed through the misaligned mirror. DIRSIG would have to compute the hit point and spectrum from the misalignment angle and azimuth of the mirror. This spectrum is required in addition to the original input spectrum.

5.4 Timetable

This section contains a timetable of the project milestones for the work described herein.

February — July 1998

- Literature review

May — July 1998

- Perform early FTS simulations using IDL

June 1998

- Introductory IFTS presentation to the DIRS group

September 1998

- Meet with DIRSIG developer for discussions on work separation and interface
- Begin translating IDL simulation code to C++

October 1998

- Write IFTS sensor package
- Introduction to *FASCODE*
- Write stand-alone program for testing of the sensor package
- Write IDL widget as user interface that generates configuration files for simulations
- Review literature on misalignment of mirrors
- Derive interferogram equation for mirror misalignments

November 1998

- Test stand-alone version of the IFTS sensor package
- Perform stand-alone simulations of mirror misalignments
- Generate test scenes

December 1998

- Integrate *FASCODE* with DIRSIG's atmospheric database generator (*make_adb*)

January 1999

- Validate use of *FASCODE* with DIRSIG
- Integrate IFTS sensor package with DIRSIG
- Run simulations and debug DIRSIG/sensor package for framing-array sensors (Michelson)

February 1999

- Regenerate test scenes to correct inverted normal problem
- Implement pushbroom-type sensors (Sagnac)
- Run simulations and debug

March 1999

- Run simulations
- Change Michelson configuration from framing array to pushbroom sensor

April 1999

- Implement detector gain and bias, spatial oversampling and sensor spectral response
- Perform simulations on demo scene

Appendix A

Beamsplitter Transmission and Reflection Effects

This appendix includes derivations of the beamsplitter effects for both the Michelson and Sagnac FTS. This effect is often called “beamsplitter RT product” in the literature, for the reflectance and transmittance (RT) of the beamsplitter.

Both the intensity transmittance T_i and reflectance R_i of a beamsplitter can vary with λ . However, the effects will be derived only for the monochromatic case. No absorption or emission effects will be considered in this derivation so that $T_i + R_i = 1$.

A.1 Michelson

Each beam in a Michelson interferometer is reflected once and transmitted once. For an incident wave of the form:

$$a_0(t) = A \cos(\omega t) \tag{A.1}$$

the amplitude of the waveform is:

$$a_1(t) = AR_a T_a \cos(\omega t) \tag{A.2}$$

where A is the maximum amplitude of the source waveform, ω is the angular temporal frequency, and t is the time. Note that R_a and T_a are the amplitude reflectance and transmittance. ($R_a = \sqrt{R_i}$ and

$T_a = \sqrt{T_i}$, where the subscript i indicates intensity.) The second waveform exhibits an additional phase delay ϕ :

$$a_2(t) = AR_a T_a \text{COS}(\omega t + \phi) \quad (\text{A.3})$$

where ϕ represents a phase shift between the two waveforms, which is associated with the OPD.

According to the superposition principle, the resulting waveform is the sum of the component waveforms, or:

$$a(t) = a_1(t) + a_2(t) = AR_a T_a [\text{COS}(\omega t) + \text{COS}(\omega t + \phi)] \quad (\text{A.4})$$

This may be rewritten as:

$$a(t) = 2AR_a T_a \text{COS}\left(\omega t + \frac{\phi}{2}\right) \text{COS}\left(\frac{\phi}{2}\right) \quad (\text{A.5})$$

The detector intensity is the time average of the squared magnitude. The intensity seen at the detector is proportional to the squared magnitude of Equation A.5:

$$\begin{aligned} I &\propto 4A^2 R_a^2 T_a^2 \text{COS}^2\left(\frac{\phi}{2}\right) \left\langle \text{COS}^2\left(\omega t + \frac{\phi}{2}\right) \right\rangle \\ &\propto A^2 R_a^2 T_a^2 [1 + \text{COS}\phi] \\ &= A^2 R_i T_i [1 + \text{COS}\phi] \\ &= A^2 R_i (1 - R_i) [1 + \text{COS}\phi] \\ &= A^2 (R_i - R_i^2) [1 + \text{COS}\phi] \end{aligned} \quad (\text{A.6})$$

Note that a time dependent sinusoidal waveform is seen as a constant by the detector if ω is sufficiently large. Equation A.6 clearly indicates that the detected intensity is a function of R_i (or T_i), and will be null when destructive interference occurs. Figure A.1 shows the normalized constructive interference intensity limits as a function of R_i and as a fraction of the source intensity.

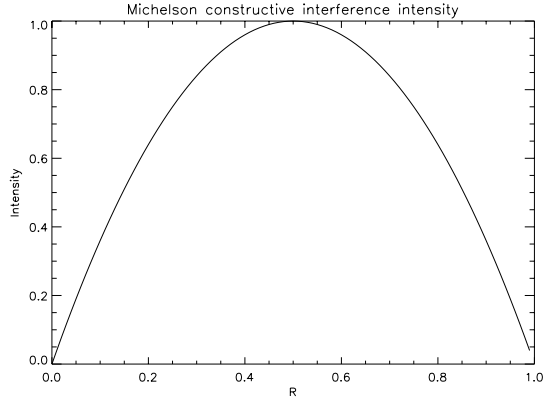


Figure A.1: Michelson interferometer constructive interference intensity limits

A.2 Sagnac

The derivation is a little more complicated for the Sagnac because of the asymmetry of the reflection and transmission for the two beams.

$$a_1(t) = AR_a^2 \text{COS}(\omega t) \quad (\text{A.7})$$

and:

$$a_2(t) = AT_a^2 \text{COS}(\omega t + \phi) \quad (\text{A.8})$$

In this case:

$$\begin{aligned} T_a^2 &= T_i \\ &= (1 - R_i) \\ &= (1 - R_a^2) \end{aligned} \quad (\text{A.9})$$

So Equation A.8 can be rewritten as:

$$a_2(t) = A(1 - R_a^2) \text{COS}(\omega t + \phi) \quad (\text{A.10})$$

The sum of the two beams gives:

$$a(t) = a_1(t) + a_2(t) = AR_a^2 [\text{COS}(\omega t) - \text{COS}(\omega t + \phi)] + A \text{COS}(\omega t + \phi) \quad (\text{A.11})$$

The time-averaged squared magnitude is:

$$\begin{aligned}
\langle a^2 \rangle &= \langle A^2 R_a^4 [\text{COS}(\omega t) - \text{COS}(\omega t + \phi)]^2 \\
&\quad + 2A^2 R_a^2 [\text{COS}(\omega t)\text{COS}(\omega t + \phi) - \text{COS}^2(\omega t + \phi)] \\
&\quad + A^2 \text{COS}^2(\omega t + \phi) \rangle \\
&= \left\langle A^2 R_a^4 \left[-2 \text{SIN} \left(\omega t + \frac{\phi}{2} \right) \text{SIN} \left(-\frac{\phi}{2} \right) \right]^2 \right. \\
&\quad \left. + 2A^2 R_a^2 \left[\frac{1}{2} \text{COS}(-\phi) + \frac{1}{2} \text{COS}(2\omega t + \phi) - \text{COS}^2(\omega t + \phi) \right] \right. \\
&\quad \left. + A^2 \text{COS}^2(\omega t + \phi) \right\rangle
\end{aligned} \tag{A.12}$$

The detected intensity may be expressed as:

$$\begin{aligned}
I &\propto A^2 R_a^4 (1 - \text{COS}(-\phi)) + \frac{A^2}{2} + A^2 R_a^2 (\text{COS}(-\phi) - 1) \\
&= A^2 R_i^2 (1 - \text{COS}(\phi)) + \frac{A^2}{2} + A^2 R_i (\text{COS}(\phi) - 1)
\end{aligned} \tag{A.13}$$

This equation indicates that the recorded intensity level for destructive interference will not be null. One of the two beams will have larger amplitude than the other. When the interfering beams do not have the same amplitude, the component that remains after summing the two beams will create a DC bias in the recorded intensity. Figure A.2 shows the DC level (fraction of the source intensity) as a function of the intensity reflectance. Note that for a totally reflective or transmissive “beamsplitter”, the detected intensity is equal to the source intensity. Contrary to the Michelson case, the recorded constructive interference will always occur at the same level as the source intensity, regardless of the transmittance or reflectance.

For nonideal beamsplitters ($R_i \neq 0.5$), a DC level is present through the whole interferogram (Figure A.2). This DC value will produce a Dirac delta function located at the origin in the spectrum, i.e., no false frequencies will be introduced in the spectrum. Subtracting the average amplitude of the interferogram prior to the Fourier transformation will preclude the generation of the Dirac delta function. The amplitude of the recovered spectrum will be reduced by a factor that is a function of the RT product of the beamsplitter. Figure A.3 shows this factor (the range of maximum interference) is the same as the Michelson. In other words, if the DC level is carefully removed from the interferogram prior to the Fourier transform, a Michelson interferometer and a Sagnac interferometer with the same beamsplitter will produce the same results.

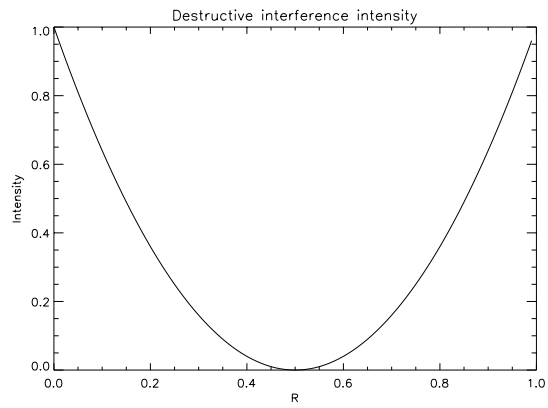


Figure A.2: Detected intensity for Sagnac destructive interference

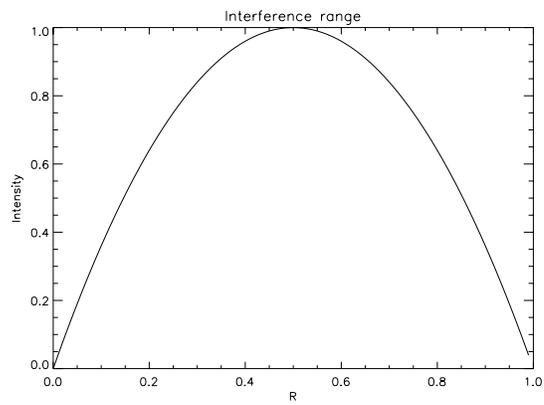


Figure A.3: Range of possible interference (constructive - destructive) for Sagnac interferometers

Appendix B

Interference of Misregistered Pixels

We have seen in Eq. 2.4 that the interferogram equation is:

$$I(\delta) = \int_0^{+\infty} S(\sigma)\{1 + \cos(2\pi\sigma\delta)\}d\sigma \quad (\text{B.1})$$

where δ is the optical path difference (OPD). The OPD of a Michelson interferometer is $2vt$, where v is the speed of the scanning mirror and t is the time and the OPD for a Sagnac is $\ell x/f$, where ℓ is the virtual object separation, x is the off-axis distance of the detector pixel, and f is the focal length of the Fourier-transform lens. However, Equation B.1 is true only when the interfering wavefronts have a common source, i.e., when the only difference in the two waves is the optical path length.

In the case where the mirrors of an interferometer are misaligned, the wavefronts detected at the interference plane will be misregistered. Because these wavefronts come from different sources or ground pixels (Figure B.1), we cannot assume that the wavefronts are temporally and spatially coherent. This incoherence may be represented by an additional phase difference between the wavefronts. This introduces another variable in the derivation. Also, the amplitudes of each wavefronts will be different.

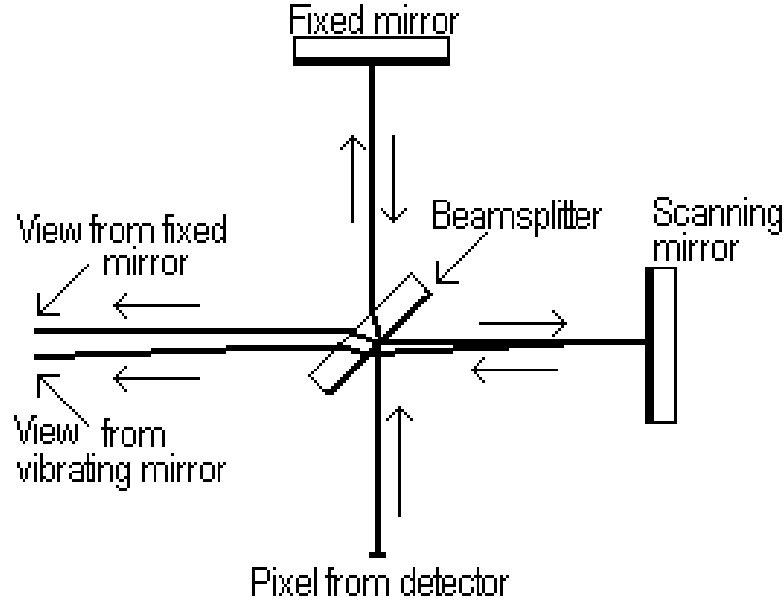


Figure B.1: One cause of image misregistration is mirror misalignment

Consider the source waveform: waveforms:

$$a_1(t) = A_1 \text{COS}(\omega t) \tag{B.2}$$

and

$$a_2(t) = A_2 \text{COS}(\omega t + \phi + \theta(t)) \tag{B.3}$$

where A_1 and A_2 are the amplitudes of the source waveform, ω is the angular frequency, t is the time, ϕ is the phase shift associated with the OPD, and θ is a phase offset associated with the fact that the two waveforms are not coherent. A_1 , A_2 , ϕ and θ are all functions of the frequency σ .

B.1 Monochromatic Radiation

The principle of superposition says that the interfering waveform will be:

$$a(t) = a_1(t) + a_2(t) = A_1 \text{COS}(\omega t) + A_2 \text{COS}(\omega t + \phi + \theta(t)) \tag{B.4}$$

The squared magnitude of the amplitude is:

$$I \propto \langle a(t)^2 \rangle = \langle A_1^2 \text{COS}^2(\omega t) + 2A_1 A_2 \text{COS}(\omega t) \text{COS}(\omega t + \phi + \theta(t)) + A_2^2 \text{COS}^2(\omega t + \phi + \theta(t)) \rangle \quad (\text{B.5})$$

Equation B.5 may be rewritten as:

$$I \propto \left\langle \frac{A_1^2}{2} [1 + \text{COS}(2\omega t)] + A_1 A_2 [\text{COS}(-\phi - \theta(t)) + \text{COS}(2\omega t + \phi + \theta(t))] + \frac{A_2^2}{2} [1 + \text{COS}(2\omega t + 2\phi + 2\theta(t))] \right\rangle \quad (\text{B.6})$$

Because the detector acts as an integrator, any temporal sinusoidal signal will be averaged. The final equation is:

$$I \propto \frac{A_1^2}{2} + \frac{A_2^2}{2} + A_1 A_2 \text{COS}(\phi + \theta(t)) \quad (\text{B.7})$$

The special case when $A_1 = A_2 = \sqrt{S}$, and $\theta = 0$ gives the familiar equation $I = S[1 + \cos(\phi)]$ (Equation B.1 monochromatic case).

If we assume that θ is constant for all frequencies, i.e., coherent light, its effect on the interferogram is a simple shift by a constant value, and that, for all frequencies. Because the magnitude of the Fourier transform of the interferogram is shift invariant, we can drop the θ phase offset.

If the sources are not coherent, then $\theta(t)$ is a random value (between 0 and 2π). Because the dynamic alignment of mirrors tend to be very good (Griffiths and de Haseth, 1986), the ground pixels of a typical IFTS should always overlap by at least 10%. Therefore, the sources may be considered partially coherent. Given these conditions, it is possible to assume that the value of $\theta(t)$ will not vary by large amounts. If we assume that the sources interfering at the detector have a 90% overlap, a random phase offset needs to be included in the equation ($\theta(t) \neq 0$). However, because 10% of the total radiation cannot have a large effect, the values of $\theta(t)$ will tend to be close to zero. This deserves more explanation. Figure B.2 shows that the effect of adding a sinusoidal function with a $\frac{\pi}{2}$ offset to a function with 9 times the amplitude causes the phase shift of the resulting function to be almost the same as the larger signal. Because the deviation from the original signal is so small, I will consider the effects θ to be negligible (assume coherent waveforms) for the purpose of the simulation. Only the amplitudes of the signals will differ. The figure shows the shift to be very small. On average these shifts will be small for all frequencies, as long as the misregistered pixels share a high degree of their sources. One could simulate the phase offset with a Gaussian distribution centered around 0 and with a standard deviation in the order of 2% of 2π

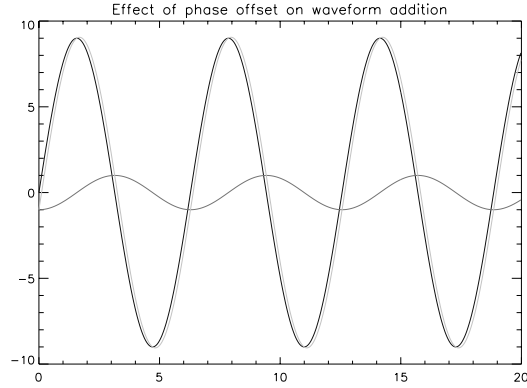


Figure B.2: Effect of phase shift on addition of waveforms

B.2 Polychromatic Case

Detected intensity is proportional to the squared intensity of a waveform, therefore:

$$\sqrt{S_1(\sigma)} \propto A_1(\sigma) \quad (\text{B.8})$$

Where $S_1(\sigma)$ represents a spectrum. Using Eq. B.8 and Eq. B.7 and integrating over all wavenumbers yields the interferogram equation for the general polychromatic case:

$$I(\delta) = \int_0^{+\infty} \frac{S_1(\sigma)}{2} + \frac{S_2(\sigma)}{2} + \sqrt{S_1(\sigma)}\sqrt{S_2(\sigma)} \cos(2\pi\sigma\delta + \theta(t)(\sigma)) d\sigma \quad (\text{B.9})$$

where S_1 and S_2 are the spectra for each misaligned waveform.

To get the equation for the Sagnac or Michelson case, simply replace δ with their respective OPD formula.

B.3 Conclusion

I performed a rapid simulation of two sources that are slightly misregistered. I set the random phase offset to 0 for this simulation (I am currently not planning to simulate a random phase offset). Figure B.3 shows the interferogram, the 2 inputs and the output. The 1st input is the lower curve, the 2nd input is the higher curve and the output is the middle curve.

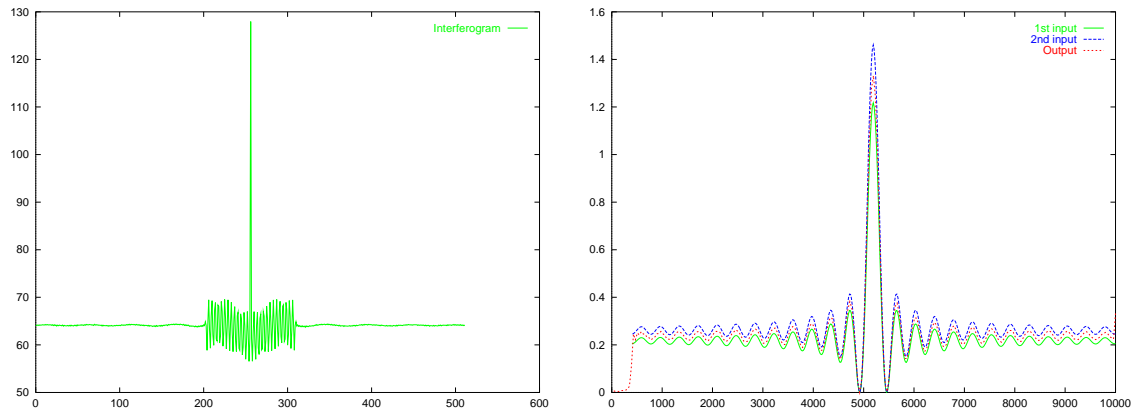


Figure B.3: Interferogram and spectrum obtained from misregistered pixels.

Appendix C

Validation of the Integration of FASCODE in the Atmospheric Database Generator

C.1 Introduction

The resolution of sensors modeled with *DIRSIG* had been larger than 2.0 cm^{-1} . The modeling of FTS reduces this maximum resolution. This improved resolution required some modifications to the atmospheric database generation program (*make_adb*). Prior to this modification, *make_adb* relied entirely on *MODTRAN* to model the transmission, scattering, and emission of the atmosphere along the various propagation paths. Although *MODTRAN* can interpolate to resolutions smaller than 2.0 cm^{-1} , this interpolation does not introduce fine spectral features (absorption and emission lines) available in *FASCODE*. However, *FASCODE* cannot create features due to the sun or moon and requires long computation times. Therefore only the sensor path transmission and path thermal emission data are generated with *FASCODE*. The remainder are collected with *MODTRAN*, whose results are linearly interpolated to the required resolution. Note that the limiting resolution of *MODTRAN* is 2.0 cm^{-1} (*MODTRAN* mode) or 5.0 cm^{-1} (*LOWTRAN* mode). Furthermore, to avoid introducing errors due to the lack of exoatmospheric sources, *FASCODE* is used only for frequencies less than 3500.0 cm^{-1} (wavelengths greater than 3.0 microns). Above the 3500.0 cm^{-1} range, the

exoatmospheric sources must be considered. Another reason for not using *FASCODE* for higher frequencies the resolution of 2.0 cm^{-1} is equivalent to a change in λ of $1.8 \cdot 10^{-3} \mu\text{m}$. No need is envisioned for simulating images with such fine resolution in the VIS/NIR region.

The purpose of this appendix is to show the validation and results of *make_adb* with *FASCODE*. This validation is meant only as a visual inspection to ensure the proper performance of the modified program and to ensure adequate agreement between *FASCODE* and *MODTRAN* up to the 3500.0 cm^{-1} cut-off frequency for *FASCODE* calculations.

For this validation, two different *make_adb* runs were processed at resolutions of 0.5 cm^{-1} over $2500 \text{ cm}^{-1} \leq \sigma \leq 4000 \text{ cm}^{-1}$. During the sensor-path calculation for a given zenith angle, the *MODTRAN* and *FASCODE* input data (*tape5*) were collected. These were used in *MODTRAN* and *FASCODE* independently. The results were then compared to the *make_adb* results. Please note that even though *FASCODE* was run, its results were identical to the *make_adb* results over the calculation range, thus demonstrating proper operation. Further comparisons between *FASCODE* results and *make_adb* were deemed unnecessary.

C.2 MODTRAN *tape5* values

The data in the *MODTRAN tape5* (Acharya, et al., 1998) used for this validation were.

Tape5 for first *make_adb* run (*mls.tp5*):

```
f 2 2 2 1 0 0 0 0 0 0 1 1 1 0.000 0.00
f 0f 0 330.00000 f f f 0.000
0 0 0 1 0 0 0.000 0.000 0.000 0.000 0.218
2.218 0.218 182.800 0.000 0.000 0.000 0
1 2 176 0
43.000 78.000 0.000 0.000 17.500 270.000 0.000 0.000
2500.000 4000.000 5.000 5.000 wtaa
0
```

Tape5 for second *make_adb* run (*test.tp5*):

```
t 2 2 2 0 0 0 0 0 0 0 1 1 0 0.000 0.00
f 0f 0 330.00000 1.00000 1.00000 f f f 0.000
1 0 0 0 0 0 4.000 0.000 0.000 0.000 0.218
2.218 0.218 205.200 0.000 0.000 0.000 0
1 2 176 0
43.000 78.000 0.000 0.000 17.500 270.000 0.000 0.000
2500.000 4000.000 2.000 2.000rn wtaa
0
```

The differences between these *tape5* are listed below. The impact of these differences on the validation is also included. In *MODTRAN*, each input line is known as a *CARD* (Acharya, et al., 1998). For the first line (*CARD1*), the differences are:

1. Flag MODTRN, set to 't' vs. 'f'. This causes the second run to use the 2.0 cm^{-1} *MODTRAN* band model versus the 5.0 cm^{-1} *LOWTRAN* band model. This could be the source of some differences between the results obtained with each run. For all runs, *FASCODE* was using a resolution of 0.5 cm^{-1} , so this difference does not apply for *FASCODE*.
2. Flag IMULT, set to 0 vs. 1. In the first run, *MODTRAN* runs with multiple scattering, while the second run is limited to single scattering. The corresponding *FASCODE* runs were both limited to single scattering (default).
3. Flag NOPRNT, set to 0 vs. 1. This flag produces no changes in the results found in output file *tape7.scn*.

For the second line of the *tape5* (*CARD1A*), the differences were:

1. Flags H2OSTR and O3STR are set to 1.0 vs. blank. Since these flags are scaling factors, scaling by 1.0 is the same as using the default value, which is what a blank entry is designed to do. So, these differences have no effect of the final results.

The third line of the *tape5* (*CARD2*) has the following differences:

1. Flag IHAZE, set to 1 vs. 0. This changes the aerosol or cloud attenuation from RURAL extinction with default visibility at 23 km to no attenuation at all. *FASCODE* input files have the same flag, which is set accordingly prior to the execution of the program.
2. Flag ICSTL, set to 0 vs. 1. Since the Navy maritime model was not used in either case, this difference in flags will have no impact on the results.
3. Flag VIS, set to 4.0 vs. 0.0. This causes the visibility for the second run to be set to 4.0 km instead of the default of 23 km. This has no effect on the first run. Since *FASCODE* shares these flags with *MODTRAN*, the same effects occurred in the corresponding *FASCODE* runs.

Only the ANGLE value was changed on the fourth line (*CARD3*):

1. The value of ANGLE was changed from 182.8 to 205.2. This angle is the zenith angle for the path of the radiation for the simulation. This value is also reproduced in the *FASCODE* input files, so similar results are expected from the *FASCODE* and *MODTRAN* executions.

The other changes are in line 7 (*CARD4*). They are:

1. Flags DV and FWHM are set to 2.0 cm^{-1} instead of 5.0 cm^{-1} . This difference is a direct result of using the *LOWTRAN* band model instead of using the *MODTRAN* band model. Once again, *FASCODE* is not limited to those resolution and the value of 0.5 cm^{-1} was used for those simulations.
2. Flags YFLAG and XFLAG set to "rn" vs. blank. These flags affect only the *pltout* files, and therefore have no impact on this validation.

The only flag that could affect the *FASCODE* execution and that is not included in the *FASCODE* input files is the “multiple scattering” flag (*IMULT*, *CARD1*). Two *MODTRAN* runs that differ only in the setting of this flag were executed. The results were compared to a *FASCODE* run with equivalent parameters. As it happens the results of both *MODTRAN* runs were identical. The multiple scattering effect can be considered negligible in the thermal region.

Another comparison was performed with different *MODTRAN* flag values (‘t’ and ‘f’), which led to different results. The *LOWTRAN* band model caused the results to differ from the *FASCODE* results more than if the *MODTRAN* band model is used. Figures C.1 and C.2 show this comparison. Note that the program used to down sample the *FASCODE* output was very crude and that a better agreement between the *FASCODE* output and the *MODTRAN* band model output could be achieved.

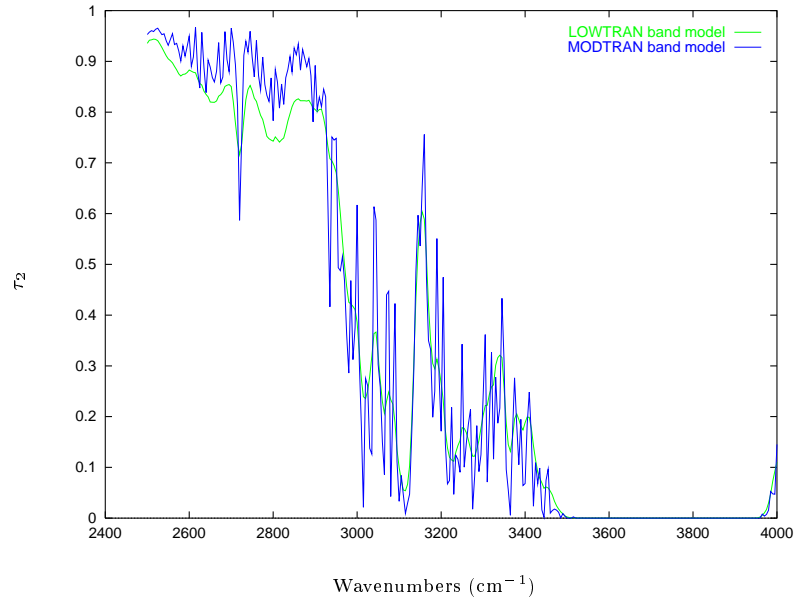


Figure C.1: Comparison between the *LOWTRAN* band model and the *MODTRAN* band model for an otherwise identical *MODTRAN* run.

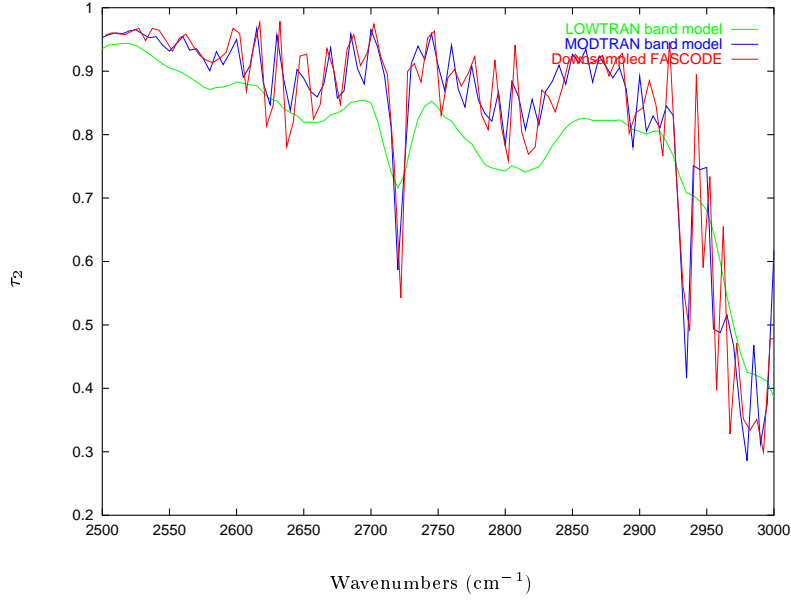


Figure C.2: A down sampled *FASCODE* run is in better agreement with the *MODTRAN* band model than the *LOWTRAN* band model.

C.3 Graphic input file name definitions

The validation graphs were plotted from different data files. Table C.1 explains the origin of each file. The legend of each plot explains the simulation output file that was used. Two different simulations were run. The *tape5* used as inputs to the configuration file also are listed in the table. Each triggered a different mode of operation for *MODTRAN* which also is responsible for some of the differences between *MODTRAN* and *FASCODE*.

Legend	Definition
<i>make_adb</i> With <i>MODTRAN</i> running under <i>LOWTRAN</i> mode (<i>tape5: mls.tp5</i>)	
LOWTRAN band model	<i>MODTRAN</i> output (at 5.0 cm^{-1})
FASCODE (<i>make_adb</i>)	<i>make_adb</i> results at zenith 182.8
Downsampled FASCODE	5.0 cm^{-1} down sampled version of the <i>make_adb</i> results
<i>make_adb</i> With <i>MODTRAN</i> running under <i>MODTRAN</i> mode (<i>tape5: test.tp5</i>)	
MODTRAN band model	<i>MODTRAN</i> output (at 2.0 cm^{-1})
FASCODE (<i>make_adb</i>)	<i>make_adb</i> results at zenith 205.2
Downsampled FASCODE	2.0 cm^{-1} down sampled version of the <i>make_adb</i> results

Table C.1: Graph input data file origins

C.4 TAU2 Comparison

The changes in path transmission between a *MODTRAN* output and the *make_adb* database were tested (Figure C.3 — Figure C.9). Note the departure from the transmission calculated by *MODTRAN* (*LOWTRAN* band model) to the down sampled version of *make_adb* in Figures C.3 and C.6. This effect is lessened for the simulations that use the *MODTRAN* band model.

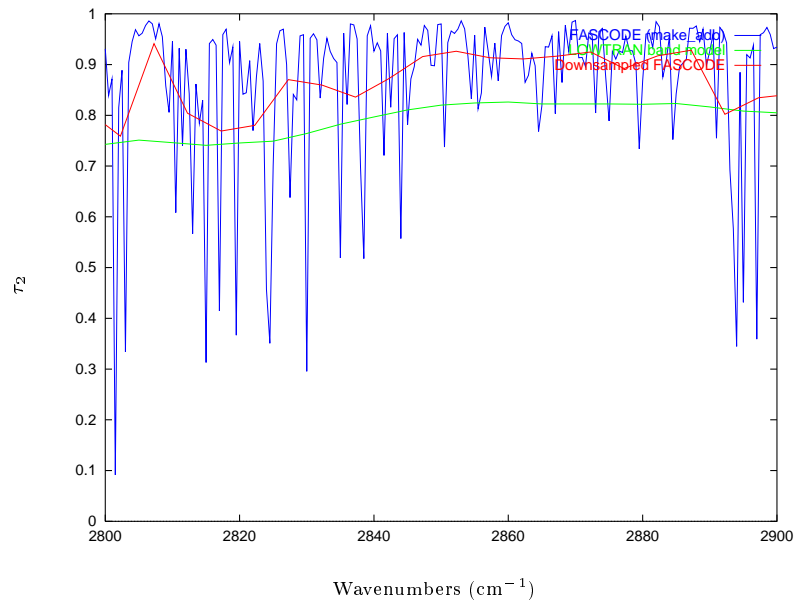


Figure C.3: TAU2 — Comparison between *make_adb* database and *MODTRAN* output for the 2800 to 2900 cm^{-1} range, with down sampled version of the *make_adb* database, to better show the continuum. Note that the continuum for *MODTRAN* is lower than for *FASCODE*. The *LOWTRAN* band model was used in this case.

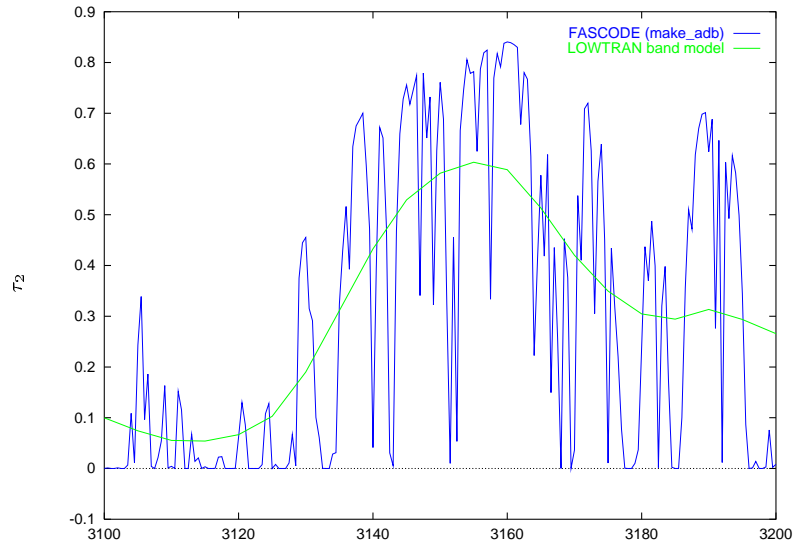


Figure C.4: TAU2 — Comparison between *make_adb* database and *MODTRAN* output for 3100 to 3200 cm^{-1} range. The *LOWTRAN* band model was used in this case.

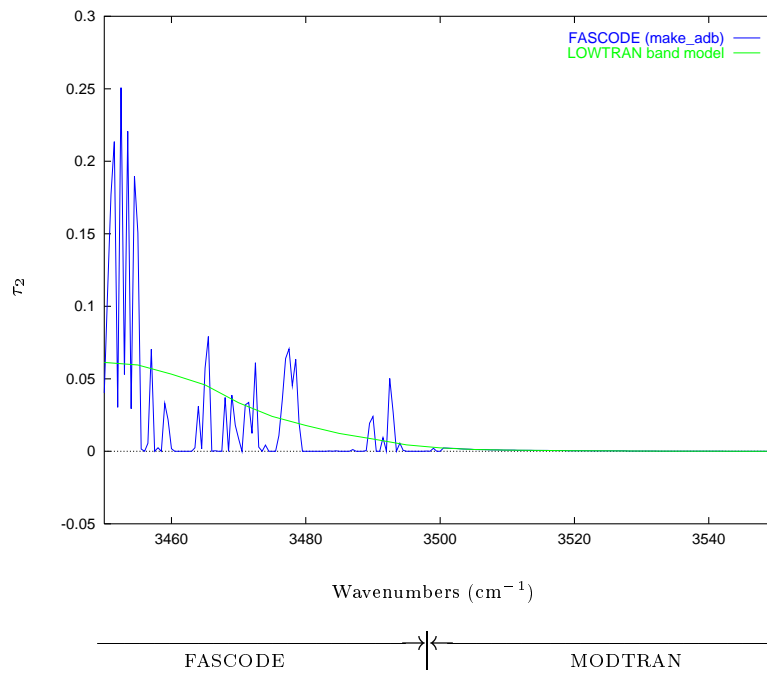


Figure C.5: TAU2 — Comparison between *make_adb* database and *MODTRAN* output for the 3450 to 3550 cm^{-1} range. Remember that *FASCODE* is only used up to 3500 cm^{-1} . The *MODTRAN* output is used past that range. The *LOWTRAN* band model was used in this case.

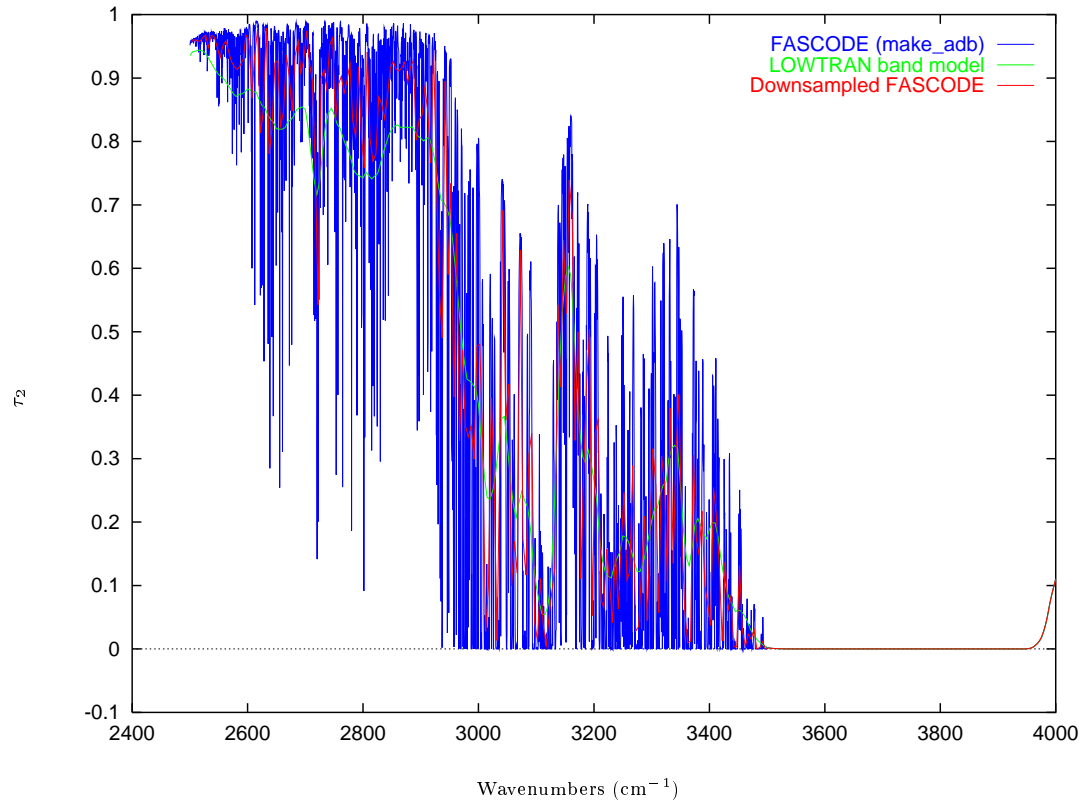


Figure C.6: TAU2 — Comparison between *make_adb* database and *MODTRAN* output for the entire simulation range, with down sampled version of the *make_adb* database, for easier comparisons with *MODTRAN*. The *LOWTRAN* band model was used in this case.

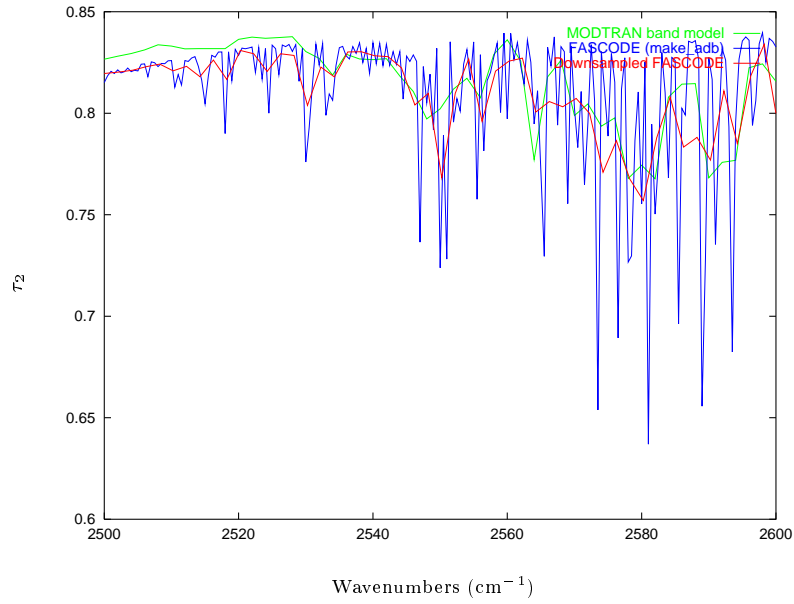


Figure C.7: TAU2 — Comparison between *make_adb* database and *MODTRAN* output for the 2500 to 2600 cm^{-1} range. The *MODTRAN* band model was used for this simulation.

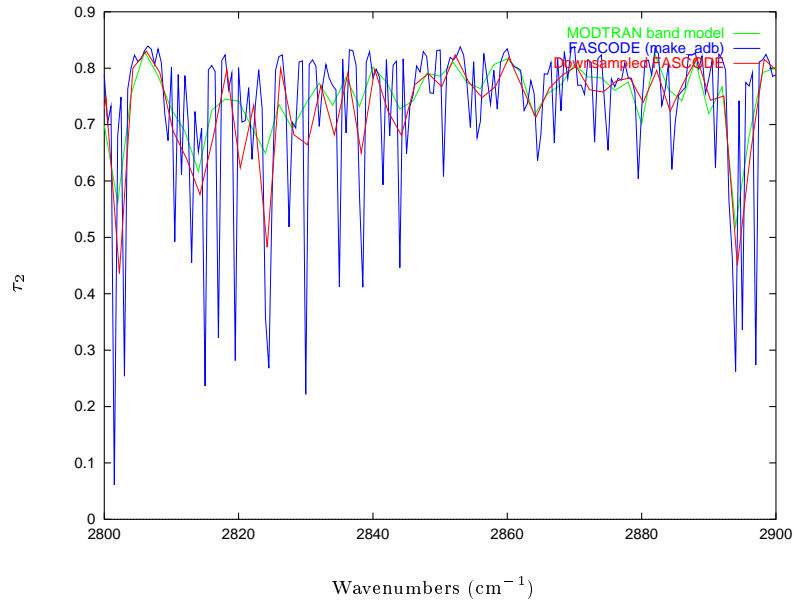


Figure C.8: TAU2 — Comparison between *make_adb* database and *MODTRAN* output for the 2800 to 2900 cm^{-1} range. The *MODTRAN* band model was used for this simulation.

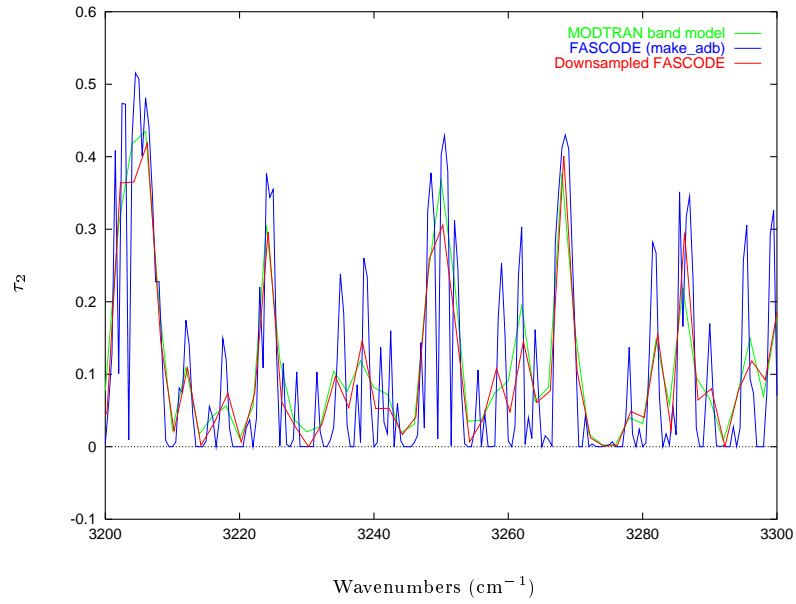


Figure C.9: TAU2 — Comparison between *make_adb* database and *MODTRAN* output for the 3200 to 3300 cm^{-1} range. The *MODTRAN* band model was used for this simulation.

C.5 PATH Thermal Comparison

The changes in path thermal radiance between a *MODTRAN* output and the *make_adb* database are shown in Figures C.10 to C.16. Note the departure from the path thermal results calculated by *MODTRAN* (*LOWTRAN* band model) to the down-sampled version of *make_adb* in Figures C.10 and C.13.

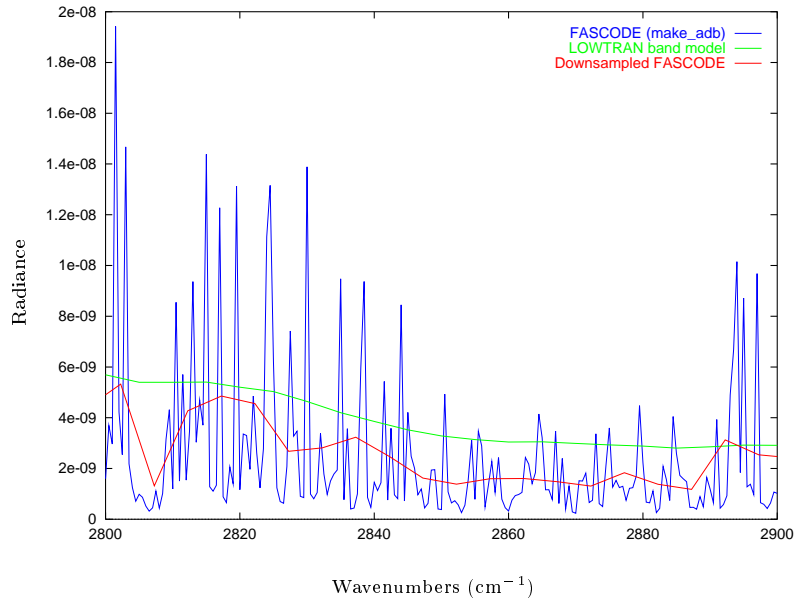


Figure C.10: PTH — Comparison between *make_adb* database and *MODTRAN* output for the 2800 to 2900 cm^{-1} range, with down sampled version of the *make_adb* database. Note once more the difference in continua. The *LOWTRAN* band model was used in this case.

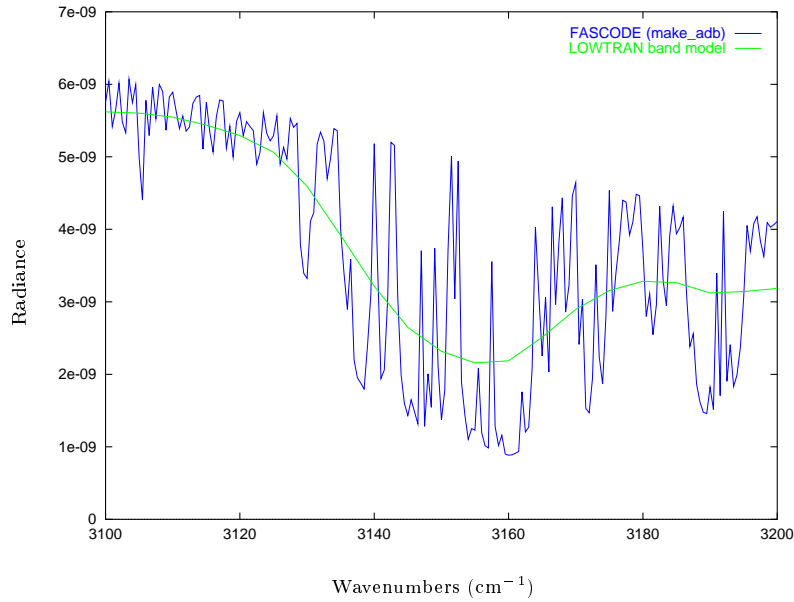


Figure C.11: PTH — Comparison between *make_adb* database and *MODTRAN* output for the 3100 to 3200 cm^{-1} range. The *LOWTRAN* band model was used in this case.

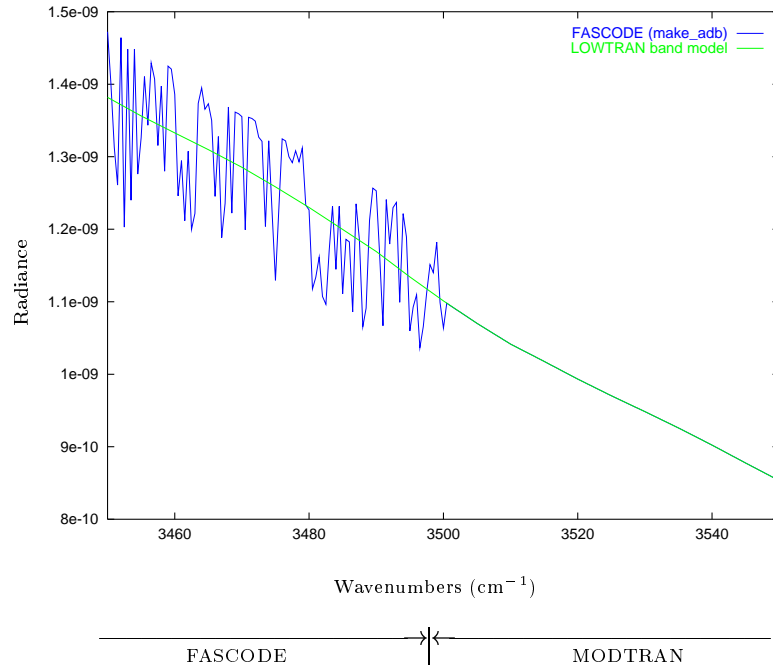


Figure C.12: PTH — Comparison between *make_adb* database and *MODTRAN* output for the 3450 to 3550 cm^{-1} range. Remember that *FASCODE* is only used up to 3500 cm^{-1} . The *MODTRAN* output is used past that range. The *LOWTRAN* band model was used in this case.

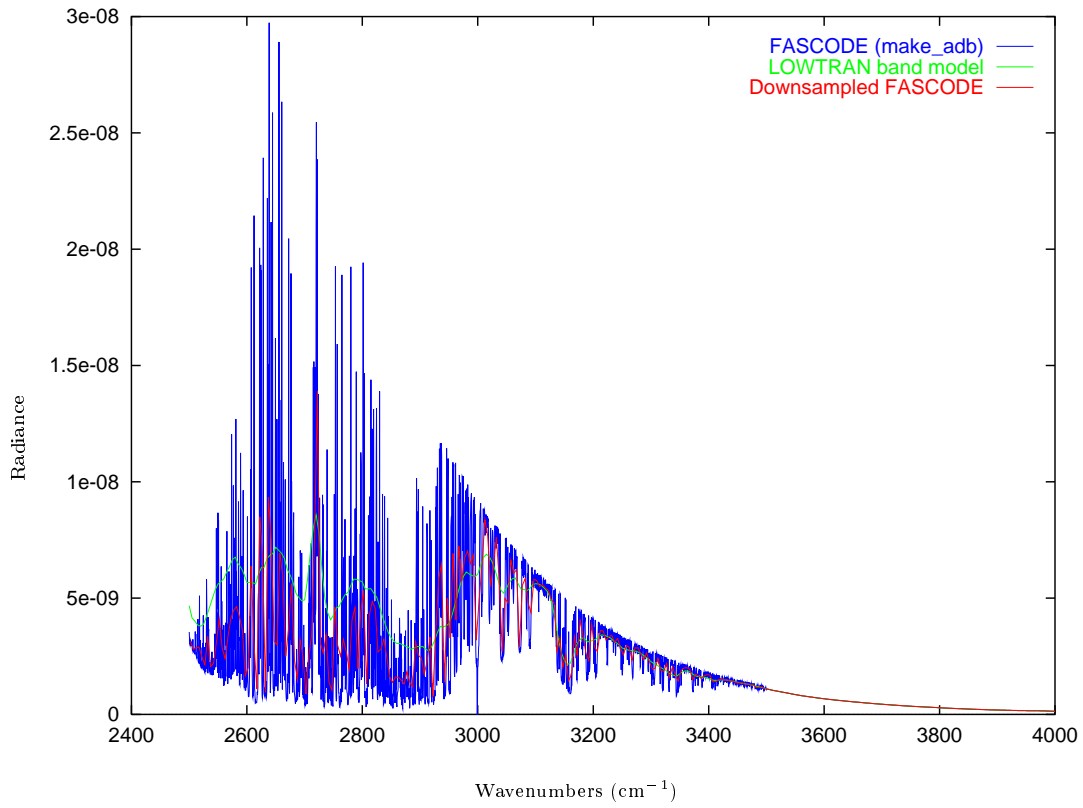


Figure C.13: PTH — Comparison between *make_adb* database and *MODTRAN* output for the entire simulation range, with down sampled version of the *make_adb* database. The *LOWTRAN* band model was used in this case.

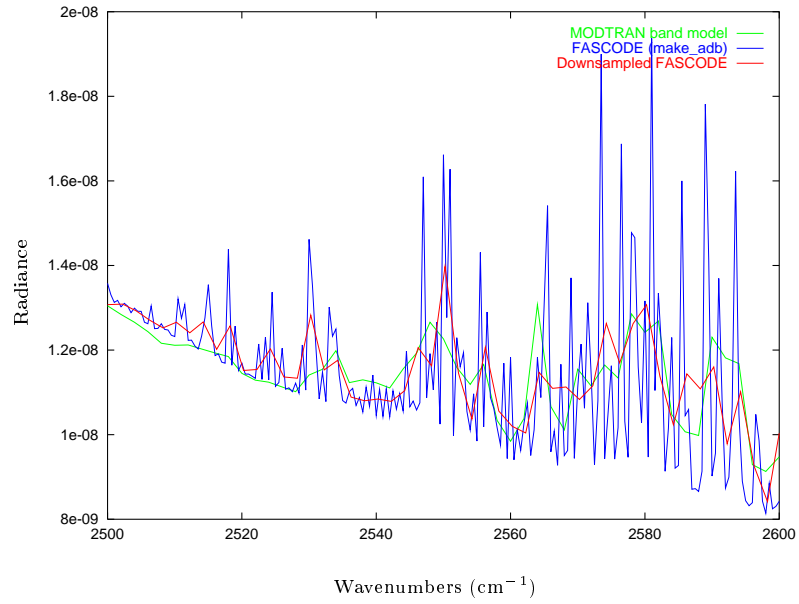


Figure C.14: PTH — Comparison between *make_adb* database and *MODTRAN* output for the 2500 to 2600 cm^{-1} range. The *MODTRAN* band model was used for this simulation.

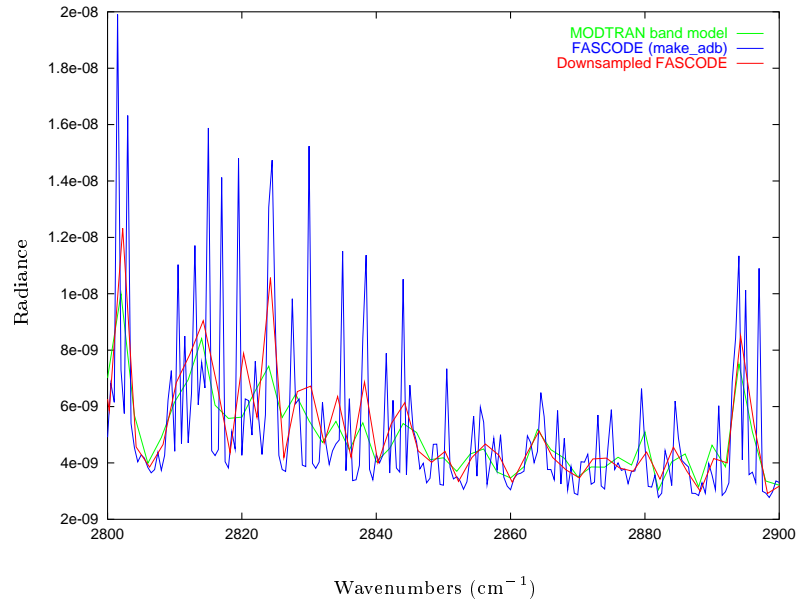


Figure C.15: PTH — Comparison between *make_adb* database and *MODTRAN* output for the 2800 to 2900 cm^{-1} range. The *MODTRAN* band model was used for this simulation.

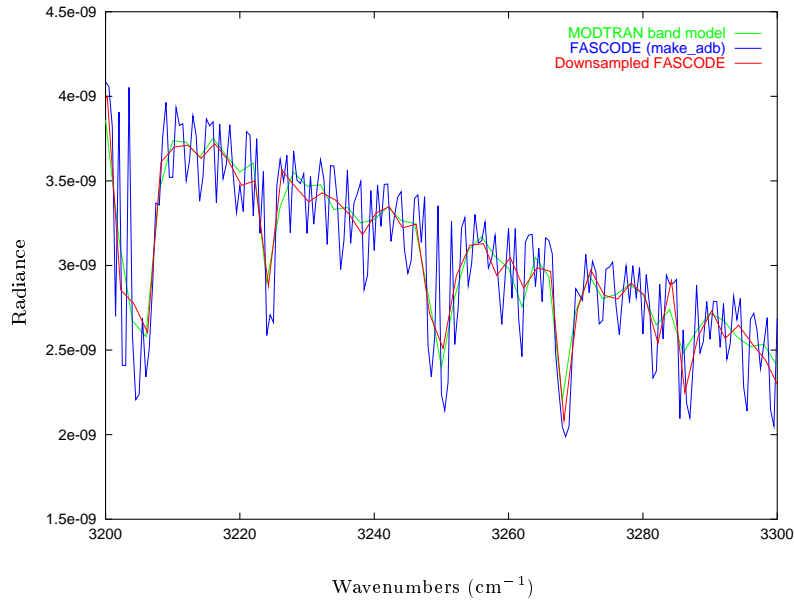


Figure C.16: PTH — Comparison between *make_adb* database and *MODTRAN* output for the 3200 to 3300 cm^{-1} range. The *MODTRAN* band model was used for this simulation.

C.6 Conclusion

From the plots, it is evident that the agreement between *FASCODE* and *MODTRAN* is much better when the *MODTRAN* band model is used instead of the *LOWTRAN* band model. Also, one of the *tape5* was set to run with the multiple scattering mode enabled. Although comparison showed the results to be identical, this might not be true for every *MODTRAN* run and care should be taken when using this mode because the results from *MODTRAN* and from *FASCODE* may differ.

Note that this validation shows only that *make_adb* works for the *tape5* used in this validation. More test with different *tape5* are required to improve this validation effort.

While the plots show that there is a slight difference for lower frequencies between the *FASCODE* calculated data and the *MODTRAN* calculated data, better agreement is reached with the use of the *MODTRAN* mode (vs. *LOWTRAN* mode). Under those conditions, *make_adb* can be used with confidence.

Appendix D

Source Code

This chapter explains where to find the source code for the simulation programs. The source code is not listed here because of the large size of these programs. The help files are listed here. The files described in this document can be accessed on the archival CD-ROM. See the *README* file in the base directory to locate the file.

D.1 Modifications to *make_adb*

To integrate *FASCODE* in *make_adb*, the main *make_adb* file (*make_adb.nw*) was modified. A new file was created that contained all *FASCODE*-related functions (*fascode.nw*). Both files are written to be used with the “noweb” pre-processing tool, which enables a developer to incorporate both code and documentation in a single file. Different calls to “noweb” yield a file (in C/C++ or other language) or a \LaTeX document.

D.1.1 Changes to *make_adb.nw*

The file listing was generated by the Unix “diff” utility, which displays the differences of two files. Comments have been added to in the first five lines of the text to show what the output represents. My comments can be found after the >>>> characters. The rest of the file has not been modified. A “+” in the margin of a line of code means that this line of code was added. A “!” means that changes were made to an existing line of code. Lines of code with no identification signs in the margin are context lines, unmodified from the original version.

See the *README* file in the archival CD-ROM to locate file *make_adb.diff*. File *make_adb.nw* can also be found on the CD-ROM.

D.1.2 New *fascode.nw* File

This file was created to contain the data types and *FASCODE* interface functions to *make_adb*. The file can be found on the archival CD-ROM.

D.2 FTS sensor module

This module contains all code necessary to simulate IFTS. A stand-alone routine that initializes the sensor and input spectrum and calls the right routines is all that is required to use this module. In this case, DIRSIG performs that work, but a stand-alone routine is also available that does a similar job. Note that libraries from DIRSIG and “Numerical Recipes” are also required to compile this module.

The first file is the header file: *FTS_Functions.h*. The body of the FTS sensor module is file *FTS_Functions.C*. The stand-alone program is file *FTS_main.C*. All files are archived on the CD-ROM.

D.3 Changes to the main DIRSIG file

The main DIRSIG file was modified to include calls to the FTS routines. To distinguish the modified file from the original, it was renamed *new_dirsig.C*. The original file *dirsig.C* is also on the CD-ROM. To see what modifications were done to the file the Unix “diff” utility can be used with the command “diff <filepath>/new_dirsig.C <filepath>/dirsig.C”.

D.4 IDL IFTS parameter generation widget

This program is an IDL widget used to generate the sensor initialization files. The help files also provide a provisional user’s guide for the FTS sensor module.

D.4.1 IDL widget

The main file for the widget is *Set_FTS_Sim_Parameters.pro*. Additional files are required to properly execute the widget. They are: *profile.pro*, *noise.pro*, *gain.pro*, and *options.pro*. All files can be found on the archival CD-ROM.

D.4.2 Help files

Help assist novice users understand the operation of the FTS sensor simulation. If the user utilizes the IDL widget, the “.help” files should be read. They can be accessed from the help button on the menu. If the user wants to modify or create the FTS sensor configuration file manually, file *sensor_para_desc.txt* should be read. The help files are included in this document to serve as a user’s guide for the simulation tools. They also are located on the archival CD-ROM.

Description of the FTS sensor configuration file, *sensor_para_desc.txt*:

This file describes the format of the sensor parameter file as created by the IDL program *Set_FTS_Sim_Parameters.pro*. This file can be used as a guideline for creating or modifying a FTS sensor configuration file manually. Note that even though some of these parameters are found in the main DIRSIG configuration file, they are replicated here in order for the program to perform correctly when operating in the stand-alone mode (*FTS_main*).

The values of the parameters are set in the following way:

<TAG> = value

If a tag is not used, the program will use the default value. This file must be terminated with a }. There can only be one parameter assignment per line. i.e. each assignment must be on a single line. If a tag is used, but does not have a value assigned to it, the default value is used.

FTS_TYPE (Required)

values: MICHELSON, SAGNAC

FTS_SCAN_SIZE (Required)

Number of points in the interferogram (integer)

Must be a power of 2

FTS_SCAN_TIME (Required for Michelson)

(This is the inverse of the SCAN_RATE value found in the DIRSIG configuration file.)

Integration time (in seconds) of the sensor FPA (float)

FTS_NB_INPUT (Required)

(This corresponds to the number of input lines in the flight profile or the NUMBER_OF_SCANS tag in the DIRSIG configuration file.)

Number of input spectra (integer)
 For Michelson, any value from 1 to ...
 Interpolation will be done for values smaller than (line 2)
 Blurring of the interferogram will be done for values larger than (line 2)
 For Sagnac, this value is the same as the image length

MICH_SCAN_SPEED (Required for Michelson)
 (Michelson only) scan_speed, speed of the scanning mirror
 (in cm/sec) (float)

SAGN_FO_FL (Required for Sagnac)
 fo_fl: Fourier optic focal length (in cm)

SAGN_PIX_SEP (Required for Sagnac)
 inter_pix_sep: distance between two neighbor FPA pixels (in cm)

SAGN_VO_SEP (Required for Sagnac)
 virtual_obj_sep: aparent distance beween virtual objects ($\sqrt{2}$ *a)
 where a is the mirror shift from zero split position (in cm)

FTS_INT_OVERSAMPLE (Defaults to 1, not required)
 Interferogram_oversampling: 1; no oversampling,
 other; oversampling value

FTS_APODIZE (Defaults to FALSE, not required)
 Apodization indication: FALSE = none, TRUE = triangular apodization

FTS_WITH_ALIGN_ERROR (Currently can only be used on the stand-alone test program.
 Defaults to FALSE. If set, FTS_ALIGN_SD,
 FTS_MIN_MIRROR_DIST, and FTS_COHERENCE_SD must
 also be set.)
 Alignment indication: FALSE = none, TRUE = use the values of
 Alignment_std_dev, Min_FPA-mirror_dist and Coherence_std_dev

FTS_ALIGN_SD (Required if FTS_WITH_ALIGN_ERROR = TRUE, no default)
 Alignment_std_dev: standard deviation of the pixel alignment (in rad)

FTS_MIN_MIRROR_DIST (Required if FTS_WITH_ALIGN_ERROR = TRUE, no default)
 Min_FPA-mirror_dist: Minimum optical path distance between
 scanning mirror and focal plane array (in mm)

FTS_COHERENCE_SD (Required if FTS_WITH_ALIGN_ERROR = TRUE, no default)
 Coherence_std_dev: standard deviation of the coherence
 at 1 registration std dev (in rad)

FTS_QUANTIZE (Defaults to 0, not required. The dynamic range (FTS_DR) should be set if this tag is used. The default value might not be appropriate.)
 Quantization: number of quantization bits (0 means no quantization)

FTS_DR (Defaults to 1.0, not required but should be set if quantization is used.)
 NOTE: SETTING THIS PARAMETER TO TOO SMALL A VALUE IS A COMMON SOURCE OF ERRORS IN SIMULATIONS. ANY SPECTRA WITH AN UNEXPECTEDLY SMOOTH SHAPE (BADLY CLIPPED INTERFEROGRAMS) OR EVEN ZERO VALUED IMAGES (CONSTANT VALUED INTERFEROGRAMS) CAN BE CAUSED BY A WRONG DYNAMIC RANGE. THIS PROBLEM WAS THE CAUSE OF A FEW DAYS LOST TRYING TO FIND ERRORS IN THE CODE, SO WATCH OUT FOR IT.
 Dynamic_range: dynamic range of the detector as a maximum interferogram value. eg: FTS_DR = 1.0E-6
 All interferogram values above 1.0E-6 will be clipped to that level.

FTS_WITH_NOISE (Defaults to no noise, not required)
 Tag that marks the start of the noise database. The database ends with the } character, which must be the first non-blank character on a line.
 eg: FTS_WITH_NOISE = {
 256 256 0.0 1.0e-7
 3 32 3.2e-9 1.52e-7
 }

FTS_WITH_GAIN (Defaults to no gain and bias, not required)
 Tag that marks the start of the gain and bias database. The database ends with the } character, which must be the first non-blank character on a line.
 eg: FTS_WITH_GAIN = {
 256 256 1.0 0.0
 3 32 0.923 4.73e-3
 }

FTS_WITH_OPD_ERROR (Defaults to FALSE, not required. If set, FTS_OPD_ERROR_SCALE must also be set.)
 OPD_error: toggle switch to simulate error in sampling distance.
 TRUE: use it, FALSE; don't

FTS_OPD_ERROR_SCALE (Required if FTS_WITH_OPD_ERROR = TRUE. Defaults to 0.0)
 OPD_error_scale: scaling factor for the random variation in sampling distance

FTS_WITH_OFF_AXIS_ERROR (Defaults to FALSE. Not required. If set, FTS_ROW_SIZE, FTS_COL_SIZE, FTS_IMAGE_LENGTH, FTS_IMAGE_WIDTH, and FTS_CL_FL must also be set. Michelson interferometer only.)
 off_axis_error: toggle switch that enables the simulation of off-axis spectral shift. TRUE: use it, FALSE; don't

FTS_ROW_SIZE (Required if FTS_WITH_OFF_AXIS_ERROR = TRUE. No default)
(Corresponds to the LINE_SPACING tag in the DIRSIG
configuration file times the number of pixels (FTS_IMAGE_LENGTH)
times a unit conversion factor (microns to mm).)
FPA_row_size: size of the Focal Plane Array in the row dimension (AT), in mm.

FTS_COL_SIZE (Required if FTS_WITH_OFF_AXIS_ERROR = TRUE. No default)
(Corresponds to the PIXEL_SPACING tag in the DIRSIG
configuration file times the number of pixels (FTS_IMAGE_WIDTH)
times a unit conversion factor (microns to mm).)
FPA_col_size: size of the Focal Plane Array in the column dimension (CT),
in mm.

FTS_IMAGE_LENGTH (Required if FTS_WITH_OFF_AXIS_ERROR = TRUE. No default)
(Corresponds to the LINES_PER_SCAN tag in the DIRSIG
configuration file for a Michelson FTS or to FTS_NB_INPUT
in this file for a Sagnac.)
Image length: For Michelson, nb of along track elements on FPA
For Sagnac, nb of lines scanned on the ground.

FTS_IMAGE_WIDTH (Required if FTS_WITH_OFF_AXIS_ERROR = TRUE. No default)
(Corresponds to the PIXELS_PER_LINE tag in the DIRSIG
configuration file.)
Image width: nb of across track pixels on the FPA

FTS_CL_FL (Required if FTS_WITH_OFF_AXIS_ERROR = TRUE. No default)
Condensing_lens_focal: Focal length of the Michelson interferometer
condensing lens in mm.

USE_RAW_SPECTRUM (Defaults to FALSE. Not required)
Toggle switch: TRUE -> The spectrum saved in the image will be the
spectrum as calculated by the Interferogram2Spectrum
routine of the FTS object.
FALSE -> The spectrum is interpolated to the min, max and delta
frequencies defined by the input spectrum.

SAVE_PROBE (Defaults to FALSE. Not required)
Toggle switch: TRUE -> Saves probe file(s) named scan_row_col.probe
every time a new facet is hit.
FALSE -> does not save the probe file(s)

SAVE_INTERFEROGRAM (Defaults to FALSE. Not required)
Toggle switch: TRUE -> Saves an interferogram image cube.
FALSE -> Does not save the interferogram image cube.

IDL widget help files, *Set_FTS_Sim_Para.help*:

Help file for the simulation parameter gathering tool.

File...

Open... : Open an existing FTS sensor description file.
Save: Save the current parameters to the active file. Does not save if no changes were made since last save.
Save As...: Change the name of the active file and saves the data.

Options... : Select whether you want some of the information to be calculated automatically or be entered manually.

Exit: Quit this program. Prompts for saving if changes were made since last save.

Help...: Display this help file.

Output file name: Name of the current active data file.

Number of interferogram points: Number of points that the interferogram calculating routine will return per interferogram.

Resolution [cm-1]: Spectral resolution of the calculated output spectrum for the given sensor parameters. This value is calculated automatically and not saved to file. It is just informational. For the Michelson, it depends on the integration time, mirror speed, max frequency and # points. For the Sagnac, it depends on the focal length, inter pixel separation, virtual object separation, max frequency, and # points. Changing any of them will change the value of the resolution (or of another parameter). The resolution also represents the maximum input delta frequency. If the input delta frequency is larger than that, the input spectrum will be interpolated in order to avoid having peaks showing in the output spectrum. i.e., each input spectra sample would look like a delta function to the interferometer, instead of looking like a continuous function. The problem is that input spectrum interpolation takes a lot of computer run-time. Because modtran only displays the frequency of the calculated values with 1 decimal point accuracy, the resolution has to be limited to that accuracy. Below a resolution of 2.0 cm-1, FASCODE kicks in, so this limit does not apply any more. (Modtran's output gets interpolated.) This feature affects the max frequency, which is calculated such that it is as close to the selected frequency while providing a correct resolution.

Integration time [sec]: Detector integration time for a single pixel.

Number of input spectra (ratio): The number of input spectra that will be used to calculate each interferogram. The values are 1, any (power of 2 + 1) greater than 1 but less than the number of interferogram points, the number of interferogram points, and an odd multiple of the number of interferogram points (3, 5, 7). These allow to simulate the sensor change in view angle. If the value is 1, the interferogram is completely calculated from this single input spectrum. For a value between 1 and # points, the spectrum needs to be interpolated for each interferogram point. For a value of # points, one interferogram point is calculated from one spectrum.

For a value greater than # points, the interferogram is calculated at a higher resolution, and is then downsampled to a resolution corresponding to # points. This value correspond to the number of entries in the flight profile file.

Simulation min/max frequency: Gives the maximum unaliased frequency (or minimum wavelength). When the mirror speed or virtual object separation are calculated automatically, changing the frequency will adjust the resolution. If the mirror speed or virtual object separation are not calculated automatically, the max frequency will be unselectable, but it will be updated after a change to any parameter. The max frequency might not be exactly the selected frequency. This feature is present because of the limitation on the resolution's decimal precision.

The min frequency (or max wavelength) is used as a limit for the configuration file and the sensor response file. The min and max frequencies are the lower and upper limits of the DIRSIG output.

Image length [pixels] (along-track): Spatial size of the final image in the along-track direction.

Image width [pixels] (across track): Spatial size of the final image in the across-track direction.

FTS type?: Type of FTS sensor to simulate.

Michelson:

Scan Speed [cm/s]: Michelson mirror scanning speed in [cm/s]. This value can be calculated automatically or entered manually. See Options...

Sagnac:

Focal Length [cm]: Focal length of the Sagnac Fourier optic lens.
Inter Pixel Separation [cm]: Distance between the center of two adjacent pixels on the Focal Plane Array (FPA).
Virtual Object Separation [cm]: Aparent distance between the virtual objects formed in a Sagnac interferometer. This value can be calculated automatically or entered manually. See Options...

Oversampling of interferogram?: Select the amount by which the interferogram will be temporally (Michelson) or spatially (Sagnac) oversampled. The oversampling represents the number of samples taken per integration. For the Michelson, it more closely simulates the movement of the scanning mirror during integration. For the Sagnac, it represents the finite size of the detector. The interferogram is then downsampled so that the oversampled values are averaged into one interferogram point. i.e. for 3X oversampling of a Michelson, the interferogram would be collected at time t , $t+1/3 dt$ and $t+2/3 dt$. These interferograms will be added and divided by 3 (averaged). And this will yield the interferogram point for time t . Note that one input

spectrum is used per integration, oversampled or not (this value doesn't affect the number of input spectra).

Spatial oversampling?: Select the amount of spatial oversampling. For a Michelson, spatial oversampling is used to simulate the finite size of the FPA pixels. For a Sagnac, it simulates the finite width of a FPA pixel, and the forward motion of the platform. This is harder to understand and implement for the Sagnac since one FPA dimension is used to record interferogram information and the other dimension is used to record spatial (across-track) information.

Quantization: Select the number of quantization bits to use for the quantization of the interferogram.

Dynamic Range: Indicate which value of the input spectrum energy can be recorded by the FPA without clipping. If the value is below the interferogram value, clipping occurs as the intensity of the signal exceeds the capacity of the detector. If the value is above the interferogram value, the detector has some "room to spare" for collecting photons. This is also used as the range over which quantization will apply. For dynamic range values greater than the interferogram value, some quantization levels will not be used.

Triangular Apodization?: Select if triangular apodization of the interferogram is wanted.

Alignment error?: Selects whether the mirror alignment error artifact will be present or not. The alignment error is like a jitter error added to the registration of the interfering images. If set to yes, the user can then change the values of the alignment and coherence standard deviation. This alignment error is saved to a file (<projectname>.alg). This is required because this misalignment needs to be passed to DIRSIG for the simulation.

Alignment std dev [rad]: I assume the mirror misregistration angle is a Gaussian with zero mean. This slider is the value of the standard deviation. The total misregistration error will be a function of the alignment standard deviation and of the scanning mirror's distance from the FPA. i.e., the farther away the mirror, the more misregistration. The misregistration shift is calculated using a filtered random sequence for the alignment angle to the mirror's normal, a random value for the rotation angle of the normal and the mirror distance.

Min FPA-mirror dist [mm]: This is the distance from the focal plane array to the mirror at the start of the scanning sequence. It is used to calculate the pixel misregistration as a function of mirror travel. This distance includes the focal length of the condensing lens, etc...

Coherence std dev [rad]: If the pixels don't overlap, the interfering waveforms will be slightly incoherent. This standard deviation is the standard

deviation of the coherence phase offset (θ) when the pixels are at one registration std dev. That is because the coherence is linked to the pixel registration. The worse the registration, the worse the coherence. For the purpose of the simulation, the coherence will be linearly linked to the registration std dev. i.e., for a registration std dev of 10% and a coherence std dev of 0.03, the following values will be used for the coherence calculations given the following registration results:

100% pixel overlap -> $\theta = 0$
90% pixel overlap -> std dev $\theta = 0.03$
80% pixel overlap -> std dev $\theta = 0.06$

OPD jitter error?: Turn on the random error in the sampling position. For a Sagnac, this means that the FPA pixels are not located at fixed intervals. For a Michelson, it means the mirror is not moving at constant speed. In both cases, the end result is to have sampling occurring at slightly different intervals.

OPD error scale: Limits the maximum size of the random error in sampling position. It is approximately represented in terms of the fraction of the inter-sampling distance. The value represents about 1 standard deviation of the error. It actually is not that simple because the random value is filtered to remove changes that are too sudden.

Off-axis spectral shift?: Toggle switch that enables the simulation of off-axis spectral shift. When simulating this effect, the simulation finds out the angle of the pixel to the optical-axis, uses that angle to modify the value of the OPD and calculates the interferogram. To recover the right values, the frequencies need to be multiplied with $\sec \theta$.

FPA row size (mm): size of the Focal Plane Array in the row dimension (along track), in mm.

FPA col size (mm): size of the Focal Plane Array in the column dimension (across track), in mm.

Condensing lens f.l. (mm): Focal length of the Michelson interferometer condensing lens.

Flight profile values: Clicking this button calls a widget that lets the user select the flight profile parameters. The button value is <UNSET> when the values have not been selected, and <SET> once the values have been modified.

Create a sensor characteristic file on save?: Specify whether you want a sensor spectral response template file created.

Sensor noise values: Lets the user modify the detector noise characteristics on a per pixel basis. The first value is for the default value, other values can be entered subsequently to modify up to 15 pixel values. If more

values are needed, the user can modify the file by hand.

Sensor gain and bias: Lets the user modify the detector gain and bias characteristics on a per pixel basis. The first value is for the default value, other values can be entered subsequently to modify up to 15 pixel values. If more values are needed, the user can modify the file by hand.

Flight profile help file, *flight_profile.help*:

Help file for the flight profile widget.

NOTE: Because profile is a /modal widget, the "Done with ..." button doesn't work properly. Either close the window or simply proceed with the profile widget. The help file will disappear when the profile widget is destroyed.

Select Speed and Altitude or Orbital Period (for satellites): Specify whether you want the flight profile to be calculated by providing the speed and altitude of the platform or by providing an orbit period.

Orbital period (min): Period of revolution of a satellite. When selected, this value automatically generates the sensor speed and altitude. NOTE: only visible if the corresponding option is selected on the toggle switch above.

Platform jitter?: Toggle switch that allows the user to specify platform pointing accuracy errors. When turned on, this option also enables the jitter standard deviation selection widgets.

Roll std dev [rad]: Standard deviation used to create the platform pointing roll jitter. This value is used to create a random sequence, which will then be filtered with a digital filter to reduce the rapid variation in the sequence.

Pitch std dev [rad]: see roll std dev.

Yaw std dev [rad]: see roll std dev.

Platform speed [km/h]: The platform speed in km/h.

Platform altitude [km]: The platform altitude in km. The altitude is from the scene's zero altitude (generally sea level).

Target x coord (North) [km]: North-South coordinate of the target (rock point). Positive values are North of the origin, negative values are South.

Target y coord (East) [km]: East-West coordinate of the target (rock point). Positive values are East of the origin, negative values are West.

Rock point altitude [km]: altitude at which the sensor is focusing. (You can rock about a cloud, a tall building, etc...)

Platform azimuth [degrees]: Direction towards which the platform is flying. 0 is North, 90 is East.

Platform median pitch [rad]: Pitch angle of the platform. 0 is pointing straight down. Negative values point backward, positive values point forward. For a Michelson, this is the pitch angle that the sensor will have when half of the view angles are collected. This could also be represented as the distance from an "on top" of the rock point. Use the small angle approximation to estimate how far from "on top" the sensor will be at median pitch (angle in rad * (alt-rock point)).

Platform median roll [rad]: Roll angle of the platform. 0 is no roll. A negative value is for roll pointing towards a azimuth-90 degrees direction (West). A positive value points towards a azimuth+90 degrees direction (East). (If the sensor is pointing North.)

Platform median yaw [rad]: Yaw angle of the platform. 0 is no yaw. Positive is clockwise, negative is counter-clockwise.

Noise characteristics collection widget help file, *noise.help*:

Help file for the FTS Focal Plane Array noise characteristics collection routine. When set, this routine will generate a sensor noise characteristics database for use in the simulation. The database is located at the FTS_WITH_NOISE tag in the FTS sensor configuration file. e.g.:

```
FTS_WITH_NOISE = {  
  256 256 0.0 1.0e-5  
  3   2   1.0e-9 1.5e-5  
}
```

Done: Commits the data.

Cancel: exits the widget without committing the data.

Help: Displays this file.

Nb of row pixels (AT): Number of pixels in the along track direction for the focal plane array.

Nb of col pixels (CT): Number of pixels in the cross track direction for the focal plane array.

Default noise mean: Mean of the noise in image units. This is the default for the entire detector.

Default noise variance: Standard deviation of the noise in image units. This is the default for the entire detector.

Add: selecting this button will generate an input form for the specification of the noise characteristics as a single pixel. Up to 15 are possible.

The values are:

Row(AT): row of the pixel

Col(CT): column of the pixel

Mean: mean of the noise in image units for the said pixel.

Var: standard deviation of the noise in image units.

Remove: Removes the last entry.

Gain and bias detector characteristics collection widget help file, *gain.help*:

Help file for the FTS detector gain and bias characteristics collection routine.

When set, this routine will generate sensor gain and bias characteristics

database for use in the simulation. The database is located at the

FTS_WITH_GAIN tag in the FTS sensor configuration file. eg:

```
FTS_WITH_GAIN = {  
  256 256 1.0 0.0  
  3   2  0.95 0.005  
}
```

Done: Commits the data.

Cancel: exits the widget without committing the data.

Help: Displays this file.

Nb of row pixels (AT): Number of pixels in the along track direction for the focal plane array.

Nb of col pixels (CT): Number of pixels in the cross track direction for the focal plane array.

Default gain: This is the default gain for the entire detector.

Default bias: This is the default bias for the entire detector [in detector units].

Add: selecting this button will generate an input form for the specification of the gain and bias characteristics of a single pixel. Up to 15 are possible.

The values are:

Row(AT): row of the pixel

Col(CT): column of the pixel

Gain: gain for the said pixel.

Bias: bias in image units for the pixel.

Remove: Removes the last entry.

D.5 Miscellaneous

Many tools were created for analyzing the results presented in this thesis. The tools are not listed here but can be found on the archival CD-ROM. The tools are located in many sub-directories. The descriptions found in the code should be sufficient to get them working.

Bibliography

- Acharya, P., Berk, A., Bernstein, L., Matthew, M., Adler-Golden, S., Robertson, D., Anderson, G., Chetwynd, J., Kneizys, F., Shettle, E., Abreu, L., Gallery, W., Selby, J., and Clough, S. (1998). Modtran user's manual versions 3.7 and 4.0. Air Force Research Laboratory. Draft.
- Aryamanya-Mugisha, H. and Williams, R. R. (1985). Fourier transform diode array spectrometer for the UV, visible, and near-IR. *Applied Spectroscopy*, 39(4):693–697.
- Author unknown (Date unknown 19XXa). DASI — digital array scanned interferometer. Internet: <http://geo.arc.nasa.gov/ERAST/pathfinder/dasi1.html>.
- Author unknown (Date unknown 19XXb). FASCODE software download. Internet: <http://www.plh.af.mil/VSBM/gpoc/fascode.html>.
- Author unknown (Date unknown 19XXc). The use of DASI in the ERAST/pathfinder science project. Internet. <http://geo.arc.nasa.gov/sge/dasi/dasipat.html>.
- Beer, R. (1992). *Remote Sensing by Fourier Transform Spectrometry*, volume 120 of *Chemical Analysis*. John Wiley & Sons, Inc, New York.
- Bell, R. J. (1972). *Introductory Fourier Transform Spectroscopy*. Academic Press, New York.
- Bennett, C. L. (1997). The effect of jitter on an imaging FTIR spectrometer. In Holst, G. C., editor, *Proceedings of SPIE — Infrared Imaging Systems: Design, Analysis, Modeling, and Testing VIII*, volume 3063, pages 174–183. SPIE — The International Society for Optical Engineering.
- Bennett, C. L., Carter, M., Fields, D., and Hernandez, J. (1993). Imaging Fourier transform spectrometer. In Vane, G., editor, *Proceedings of SPIE — Imaging Spectrometry of the Terrestrial Environment*, volume 1937, pages 191–200. SPIE — The International Society for Optical Engineering.
- Bennett, C. L., Carter, M. R., Fields, D. J., and Lee, F. D. (1995). Infrared hyperspectral imaging results from vapor plume experiments. In Descour, M. R., Mooney, J. M., Perry, D. L., and Illing, L., editors, *Proceedings of SPIE — Imaging Spectrometry*, volume 2480, pages 435–444. SPIE — The International Society for Optical Engineering.
- Blonski, S., Lean, M. H., Jensen, J. L., Crosier, R. B., and Schlein, M. S. (1997). Computational prototyping of the chemical imaging sensor. In Descour, M. R. and Shen, S. S., editors, *Proceedings of SPIE — Imaging Spectrometry III*, volume 3118, pages 330–338. SPIE — The International Society for Optical Engineering.
- Bohlender, D. A. (1994). Users' manual for the CFHT Fourier transform spectrometer. Internet. http://www.cfht.hawaii.edu/manuals/fts/fts_man.html.

- Brown, S. D. (Date unknown 19XX). A brief overview of DIRSIG. Internet. <http://www.cis.rit.edu/research/dirs/dirsig/overview/index.html>.
- Calfas, R. (Date unknown 19XX). MODTRAN software download. Internet. <http://www.plh.af.mil/VSBM/gpoc/modtran.html>.
- Carter, M. R., Bennett, C. L., Fields, D. J., and Lee, F. D. (1995). Livermore imaging Fourier transform infrared spectrometer. In Descour, M. R., Mooney, J. M., Perry, D. L., and Illing, L., editors, *Proceedings of SPIE — Imaging Spectrometry*, volume 2480, pages 380–386. SPIE — The International Society for Optical Engineering.
- Caulfield, H. J. (1979). *Handbook of Optical Holography*. Academic Press, New York. Spectroscopy, chapter 10.9, pp. 587-594.
- Cohen, D. L. (1997). Performance degradation of a michelson interferometer when its misalignment angle is a rapidly varying, random time series. *Applied Optics*, 36(18):4034–4042.
- Cohen, D. L. (1999). Performance degradation of a michelson interferometer due to random sampling errors. *Applied Optics*, 38(1):139–151.
- Cooke, B. J., Smith, B. W., Laubscher, B. E., Villeneuve, P. V., and Briles, S. D. (1999). Analysis and system design framework for infrared spatial heterodyne spectrometers. In *Proceedings of SPIE — Infrared Imaging Systems: Design, Analysis, and Testing X (In press)*. SPIE — The International Society for Optical Engineering.
- Descour, M. R. (1996). The throughput advantage in imaging Fourier-transform spectrometers. In Descour, M. R. and Mooney, J. M., editors, *Proceedings of SPIE — Imaging Spectrometry II*, volume 2819, pages 285–290. SPIE — The International Society for Optical Engineering.
- Dorf, R. C. (1993). *The Electrical Engineering Handbook*. CRC Press, Boca Raton.
- Eismann, M. T., Schwartz, C. R., Cederquist, J. N., Hackwell, J. A., and Huppi, R. J. (1996). Comparison of infrared imaging hyperspectral sensors for military target detection applications. In Descour, M. R. and Mooney, J. M., editors, *Proceedings of SPIE — Imaging Spectrometry II*, volume 2819, pages 91–101. SPIE — The International Society for Optical Engineering.
- Feng, X., Schott, J. R., and Gallagher, T. W. (1994). Modeling and testing of a modular imaging spectrometer instrument. In Holst, G. C., editor, *Proceedings of SPIE — Infrared Imaging Systems: Design, Analysis, Modeling, and Testing V*, volume 2224, pages 215–224. SPIE — The International Society for Optical Engineering.
- Gaskill, J. D. (1978). *Linear Systems, Fourier Transforms, and Optics*. Wiley Series in Pure and Applied Optics. John Wiley & Sons, New York.
- Goetz, A. F. H. (1995). Imaging spectrometry for remote sensing: Vision to reality in 15 years. In Descour, M. R., Mooney, J. M., Perry, D. L., and Illing, L., editors, *Proceedings of SPIE — Imaging Spectrometry*, volume 2480, pages 2–13. SPIE — The International Society for Optical Engineering.
- Gonzalez, R. C. and Woods, R. E. (1993). *Digital Image Processing*. Addison-Wesley Publishing Company.
- Griffiths, P. R. and de Haseth, J. A. (1986). *Fourier Transform Infrared Spectroscopy*, volume 83 of *Chemical Analysis*. John Wiley & Sons, New York.

- Hammer, P. D., Peterson, D. L., and Smith, W. H. (1995). Imaging interferometry for terrestrial remote sensing — digital array scanned interferometer instrument developments. In Descour, M. R., Mooney, J. M., Perry, D. L., and Illing, L., editors, *Proceedings of SPIE — Imaging Spectrometry*, volume 2480, pages 153–164. SPIE — The International Society for Optical Engineering.
- Hammer, P. D., Valero, F. P. J., and Peterson, D. L. (1992). Remote sensing of earth’s atmosphere and surface using a digital array scanned interferometer: A new type of imaging spectrometer. *Journal of Imaging Science and Technology*, 36(5):417–421.
- Hammer, P. D., Valero, F. P. J., Peterson, D. L., and Smith, W. H. (1993). An imaging interferometer for terrestrial remote sensing. In Vane, G., editor, *Proceedings of SPIE — Imaging Spectrometry of the Terrestrial Environment*, volume 1937, pages 244–255. SPIE — The International Society for Optical Engineering.
- Hayden Smith, W. M. and Schempp, W. V. (1991). Digital array scanned interferometers for astronomy. *Experimental Astronomy*, 1:389–405.
- Herring, M., Chrien, T., Duval, V., and Krabach, T. (1993). Imaging spectrometry — concepts and system trade-offs. In Buscher, H., editor, *Infrared and Millimeter-Wave Engineering*, volume 1874, pages 11–23. SPIE — The International Society for Optical Engineering.
- Holbert, E., Rafert, J. B., and Ryan, T. L. (1995). Verification of the spectral performance model of an imaging Fourier transform spectrometer. In Descour, M. R., Mooney, J. M., Perry, D. L., and Illing, L., editors, *Proceedings of SPIE — Imaging Spectrometry*, volume 2480, pages 398–409. SPIE — The International Society for Optical Engineering.
- Horton, R. F. (1996). Optical design for a high Étendue imaging Fourier transform spectrometer. In Descour, M. R. and Mooney, J. M., editors, *Proceedings of SPIE — Imaging Spectrometry II*, volume 2819, pages 300–315. SPIE — The International Society for Optical Engineering.
- Horton, R. F., Conger, C. A., and Pellegrino, L. S. (1997). High Étendue imaging Fourier transform spectrometer — initial results. In Descour, M. R. and Shen, S. S., editors, *Proceedings of SPIE — Imaging Spectrometry III*, volume 3118, pages 380–390. SPIE — The International Society for Optical Engineering.
- Johnston, S. F. (1991). *Fourier Transform Infrared, a Constantly Evolving Technology*. Ellis Horwood Series in Analytical Chemistry. Ellis Horwood Limited.
- Junttila, M.-L. (1992). Stationary Fourier-transform spectrometer. *Applied Optics*, 31(21):4106–4112.
- Laubscher, B. E., Cooke, B. J., Goeller, R. M., Obbink, G., Smith, B. W., LaDelfe, P., Villeneuve, P. V., Berggren, R. R., Milligan, S., Howard, J. W., Norton, P. R., Stegall, M., Burgett, C. B., Harlander, J. M., and Horton, R. F. (1999). The infrared imaging spatial heterodyne spectrometer (irishs) experiment effort. In *Proceedings of SPIE — Infrared Imaging Systems: Design, Analysis, and Testing X (In press)*. SPIE — The International Society for Optical Engineering.
- Lucey, P. G., Horton, K., Williams, T., Hinck, K., Budney, C., Rafert, J. B., and Rusk, T. B. (1993). SMIFTS: A cryogenically-cooled spatially-modulated imaging infrared interferometer spectrometer. In Vane, G., editor, *Proceedings of SPIE — Imaging Spectrometry of the Terrestrial Environment*, volume 1937, pages 130–141. SPIE — The International Society for Optical Engineering.

- Lucey, P. G., Williams, T., and Horton, K. (1995). Characterization of SMIFTS, spatially modulated fourier transform spectrometer. Internet: <http://ltpwww.gsfc.nasa.gov/ISSR-95/characte.htm>.
- Meigs, A. D., Butler, E. W., Jones, B. A., Otten III, L. J., Sellar, R. G., and Rafert, J. B. (1996). Airborne visible hyperspectral imaging spectrometer: optical and system level description. In Descour, M. R. and Mooney, J. M., editors, *Proceedings of SPIE — Imaging Spectrometry II*, volume 2819, pages 278–284. SPIE — The International Society for Optical Engineering.
- Mertz, L. (1965). *Transformations in Optics*. John Wiley & Sons, New York.
- Nieke, J., Schwarzer, H., Neumann, A., and Zimmermann, G. (1997). Imaging spaceborne and airborne sensor systems in the beginning of the next century. Internet: <http://www.ba.dlr.de/NEWS/ws5/sensor/sensors.html>.
- Norton, M. C., Kindsfather, R., and Dixon, R. (1995). Infrared (3 to 12 μm) narrowband and hyperspectral imaging review. In Descour, M. R., Mooney, J. M., Perry, D. L., and Illing, L., editors, *Proceedings of SPIE — Imaging Spectrometry*, volume 2480, pages 295–313. SPIE — The International Society for Optical Engineering.
- Oermann, R. and Smithson, T. (1995). The DREV infrared imaging spectrometer (phase II). Internet: <http://ltpwww.gsfc.nasa.gov/ISSR-95/drevinfr.htm>.
- Okamoto, T., Kawata, S., and Minami, S. (1986). A photodiode array Fourier transform spectrometer based on a birefringent interferometer. *Applied Spectroscopy*, 40(5):691–695.
- Otten III, L. J., Butler, E. W., Rafert, J. B., and Sellar, R. G. (1995). The design of an airborne Fourier transform visible hyperspectral imaging system for light aircraft environmental remote sensing. In Descour, M. R., Mooney, J. M., Perry, D. L., and Illing, L., editors, *Proceedings of SPIE — Imaging Spectrometry*, volume 2480, pages 418–423. SPIE — The International Society for Optical Engineering.
- Otten III, L. J., Meigs, A. D., Sellar, R. G., and Rafert, J. B. (1996). Measured performance of an airborne Fourier transform hyperspectral imager. In Descour, M. R. and Mooney, J. M., editors, *Proceedings of SPIE — Imaging Spectrometry II*, volume 2819, pages 291–299. SPIE — The International Society for Optical Engineering.
- Persky, M. J. (1995). A review of spaceborne infrared Fourier transform spectrometers for remote sensing. *Rev. Sci. Instrum.*, 66(10):4763–4797.
- Press, W. H., et al. (1992). *Numerical recipes in C : the art of scientific computing*. Cambridge University Press, New York, 2 edition.
- Pritt, Jr., A. T., Kupferman, P. N., Young, S. J., and Keller, R. A. (1997). Imaging LWIR spectrometers for remote sensing applications. In Holst, G. C., editor, *Proceedings of SPIE — Infrared Imaging Systems: Design, Analysis, Modeling, and Testing VIII*, volume 3063, pages 138–149. SPIE — The International Society for Optical Engineering.
- Rafert, B., Lucey, P., and Newby, H. (1992). A spatially modulated imaging fourier transform spectrometer (SMIFTS) for astronomical and booster plume observations. In Ulrich, M.-H., editor, *ESO Conference and Workshop Proceedings — Progress in Telescope and Instrumentation Technologies*, volume 42, page 721, Garching, Germany. ESO.

- Rafert, J. B., Sellar, G., and Otten III, L. J. (1995). An interactive performance model for spatially modulated Fourier transform spectrometers. In Descour, M. R., Mooney, J. M., Perry, D. L., and Illing, L., editors, *Proceedings of SPIE — Imaging Spectrometry*, volume 2480, pages 410–417. SPIE — The International Society for Optical Engineering.
- Rapp, R. J. and Register, H. I. (1995). Infrared imaging spectroradiometer program overview. In Descour, M. R., Mooney, J. M., Perry, D. L., and Illing, L., editors, *Proceedings of SPIE — Imaging Spectrometry*, volume 2480, pages 314–321. SPIE — The International Society for Optical Engineering.
- Revercomb, H. E., Buijs, H., Howell, H. B., LaPorte, D. D., Smith, W. L., and Sromovsky, L. A. (1988). Radiometric calibration of IR Fourier transform spectrometers: solution to a problem with the high-resolution interferometer sounder. *Applied Optics*, 27(15):3210–3218.
- Schott, J. R. (1997). *Remote Sensing, The Image Chain Approach*. Oxford University Press, New York.
- Schumann, L. W., Lomheim, T., and Johnson, J. F. (1997). Design constraints on advanced two-dimensional LWIR focal planes for imaging Fourier transform spectrometer sensors. In Holst, G. C., editor, *Proceedings of SPIE — Infrared Imaging Systems: Design, Analysis, Modeling, and Testing VIII*, volume 3063, pages 150–163. SPIE — The International Society for Optical Engineering.
- Sellar, R. G. and Rafert, J. B. (1994). Effects of aberrations on spatially modulated Fourier transform spectrometers. *Optical Engineering*, 33(9):3087–3092.
- Smith, W. H. and Hammer, P. D. (1996). Digital array scanned interferometer: sensor and results. *Applied Optics*, 35(16):2902–2909.
- Steel, W. H. (1983). *Interferometry*. Cambridge University Press, New York.
- Sweedler, J. V. and Denton, M. B. (1989). Spatially encoded Fourier transform spectroscopy in the ultraviolet to near-infrared. *Applied Spectroscopy*, 43(8):1378–1384.
- Tanner, D. B. and McCall, R. P. (1984). Source of problem with Fourier transform spectroscopy. *Applied Optics*, 23(14):2363–2368.
- Tantalo, F. J. (1996). Modeling the MTF and noise characteristics of an image chain for a synthetic image generation system. Master’s thesis, Rochester Institute of Technology.
- Treffers, R. R. (1977). Signal-to-noise ratio in Fourier spectroscopy. *Applied Optics*, 16(12):3103–3106.
- Villemaire, A., Fortin, S., and Giroux, J. (1995). An imaging Fourier transform spectrometer. In Descour, M. R., Mooney, J. M., Perry, D. L., and Illing, L., editors, *Proceedings of SPIE — Imaging Spectrometry*, volume 2480, pages 387–397. SPIE — The International Society for Optical Engineering.
- Wadsworth, W. and Dybwad, J. P. (1997). Ultra high speed chemical imaging spectrometer. In Fallahi, M. and Howden, E., editors, *Proceedings of SPIE — Electro-Optical Technology for Remote Chemical Detection and Identification II*, volume 3082, pages 148–154. SPIE — The International Society for Optical Engineering.

- Wang, J., Anderson, G. P., Revercomb, H. E., and Knuteson, R. O. (1996). Validation of FAS-COD3 and MODTRAN3: comparison of model calculations with ground-based and airborne interferometer observations under clear-sky conditions. *Applied Optics*, 35(30):6028–6040.
- Wolfe, W. L. (1997). *Introduction to Imaging Spectrometers*, volume 25 of *Tutorial Text Volume*. SPIE Optical Engineering Press.
- Yap, B. K., Blumberg, W. A. M., and Murphy, R. E. (1982). Off-axis effects in a mosaic Michelson interferometer. *Applied Optics*, 21(22):4176–4182.

Glossary

DASI	Digital Array Scanned Interferometer	19
DIRSIG	DIRS Image Generation model	3
DIRS	Digital Imaging and Remote Sensing	3
FASCODE	Fast Atmospheric Signature CODE	3
FFT	Fast Fourier Transform	2
FOV	Field Of View	4
FPA	Focal Plane Array	24
FTS	Fourier Transform Spectrometers	2
FT	Fourier Transform	10
FWHM	Full Width at Half Max	5
GIFOV	Ground Instantaneous Field Of View	39
GUI	Graphic User Interface	57
HITRAN	High-resolution TRANsmission molecular database	7
IFTS	Imaging Fourier Transform Spectrometer	4
ILS	Instrument LineShape	42
LOS	Line Of Sight	46
MODTRAN	MODerate resolution TRANsmittance code	3
MTF	Modulation Transfer Function	46
OPD	Optical Path Difference	5
PSF	Point Spread Function	47
RP	Resolving Power	5
SNR	Signal-to-Noise Ratio	2
ZPD	Zero Path Difference	5